

Università degli Studi di Bologna

FACOLTA' DI INGEGNERIA

INTERNATIONAL MASTER COURSE IN CIVIL ENGINEERING

DICAM

Dipartimento di Ingegneria Civile, Ambientale e dei Materiali

TESI DI LAUREA

in

Earthquake Engineering

**SEISMIC RESPONSE OF TANK-FLUID SYSTEMS:
STATE OF THE ART REVIEW AND
DYNAMIC BUCKLING ANALYSIS OF A STEEL TANK
WITH THE ADDED MASS METHOD**

CANDIDATO:

Matteo Tavano

RELATORE:

Chiar.mo Prof. Marco Savoia

CORRELATORE:

Prof. Nicola Buratti

Anno Accademico 2010/11

Sessione III

“Questa Tesi non ci sarebbe senza l’aiuto, la guida e la spinta di Nicola Buratti. Colgo l’occasione per ringraziare ed esprimere tutta la mia stima nei Suoi confronti.

Ringrazio i miei genitori. Senza di voi questo percorso durato cinque anni non sarebbe mai iniziato e questa Tesi finale spero possa ripagare almeno una parte dei vostri sforzi.

Ringrazio tutto il resto della family, in particolare Giulia, i miei compagni d’avventura Spacchio e Christian e tutti i miei amici. Grazie per l’aiuto e il supporto che mi avete sempre dato, chi in maniera diretta e chi in maniera indiretta. Per me è stato ugualmente importante.

Ringrazio i Professori Alessandro Marzani e Luca Lanzoni, il cui incontro è stato fondamentale nella mia carriera universitaria e per la mia formazione come ingegnere.

Un grazie speciale al Bone e a Vania. Voi sapete perché.”

PART I: Methods of Analysis and Design of Liquid-Storage Tanks under Earthquake Excitation.

Keywords: *Liquid-storage tanks; dynamic response; earthquake excitation; code provisions; buckling of steel shells; elephant's foot buckling.*

PART II: Numerical Modeling and Dynamic Analyses of a Clamped Steel Tank.

Keywords: *Finite element model, added mass method, time-history analyses, dynamic buckling, Budiansky-Roth criterion, fragility curves.*

Contents

Foreword	XIII
Preface.....	XV

PART I: Methods of Analysis and Design of Liquid-Storage Tanks under Earthquake Excitation.

1. Dynamics of tank-fluid systems.....	3
1.1 Possible failure modes	3
1.2 What's behind the codes.....	8
1.2.1 System, assumptions and terminology.....	8
1.2.2 Governing equations and boundary conditions	9
1.2.3 Impulsive solution for rigid tanks.....	11
1.2.4 Convective solution for flexible tanks	12
1.2.5 Recast expressions	13
1.2.6 Fluid-tank interaction under assumed mode.....	15
1.3 Mechanical models.....	17
1.3.1 Analogues currently available in literature	17
1.3.2 Unanchored tanks – General remarks and mechanical models.....	21
1.3.3 Fluid-structure interaction.....	25
1.3.4 Soil-structure interaction	29
1.4 Draft conclusions and research needs.....	31
2. Review of codes provisions	35
2.1 Types of tanks	35
2.2 Rigid vs Deformable tanks.....	36
2.2.1 Basic assumptions and terminology.....	36
2.2.2 Eurocode 8: rigid anchored tanks.....	39
2.2.3 Eurocode 8: deformable anchored tanks	42
2.2.4 Eurocode 8: a simplified procedure for deformable anchored tanks.....	45
2.2.5 ACI 350.3 and API 650: concrete and steel tanks.....	48
2.2.6 Vertical component of the seismic action.....	54
2.2.7 A worked example	57

2.3	Anchored vs Unanchored tanks	63
2.3.1	<i>Eurocode 8: unanchored tanks</i>	63
2.3.2	<i>API 650: self-anchored steel tanks</i>	65
2.3.3	<i>ACI 350.3: uplifting in concrete tanks</i>	67
2.3.4	<i>A worked example</i>	68
2.4	Rigidly supported vs Flexibly supported tanks.....	70
2.4.1	<i>Simplified model and its application to Eurocode 8</i>	70
2.4.2	<i>A more rough procedure from NZSEE</i>	72
2.4.3	<i>ACI 350.3: the importance of the base connection</i>	73
2.5	Assessment of codes guidelines	76
2.5.1	<i>Seismic design loads</i>	76
2.5.2	<i>Damping ratios and behavior factors</i>	77
2.5.3	<i>Combination of impulsive and convective effects</i>	79
2.5.4	<i>Enhancement of uplift analysis in current standards</i>	80
2.5.5	<i>Soil-structure interaction</i>	84
2.5.6	<i>Combined action of horizontal and vertical earthquake components</i>	87
2.6	Concluding remarks and future deepenings	89
3.	Buckling of steel tanks	91
3.1	Buckling modes	91
3.1.1	<i>Elastic buckling</i>	91
3.1.2	<i>Elastic-plastic buckling</i>	93
3.1.3	<i>Secondary buckling</i>	97
3.2	Buckling in current standards	103
3.2.1	<i>API 650</i>	103
3.2.2	<i>A worked example</i>	106
3.2.3	<i>ECCS recommendations</i>	106
3.2.4	<i>Eurocode 8</i>	111
3.3	Design of a new tank shell for seismic loads	115
3.4	Concluding remarks and possible enhancements.....	119
 PART II: Numerical Modeling and Dynamic Analyses of a Clamped Steel Tank.		
4.	Finite element model.....	123
4.1	Tank model	123
4.1.1	<i>Geometry, material and boundary conditions</i>	123
4.1.2	<i>Mesh details</i>	124
4.2	Liquid model.....	131

4.2.1	<i>The added mass model</i>	131
4.2.2	<i>Added mass calculation</i>	133
4.3	Systems nonlinearities	135
4.3.1	<i>Material nonlinearity</i>	135
4.3.2	<i>Geometric nonlinearity</i>	136
5.	Dynamic analyses	139
5.1	Modal analysis	139
5.1.1	<i>Effect of pre-stress states on the impulsive modes of vibration</i>	139
5.1.2	<i>Fundamental mode shapes</i>	142
5.2	Dynamic buckling analyses	144
5.2.1	<i>Setting analysis</i>	144
5.2.2	<i>Damping of the tank-fluid system</i>	146
5.2.3	<i>Selection of the earthquake accelerograms</i>	147
5.2.4	<i>Implicit time integration method</i>	155
5.3	Results	157
5.3.1	<i>Observed tank behavior</i>	157
5.3.2	<i>Dynamic buckling criterion</i>	161
5.3.3	<i>Control node selection</i>	165
5.3.4	<i>The influence of plasticity</i>	166
5.3.5	<i>Failure modes</i>	171
5.4	Fragility curves development	174
5.4.1	<i>Generalities on fragility curves</i>	174
5.4.2	<i>New accelerograms and dynamic analyses</i>	176
5.4.3	<i>Efficiency of ground motion intensity measures</i>	181
5.4.4	<i>Fragility curves</i>	183
6.	Concluding remarks	187
6.1	Conclusions	187
6.2	Future works	188
Appendix A	191
Appendix B	193
Appendix C	195
Appendix D	201
Appendix E	207

Notation	215
References	221

Foreword

The earthquakes certainly represent one of the most critical events to the safety of industrial plants. In order to estimate the risk associated with the industrial plants, it is of crucial importance the knowledge of the vulnerability of each single component of the plant itself. In fact the structural collapse of just one of these components can trigger more catastrophic events such as explosions, fire, dispersion of toxic materials, water shortages, pollution or contamination, thus putting in danger the life of people who work in the plant and who live in the urban area where the plant is located. A key aspect in the risk analysis of industrial plants is the detailed knowledge of each component and sub-system, in terms of design installation and operation mode. This step gives a contribution to the ranking of facilities depending on hazard or the individuation of critical components that can dramatically increase the seismic risk. To this aim it is common to divide the system in a number of sub-systems that have to be analyzed in detail up to component level. These are the basic information for the construction of fault-tree and sequences of events. A review of the printout of design of the plant and all information relative to the boundary conditions is fundamental; at the same time the inspection of the plant is recommended to establish the maintenance status of the facilities and upgrade models for capacity estimation.

Industrial facilities show a large number of constructions and structural components. As materials are concerned, it is easy to recognize that both reinforced concrete and steel constructions are commonly used, even in combination like composite structures. Large installations can be characterized by use of pre-stressed members, especially when long spans are required. However, it is worth noting that a large variety of functions have to be accomplished by structural components so that the latter can be classified as follows:

- *Building like structures*: administration buildings, control buildings, substations, warehouses, firehouses, maintenance buildings, and compressor shelters or buildings. These are structures having a lateral force resisting system similar to those of building systems, such as braced frames, moment resisting frames or shear wall systems.
- *Non-Building like structures*: such class of structures covers many industrial constructions and self-supporting equipment items found in a typical industrial plant, such as tanks, vertical vessels, horizontal vessels and exchangers, stacks and towers.

Atmospheric tanks certainly represent the most spread and common component in an industrial plant; this is the reason why the present thesis is addressed to the increase of knowledge about their methods of analysis and design. Large-capacity ground-supported cylindrical tanks are used to store a variety of liquids or liquid-like materials, e.g. water for drinking and fire-fighting, petroleum, chemicals, liquefied natural gas and wastes of different forms. Satisfactory performance of tanks during strong ground shaking is crucial for modern facilities. Tanks that were inadequately designed have suffered extensive damage during past earthquakes.

Preface

Primary objectives of the thesis are: (a) to provide an overview of the salient aspects of the dynamic response of vertical, cylindrical, ground-supported tanks storing a homogeneous liquid; (b) to present different methods of analysis and design criteria, especially looking at the different codes provisions but also at alternative simplified procedures or innovative approaches given by other authors; (c) to set up a finite element model able to correctly represent the seismic behavior of the fluid-tank system; (d) investigate the complex phenomenon of buckling by means of dynamic numerical simulations and by establishing a buckling criterion; (e) to provide comments on the seismic vulnerability of liquid-storage tanks, using the results of dynamic analyses for the development of fragility curves. Secondary objectives are: (f) to create a sort of archive, based on which a designer can get design information/criteria according to the kind of tank he has to deal with; (g) to give a contribution in understanding the efficiency of different ground motion intensity measures with respect to the structural response (h) to suggest areas where possible future works should be oriented, especially looking at those topics where current design guidelines need further development.

The thesis is organized into two parts: I. Methods of Analysis and Design of Liquid-Storage Tanks under Earthquake Excitation; II. Numerical Modeling and Dynamic Analyses of a Clamped Steel Tank. Part I includes the first three chapters, where all issues relating to methods of seismic analysis and design of concrete and steel tanks are discussed in detail. In the second Part, including chapters four, five and six, a specific type of tank is chosen and a finite element model of it is set up. The results of modal analysis and dynamic simulations using the added mass technique for fluid modeling are presented, discussed and compared to those available in literature. Furthermore, based on these results, fragility curves are developed.

The first chapter deals with the theoretical basis of the dynamic behavior of liquid-storage tanks. Here, after a brief discussion on the possible failure modes, the governing equation and the analytical solution are presented. Then, the most important mechanical models (or analogues) used by the various international codes are introduced. The main studies of the most important scientist and engineers who investigated the seismic behavior of liquid-storage tanks are listed in chronological order. In this way the reader can have an idea of the successive developments on these topic and can understand the basis of the current sophisticated models. The modeling

aspects of the fluid-tank-soil system are covered, but since the subject is very wide and not yet fully understood, also suggestions on possible future works are given.

In the second chapter the main categories of tanks and the most important classification criteria are discussed. Here, attention is given to how the various international codes treat the different tanks categories. Codes provisions are analyzed and compared in detail. Such provisions are mainly related to the analysis and modeling aspects, but also to the design seismic forces calculation and verification criteria. The codes reviewed are: ACI 350.3, API 650 and Eurocode 8, but also New Zealand guidelines are sometimes mentioned. As the different guidelines are illustrated, also a numerical example is worked out through the chapter. The chapter ends with an assessment of code guidelines; here all the codes are compared and the results of the worked example are discussed. The quality of the different codes provisions is also assessed on the basis of numerical results and research works of many different authors. Areas where possible developments of the current codes should be oriented are indicated.

The third chapter is entirely devoted to the buckling phenomenon, which definitely plays a fundamental role in steel tanks design due to the small thicknesses used for this class of structures. First, an overview on the possible buckling modes with related causes and effects is given, especially looking at the correspondence between damages observed in real tanks during past earthquakes and analytical studies on simplified models performed by different authors. Then, attention is given on how buckling is treated by the various codes and deficiencies on the subject are highlighted. Since in the codes there is not a relevant theoretical background, but just simple formulas to be applied in order to verify structural elements, a great effort is done in this chapter in order to understand what is behind the above mentioned formulas and to relate them to the possible buckling modes. The API verification formulas are then applied to a worked example. Chapter three also involves very brief notes on possible methods to strengthen tanks against “elephant’s foot” buckling. Since these methods make use of innovative techniques that are still under verification, this could be an area of interest for future studies. The chapter ends with the proposal of a very simple but efficient method to preliminarily design the tank’s thickness against elastic-plastic buckling.

In the fourth chapter the tank model used for numerical computations is presented. All the details about geometry, materials, boundary conditions and sources of nonlinearity are highlighted. The method used to obtain a good finite element mesh on the tank is discussed. The added mass technique used to model the fluid is shown and the added masses are calculated explicitly.

The fifth chapter can be considered as the central chapter of the second part. Here, the type of dynamic analysis used to study the buckling phenomenon is explained in detail, from the governing equation and the numerical method used to solve it to the criterion chosen to select the earthquake accelerograms. The results of the dynamic buckling simulations are presented, compared and discussed in details. Prior to the nonlinear dynamic simulations, a modal analysis is also performed in this chapter, with the aim of studying the dynamic properties of the model. At the end of the chapter, the results obtained from the dynamic analyses of the added mass model of the tank are used to develop fragility curves and to understand the efficiency of different ground motion intensity measures on the structural response.

The sixth chapter collects all the conclusions resulting from the analyses carried out in Part II. Also suggestions on possible improvements and future developments of this thesis can be found in this last chapter.

Appendix A contains the mathematical formulation of the Bessel's functions. These functions are found in the solution of the fundamental equation that governs the dynamic behavior of liquid-storage tanks but since they are not recurrent in typical civil engineering problems, it was considered important to give further information about them. Appendix B contains the MATLAB code used to calculate the added mass. Appendices C and D contain the MATLAB codes used to generate the input files for ABAQUS and run the analyses. Appendix E contains the MATLAB codes use to handle and elaborate the output files from ABAQUS.

As already mentioned, one of the main objectives of the thesis is the comparison between the different provisions of the various codes. So, a uniform notation among all the codes has been used in order to facilitate the reader in doing and understanding this comparison. In this view a "Notation" Section has been prepared at the end of the thesis. However, the corresponding formulas in the codes (in their original notation) are always indicated.

Finally, it is noted that the subject is very wide and a full coverage of it is not possible due to clear reasons of space and time limitation. Therefore, to the opinion of the author, since sometimes it is very useful just to know "where to find information" about a specific problem, a great importance is given also to the last section "References".

PART I

**METHODS OF ANALYSIS AND DESIGN
OF LIQUID-STORAGE TANKS UNDER
EARTHQUAKE EXCITATION**

Dynamics of tank-fluid systems

1.1 Possible failure modes

The complicated deformed configurations of liquid storage tanks and the interaction between fluid and structure result in a wide variety of possible failure mechanisms. This section discusses the different collapse modes in the light of the performances of existing tanks during past earthquakes (Northridge earthquake, [6], and Imperial Valley earthquake, [19]).

- *Shell Buckling Mode.* One of the most common forms of damage in steel tanks involves outward buckling of the bottom shell courses, a phenomenon known as “elephant’s foot” buckling. It usually occurs in tanks with a low height to radius ratio. Initial studies claimed that the “elephant’s foot” buckle mechanism results from the combined action of vertical compressive stresses exceeding the critical stress and hoop tension close to the yield limit. However, Rammerstorfer et al. in [16] attributed the bulge formation to three components; the third being the local bending stresses due to the restraints at the tank base. Seiler, Wunderlich et al. in [39] and [42] differentiated this phenomenon for slender and broad tanks. The “elephant’s foot” buckle often extends around the circumference of the tank. Buckling of the lower courses has occasionally resulted in the loss of tank contents due to weld or piping fracture and, in some cases, total collapse of the tank. Figures 1.1.1 show two examples of “elephant’s foot” buckle for tanks destroyed by an earthquake. In Figure 1.1.2 a second kind of buckling is reported: the so called “diamond shape” buckling. It is an elastic buckling phenomenon due to the presence of high axial compressive stresses. The rocking motion which develops at the base of unanchored tanks generates very high compressive axial stresses surrounding the contact zone which in turn lead to the “diamond shape” buckle. This kind of damage may also occur well above the base of the tank where the hydrodynamic pressure, which leads to an increase in the elastic buckling load, is small as compared to its magnitude at the tank base, see Figure 1.1.3.

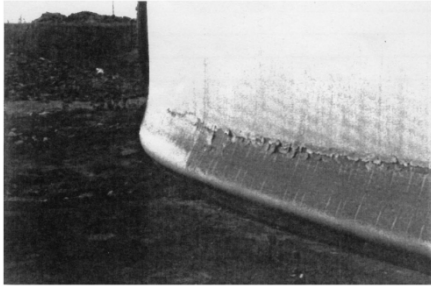


Fig. 1.1.1: “Elephant’s foot” buckling (after [20]-[30]).

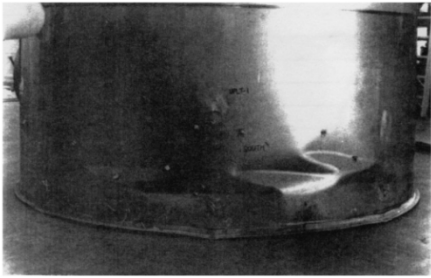


Fig. 1.1.2: Diamond shape buckling (after [18]).

Fig. 1.1.3: Elastic buckling at the top (after [30]).

- *Damage and collapse of tank roofs.* A sloshing motion of the tank contents occurs during earthquake motion, as explained in Section 1.2. The actual amplitude of motion at the tank circumference has been estimated, on the basis of scratch marks produced by floating roofs, to have exceeded several meters in some cases, Hamdan [18]. For full or near full tanks, the free sloshing results in an upward pressure distribution on the roof. Common design codes do not provide guidance on the seismic design of tank roof systems for slosh impact forces. Modern tanks built after 1980 and designed to resist “elephant’s foot buckling” or other failure modes may still have inadequate designs for roof slosh impact forces. In past earthquakes, damage has frequently occurred to the joints between walls and cone roof, with accompanying spillage of tank contents over the top of the wall. Extensive buckling of the upper courses of the shell walls has occurred. Floating roofs have also sustained extensive damage to support guides from the sloshing of contents. Extensive damage to roofs can cause extensive damage to upper course of a steel tank. Less common are roof damages due to wind suction, Figure 1.1.5. However, roof damage or broken appurtenances, although expensive to repair, usually lead to more than a third of total fluid contents loss.
- *Anchorage Failure.* Many steel tanks have hold-down bolts, straps or chairs. However, these anchors may be insufficient to withstand the total imposed load in large earthquake events and still can be damaged. As noted by field inspection, seismic overloads often

result in anchor pull-out, stretching or failure. However, failure of an anchor does not always lead to loss of tank contents.

- *Tank Support System Failure.* Steel and concrete storage tanks supported above grade by columns or frames have failed because of the inadequacy of the support system under lateral seismic forces, see Figure 1.1.6. Such failure most often leads to complete loss of contents.
- *Differential settlements and partial uplifting.* The January, 1994, Northridge earthquake had an immediate impact on the City of Los Angeles Department of Water and Power's (LADWP) water system. Between all types of damages observed, Beverly Glen Tank experienced differential settlement varying from 7.5 to 20.3 cm and Coldwater Canyon Tank incurred a nearly uniform 10 cm settlement. Moreover, it was estimated that the Zelzah Tank uplifted well over 30 cm due to a poor anchorage system. The valve bodies on the inlet/outlet lines sheared from vertical displacements caused by tanks settlement or uplift.
- *Connecting Pipe Failure.* One of the most common cause of loss of tank contents in earthquakes has been the fracture of piping at inlet/outlet (I/O) connections to the tank. This generally results from large vertical displacements of the tank caused by tank buckling, wall uplift or foundation failure. Failure of rigid piping (including cast iron valves and fittings, Figure 1.1.4b) that connects adjacent tanks has also been caused by relative horizontal displacements of the tanks. Another failure mode has been the breaking of pipes that penetrate into the tank from underground due to the relative movement of the tank and pipe, Figure 1.1.7. Water leaking from the broken pipe connections cause soil erosion and this can undermine the performances of the closest tanks.

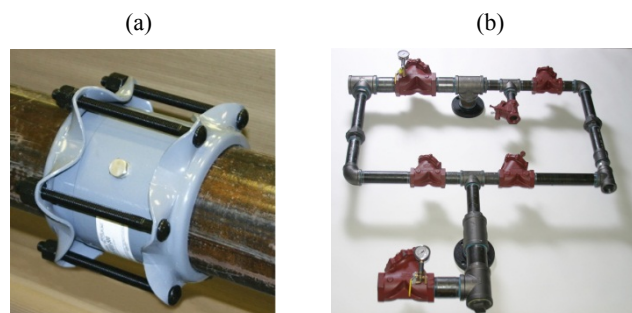


Fig. 1.1.4: Examples of (a) flexible piping connection (Dresser couplings) and (b) brittle piping connections (cast iron valves and fittings).

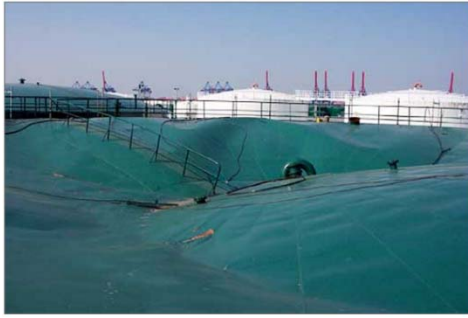


Fig. 1.1.5: Damage to tank roof caused by wind suction (underpressure).



Fig. 1.1.6: Elevated tank overturning.



Fig. 1.1.7: Water loss due to breaking of tank-pipe connection.



Fig. 1.1.8: Tank uplifting.

In Table 1.1.1 from [18], Hamdan F.H. summarizes some of the buckling damage and collapse of steel tanks during past earthquakes. It can be seen that unanchored tanks are more prone to buckling. Furthermore, there is a very little published data on the seismic-induced buckling of concrete tanks. However, observations from available field reports on the structural response of tanks during recent earthquake indicate that steel tanks, rather than concrete tanks, are more susceptible to damage and eventual collapse. This is one of the reason why the present thesis is mainly addressed to the steel tank analysis and design.

Pre-stressed concrete tanks have become common in the liquid-storage systems over the last twenty years. The newer concrete tank walls are reinforced with circumferentially-wrapped, high-strength pre-stressing steel cables and vertical post-tensioning bars (Figures 1.1.9). The wall-to-footing connection is a flexible joint utilizing hard rubber bearing pads and seismic anchor cables (Section 2.4.3). The system allows limited rotation and movement, providing ductility to the joint. The cast-in-place reinforced concrete roof functions as a rigid diaphragm. All of the pre-stressed concrete tanks owned by LADWP performed well during the Northridge earthquake. Damages were limited to minor spalling of concrete, due to the

earthquake-induced pounding action, at a roof panel joint (Figure 1.1.10a) and opening of narrow gaps between roof panels.

Tank name	Radius R (m)	Height h (m)	Number anchors	% Full	Thick. (mm)	Damage	Earthquake	Type of product
AL-1	3.05	12.2	0	100	4.766	i ^a	Alaska 1964	* ^d
AL-2	4.27	12.2	0	100	4.766	ii ^b	Alaska 1964	* ^d
AL-3	4.575	10.675	0	100	4.766	i ^a	Alaska 1964	* ^d
AL-4	6.1	12.963	0	100	7.116	i ^a	Alaska 1964	* ^d
AL-5	6.405	12.2	0	100	5.846	i ^a	Alaska 1964	* ^d
Sesnon	14.02	12.16	0	95	N/A	i ^a	San Fernando, 1971	Water
Wash	15.24	5.565	12	50	17.5	iii ^c	San Fernando, 1971	Water
SJ1/A	3.75	12.667	29	100	6.375	i ^a	San Juan, 1977	Wine
SJ2/	3.83	10.97	27	100	4.596	i ^a	San Juan, 1977	Wine
SJ4/	2.6	12.0	16	100	4.68	ii ^b	San Juan, 1977	Wine
IP-5	7.289	10.63	0	73	N/A	i ^a	Imperial Valley, 1979	Gasoline
IP13	6.283	13.27	0	89	6.93	i ^a	Imperial Valley, 1979	Gasoline
GV1	1.983	6.096	8	100	1.981	ii ^b	Greenville, 1980	Wine
GV3	1.448	5.337	2	100	1.981	i ^a	Greenville, 1980	Wine
T-400	8.38	7.32	0	75	N/A	i ^a	Coalinga, 1983	Oil
T-262	10.668	10.668	0	100	N/A	iii ^c	Coalinga, 1983	Oil
3978	6.48	8.53	0	100	N/A	i ^a	Loma Prieta, 1989	Lube oil
A	6.48	8.53	0	82	N/A	i ^a	Loma Prieta, 1989	Lube oil
Nor 1	9.14	9.0	0	98	N/A	i ^a	Northridge, 1994	Water
BG	15.24	11.67	0	94.5	N/A	i ^a	Northridge, 1994	Water
ANC	5.64	8.63	0	88.5	10	i ^a	Northridge, 1994	Water

Table 1.1.1: Buckled and collapsed steel tanks during past earthquakes (after [18]).

^a i: Buckled.
^b ii: Collapsed.
^c iii: Buckling in upper tank walls.
^d *: specific gravity =0.8.

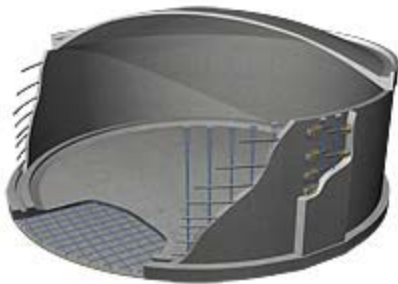


Fig. 1.1.9: Examples of rebar arrangement in concrete tanks.

(a)

(b)

Fig. 1.1.10: Concrete spalling (a) at the roof-wall joint (b) at the base.



(a)

(b)



Fig. 1.1.11: (a) Silo with extensive spalling and exposed rebar (b) Close up of exposed rebar.

1.2 What's behind the codes

1.2.1 System, assumptions and terminology

The first system considered is shown in Figure 1.2.1.1. It is a rigid circular cylinder of radius R fixed to a rigid base. The tank is filled with a fluid of density ρ to a level H . The fluid is assumed to be incompressible and inviscid (or nonviscous). The fluid tank-system is presumed to be subjected to a horizontal ground acceleration directed along the x -axis, $\ddot{x}(t)$. Use is made of a cylindrical coordinate system: r, z, ϑ , with origin at the centre of the tank bottom and the z -axis vertical.

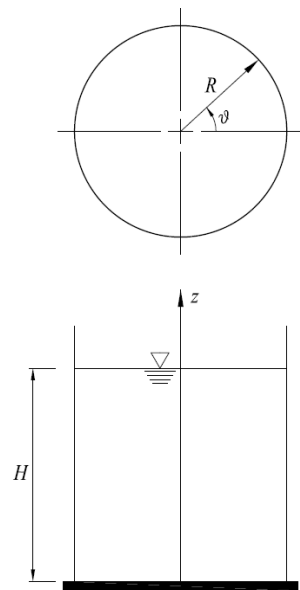


Fig. 1.2.1.1: Rigid tank anchored to the foundation. ϑ, z, r cylindrical coordinates (after [48]).

Before investigating the response of flexible tanks, it is desirable to study the hydrodynamic forces induced on rigid tanks.

In all previous studies on this subject it was found convenient to divide these effects into two parts:

- the impulsive effects, which are computed by neglecting the effect of surface waves, i.e., by assuming the pressure at the free surface to be zero. The impulsive effects for rigid tanks are proportional to the ground acceleration.
- the convective forces, which are associated with the sloshing of the fluid inside the tank. The convective effects depend on the sloshing frequencies of the fluid.

In order to visualize the problem from a physical point of view, consider first a system for which the upper surface of the contained liquid is rigidly capped so that it can't experience vertical motion; in this case, the entire liquid acts in unison with the tank wall as a rigid body.

For a tank with a free liquid surface, only a portion of the contained liquid in the lower part of the tank responds synchronously with the tank wall as if it were rigidly attached to it. The remaining part (convective component) experiences a sloshing or rocking motion, which mainly depends on the tank dimensions and on the temporal characteristics of the base excitation. The convective component of the liquid responds as a continuous system with an infinite number of degrees of freedom, each one corresponding to a distinct mode of vibration, as shown in Figure 1.2.1.2.

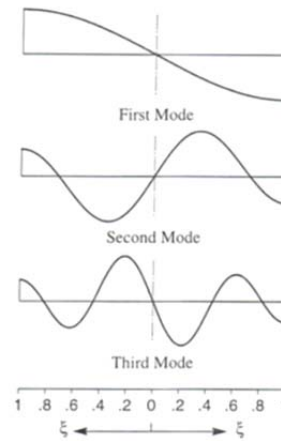


Fig. 1.2.1.2: Radial variation of vertical surface displacements for first three sloshing modes of vibration in rigid tanks. $\xi=r/R$ is the dimensionless distance from the tank vertical axis (after [48]).

1.2.2 Governing equations and boundary conditions

The equation of motion for the fluid, referred to the system shown in Figure 1.2.1.1, is a Laplace's equation, i.e., a second-order partial differential equation belonging to the category of elliptic partial differential equations (Appendix A). Written in the cylindrical coordinates r, ϑ, z , it takes the form

$$\frac{\partial^2 \phi}{\partial r^2} + \frac{1}{r} \frac{\partial \phi}{\partial r} + \frac{1}{r^2} \frac{\partial^2 \phi}{\partial \vartheta^2} + \frac{\partial^2 \phi}{\partial z^2} = 0 \quad (1.2.2.1)$$

in which ϕ is the velocity potential function. The velocity component of the fluid in the radial, tangential and vertical directions are

$$v_r = -\frac{\partial \phi}{\partial r} \quad (1.2.2.2a)$$

$$v_\vartheta = -\frac{\partial \phi}{r \partial \vartheta} \quad (1.2.2.2b)$$

$$v_z = -\frac{\partial \phi}{\partial z} \quad (1.2.2.2c)$$

and the dynamic pressure is related to ϕ by the equation

$$p = \rho \frac{\partial \phi}{\partial t} \quad (1.2.2.3)$$

The boundary conditions of the problem are as follows:

- at $z=0$, v_z must be zero; therefore

$$\left. \frac{\partial \phi}{\partial z} \right|_{z=0} = 0 \quad (1.2.2.4a)$$

- at $r=R$, the radial velocity component of the fluid v_r must be equal to the corresponding component of the ground motion; therefore

$$-\left. \frac{\partial \phi}{\partial r} \right|_{r=R} = \dot{x}(t) \cos \vartheta \quad (1.2.2.4b)$$

- let $\delta(t)$ be the instantaneous value of the vertical displacement of the fluid at the surface, then the pressure at $z=H$ is given approximately by

$$p = \rho g \delta(t) \quad (1.2.2.4c)$$

Now, using equations 1.2.2.3 and 1.2.2.4c and differentiating with respect to time, one obtains

$$\frac{\partial^2 \phi}{\partial t^2} + g \frac{\partial \phi}{\partial z} = 0 \quad (1.2.2.4d)$$

It is convenient to express the solution of equation 1.2.2.1 as the sum of two partial solutions:

$$\phi = \phi_i + \phi_c \quad (1.2.2.5)$$

with ϕ_i subjected to the following boundary conditions:

$$\text{at } z=0 \quad \rightarrow \quad \frac{\partial \phi_i}{\partial z} = 0 \quad (1.2.2.6a)$$

$$\text{at } r=R \quad \rightarrow \quad \frac{\partial \phi_i}{\partial r} = -\dot{x}(t) \cos \vartheta \quad (1.2.2.6b)$$

$$\text{at } z=H \quad \rightarrow \quad \frac{\partial \phi_i}{\partial t} = 0 \quad (1.2.2.6c)$$

and ϕ_c subjected to the following boundary conditions:

$$\text{at } z=0 \quad \rightarrow \quad \frac{\partial \phi_c}{\partial z} = 0 \quad (1.2.2.7a)$$

$$\text{at } r=R \quad \rightarrow \quad \frac{\partial \phi_c}{\partial r} = 0 \quad (1.2.2.7b)$$

$$\text{at } z=H \quad \rightarrow \quad \frac{\partial^2 \phi_c}{\partial t^2} + g \frac{\partial \phi_c}{\partial z} = -g \frac{\partial \phi_i}{\partial z} \quad (1.2.2.7c)$$

The physical meaning of equation 1.2.2.6c is that the pressure at $z=H$ is zero. Thus, ϕ_i represents the solution for the so called impulsive effects. The solution ϕ_c , which effectively corrects for the difference between the correct boundary condition 1.2.2.4d and the one defined by 1.2.2.6c, represents the so called convective effects.

1.2.3 Impulsive solution for rigid tanks

The solution for this case is given by

$$\phi_i = -\dot{x}(t)H \cos \vartheta \sum_{n=1}^{\infty} \frac{8(-1)^{n+1}}{[(2n-1)\pi]^2} \frac{I_1 \left[(2n-1) \frac{\pi r}{2H} \right]}{I_1' \left[(2n-1) \frac{\pi R}{2H} \right]} \cos \left[(2n-1) \frac{\pi z}{2H} \right] \quad (1.2.3.1)$$

where $I_1(\cdot)$ and $I_1'(\cdot)$ denote the modified Bessel function of the first order and its derivative (see Appendix A).

The pressure p_i induced by the impulsive effects is obtained by application of equation 1.2.3.1 into equation 1.2.2.3:

$$p_i = -\ddot{x}(t)\rho H \cos \vartheta \sum_{n=1}^{\infty} \frac{8(-1)^{n+1}}{[(2n-1)\pi]^2} \frac{I_1 \left[(2n-1) \frac{\pi r}{2H} \right]}{I_1' \left[(2n-1) \frac{\pi R}{2H} \right]} \cos \left[(2n-1) \frac{\pi z}{2H} \right] \quad (1.2.3.2)$$

The total hydrodynamic force exerted by the liquid on the tank (total impulsive base shear) is determined from:

$$Q_i = \int_0^H \int_0^{2\pi} p_i|_{r=R} \cos \vartheta R d\vartheta dz \quad (1.2.3.3a)$$

The corresponding impulsive overturning moment above the base of the tank is determined from:

$$M_i = \int_0^H \int_0^{2\pi} p_i|_{r=R} \cos \vartheta \cdot z \cdot R d\vartheta dz \quad (1.2.3.3b)$$

The hydrodynamic pressure on the base of the tank is determined from equation 1.2.3.2 by setting $z=0$, and the corresponding impulsive overturning moment is obtained from:

$$M'_i = \int_0^H \int_0^{2\pi} p_i|_{z=0} \cos \vartheta \cdot r^2 dr d\vartheta \quad (1.2.3.3c)$$

The solutions of equations 1.2.3.3 is given in Section 1.2.5 in a more convenient format.

1.2.4 Convective solution for flexible tanks

The convective solution for an arbitrary ground motion is derived from the convective solution for an harmonic ground acceleration by means of the inverse Fourier transform and the convolution (Duhamel's) integral. In this section only the main steps of the procedure are reported. The reader is referred to Yang [56] for all the mathematical manipulations.

Considering an harmonic ground acceleration $\ddot{x} = \ddot{x}_0 e^{i\omega t}$, the function ϕ_c which satisfies equation 1.2.2.1 and boundary conditions 1.2.2.7 is given by

$$\phi_c = -\frac{1}{i\omega} \ddot{x}_0 e^{i\omega t} H \frac{R}{H} \cos \vartheta \sum_{n=1}^{\infty} \frac{1}{1 - \left(\frac{\omega}{\omega_{cn}}\right)^2} \frac{2}{\lambda_n^2 - 1} \frac{J_1\left(\lambda_n \frac{r}{R}\right)}{J_1(\lambda_n)} \frac{\cosh\left(\lambda_n \frac{z}{R}\right)}{\cosh\left(\lambda_n \frac{H}{R}\right)} \quad (1.2.4.1)$$

where $J_1(\cdot)$ denotes the Bessel function of the first order (see Appendix A), λ_n 's are the zeros of $J_1'(x)=0$ and ω_{cn} are the natural frequencies of sloshing fluid, given by

$$\omega_{cn} = \sqrt{\frac{\lambda_n g}{R} \tanh\left(\lambda_n \frac{H}{R}\right)} \quad (1.2.4.2)$$

The harmonic convective pressure for the tank is obtained by application of equation 1.2.4.2 into equation 1.2.2.3:

$$p_c = \ddot{x}_0 e^{i\omega t} \rho H \frac{R}{H} \cos \vartheta \sum_{n=1}^{\infty} \frac{1}{1 - \left(\frac{\omega}{\omega_{cn}}\right)^2} \frac{2}{\lambda_n^2 - 1} \frac{J_1\left(\lambda_n \frac{r}{R}\right)}{J_1(\lambda_n)} \frac{\cosh\left(\lambda_n \frac{z}{R}\right)}{\cosh\left(\lambda_n \frac{H}{R}\right)} \quad (1.2.4.3)$$

The corresponding total base shear and overturning moments are obtained by application of equations 1.2.3.3.

Now, note that the frequency response function defined by equation 1.2.4.3 is of the form

$$p_c(\omega) = \sum_{n=1}^{\infty} \frac{f(r, \vartheta, z)}{1 - \left(\frac{\omega}{\omega_{cn}}\right)^2} \quad (1.2.4.4)$$

and so, by application on the inverse Fourier transform and the convolution (Duhamel's) integral, the pressure $p_c(t)$ for an arbitrary acceleration input $\ddot{x}(t)$ is given by

$$p_c = \sum_{n=1}^{\infty} f(r, \vartheta, z) \int_0^t \omega_{cn} \ddot{x}(t) \sin[\omega_{cn}(t - \tau)] d\tau \quad (1.2.4.5)$$

in which the integral is the well-known Duhamel's integral which represents the instantaneous value of the pseudo-acceleration, $A_{cn}(t)$, of a single-degree-of-freedom system having a circular natural frequency ω_{cn} and subjected to the prescribed ground acceleration $\ddot{x}(t)$. Thus, the counterpart of equation 1.2.4.3 for transient response may be written as

$$p_c = \rho H \cos \vartheta \sum_{n=1}^{\infty} \frac{2}{\lambda_n^2 - 1} \frac{R J_1\left(\lambda_n \frac{r}{R}\right)}{H J_1(\lambda_n)} \frac{\cosh\left(\lambda_n \frac{z}{R}\right)}{\cosh\left(\lambda_n \frac{H}{R}\right)} A_{cn}(t) \tag{1.2.4.6}$$

Proceeding in a similar manner, one finds the expressions for the other response quantities: convective base shear Q_c and convective overturning moments M_c, M'_c .

1.2.5 Recast expressions

The hydrodynamic pressure exerted on the tank wall may conveniently be expressed in the form

$$p(z, \vartheta, t) = \sum_{n=0}^{\infty} C_n^p \rho H \cos \vartheta A_{cn}(t) \tag{1.2.5.1}$$

where C_n^p is a dimensionless function of z , which depends on the ratio H/R . A value of $n=0$ corresponds to the impulsive solution (in this case $A_{c0}=\ddot{x}(t)$). Whereas $n=1,2,3\dots$ correspond to the convective solution. The function C_n^p for $n=0$ and for $n=1,2$ are given in Figures 1.2.5.1.

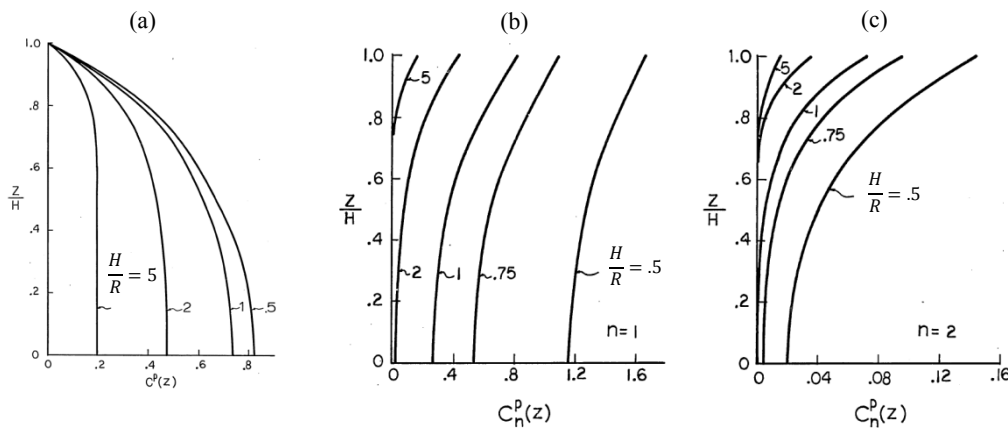


Fig. 1.2.5.1: Distribution of hydrodynamic pressures on tank wall (a) impulsive pressure component, (b) 1st convective pressure component, (c) 2nd convective pressure component (after [56]).

It can be seen that, whereas for large values of H/R , the convective pressure coefficient is small and localized near the free surface, for small values of H/R , the convective pressure is large and penetrates the base of the tank. It should be noted, however, that large values of C_n^p do not

necessarily imply a large pressure, as the latter is also function of $A_{cn}(t)$ which depends on the natural frequency of sloshing motion of the liquid.

The base shear induced by the hydrodynamic pressures can be expressed as

$$Q = \sum_{n=0}^{\infty} C_n^Q m A_{cn}(t) \tag{1.2.5.2}$$

where m is the mass of the fluid and C_n^Q is a dimensionless coefficient, plotted in Figure 1.2.5.2. Note that whereas C_0^Q increases with increasing H/R , the reverse is true for C_1^Q and C_2^Q . Note further that C_2^Q is generally small compared to C_1^Q . However, the base shear associated to the second convective term may be not negligible since the maximum value of A_{c2} may be larger than A_{c1} . This is likely to be the case for tanks having small values of H/R .

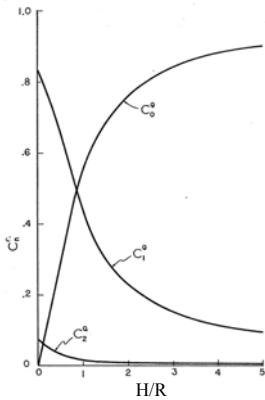


Fig. 1.2.5.2: Base shear coefficient (after [56]).

The overturning moment induced by the hydrodynamic pressures on the wall can be expressed as

$$M = \sum_{n=0}^{\infty} C_n^M m A_{cn}(t) \tag{1.2.5.3}$$

where C_n^M is a dimensionless coefficient, plotted in Figure 1.2.5.3. The general trend of this coefficient is similar to that of the base shear.

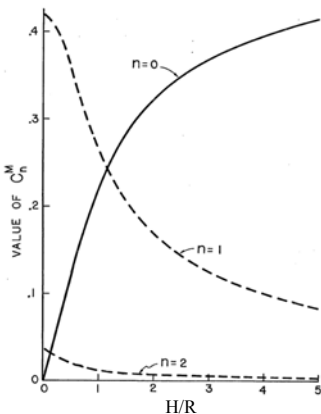


Fig. 1.2.5.3: Overturning moment above the base coefficient (after [56]).

The overturning moment induced by the hydrodynamic pressures on the tank base can be expressed as

$$M' = \sum_{n=0}^{\infty} C_n^{M'} m A_{cn}(t) \quad (1.2.5.4)$$

where $C_n^{M'}$ is a dimensionless coefficient, plotted in Figure 1.2.5.4.

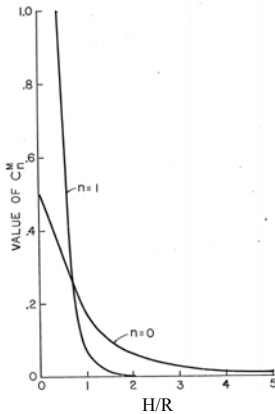


Fig. 1.2.5.4: Overturning moment on the base coefficient (after [56]).

1.2.6 Fluid-tank interaction under assumed mode

One of the first study that considered the tank as a flexible structure may be found in Yang (1976), [56]. Here, the fluid-tank system is analyzed approximately by assuming that the tank behaves as a beam, without change of its cross section. The same approach was used in even older studies by Veletsos, based on the further assumption that the hydrodynamic pressure at $\vartheta=0$ is equal to the pressure induced against a straight wall storing a reservoir. In [56] this assumption is relaxed, but, as before, it is assumed that the tank cross section does not change in shape during deformation and the deflection configuration of the tank at any time is of a prescribed term.

In defining the response of flexible tanks only the impulsive effect are considered. It is presumed that the convective effects are not influenced by tank flexibility and that they can be evaluated by the procedure described in Section 1.2.4 and appropriately superimposed on the impulsive effects evaluated herein. This assumption can be better understood by thinking at the response spectrum method. In fact, for representative earthquake ground motions and realistic tank proportions, the natural periods of the convective modes fall in the highly amplified region of the relevant pseudo-acceleration response spectrum. As a result, the hydrodynamic effects associated to convective modes give rise to low seismic forces. That is way the convective components of the response are considered insensitive to variations in wall flexibility and may be assumed to be the same as those obtained for rigid tanks.

Let $\psi(z)$ be a dimensionless function defining the heightwise distribution of the mode of vibration and let $\ddot{u}(t)$ be the acceleration of the tank wall at the surface of the liquid, then the acceleration of the tank at any height z is $\ddot{u}(t)\psi(z)$, and the corresponding velocity is $\dot{u}(t)\psi(z)$. Since the fluid is considered incompressible and nonviscous, the velocity potential function of fluid ϕ must satisfy Laplace's equation 1.2.2.1 and the following boundary conditions:

$$\text{at } z=0 \quad \rightarrow \quad \frac{\partial \phi}{\partial z} = 0 \quad (1.2.6.1a)$$

$$\text{at } r=R \quad \rightarrow \quad \frac{\partial \phi}{\partial r} = -\dot{u}(t)\psi(z) \cos \vartheta \quad (1.2.6.1b)$$

$$\text{at } z=H \quad \rightarrow \quad \rho \frac{\partial \phi}{\partial t} = 0 \quad (1.2.6.1c)$$

The solution to this problem is given by

$$\phi = -\dot{u}(t) \cos \vartheta \sum_{n=1}^{\infty} \frac{4H}{(2n-1)\pi} \frac{I_1 \left[(2n-1) \frac{\pi r}{2H} \right]}{I_1' \left[(2n-1) \frac{\pi R}{2H} \right]} \alpha_n \cos \left[(2n-1) \frac{\pi z}{2H} \right] \quad (1.2.6.2)$$

where

$$\alpha_n = \frac{1}{H} \int_0^H \psi(z) \cos \left[(2n-1) \frac{\pi z}{2H} \right] dz \quad (1.2.6.3)$$

Then, the hydrodynamic pressure, in excess of the hydrostatic, acting on the tank wall is obtained by application of equation 1.2.2.3 of Section 1.2.2.

$$p_i = \ddot{u}(t)\rho H \cos \vartheta \sum_{n=1}^{\infty} \frac{4\alpha_n}{(2n-1)\pi} \frac{I_1 \left[(2n-1) \frac{\pi R}{2H} \right]}{I_1' \left[(2n-1) \frac{\pi R}{2H} \right]} \cos \left[(2n-1) \frac{\pi z}{2H} \right] \quad (1.2.6.4)$$

The configuration of the assumed mode $\psi(z)$ depends on the relative magnitudes of flexural and shearing deformations of the fluid-tank system during free vibration. These magnitudes, in turn, depend on the dimensions of the tank, such as H/R and t_w/R , and on the relative weights of the roof system m_r to the mass of the contained fluid. In general, for large H/R , t_w/R and m_r , the mode $\psi(z)$ will be more like a flexural type. In contrast, for small H/R , t_w/R and m_r , the mode $\psi(z)$ will be more like a shear beam type. The following procedure, proposed by Veletsos, to select a reasonable vibration mode is given in Yang [56]:

1. Assume a trial configuration $\psi(z)$; for convenience, it may be taken equal to one of the functions of Figure 1.2.6.1.
2. Compute the resulting inertia forces and hydrodynamic forces corresponding to the pressure described by equation 1.2.6.4.

3. Compute the deflection of the tank due to the forces determined at step 2, considering the effects of both flexural and shearing deformations.
4. The desired $\psi(z)$ is the deflection determined in step 3, normalized with respect to the deflection value computed at $z=H$.

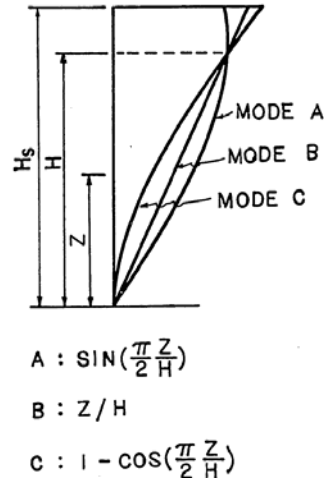


Fig. 1.2.6.1: Vibration modes for initiating the trial procedure (after [56]).

1.3 Mechanical models

1.3.1 Analogues currently available in literature

Initial analytical studies, Yang [56], dealt with the hydrodynamic of liquids in rigid tanks fully anchored to rigid foundations. The term hydrodynamic is used in a generalized sense to represent the dynamic effect of any contained liquid. It was shown that a part of the liquid moves in long-period sloshing motion, while the rest moves rigidly with the tank wall. The latter part of the liquid, also known as the impulsive liquid, experiences the same acceleration as the ground and contributes predominantly to the base shear and overturning moment. The sloshing liquid determines the height of the free-surface waves, and hence the freeboard requirement.

It was shown later that the flexibility of the tank wall may cause the impulsive liquid to experience accelerations that are several times greater than the peak ground acceleration. Thus, the base shear and overturning moment calculated by assuming the tank to be rigid can be non-conservative. Tanks supported on flexible foundations, through rigid base mats, experience base translation and rocking, resulting in longer impulsive periods and generally greater effective damping. These changes may affect the impulsive response significantly. The convective (or sloshing) response is practically insensitive to both the tank wall and the foundation flexibility due to its long period of oscillation. Tanks analyzed in the above studies were assumed to be completely anchored at their base. In practice, a complete base anchorage is not always feasible

or economical. As a result, many tanks are either unanchored or only partially anchored at their base. The effects of base uplifting on the seismic response of partially anchored and unanchored tanks supported on rigid foundations were therefore studied. It was shown that base uplifting reduces the hydrodynamic forces in the tank, but increases significantly the axial compressive stress in the tank wall. Further studies showed that base uplifting in tanks supported directly on flexible soil foundations does not lead to a significant increase in the axial compressive stress in the tank wall, but may lead to large foundation penetrations and several cycles of large plastic rotations at the plate boundary. Flexibly supported unanchored tanks are therefore less prone to “elephant’s foot” buckling damage, but more prone to uneven settlement of the foundation and fatigue rupture at the plate-shell junction.

According to Haroun and Housner (1981), the dynamic analysis of a liquid-filled tank may be carried out using the concept of generalized single-degree-of freedom (SDOF) systems representing the impulsive and convective modes of vibration of the tank-liquid system (Figure 1.3.1.1).

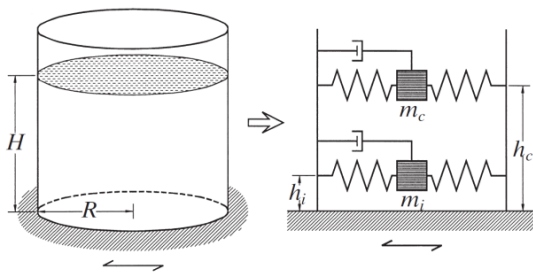


Fig. 1.3.1.1: Liquid filled tank modeled by a generalized SDOF system (after [30]).

For practical applications, only the first few modes of vibration need to be considered in the analysis. The mass, height and natural period of each SDOF system are obtained by the methods described in [47-51] by Veletsos et al. For a given earthquake ground motion, the response of various SDOF systems may be calculated independently and then combined to give the net base shear and overturning moment.

For most tanks, $0.3 < H/R < 3$, the first impulsive and first convective modes together account for 85–98% of the total liquid mass in the tank. The remaining mass of the liquid vibrates primarily in higher impulsive modes for tall tanks ($H/R > 1$), and higher convective modes for broad tanks ($H/R \leq 1$). The results obtained using only the first impulsive and first convective modes are considered satisfactory in most cases.

All the design codes use these analogues (which convert the tank-liquid system into an equivalent spring-mass system) to evaluate the seismic response of tanks. Figures 1.3.1.2 schematically demonstrate such mechanical models both for rigid and for flexible tanks. Various quantities associated with a mechanical model are: impulsive mass m_i , convective mass m_c ,

height of impulsive mass h_i , height of convective mass h_c , impulsive and convective time period T_i and T_c . It may be noted that heights h_i and h_c are used when base pressure is not considered. If base pressure is included, then the corresponding heights are denoted by h_i' and h_c' respectively. In this way, the global overturning moment above and below the base plate is different, see Figure 1.3.1.3. The one above the base plate is used to design the tank walls, whereas the one below the base plate is used to design the foundation (this is why it is also named “foundation moment”).

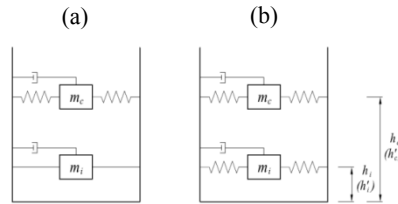


Fig. 1.3.1.2: (a) Mechanical model (a) for rigid tanks, (b) for flexible tanks.

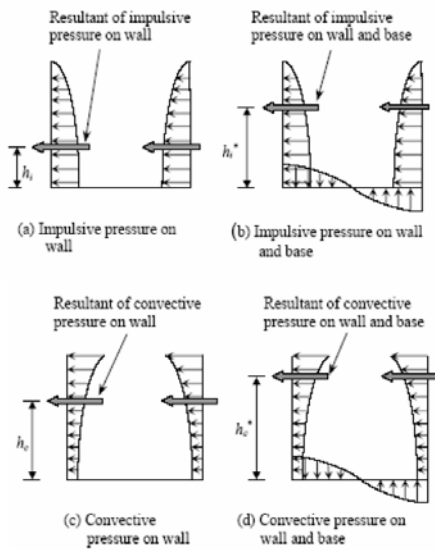


Fig. 1.3.1.3: Impulsive and convective pressures.

In Table 1.3.1.1 the most important contributions to the tank-liquid system modeling are reported in chronological order.

Table 1.3.1.1: Time history of the mechanical models currently available in literature.

	Rigid tank models	Flexible tank models
1963	Housner model for rigid circular and rectangular tanks [26].	
1977	Veletsos and Yang model for circular rigid tanks [56].	
1978	Wozniak and Mitchell generalized the Housner model.	
1981		Haroun and Housner model for flexible tanks [22].
1984		Veletsos model for flexible tanks [47].
2000		Malhotra proposed a simplified version of the Veletsos model [30].

Various codes adopt one or the other mechanical models described above. ACI 350.3 and API 650 use mechanical model of Housner (1963) with modifications of Wozniak and Mitchell (1978). It is interesting to note that API 650 deal with circular steel tanks, which are flexible tanks. However, since there is no appreciable difference in the parameters of mechanical models of rigid and flexible tank models (Figures 1.3.1.4), this code evaluate parameters of impulsive and convective modes from rigid tank models.

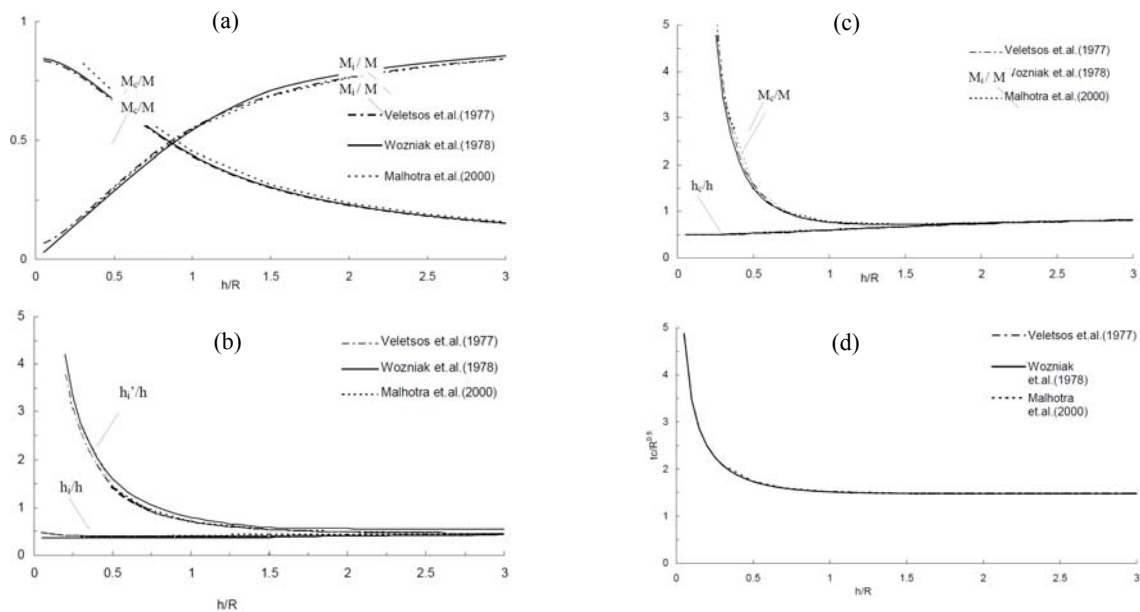


Fig. 1.3.1.4: Rigid models (Veletsos, Wozniak) vs. Flexible models (Malhotra). Comparison of (a) impulsive and convective masses, (b) impulsive heights, (c) convective heights, (d) convective time period (after [28]).

E

Eurocode 8 mentions mechanical model of Veletsos and Yang (1977) as an acceptable procedure for rigid circular tanks. For flexible circular tanks, models of Veletsos (1984) and Haroun and Housner (1981) are described along with the procedure of Malhotra et al. (2000).

1.3.2 Unanchored tanks – General remarks and mechanical models

In the case of unanchored tanks, the tank bottom edge is not fixed to the foundation. Many tanks currently in operation, especially with great dimensions, are unanchored, because concrete foundations, which are needed for the anchors and the anchors themselves are very expensive. Furthermore, because improperly detailed anchors can cause damage to the shell under seismic loading, it is common, particularly for large tanks, to support the tank wall on a ring-wall foundation without anchor bolts and the bottom plate to rest on a compacted soil (though sometimes the ring-wall is omitted). For such tanks, the overturning moment caused by the hydrodynamic pressure tends to lift the shell off the foundation as shown in Figure 1.3.2.1. As the shell displaces upward, it pulls against the tank bottom causing the bottom plate to pick up liquid to provide resistance to the upward shell movement. On the opposite side, high compressive stresses are developed which may cause buckling of the shell.

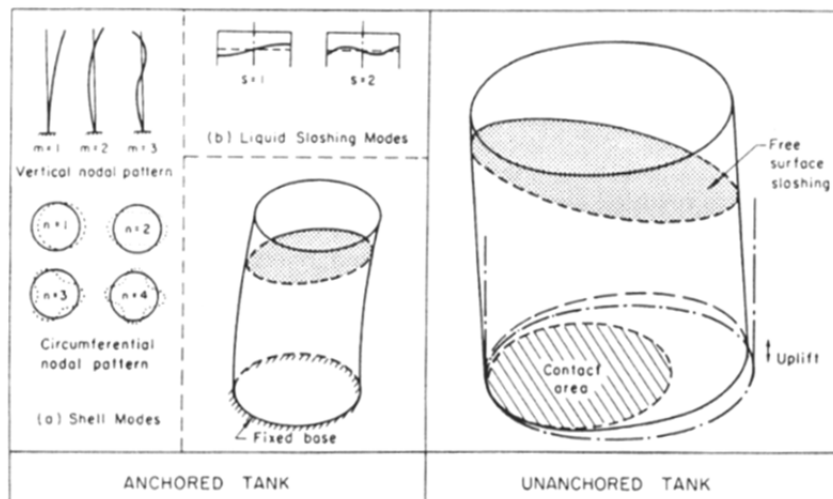


Fig. 1.3.2.1: Seismic behavior of ground-based tank (after [19]).

The dynamic behavior is quite different from that of anchored tanks. As a consequence of the overturning moment caused by the dynamically activated pressures due to earthquake, partial uplift of the boundary of the bottom plate is possible. This uplift of the bottom plate gives rise to the following phenomena:

- a strongly nonlinear fluid-shell-soil interaction problem has to be considered;
- the maximum axial membrane compression force in the tank wall increases significantly, and loss of stability may occur at lower overturning moments;
- uplift of the bottom plate represents a stiffness loss of the whole fluid-shell system. The natural frequencies of the fluid-shell interaction vibration decrease. The corresponding mode shapes, the damping values and the dynamically activated pressures are changed;

- the contribution to the dynamically activated loads due to sloshing may increase because of the decreased natural frequencies of the interaction vibration.

Few approximate methods are currently available to estimate the stress level at the shell bottom, and none are based on a rigorous treatment of this nonlinear problem. On the contrary, numerous sophisticated analyses have been carried out to investigate the dynamic response of anchored tanks. For such structures, vertical motion of the shell at the foundation level is prevented, and therefore, their seismic behavior can be analyzed by evaluating the natural modes of vibration (Figure 1.3.2.1) and superposing them properly. Field observations and studies of the performances of uplifting tanks during past earthquakes (Northridge earthquake, [6], and Imperial Valley earthquake, [19]) have revealed that such systems are prone to extensive damage due to:

- buckling of the tank wall, caused by large compressive stresses;
- rupture at the plate-shell junction, caused by excessive plastic yielding;
- failure of the piping connections to the wall that are incapable of adsorbing large base uplifts.

Dynamic tests as well as static tilt tests have been performed to study the behavior of unanchored tanks. Much data are available on the phenomena, but only a limited amount of interpretations was given. One can conclude from the results that the response of unanchored tanks is dominated by the uplift mechanism. Wozniak and Mitchell (1978) published the first recommendations for design rules of unanchored tanks, taking into account the increased axial membrane force in the tank wall. The same procedure, adopted in the API 650 standard, is studied here in Section 2.3.2. Many authors concluded from their investigations that this procedure is not sufficiently accurate and gives conservative estimates for unanchored tanks only under specific conditions.

Past studies relevant to unanchored tanks can be divided into:

- theoretical studies using static models, often combined with static tilt tests. The main purpose of such quasi-static investigations is to study the influence of uplift on the stresses in the tank;
- theoretical studies which deal with the dynamic behavior of unanchored tanks. In these investigations dynamic nonlinear models have been proposed for calculating the amplitude dependent natural frequencies, mode shapes, and the dynamically activated pressures.

- *Static studies*

As already said, one of the first static study was taken by Wozniak and Mitchell (1978). They presented a very simple uplift model in which the resistance to overturning moment is provided by a portion of the weight of the fluid content W_L ; and this depends on the width of a ring of the bottom plate that is lifted off the foundation. The calculation of this width is based on a small deflection theory of an elementary strip of the bottom plate which can be lifted off the ground with the assumption of two plastic hinges: one at the plate-shell junction and the other at some point on the uplifted part L , as shown in Figure 1.3.2.2. Using translational and rotational equilibrium one can calculate the uplifted length and the uplifting force (as the force which brings a beam to a kinematic mechanism with two plastic hinges in the sense of the limit load of the beam). For explicit calculations see Section 2.3.2. In this model the horizontal membrane force and the friction between bottom plate and soil were neglected.

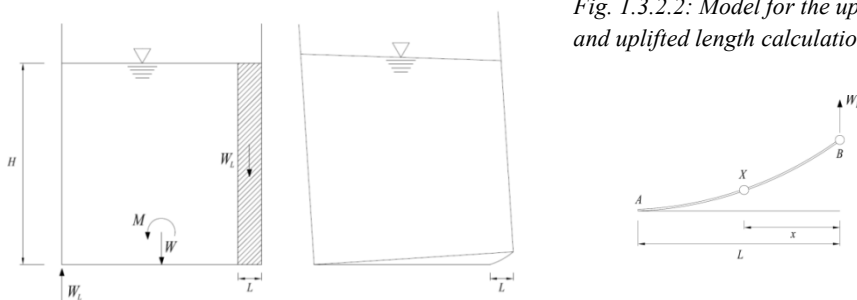


Fig. 1.3.2.2: Model for the uplifting force and uplifted length calculation.

A more sophisticated model to solve the contact problem of the partially uplifted base plate and its interaction with the cylindrical shell is solved by Peek and Jennings (1988) using the finite difference energy method and a Fourier decomposition of the displacements in the circumferential direction, [36]-[37]. Nonlinearities due to contact, finite displacements and yielding of the tank material were included in the analysis. Furthermore, a method of analysis is presented in which the tank is supported from below by a circular bed of nonlinear springs, representing the retaining action of the bottom force. According to the so called “shell-spring model” (Auli et al. (1985), [15]-[16]), the nonlinear springs characteristic may be calculated by applying analytical procedures or by the finite element method. For example, an axisymmetric finite element model can be used, taking into account geometrical and material nonlinearities. For every uplift force, the uplift height is determined. Scharf (1990) calculated the nonlinear springs characteristics for real liquid storage tanks. The results for three specific tanks are shown in Figure 1.3.2.3a and compared with the constant uplift force of Wozniak and Mitchell, which overestimates the retaining action of the bottom plate for lower uplift heights. Figure 1.3.2.3b

shows the deformed shape of the tank bottom edge for different values of the uplift force. Especially in broad tank a third plastic hinge may develop at the thickness step of the bottom plate.

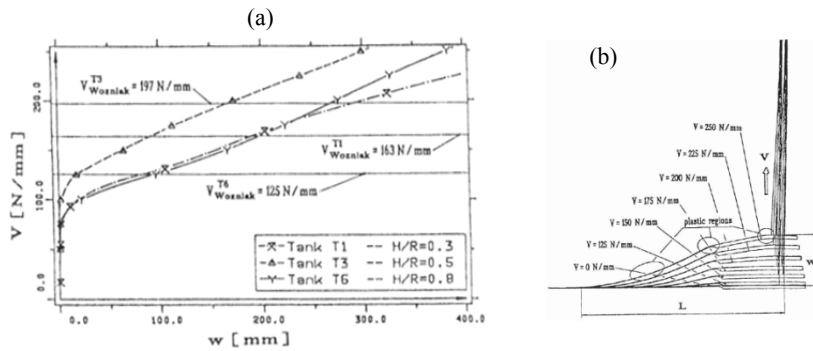


Fig. 1.3.2.3: Uplift force V vs uplift height w (after [16]).

- **Dynamic studies**

Since a strongly nonlinear (geometric and material) fluid-structure-soil interaction and contact problem has to be solved, the calculation of the dynamic response of unanchored tanks is very complicated. Hence, no fully satisfying models are available.

Two simplified nonlinear analytical models were developed by Natsiavas, (1987,1988,1989), taking into account separation of the bottom plate, soil flexibility and liquid sloshing effects, [32]. Results obtained by an application of these models were published by Natsiavas and Babcock (1988), [33]. They conclude that the hydrodynamic pressure of unanchored tanks is mainly caused by the rigid body translation and by the rigid body rotation due to uplift. There is practically no contribution from the shell flexibility. It should, however, be investigated if uncoupling of the rocking motion due to uplift and the motion due to shell flexibility is really realistic. Nevertheless, the investigations of Natsiavas give an excellent insight into the problems of estimating the dynamic response and failure mechanism of unanchored earthquake excited liquid storage tanks.

In [15]-[16] Scharf (1990) proposed a modified response spectrum method for estimating the maximum dynamic response of unanchored tanks. Similar to Natsiavas, the Housner model was modified. Instead of a contribution due to the common vibration of the shell and the liquid, a contribution due to the interaction vibration including the rocking motion due to uplift was assumed. The resulting contribution to the overturning moment is represented by a single-mass oscillator with a nonlinear spring characteristic. It can be shown that an equivalent period for the amplitude interaction vibration including the uplift motion in combination with an iteration

procedure and displacement response spectra yields sufficiently accurate estimates for the maximum dynamic response.

As a consequence of the uplift motion of the bottom plate and additional contribution to the hydrodynamic pressure is activated. This contribution is taken into account in the models of Natsiavas and Scharf. The analytical solution of Scharf agrees well with that of Veletsos and Tang (1987), [50], who investigated a rocking rigid tank, but Scharf's solution is more general.

Dynamical investigations of earthquake excited unanchored tanks can be performed by the finite element method. The advantage of using such a method is that the whole fluid-shell-foundation system can be modeled and various types of results, such as natural frequencies, mode shapes, the hydrodynamic pressure, the stresses in the shell and the stability loss, can be obtained. But the effort as well the requirements of CPU time and core memory increase dramatically if nonlinear effects such as yielding and partial uplift of the bottom plate are included in the analyses. That is why finite element models for dynamic analyses employ simplifications such as “the shell-spring model” (Auli et al. (1985), [15]-[16]).

All studies mentioned above allow the conclusion that there is a need for more research in the field of earthquake excited unanchored tanks to reach a deeper insight into this strongly nonlinear problem.

1.3.3 Fluid-structure interaction

For design purposes, fluid-structure interaction is typically modeled using the simplified codes provisions. In this case the most common way to proceed is to carry out linear elastic analyses on a finite element model of the tank, in which the fluid is replaced by the hydrodynamic pressure distribution suggested by the codes. Then, the nonlinear behavior of the structure is taken into account by computing the elastic and elasto-plastic buckling stress and checking that they are not reached at any point of the finite element model. Examples of fluid-as-external-pressure modeling may be found in [39] and [42] by Wunderlich et al. In [39], a detailed numerical example of hydrodynamic pressure derivation can be found.

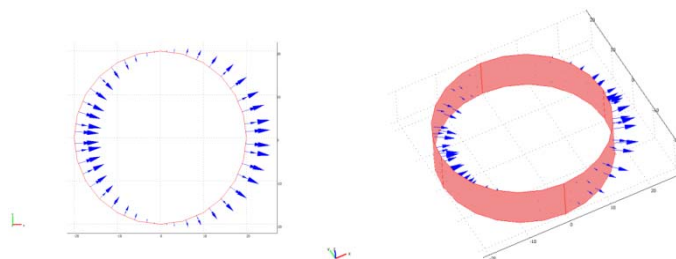


Fig. 1.3.3.1: Hydrodynamic pressure due to horizontal shaking (after [39]).

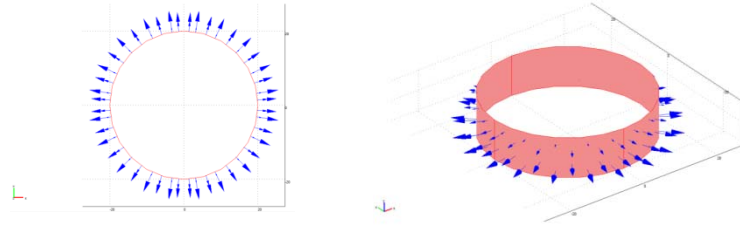


Fig. 1.3.3.2: Hydrodynamic pressure due to vertical shaking (after [39]).

Since the simplified models adopted by the codes are often “too much simplified” because they are based on outdated assumptions and results, two different methods are currently used for research purposes. The first one is the so called “added mass method” and the second one directly involves “fluid finite elements”.

The “added mass method” was first developed by Westergaard (1933) in a study on the dynamic interaction between a dam and a reservoir system, Figure 1.3.3.3. According to Westergaard, the hydrodynamic pressures that the water exerts on the dam during an earthquake are the same as if a certain body of water moves back and forth with the dam while the remainder of the reservoir is left inactive. The dam was initially considered as rigid by Westergaard. Then, the dynamic interaction between the retained water and a flexible dam was studied by Lee and Tsai using modal superposition analysis. They considered the dam as an Euler-Bernoulli beam and showed that the added mass, which vibrates together with the structure during the imposed excitation, results from the hydrodynamic effect due to the current deflection of the structure and the current response of the entire system. It is a function of the mode shapes of both the structure and the reservoir. So, in case of a flexible dam, the added mass is varying during the dynamic analysis.

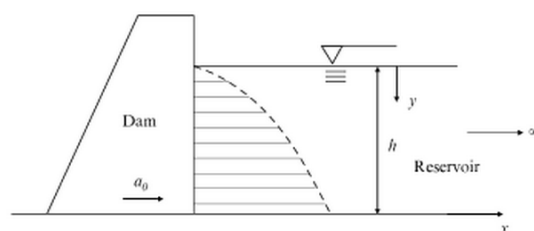


Fig. 1.3.3.3: The dam-reservoir system examined by Westergaard.

Examples of the “added mass method” application to tank-liquid systems can be found in [52]-[53]-[54] by Virella et al. Here, the idea is that the inertia of that portion of the fluid which acts impulsively is somehow lumped in with the inertia of the tank walls. The added masses are calculated from pressure distributions of rigid tanks and they do not vary during the dynamic analysis. This assumption is not strictly correct; in fact, in the light of what shown by Lee and

Tsai, for flexible structures the added mass depend on the flexibility of the structure itself. In case of tank-liquid systems, studies by Veletsos and Yang (1977) and Haroun and Housner (1981) showed that the pressure distribution due to the liquid impulsive component in rigid and flexible tanks were similar, especially for broad tank ($H/R < 1$), Figure 1.3.3.4. However, the magnitude was highly dependent on the flexibility of the tank wall.

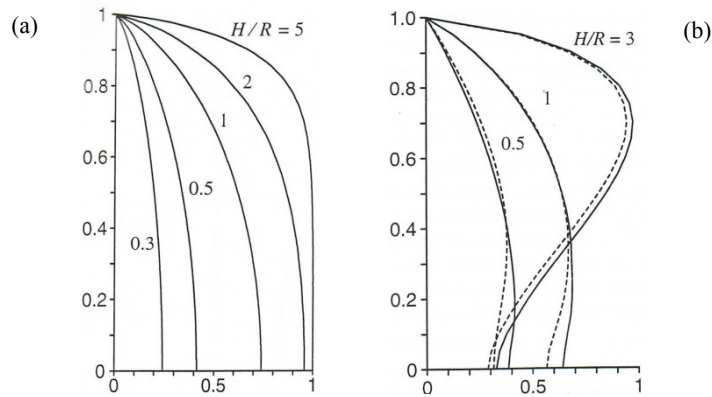


Fig. 1.3.3.4: Pressure distribution along the tank height (a) for rigid and (b) for the 1st mode of flexible tanks (after [48]).

As a conclusion, the “added mass method” which employs masses that do not vary during the analysis is particularly correct for broad tank. From a practical point of view, the added mass approach essentially consists in deriving liquid masses from pressure distributions and to attach them to the shell nodes of a finite element model, by means of massless rigid elements, as shown in Figures 1.3.3.5.

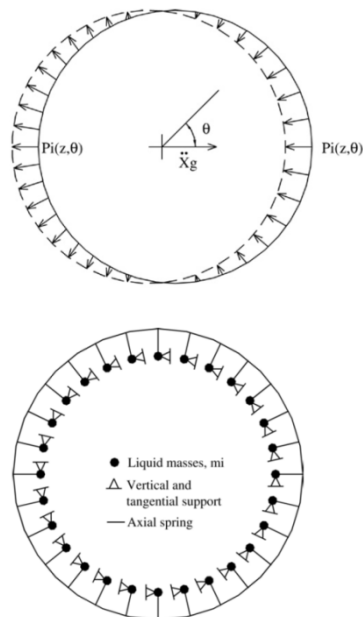
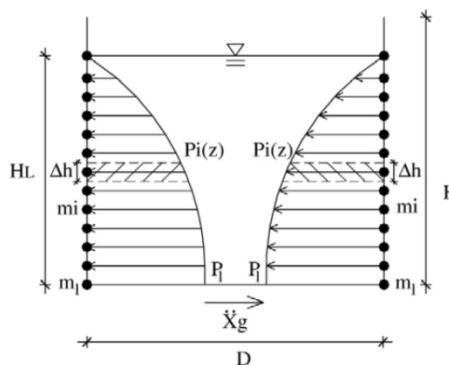


Fig. 1.3.3.5: Model with added masses around the circumference and along the height (after [53]).



Because the added masses are determined from the impulsive pressure which is normal to the shell surface, they must be added in such a way that they only add inertia in this direction. For this reason, the added masses are sometimes referred to as the “normal masses”. The one-direction elements have supports oriented in their local axes that constrained the motion of the nodal masses to the normal direction of the shell. The motions of each support are restricted in the global tangential direction (i.e. perpendicular to the element axis) and in the vertical direction, whereas it is free to move in the radial direction (i.e. local axial direction of the rigid element). To obtain the lumped mass m_i at each node, the height of the cylinder is divided into several segments. For a radial section of the tank, the lumped mass m_i at each location is computed using the rectangular rule. For an interior node at the tank shell:

$$m_i = \frac{p_i \Delta h}{a_n} \quad (1.3.3.1a)$$

where p_i is the pressure at node i , Δh is the constant distance between nodes and a_n is the reference normal acceleration ($a_n = \ddot{x}_g$ for $\vartheta=0$). For nodes at the liquid surface and at the bottom of the tank:

$$m_i = \frac{p_i \Delta h}{2 a_n} \quad (1.3.3.1b)$$

As already mentioned, the “added mass method” with masses derived from the rigid impulsive pressure is not really accurate for slender tanks, in which the pressure distribution is quite different depending on whether the tank is considered rigid or flexible, and also modes higher than the first play a significant role. For slender tank, the added mass are really varying during the dynamic analysis. Furthermore, previous works suggest that the added mass techniques should give reasonably accurate predictions for a rigidly anchored tank. However, it is not clear how successful such an approach would be for the case where the tank base can separate from the floor.

Due to these limitations, as an alternative to the above mentioned method, a very recent technique is to model the liquid by directly using “fluid finite elements”. With such a method we are totally released from the codes provisions and spring-mass models, thus studying the problem into a “global finite element framework”. A class of elements is available in ANSYS and ABAQUS which are specially formulated to model fluids contained within vessels having no yet flow rate. These elements are displacement-based, which makes them easier to integrate into a general finite element structural analysis program than the alternative formulation in which the

pressure is the variable in the fluid. Numerical models which make use of fluid finite elements may be found in [4]-[5]-[10]-[54] by Di Carluccio, Fabbrocino et al.

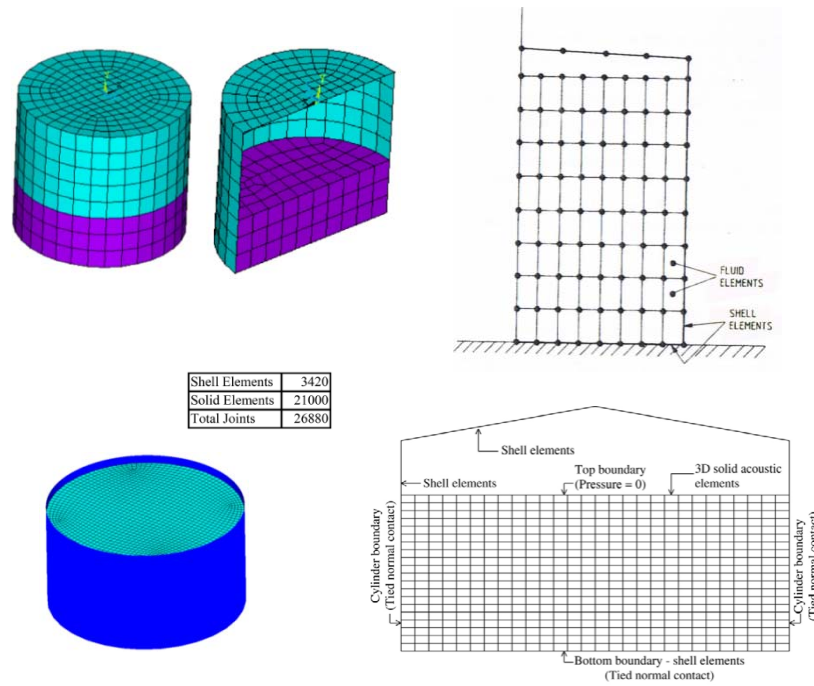


Fig. 1.3.3.6: Examples of finite element models for fluid element analysis (after [4]-[5]-[10]-[53]).

For example, in [4] the behavior of the liquid fuel oil is represented by the Lagrangian approach. In this approach, fuel oil is assumed to be linearly elastic, inviscid and irrotational. The formulation of the fluid system based on Lagrangian approach is given in literature. The determination of the interface condition is required to obtain the coupled equations of the storage tank-liquid fuel oil system. Because the fuel oil is assumed to be inviscid, only the displacement in the normal direction is continuous at the interface of the system. Lengths of coupling elements as 0.001m are used to supply fluid-structure interaction between liquid fuel oil and storage tank interface. The main objective of the couplings is to hold equal the displacements between two reciprocal nodes in normal direction to the interface.

1.3.4 Soil-structure interaction

The flexibility of the supporting medium, like that of the tank wall itself, may be considered to affect only the impulsive effects. Accordingly, the convective components of the response, like those for rigidly supported flexible tanks, may be evaluated with reasonable accuracy considering both the tank and the supporting medium to be rigid, because it is associated with actions of significantly lower frequencies than the natural frequencies of the

tank-liquid system or the dominant frequencies of the excitation. Therefore, the following discussion deals exclusively with the impulsive effects.

For a specified free-field ground motion, the impulsive component of the response of a flexibly supported tank may differ significantly from that of the same tank when rigidly supported. Two factors are responsible for this difference:

- the flexibly supported system has more degrees of freedom and, therefore, different response characteristics from those of the rigidly supported system. In particular, whereas the foundation motion of the rigidly supported system is the same as the free-field ground motion, the corresponding motion of the flexibly supported system, because of its interaction or coupling with the supporting medium, may be significantly different, and will generally include a rocking component even for a purely horizontal free-field motion. The rocking component may be particularly prominent for tall tanks and very flexible soil;
- part of the vibrational energy of the elastically supported system may be dissipated into the supporting medium by radiation of waves and by hysteretic action in the soil itself. There is, of course, no counterpart of these forms of energy dissipation for a rigidly supported system.

Based on available solutions for rigidly supported tanks and of elastically supported structures of the building type, it was estimate that the single-degree-of-freedom approximation would probably be quite adequate for relatively broad tank with H/R of the order of 1.5 or less, but might lead to non-conservative results for tall, slender tanks.

In addition to the parameters enumerated previously (Section 1.3.1) for rigidly supported systems, the response of a flexibly supported tank depends on:

- the stiffness of the supporting soil, specified by the velocity of shear wave propagation in the soil, $v_s = \sqrt{G_s/\rho_s}$;
- Poisson's ratio of the soil ν_s and the associated damping factor ξ_s ;
- radius and mass of the foundation, R_0 and m_0 .

Two factors complicate the analysis of elastically supported systems:

- system damping is of a form for which the classical modal superposition method of analysis is not applicable;
- the resistances of the foundation, the so called foundation impedances, are frequency-dependent quantities.

The analysis can, however, effectively be implemented in the frequency domain making use of the discrete Fourier transform (DFT) technique in combination with the fast Fourier transform (FFT) algorithm. Apart from the exact method, not covered by the present work, several simpler, approximate procedures have been used to evaluate the response of the flexibly supported tank-liquid system and to assess the effects of soil-structure interaction (SSI). In the most accurate of these approaches, by Veletsos and Tang [49], the tank-liquid system in its fixed-base condition is treated as a multi-degrees-of-freedom system, but SSI is considered to affect the contribution of the fundamental impulsive mode of vibration only. The contributions of the higher modes in this approach are evaluated approximately by considering the tank to be rigidly supported at the base. Additionally, the interaction effects for the fundamental mode of vibration are accounted for indirectly by modifying the natural frequency and damping of that mode and evaluating its response to the prescribed free-field ground motion considering the tank to be rigidly supported at the base. For the justification of this approach and for the procedure used to arrive at the modified natural frequency and damping, the reader is referred to [49].

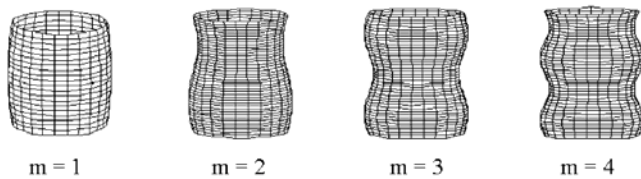
Provisions for consideration of SSI are provided only in NZSEE guidelines and Eurocode 8. First provision pertains to influence of soil flexibility on time period of tank. Expressions for time period of lateral and vertical mode of tank, including the effect of soil flexibility are provided. These expressions are taken from Veletsos (1984). Secondly, inclusion of soil also increases the damping of the structure. Expressions are also provided for equivalent damping of tank-fluid-soil system. In EC8, to investigate the influence of the foundation flexibility on the seismic response of tanks the mechanical model developed by Veletsos and Tang (1992) is used.

1.4 Draft conclusions and research needs

Although these design provisions represent a significant advance in the design of tanks, observations in recent earthquakes and experimental studies seem to indicate that they may not be adequate to accurately predict the seismic response of cylindrical tanks. It must be noted that in perfect circular cylindrical tanks, the $\cos n\theta$ -type modes cannot be excited by rigid base motion; however, fabrication tolerances in civil engineering tanks permit a departure from a nominal circular cross section and this tends to excite these modes. Little can be found in literature about the importance of the $\cos n\theta$ -type modes in an earthquake response analysis. This is probably due to the fact that the magnitude and distribution of fabrication errors cannot be predicted, and consequently, only hypothetical analyses can be made.

Differences between the results of theoretical models, experimental studies (tanks tested on a shaking table at the University of California, Berkeley, Nachtigall [31]) and the real behavior of storage tanks (Imperial Valley and Northridge earthquakes [6],[19]) are often justified with the influence of material nonlinearities and/or structural imperfections and/or damping. Therefore, many research projects have been conducted in order to examine these influences. But up to now no satisfactory results have been obtained. This fact motivated many authors to analyze seismically excited liquid storage tanks from a new point of view. A very interesting method is discussed by Nachtigall in [31], where the fundamental hypothesis of cantilever beam model is removed. In fact, the assumed vertical cantilever-beam model might be acceptable for a very tall, stiff and slender tank. However, regarding a tank of typical practical proportions with for example a diameter of 54 m, a height of 14 m, and a wall thickness of 31 mm, it is hard to imagine this tank behaving like a cantilever. The shell modal forms should be taken into account for such flexible tanks. However, analyzing the fundamental modal forms of a shell instead of using the cantilever-beam model, we are actually dealing with a completely different set of natural modes and frequencies for the coupled tank fluid systems. In [54] the effect of the geometry on the fundamental modes for the tank-liquid systems is studied using eigenvalue and harmonic response analyses. Similar fundamental periods and mode shapes were found from these two approaches. The fundamental modes of tank models with $H/D > 0.63$ were very similar to the first mode of a cantilever beam. For the shortest tank ($H/D = 0.40$), the fundamental mode was a bending mode with a circumferential wave $n=1$ and an axial half-wave (m) characterized by a bulge formed near the mid-height of the cylinder, Figure 1.4.2.

Axial wave numbers:



Circumferential wave numbers:

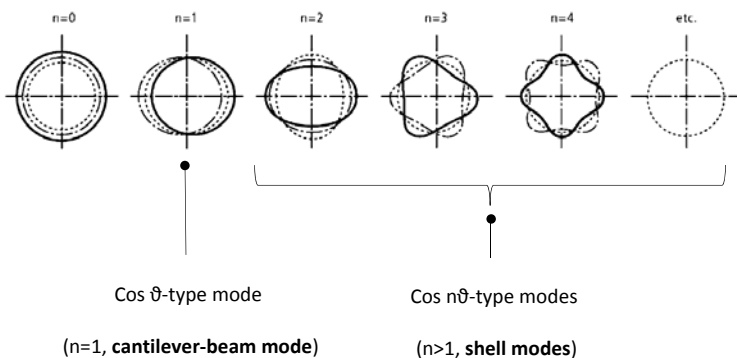


Fig. 1.4.1: Axial and circumferential modal forms. ϑ polar coordinate angle (after [31]).

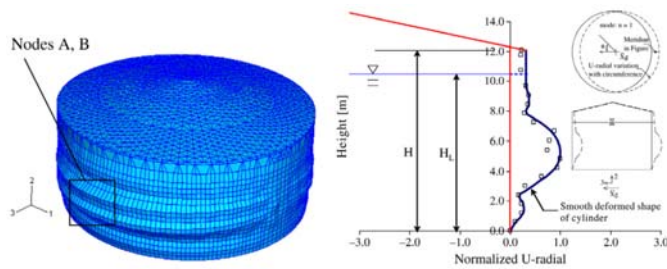


Fig. 1.4.2: Fundamental mode for Model A ($H/D=0.40$), (a) 3D view (b) deformed shape in the meridian with maximum displacements (after [53]).

Regardless the influence of tanks flexibility on the seismic response of these structures, past studies and current mechanical models give quite accurate results for the predictions of the seismic forces, and so there is not the need for further research developments in this field.

To the opinion of the author, future works must be addressed mainly to the problem of uplifting in tanks. In fact, all studies mentioned in Section 1.3.2 allow the conclusion that there is a need for more research in the field of earthquake excited unanchored tanks to reach a deeper insight into this strongly nonlinear problem.

Regardless fluid-structure and soil-structure interaction, current models are quite satisfactory. However, a possible future work could be the set up of a very refined finite element model, taking into account material and geometric nonlinearities, in which the fluid is represented by appropriate fluid finite elements and the soil is made up of finite elements with the correct dissipative capacity. With such a model, the global behavior of the tank-fluid-soil system can be investigated. At present, only few “global models” are available, one example may be found in [55] by Wunderlich et al. The reason is that the set up of them requires a great computational effort. The great majority of FE models deals only with the structure itself; in these models the supporting soil is assumed to have a certain stiffness and the fluid is modeled through the hydrodynamic pressure corresponding to the first impulsive mode. It is immediate to note that the results of these models are of very limited validity and it is almost impossible to generalize them.

Finally, it must be emphasized that the choice of a more or less accurate model strongly depends on the research objectives. For example, if a study is focused on the risk analysis of liquid storage tanks through the development of fragility curves, the structural model for the dynamic analysis must be as simple as possible for efficiency purposes. A very interesting example of such “extra-simplified model” can be found in Talaslidis [44]. Here a quite refined FE model is used to calibrate a simplified equivalent multi-degrees-of-freedom model taking into account also soil-structure interaction effects, Figure 1.4.3. This cantilever beam model is far more efficient for the ensuing stochastic analysis than the 3D finite element model. Obviously,

although it cannot provide all the details that a 3D FE model does, it gives a good overall picture of the dynamic response which is on the conservative side. Also, it is well suited for intense sudden loads that produce non-linear response, since in this case mostly lower modes of vibration contribute to the gross displacement time history. If additional effects such as instability need to be studied, then recourse must be made to the FE model. In principle, risk analysis is still possible, but becomes extremely time-consuming because a very large number of fully non-linear time-stepping analyses need to be performed at each load level.

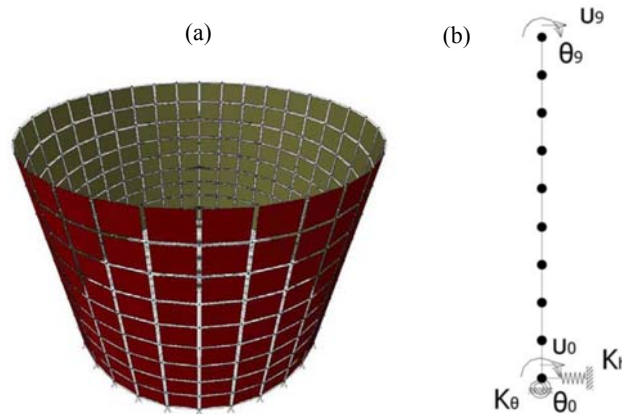


Fig. 1.4.3: (a) FE model and (b) equivalent twenty-dofs simplified model (after [44]).




Review of codes provisions

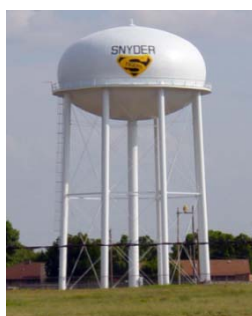
2.1 Types of tanks

Many different configurations of liquid storage tanks can be found in civil engineering applications. However, ground supported, circular cylindrical tanks are more numerous than any other type because they are simpler in design, more efficient in resisting hydrostatic pressure, and can be easily constructed.

Provisions given in ACI 350.3, API 650 and Eurocode 8 guidelines will be reviewed. It may be noted that some of these codes deal with only specific types of tanks. Table 2.1.1 provides details of types of tanks considered in each of these codes. It is seen that ground supported tanks are either fixed at base or rest on flexible base. The type of flexible base used and its description varies from code to code.

Table 2.1.1: Types of tanks considered in various codes.

Code		Types of tank
ACI 350.3 (Appendix A-B)		<ul style="list-style-type: none"> • Ground supported circular and rectangular concrete tanks with fixed and flexible base. • Pedestal supported elevated tanks.
API 650 (Appendix E-EC)		<ul style="list-style-type: none"> • Ground supported steel petroleum tanks (types of base support are not described).
Eurocode 8 (part 4 – Annex A)		<ul style="list-style-type: none"> • Ground supported circular and rectangular tanks with fixed base. • Elevated tanks.



(a)



(b)



(c)

Fig. 2.1.1: (a) Pedestal supported elevated tank. (b) Ground supported concrete tank. (c) Ground supported steel tanks.

As regards ground-supported tanks it is possible to classify them into three main different classes.

1. Rigid vs. Deformable tanks,
2. Anchored vs. Unanchored tanks, and
3. Rigidly supported vs. Flexibly supported tanks.

The first distinction is explicitly reported only in the Eurocode, because the API 350 standards deal only with steel tanks, which may be assumed to be deformable; in the same way, ACI 350.3 standards deal only with concrete tanks, which may be assumed always to be rigid. A very good distinction in the analysis of rigidly or flexibly supported tanks may be found in [48] by Veletsos et al.; here, the influence of the supporting soil on the seismic performances of the tank is studied. According to ACI 350.3, the difference between rigidly supported or flexible supported tank is the key point for the determination of the seismic actions. However, it must be noted that in this standard the flexibility of the supporting medium has nothing to do with the soil properties, but it deals only with the type of base connection, see Section 2.4.3. A common feature to all the codes is the clear distinction in the analysis of anchored and unanchored tanks. While there is a consensus in the codes on the treatment of the phenomenon, various other aspects remain controversial or unresolved, e.g. vertical earthquake motion, effect of tank roof, redistribution of stresses during tank uplift, etc...

In this chapter use is made of the cylindrical coordinate system of Figure 1.2.1.1: $\xi=r/R$ and $\zeta=z/H$ are the dimensionless coordinates.

2.2 Rigid vs Deformable tanks

2.2.1 Basic assumptions and terminology

With the objective of improving the seismic safety and reducing the risk of damage or failure of thin walled cylindrical liquid storage tanks, numerous experimental studies and theoretical research projects have been carried out in recent years in order to better understand the behavior of liquid-storage tanks. Based on analytical results of Veletsos, Haroun and Housner, obtained from simplified beam models and in addition to experimental research, different simplified design provisions for anchored and unanchored tanks have been developed.

Such simplified design provisions can be found, for example, in the American Petroleum Industry (API) standard 650 Appendix E - “*Seismic design of storage tanks*” [2], Eurocode 8-Part 4 “*Tanks, Silos and Pipelines*” in Appendix B “Seismic analysis procedure for anchored

cylindrical tanks” [13], or ACI 350.3 “*Seismic Design of Liquid-Containing Concrete Structures*” [1].

Two basic assumptions of the current design provisions, which are based mainly on the research work of Haroun, Housner, Veletsos and others, are:

- the tank oscillates relative to the base as “vertical cantilever beam”;
- the initial circular cross-section maintains circular (no ovalization).

Although it is a very simple matter to deal with the design provisions, it is a difficult or even an impossible task to understand the applied formulas and to gain further knowledge about their background. This statement is especially true for the API standard. Eurocode 8 gives more insight into its background, but leaves many uncertainties to the user in questions of applicability.

Both EC8 and API standard use nearly the same approaches to include the time dependent behavior of the liquid. They can be explained as follows: one portion of the liquid along the walls and the bottom moves in unison with the tank as a rigidly attached mass. The other portion moves independently, experiencing sloshing or rocking oscillations. This latter portion undergoing sloshing motion is known as the “convective” mass component, whereas the other portion of liquid moving synchronously with the tank is termed as the “impulsive” mass component. The impulsive and convective components should be separated to characterize the hydrodynamic response of the tank. These two actions may be considered uncoupled in most cases, because there are significant differences in the natural periods; namely the convective natural period is much longer than the impulsive one, leading to smaller seismic forces. Both components cause a pressure loading, even though most of the response is affected by the motion of the liquid due to the impulsive component. The two pressure components are considered in both design provisions.

In Eurocode 8, when dealing with deformable tanks, the fluid pressure is the sum of three contributions referred as: “rigid impulsive”, “sloshing”, “flexible”. According to the methodology of Eurocode 8 “fluid particles oscillate rigidly with the tank in its deformation relative to the base as a vertical cantilever”. A third pressure component is not specifically regarded in the API standard as an additional mass. According to Veletsos and Yang [56] and Haroun and Housner [22] the pressure distributions for rigid and flexible tanks are very much alike, as indicated in Figures. 2.2.1.1, especially in case of broad tanks ($H/R < 1$).

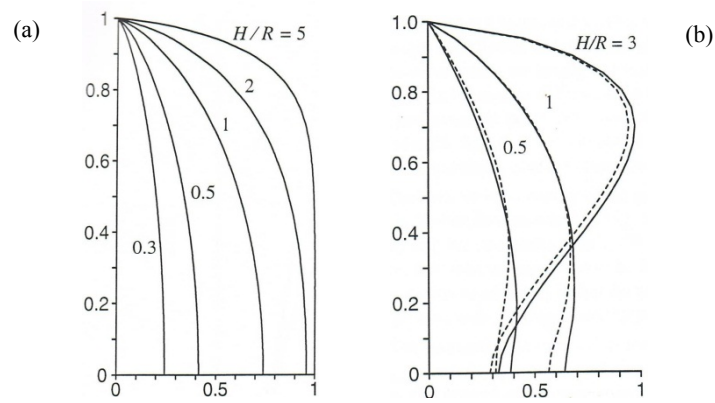


Fig. 2.2.1.1: Pressure distribution along the tank height (a) for rigid and (b) for the 1st mode of flexible tanks (after [48]).

But even if the pressure distribution of the hydrodynamic wall pressure is considered to be independent of the wall flexibility, the magnitude of the pressure is highly dependent on the wall flexibility. This is proved by the fact that the resulting pressure is calculated by multiplying the pressure distribution function by the spectral value of the pseudo-acceleration function $A(t)$, instead of the ground acceleration, as it is done for rigid tanks. The acceleration response function represents the instantaneous value of the pseudo-acceleration induced by the seismic movements in a single-degree of freedom oscillator, having the natural frequency and damping of the first impulsive and sloshing modes. If the fundamental natural frequency of the tank-liquid system falls in the amplified acceleration region of the design response spectrum, the spectral value of $A(t)$ will be significantly greater than the ground acceleration. This leads to a higher corresponding maximum wall pressure than that given by the rigid tank solution. Therefore in both design provisions the knowledge of the fundamental frequency of the tank liquid system is necessary in order to

- (a) calculate the wall pressures,
- (b) avoid resonance effects.

Expressions of the fundamental frequency are different in EC8 and API standards because they were found independently in different research works applying different methods. However, all these results are based on the same assumption that the tank vibrates in a combination of the following modes:

1. As a cantilever flexural beam, without distortion of its cross-section,
2. As a cantilever shear beam, again without distortion of its cross-section, and
3. As a series of independent rings undergoing extensional, arching-ovalling motion.

2.2.2 Eurocode 8: rigid anchored tanks

In this Section the Eurocode prescriptions for rigid tanks rigidly anchored to the foundations are reviewed. The reference spring-mass model is the one of Figure 2.2.2.1.

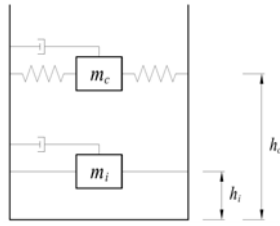


Fig. 2.2.2.1: Spring-mass model for rigid tanks, employed by Eurocode 8.

- **Impulsive pressure component**

For rigid tanks, the instantaneous value of the hydrodynamic pressure at an arbitrary point, $p(\xi, \zeta, \vartheta, t)$, is defined by the superposition of the impulsive component, $p_i(\xi, \zeta, \vartheta, t)$, and the convective component, $p_c(\xi, \zeta, \vartheta, t)$.

The spatial-temporal variation of the rigid impulsive pressure is given by the expression:

$$p_i(\xi, \zeta, \vartheta, t) = C_i(\xi, \zeta) \rho H \cos \vartheta A_g(t) \tag{2.2.2.1}$$

where:

$A_g(t)$ is the ground acceleration time-history in the free-field (with peak value a_g)

$$C_i(\xi, \zeta) = 2 \sum_{n=1}^{\infty} \frac{(-1)^n}{I_1'(v_n/\gamma) v_n^2} \cos(v_n \zeta) I_1\left(\frac{v_n}{\gamma} \xi\right)$$

in which:

$$v_n = \frac{2n + 1}{2} \pi$$

$I_1(\cdot)$ and $I_1'(\cdot)$ denotes the modified Bessel function of order 1 and its derivative.

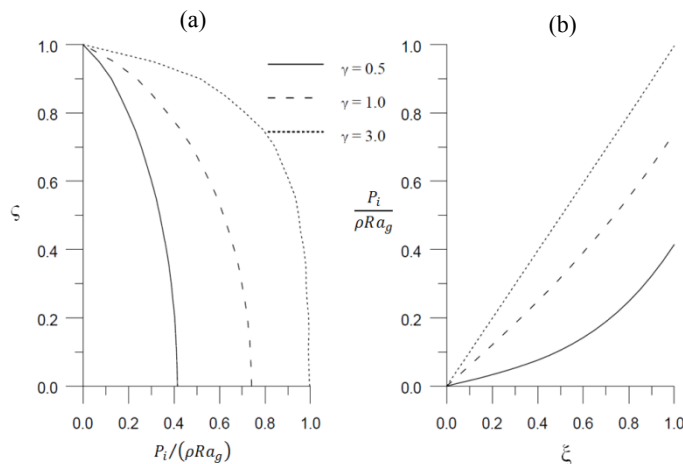


Fig. 2.2.2.2: Variation of the impulsive pressure (normalized to $\rho R a_g$) for three different values of γ . a) Variation along the height; b) radial variation on the tank bottom, (after [13]).

In Figure 2.2.2.2a the variation of p_i (normalized) for $\xi=1$ (i.e. at the wall of the tank) and $\cos\theta=1$ (i.e. in the plane of the horizontal seismic action) is shown for three different value of the slenderness parameter γ . Figure 2.2.2.2b shows the radial variation of p_i on the tank bottom (i.e. for $\xi=0$). Note that for large values of γ (i.e. for slender tanks) the pressure distribution on the tank bottom becomes linear.

Pressure resultants: The horizontal resultant of the rigid impulsive pressure from expression 2.2.2.1 at the base of the wall, Q_i , is:

$$Q_i(t) = m_i A_g(t) \quad (2.2.2.2)$$

where m_i , named impulsive mass, denotes the mass of the contained fluid which moves together with the walls and is given by:

$$m_i = m 2\gamma \sum_{n=1}^{\infty} \frac{I_1(v_n/\gamma)}{v_n^3 I_1'(v_n/\gamma)} \quad (2.2.2.3)$$

where $m = \rho\pi R^2 H$ is the total mass of the fluid.

The total moment with respect to an axis orthogonal to the direction of the seismic action motion, M'_i , immediately below the tank bottom includes the contributions of the pressures on the walls from expression 2.2.2.1 and of those on the tank bottom. The total moment M_i immediately above the tank bottom includes only the contributions of the pressures on the walls.

Impulsive base moment (immediately below the tank bottom):

$$M'_i = m_i h'_i A_g(t) \quad (2.2.2.4a)$$

where

$$h'_i = H \frac{\frac{1}{2} + 2\gamma \sum_{n=0}^{\infty} \frac{v_n + 2(-1)^{n+1} I_1(v_n/\gamma)}{v_n^4 I_1'(v_n/\gamma)}}{2\gamma \sum_{n=0}^{\infty} \frac{I_1(v_n/\gamma)}{v_n^3 I_1'(v_n/\gamma)}} \quad (2.2.2.5a)$$

Impulsive base moment (immediately above the tank bottom):

$$M_i = m_i h_i A_g(t) \quad (2.2.2.4b)$$

with

$$h_i = H \frac{\sum_{n=0}^{\infty} \frac{(-1)^n I_1(v_n/\gamma)}{v_n^4 I_1'(v_n/\gamma)} (v_n (-1)^n - 1)}{\sum_{n=0}^{\infty} \frac{I_1(v_n/\gamma)}{v_n^3 I_1'(v_n/\gamma)}} \quad (2.2.2.5b)$$

• **Convective pressure component**

The spatial-temporal variation of the convective pressure is given by:

$$p_c(\xi, \varsigma, \vartheta, t) = \rho \sum_{n=1}^{\infty} \psi_n \cosh(\lambda_n \gamma \varsigma) J_1(\lambda_n \xi) \cos \vartheta A_{cn}(t) \tag{2.2.2.6}$$

where:

$$\psi_n = \frac{2R}{(\lambda_n^2 - 1) J_1 \lambda_n \cosh(\lambda_n \gamma)}$$

J_1 is the Bessel function of the 1st order

λ_n stands for the n^{th} root of the 1st derivative of the Bessel function of the 1st kind and 1st order.

The first three of these roots are: $\lambda_1=1.841$, $\lambda_2=5.311$, $\lambda_3=8.536$.

$A_{cn}(t)$ is the acceleration time-history of the response of a single degrees of freedom oscillator

having a circular frequency $\omega_{cn} = \sqrt{g \frac{\lambda_n}{R} \tanh(\lambda_n \gamma)}$ and a damping ratio appropriate for the sloshing of the fluid.

Only the first oscillating, or sloshing, mode and frequency of the oscillating liquid ($n=1$) needs to be considered in expression 2.2.2.6 for design purposes.

The vertical distribution of the sloshing pressures for the first two modes is shown in Figure 2.2.2.3. In squat tanks the sloshing pressures maintain relatively high values down to the bottom, while in slender tanks the sloshing effect is limited to the vicinity of the surface of the liquid.

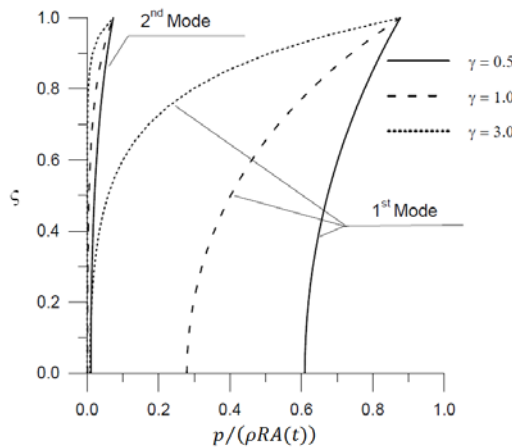


Fig. 2.2.2.3: Variation of sloshing pressure (normalized) along the height in the first two mode (after [13]).

Pressure resultants: Convective base shear:

$$Q_c(t) = \sum_{n=1}^{\infty} m_{cn} A_{cn}(t) \tag{2.2.2.7}$$

where the n^{th} modal convective mass is:

$$m_{cn} = m \frac{2 \tanh(\lambda_n \gamma)}{\lambda_n \gamma (\lambda_n^2 - 1)} \quad (2.2.2.8)$$

Convective base moment (immediately below the tank bottom):

$$M'_c = \sum_{n=1}^{\infty} (m_{cn} A_{cn}(t)) h'_{cn} = \sum_{n=1}^{\infty} Q_{cn} h'_{cn} \quad (2.2.2.9a)$$

where

$$h'_{cn} = H \left(1 + \frac{2 - \cosh(\lambda_n \gamma)}{\lambda_n \gamma \sinh(\lambda_n \gamma)} \right) \quad (2.2.2.10a)$$

Convective base moment (immediately above the tank bottom):

$$M_c = \sum_{n=1}^{\infty} (m_{cn} A_{cn}(t)) h_{cn} = \sum_{n=1}^{\infty} Q_{cn} h_{cn} \quad (2.2.2.9b)$$

with

$$h_{cn} = H \left(1 + \frac{1 - \cosh(\lambda_n \gamma)}{\lambda_n \gamma \sinh(\lambda_n \gamma)} \right) \quad (2.2.2.10b)$$

The convective component of the response may be obtained from that of oscillators having masses m_{cn} , attached to the rigid tank through springs having stiffnesses $K_n = \omega_{cn}^2 m_{cn}$. The tank is subjected to the ground acceleration time-history $A_g(t)$ and the masses respond with accelerations $A_{cn}(t)$. h'_{cn} or h_{cn} is the level where the oscillator needs to be applied in order to give the correct value of M'_c or M_c , respectively.

2.2.3 Eurocode 8: deformable anchored tanks

It is normally un-conservative to consider the tank as rigid (especially for steel tanks). In flexible tanks the fluid pressure is usually expressed as the sum of three contributions, referred to as: “rigid impulsive”, “sloshing” and “flexible”. The third satisfies the condition that the radial velocity of the fluid along the wall equals the deformation velocity of the tank wall, as well as the conditions of zero vertical velocity at the tank bottom and zero pressure at the free surface of the fluid. The dynamic coupling between the sloshing and the flexible components is very weak, due to the large differences between the frequencies of the sloshing motion and of the deformation of the wall, which allows determining the third component independently of the others. The rigid impulsive and the sloshing components in Section 2.2.2 remain therefore unaffected.

Then, the reference spring-mass model is the one of Figure 2.2.3.1.

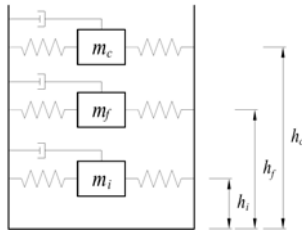


Fig. 2.2.3.1: Spring-mass model for deformable tanks employed by Eurocode 8.

However, the procedure suggested by the Eurocode for flexible tanks requires a very high computational effort. It is definitely cumbersome from a computational point of view. This is mainly due to the fact that the flexible pressure distribution p_f (equation A.19 in Eurocode 8, Part 4, Appendix A) depends on the modes of vibration of the tank-fluid system, among which only those with one circumferential wave ($n=1$), of the following type, are of interest:

$$\phi(\zeta, \vartheta) = f(\zeta) \cos \vartheta \tag{2.2.3.1}$$

Higher order modes would lead to rather small participation factors in the response spectrum analysis and to negligibly small contributions to the overturning moment. So, the term fundamental or first frequency, or first mode, is not related to the real fundamental modes of the full tank, but only to eigen-modes of the type of expression 2.2.3.1.

For the determination of the first mode shape of the tank, an iterative procedure suggested by Fischer et al. in [15] is reported in the Eurocode. It consists in a numerical algorithm based on the “added mass concept”. Starting with an assumed vibration mode $f^i(\zeta)$ a first approximation ($i=1$) of the flexible pressure distribution p_f^i can be computed from expression A.19 in Eurocode 8. Following the added mass concept an effective mass density $\rho^i(\zeta)$ of the shell can be calculated from the pressure p_f^i . Then, this effective mass density may be used in a structural analysis of the tank to evaluate the mode shape in the $(i+1)$ -th iteration, and so forth until convergence. For convergence criteria see [15]. Finally, the fundamental circular frequency ω_f , the contributions to the base shear and bending moment are reported in equations (A.24)-(A.25)-(A.27) of the Eurocode.

The time-history of the base shear produced by the three pressure components is:

$$Q(t) = m_i A_g(t) + \sum_{n=1}^{\infty} m_{cn} A_{cn}(t) + m_f A_f(t) \tag{2.2.3.2}$$

where $A_{cn}(t)$ is the pseudo-acceleration of a simple oscillator with circular frequency ω_{cn} (see Section 2.2.2), an appropriate damping ratio and subjected to a base acceleration $A_g(t)$; $A_f(t)$ is

the pseudo-acceleration of a simple oscillator with circular frequency ω_f and an appropriate damping ratio and subjected to a base acceleration $A_g(t)$.

However, in a response spectrum analysis only the individual maxima of the terms in expression 2.2.3.2 are known. So, the use of this equation poses the question of the combination of the maxima. Apart from the need to derive a relative acceleration response spectrum for $A_f(t)$, there is no accurate way of combining the peak of $A_g(t)$ with that of $A_f(t)$. As a matter of fact, since the input and its response cannot be assumed as independent in the range of relatively high frequencies under consideration, the “square root of the sum of squares” rule is not sufficiently accurate. On the other hand, addition of the individual maxima could lead to over-conservative estimates. Given these difficulties, various approximate approaches based on the theory above have been proposed. Three of these are due to Veletsos and Yang, Haroun and Housner, and Scharf and are presented in details in the Eurocode.

The theoretical basis of the Eurocode procedure for flexible tanks can be found in Haroun and Housner [22], where the hydrodynamic fluid pressure is given by the superposition of four pressure components:

- p_1 = the long period component contributed by the convective fluid motion (p_c in the Eurocode);
- p_2 = the impulsive fluid pressure component which varies in synchronism with the horizontal ground acceleration (p_i in the Eurocode);
- p_3 = the short period component contributed by the $\cos \vartheta$ -type modes of the tank walls (p_r in the Eurocode);
- p_4 = the contributions of the $\cos n\vartheta$ -type modes ($n \geq 2$) of the tank walls (neglected in the Eurocode, since such modes are excited only in case of noncircular imperfections of the cross section).

In Haroun [22] the dynamic characteristics of the liquid-shell system are determined by means of a discretization scheme in which the elastic shell is modeled by finite elements and the liquid region is treated as a continuum by boundary solution techniques.

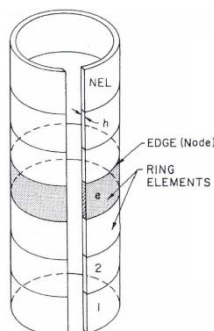


Fig. 2.2.3.1: Finite element discretization of the shell (after [22]).

2.2.4 Eurocode 8: a simplified procedure for deformable anchored tanks

The procedure takes into account impulsive and convective actions of the liquid in flexible steel or concrete tanks fixed to rigid foundations. It deals only with the linear elastic analysis of fully anchored, rigidly supported tanks. It was proposed by Malhotra in [30] and adopted also by the Eurocode 8; it is a simplified version of Veletsos' works [47-51]. Specifically, the simplifications include:

- representing the tank-liquid system by the first impulsive and first convective modes only;
- combining the higher impulsive modal mass with the first impulsive mode and the higher convective modal mass with the first convective mode;
- adjusting the impulsive and convective heights to account for the overturning effect of the higher modes;
- generalizing the impulsive period formulas given by Veletsos in [48] so that it can be applied to steel as well as concrete tanks of various wall thicknesses.

The impulsive and convective responses are combined by taking their numerical sum rather than their root-mean-square value.

The natural periods of the impulsive (T_{imp}) and the convective (T_{con}) responses are:

$$T_i = C_i \frac{H\sqrt{\rho}}{\sqrt{t_w/R} \cdot \sqrt{E_w}} \quad (2.2.4.1a)$$

$$T_c = C_c \sqrt{R} \quad (2.2.4.1b)$$

where t_w is the equivalent uniform thickness of the tank wall, R the tank radius, H the height of liquid, ρ the mass density of liquid, and E_w the modulus of elasticity of the tank material. The coefficients C_i and C_c are obtained from Table 2.2.4.1. The coefficient C_i is dimensionless, while C_c is expressed in s/\sqrt{m} . For tanks with non-uniform wall thickness, t_w may be calculated by taking a weighted average over the wetted height of the tank wall (see the worked example of Section 2.2.7). The impulsive and convective masses m_i and m_c are obtained from Table 2.2.4.1 as fractions of the total liquid mass m (m_i in Table 2.2.4.1).

H/r	C_i	$C_c [s/\sqrt{m}]$	m_i/m_t	m_c/m_t	h_i/H	h_c/H	h_i'/H	h_c'/H
0.3	9.28	2.09	0.176	0.824	0.400	0.521	2.640	3.414
0.5	7.74	1.74	0.300	0.700	0.400	0.543	1.460	1.517
0.7	6.97	1.60	0.414	0.586	0.401	0.571	1.009	1.011
1.0	6.36	1.52	0.548	0.452	0.419	0.616	0.721	0.785
1.5	6.06	1.48	0.686	0.314	0.439	0.690	0.555	0.734
2.0	6.21	1.48	0.763	0.237	0.448	0.751	0.500	0.764
2.5	6.56	1.48	0.810	0.190	0.452	0.794	0.480	0.796
3.0	7.03	1.48	0.842	0.158	0.453	0.825	0.472	0.825

Table 2.2.4.1: Recommended design value for the first impulsive and convective modes of vibration as a function of the tank height-to-radius ratio H/r (after [30]).

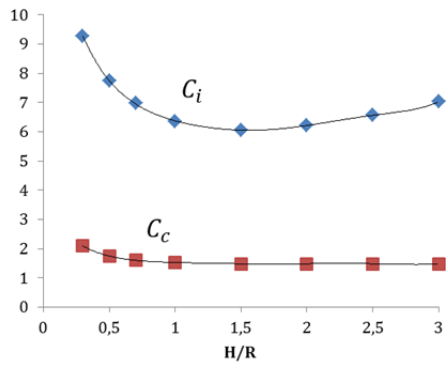


Fig. 2.2.4.1: Impulsive and convective coefficients, obtained by interpolation.

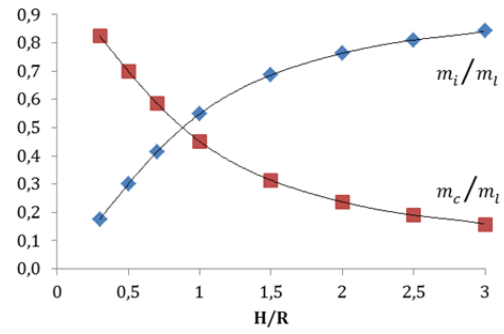


Fig. 2.2.4.2: Impulsive and convective masses as fractions of the total liquid mass in the tank, obtained by interpolation.

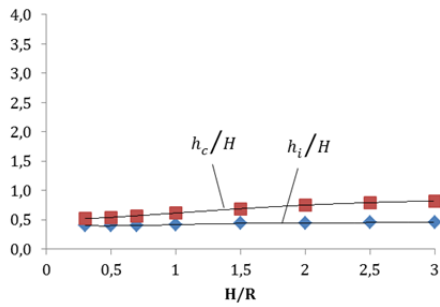


Fig. 2.2.4.3: Impulsive and convective heights, obtained by interpolation.

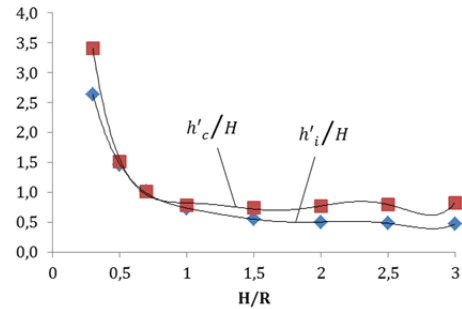


Fig. 2.2.4.4: Impulsive and convective heights, obtained by interpolation.

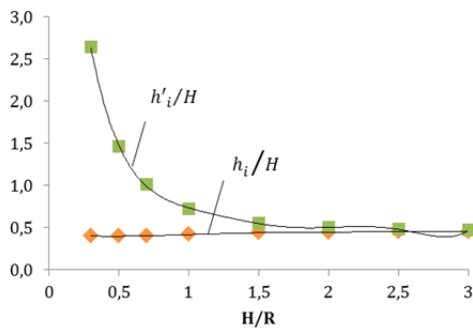


Fig. 2.2.4.5: Impulsive heights for the determination of the moment above and below the plate, obtained by interpolation.

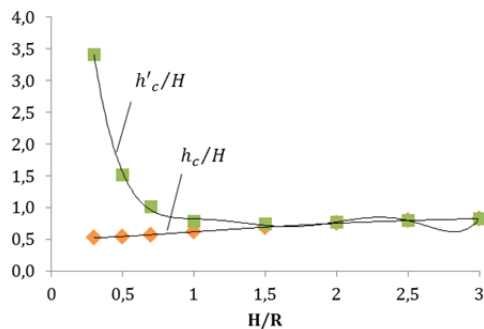


Fig. 2.2.4.6: Convective heights for the determination of the moment above and below the plate, obtained by interpolation.

From Figures 2.2.4.5 and 2.2.4.6 note that for large values of H/R (slender tanks) the height for the calculation of the moment above the base plate h is very close to the one for the moment below the base plate h' , both for impulsive (Figure 2.2.4.5) and for convective component (Figure 2.2.4.6). It follows that the contribution to the foundation moment of the base pressure is not important in this case. By contrast, for shallower, broader systems, the values of h'_i and h'_c are significantly larger than those of h_i , h_c . As a result, provided that the spectral pseudo-acceleration for the fundamental convective mode is not negligibly small compared to

the maximum ground acceleration, the base pressure in broad tanks may be a significant contributor to the foundation moment.

The base shear (or total hydrodynamic wall force) is given by

$$Q = (m_i + m_w + m_r) \cdot S_e(T_i) + m_c \cdot S_e(T_c) \quad (2.2.4.2)$$

where m_w is the mass of tank wall, m_r the mass of tank roof, $S_e(T_{imp})$ the impulsive spectral acceleration (obtained from an elastic response spectrum for a value of damping consistent with Section 2.5.2), and $S_e(T_{con})$ the convective spectral acceleration (obtained from a 0,5% damped elastic response spectrum).

The overturning moment above the base plate, in combination with ordinary beam theory, leads to the axial stress at the base of the tank wall. The net overturning moment immediately above the base plate is given by

$$M = (m_i h_i + m_w h_w + m_r h_r) \cdot S_e(T_i) + m_c h_c \cdot S_e(T_c) \quad (2.2.4.3)$$

where h_i and h_c are the heights of the centroids of the impulsive and convective hydrodynamic wall pressures (Figure 2.2.4.3, Table 2.2.4.1), and h_w and h_r are the heights of the centers of gravity of the tank wall and roof, respectively.

The overturning moment immediately below the base plate is dependent on the hydrodynamic pressure on the tank wall as well as that on the base plate. It is given by

$$M' = (m_i h'_i + m_w h_w + m_r h_r) \cdot S_e(T_i) + m_c h'_c \cdot S_e(T_c) \quad (2.2.4.4)$$

where the heights h'_i and h'_c are obtained from Figure 2.2.4.4 or Table 2.2.4.1.

In general, the moment immediately above the tank base, in combination with the ordinary beam theory, is used to evaluate the axial forces induced at the base of the tank wall, whereas the forces beneath the base are used in the design of the foundation. Note that if the tank is supported on a ring foundation, M should be used to design the tank wall, base anchors and the foundation. If the tank is supported on a mat foundation, M should be used to design the tank wall and anchors only, while M' should be used to design the foundation. For this reason M' is also called “foundation moment”.

The vertical displacement of the liquid surface due to sloshing is given by

$$\delta = R \frac{S_e(T_c)}{g} \quad (2.2.4.5)$$

where g is the gravity acceleration.

The values of base shear and moments obtained from the proposed procedure are 2–10% higher than those from the detailed modal analysis performed by Malhotra et al. in [30]. The values of sloshing wave height obtained from the proposed procedure were 12–18% higher than those from the detailed modal analysis performed in [30]. The results of the proposed procedure are therefore conservative but close to those from the detailed modal analysis.

As already mentioned, the presented simple procedure is suggested also by the Eurocode 8. Once the design seismic forces have been obtained, the serviceability and ultimate limit states needs to be verified. The specification of the corresponding seismic actions is left to the national authorities. The level of seismic protection is established based on the risk to life and the economic and environmental consequences. This reliability differentiation is achieved by adjusting the return period of the design seismic event. Three tank reliability classes are defined corresponding to situations with high (Class 1), medium (Class 2) and low (Class 3) risk. Depending on the tank contents, an importance factor γ_I is assigned to each of the three classes (Table 2.2.4.2).

Tank contents	Importance factor (γ_I) for		
	Class 1	Class 2	Class 3
Drinking water, non-toxic non-flammable chemicals	1.2	1.0	0.8
Fire-fighting water, non-volatile toxic chemicals, lowly flammable petrochemicals	1.4	1.2	1.0
Volatile toxic chemicals, explosive and highly flammable liquids	1.6	1.4	1.2

Table 2.2.4.2: Importance factor for tanks according to Eurocode 8 (after [12]).

The seismic action effects have to be multiplied by the selected importance factor. For the reference case ($\gamma_I = 1$), the recommended return periods of the design seismic event are 475 years for the ultimate limit state and 50–70 years for the serviceability limit state. In the case of the largest importance factor ($\gamma_I = 1.6$), the return period of the design event for the ultimate limit state is about 2000 years. According to Eurocode 8, the analysis has to assume linear elastic behavior, allowing only for localized non-linear phenomena without affecting the global response, and to include the hydrodynamic response of the fluid. Particularly, it should account for the convective and impulsive components of fluid motion as well as the tank shell deformation due to hydrodynamic pressure.

The proposed procedure satisfies these principles in a simple and efficient way for the design of fixed-base cylindrical tanks.

2.2.5 ACI 350.3 and API 650: concrete and steel tanks

ACI 350.3 and API 650 prescribe procedures for concrete and steel tanks, respectively. Steel tanks are clearly considered deformable by API 650. ACI 350.3, even if it deals only with

concrete tanks, instead of assuming a rigid tank model directly accelerated by ground acceleration, it also assumes amplification of response due to natural frequency of the tank itself. However, as already proved in Section 1.2 (Figures 1.2.4), there is no appreciable difference in the parameters of mechanical models of rigid and flexible tank models. Therefore, the reference spring-mass model is the one of Figure 2.2.5.1, both for concrete and steel tanks.

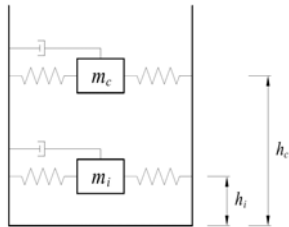


Fig. 2.2.5.1: Spring-mass model for flexible tanks.

The theoretical background of ACI 350.3 and API 650 prescriptions may be found in Veletsos [48]. For sake of simplicity, all the formulas reported in this Section are in the notation of this reference document; however, ACI 350.3 and API 650 use the same formulas, just rearranged in a slightly different way and rewritten for both the US Customary units system and the SI units system. All the coefficients are recalculated and given in graphical form. In any of the the two codes thr expression of the hydrodynamic pressure is given, but just the pressure resultants. However, this expression may be found in Veletsos [48].

As already mentioned in Section 1.2.6, for representative earthquake ground motions and realistic tank proportions, the natural frequencies of the impulsive modes that significantly contribute to the response fall in the highly amplified region of the relevant pseudo-acceleration response spectrum. As a result, the hydrodynamic effects for flexible tanks are generally larger than those for rigid tanks. The flexibility of the tank wall affects almost exclusively the impulsive component of the response. Since they are associated with natural periods of vibration that are significantly longer than the dominant periods of the ground motion or of the resulting wall motion, the convective components of the response are insensitive to variations in wall flexibility and may be considered to be the same as those obtained for rigid tanks.

It is also important to point out that the Malhotra's simplified procedure adopted by Eurocode 8 (see Section 2.2.4), is a generalization of the Veletsos' procedure presented in this Section. Specifically, the generalizations include:

- representing the tank-liquid system by the first impulsive and first convective modes only;
- combining the higher impulsive modal mass with the first impulsive mode and the higher convective modal mass with the first convective mode;

- adjusting the impulsive and convective heights to account for the overturning effect of the higher modes;
 - generalizing the impulsive period formulas given by Veletsos in [48] so that it can be applied to steel as well as concrete tanks of various wall thicknesses.
- ***Natural impulsive period***

The impulsive effects were evaluated by rigorous analyses of the tank-liquid system making use of the Rayleigh-Ritz energy procedure in combination with energy expressions for the system that are consistent with Flugge's theory for cylindrical shells. The radial and axial displacements of the tank wall were expressed as linear combinations of the natural modes of vibration of a uniform cantilever beam; the circumferential displacements were expressed as linear combinations of the first derivatives of these modes.

In case of flexible tank, the wall and participating liquid mass responds as a continuous cantilever system with an infinite number of degrees of freedom, each one corresponding to a distinct natural mode of vibration. These modes and the associated periods will be referred to as impulsive. In practice, the contribution of only the first few modes is likely to be important.

The j^{th} impulsive natural cyclic frequency, in cycles per second may be expressed as

$$f_{ij} = \frac{1}{2\pi} \frac{C_{ij}}{H} \sqrt{\frac{E_w}{\rho_w}} \quad (2.2.5.1)$$

where C_{ij} is a dimensionless coefficient that depends on:

- the order j of the frequency considered
- the slenderness H/R
- the ratio of the wall thickness to tank radius t_w/R
- the ratio of mass densities for the liquid and tank wall material ρ/ρ_w
- Poisson's ratio of the tank material ν_w

The values of C_{ij} for the first three modes for a group of steel tanks filled with water is listed in Table 2.2.5.1a for $\rho/\rho_w=0.127$ and $\nu_w=0.3$. Table 2.2.5.1b gives the corresponding informations for concrete tanks with $t_w/R=0.01$, $\rho/\rho_w=0.4$ and $\nu_w=0.17$.

(a)	H/R									(b)			
	For $t_w/R = 0.0005$			For $t_w/R = 0.001$			For $t_w/R = 0.002$						
	C_{i1}	C_{i2}	C_{i3}	C_{i1}	C_{i2}	C_{i3}	C_{i1}	C_{i2}	C_{i3}				
0.3	0.0421	0.0737	0.0954	0.0600	0.1035	0.1344	0.0856	0.1446	0.1920	1.5	0.1681	0.3390	0.4821
0.4	0.0468	0.0834	0.1091	0.0666	0.1171	0.1521	0.0946	0.1628	0.2116	1.6	0.1679	0.3460	0.4934
0.5	0.0506	0.0914	0.1213	0.0719	0.1284	0.1688	0.1019	0.1787	0.2326	1.7	0.1673	0.3526	0.5039
0.6	0.0538	0.0981	0.1321	0.0762	0.1380	0.1841	0.1079	0.1924	0.2532	1.8	0.1664	0.3590	0.5137
0.7	0.0564	0.1039	0.1418	0.0799	0.1462	0.1978	0.1129	0.2042	0.2725	1.9	0.1652	0.3650	0.5230
0.8	0.0587	0.1089	0.1506	0.0829	0.1534	0.2103	0.1170	0.2145	0.2903	2.0	0.1638	0.3706	0.5317
0.9	0.0605	0.1135	0.1586	0.0855	0.1598	0.2217	0.1204	0.2237	0.3066	2.2	0.1604	0.3806	0.5477
1.0	0.0620	0.1177	0.1660	0.0875	0.1657	0.2322	0.1231	0.2322	0.3216	2.4	0.1565	0.3889	0.5622
1.1	0.0632	0.1217	0.1728	0.0891	0.1712	0.2418	0.1252	0.2400	0.3354	2.6	0.1522	0.3955	0.5757
1.2	0.0641	0.1254	0.1790	0.0903	0.1765	0.2507	0.1268	0.2475	0.3481	2.8	0.1478	0.4003	0.5884
1.3	0.0647	0.1290	0.1848	0.0911	0.1815	0.2589	0.1278	0.2546	0.3598	3.0	0.1434	0.4035	0.6004
1.4	0.0650	0.1325	0.1901	0.0916	0.1864	0.2665	0.1284	0.2614	0.3707				
1.5	0.0652	0.1358	0.1951	0.0918	0.1911	0.2735	0.1286	0.2680	0.3807				
1.6	0.0652	0.1390	0.1997	0.0917	0.1956	0.2800	0.1284	0.2743	0.3900				
1.7	0.0650	0.1420	0.2039	0.0914	0.1999	0.2861	0.1280	0.2804	0.3987				
1.8	0.0647	0.1449	0.2079	0.0910	0.2040	0.2918	0.1273	0.2861	0.4068				
1.9	0.0642	0.1477	0.2117	0.0904	0.2079	0.2971	0.1265	0.2916	0.4144				
2.0	0.0637	0.1503	0.2152	0.0896	0.2116	0.3021	0.1254	0.2967	0.4215				
2.2	0.0625	0.1549	0.2217	0.0879	0.2181	0.3113	0.1230	0.3057	0.4347				
2.4	0.0611	0.1587	0.2276	0.0859	0.2234	0.3198	0.1202	0.3132	0.4468				
2.6	0.0596	0.1616	0.2331	0.0838	0.2275	0.3276	0.1172	0.3189	0.4580				
2.8	0.0580	0.1637	0.2383	0.0815	0.2305	0.3351	0.1140	0.3229	0.4686				
3.0	0.0563	0.1651	0.2433	0.0792	0.2323	0.3421	0.1108	0.3254	0.4787				

Table 2.2.5.1: Dimensionless factor C_{ij} (a) for steel tanks with $\rho/\rho_w=0.127$ and $v_w=0.3$ and (b) for concrete tanks with $t_w/R=0.01$, $\rho/\rho_w=0.4$ and $v_w=0.17$ (after [48]).

From the tabulated informations, the results for any other combination of the parameters t_w/R and ρ/ρ_w . If the values of t_w/R , ρ/ρ_w and C_{ij} for some reference system is identified by the subscript r, the value of C_{ij} for any other system may be determined from

$$C_{ij} = (C_{ij})_r \sqrt{\frac{t_w/R}{(t_w/R)_r} \frac{(\rho/\rho_w)_r}{\rho/\rho_w}} \tag{2.2.5.2}$$

The inverse of expression 2.2.5.1 gives the j^{th} impulsive natural period, in seconds.

$$T_{ij} = \frac{2\pi}{C_{ij}} H \sqrt{\frac{\rho_w}{E_w}} \tag{2.2.5.3}$$

Note that expression 2.2.5.3, if calculated for the first mode T_{i1} , gives the same result of formula (E.4.5.1-1a) of API 650 when C_{i1} is read from Table 2.2.5.1a and the same result of formula (9.25) of ACI 350.3 when C_{i1} is read from Table 2.2.5.1b. An important remark must be made about concrete tanks: equation 2.2.5.3 is valid only for non-sliding base connected tanks. In fact, ACI 350.3 differentiate the formulation of the impulsive period for sliding and non-sliding base connected tanks. For further details see Section 2.4.3.

- **Natural sloshing period**

The natural frequency, in cycles per second, of the n^{th} convective or sloshing mode of vibration is given by:

$$f_{cn} = \frac{1}{2\pi} \sqrt{\lambda_n \frac{g}{R} \tanh[\lambda_n(H/R)]} \quad (2.2.5.4)$$

in which the first three values of λ_n are: $\lambda_1=1.841$, $\lambda_2=5.311$, $\lambda_3=8.536$.

The inverse of expression 2.2.5.4 gives the n^{th} convective natural period, in seconds.

$$T_{cn} = \frac{2\pi}{\sqrt{\lambda_n \frac{g}{R} \tanh[\lambda_n(H/R)]}} \quad (2.2.5.5)$$

Note that expression 2.2.5.5, if calculated for the first mode T_{c1} , gives the same result of formula (E.4.5.2-a) of API 650 and the same result of formula (9.30) of ACI 350.3. As an indication, it can be noted that, for relatively broad tanks ($H/R=0,5$), expression 2.2.5.5 leads to the following expressions for the first three sloshing periods, in seconds: $T_{c1}=5.49$, $T_{c2}=2.77$, $T_{c3}=2.17$. From Figure 2.2.7.3 of Section 2.2.7 it is evident how the spectral accelerations corresponding to these periods are significantly smaller than the maximum ground acceleration. As a result, the contribution of the sloshing modes to the magnitude of the wall pressures is practically negligible.

- **Other dynamic model parameters**

The dynamic model parameters are exactly the same for ACI 350.3 and API 650 and they are derived from the rigid tanks mechanical analogue.

Effective impulsive and convective masses:

$$m_i = \frac{\tanh\left(0,866 \frac{D}{H}\right)}{0,866 \frac{D}{H}} \cdot m \quad (2.2.5.6a)$$

$$m_c = 0,230 \frac{D}{H} \tanh\left(\frac{3,67 H}{D}\right) \cdot m \quad (2.2.5.6b)$$

Impulsive and convective heights for the determination of the overturning moment above the base plate:

$$h_i = 0,375 \cdot H \quad (2.2.5.7a)$$

$$h_c = \left[1 - \frac{\cosh\left(\frac{3,67 H}{D}\right)}{\frac{3,67 H}{D} \sinh\left(\frac{3,67 H}{D}\right)} \right] \cdot H \quad (2.2.5.7b)$$

Impulsive and convective heights for the determination of the overturning moment immediately below the base plate:

$$h'_i = 0,375 \cdot \left[1 + 1,333 \left(\frac{0,866 \frac{D}{H}}{\tanh \left(0,866 \frac{D}{H} \right)} - 1 \right) \right] \cdot H \quad (2.2.5.8a)$$

$$h'_c = \left[1 - \frac{\cosh \left(\frac{3,67 H}{D} \right) - 1,937}{\frac{3,67 H}{D} \sinh \left(\frac{3,67 H}{D} \right)} \right] \cdot H \quad (2.2.5.8b)$$

where m is the liquid mass, R is the tank radius and H is the liquid height.

- **Base shear and overturning moments**

In regions outside USA, both ACI 350.3 and API 650 allow to use a site-specific response spectrum for the calculation of the impulsive and convective pseudo-accelerations, based on the natural periods computed using expressions 2.2.4.3 and 2.2.4.5. In both the standards, it is suggested to use a design response spectrum, which must include the effect of site amplification, importance factor and response modification. The impulsive pseudo-acceleration A_i shall be calculated using a 5% damped spectrum, while the convective pseudo-acceleration A_c using a 0,5% damped spectrum. Actually, ACI 350.3 suggests to use 5% and 0,5% damped elastic response spectra constructed for ground motions having a maximum 10% probability of exceedance in 50 years. Then, the response modification factors (or behavior factors) R_{wi} and R_{wc} are applied directly on the forces (see ACI 350.3 formulas 4-1 to 4-4). For numerical values of these factors see Section 2.5.2.

The seismic base shear shall Q be defined as the square root of the sum of squares (SRSS) combination of the impulsive and convective components Q_i and Q_c .

$$Q = \sqrt{Q_i^2 + Q_c^2} \quad (2.2.5.9)$$

where:

$$Q_i = A_i(m_w + m_r + m_i) \quad (2.2.5.10a)$$

$$Q_c = A_c m_c \quad (2.2.5.10b)$$

In expressions 2.2.5.10 m_w and m_r are the masses of the tank walls and roof, respectively. m_i and m_c are the impulsive and convective mass defined in expressions 2.2.5.6. The SRSS is also

adopted to obtain the seismic overturning moments M and M' above and below the base plate are:

$$M = \sqrt{[(m_i h_i + m_w h_w + m_r h_r) \cdot A_i]^2 + [m_c h_c \cdot A_c]^2} \quad (2.2.5.11)$$

$$M' = \sqrt{[(m_i h'_i + m_w h_w + m_r h_r) \cdot A_i]^2 + [m_c h'_c \cdot A_c]^2} \quad (2.2.5.11)$$

2.2.6 Vertical component of the seismic action

The seismic response of fluid-filled tanks to earthquake excitations should combine its response to both horizontal and vertical components of ground motion. The horizontal component of the earthquake produces lateral shear force and overturning moments on the tank, as shown in Sections 2.2.2 to 2.2.5. However, the vertical component results in an axisymmetric increase or decrease of the hydrodynamic pressure with no additional lateral forces. Thus, unlike other structures, vertical earthquake motion may play a measurable role due to the development of additional hydrodynamic pressures which, in turn, induce hoop stresses in the shell.

The vertical component of an earthquake has a negligible contribution to the base shear and overturning moment, which are mainly caused by the two horizontal components. However, the vertical component of an earthquake amplifies the axisymmetric pressure. The peak hydrodynamic pressure occurs near the base of the tank and is approximately equal to a fraction of the peak hydrostatic pressure. In the most general case of a deformable tanks, this is computed by replacing the acceleration of gravity by the spectral vertical acceleration corresponding to the period of vibration of shell under axisymmetric vibration. Knowledge of the pressure component due to vertical excitation is essential in properly assessing the safety and strength of tank wall against buckling.

In all the codes effect of vertical acceleration is considered only for circular tanks, and there are no provisions on rectangular tanks. This is because response to vertical excitation is mainly governed by the time period of fundamental breathing mode or axisymmetric mode of vibration of tank-liquid system. It may be noted that this mode is for the case of circular tanks only. Expression for exact time period of axisymmetric mode of a circular tank is quite involved. However, considering certain approximations like, mass of tank wall is quite small as compared to fluid mass, some simple closed form expressions have been given by Veletsos (1984) in [47], and by Haroun and Tayel (1985).

All codes do have provisions to consider tank response under vertical excitation. Expressions for time period of vertical mode (axisymmetric breathing mode), from various codes are given in Table 2.2.6.1.

Code	Time period of vertical mode
ACI 350.3	$T_v = \frac{2}{\sqrt{t_w/R}} \pi H \sqrt{\frac{\rho}{E_w}}$
API 650	Evaluation of vertical time period is not described.
NZSEE Guidelines	$T_v = \frac{5,61}{K_v} \pi H \sqrt{\frac{\rho}{E_w}}$ K _v is given in graphical form as function of H/R and t _w /R
Eurocode 8	$T_v = \sqrt{\frac{8(1 - \nu_w^2) I_0(\lambda)}{\pi(t_w/R)(H/R) I_1(\lambda)}} \pi H \sqrt{\frac{\rho}{E_w}}$ where $\lambda = \pi/(2\gamma)$

Table 2.2.6.1: Expressions for time period of vertical mode in various codes.

EC8 uses expression from Haroun and Tayel (1985). ACI 350.3 suggest simpler expressions. Luft (1984) has described that such a simpler formula is good approximation for tall tanks. A comparison of variation of time period of vertical mode with H/R as obtained from ACI 350.3, NZSEE guidelines and Eurocode 8 is shown in Figure 2.2.6.1. It is noted that as per simplified formula of ACI 350.3, time period is independent of H/R and results of ACI 350.3 match well with those of EC8 for tall tanks. Further it is noted that NZSEE results are on higher side for tanks with large values of t_w/R.

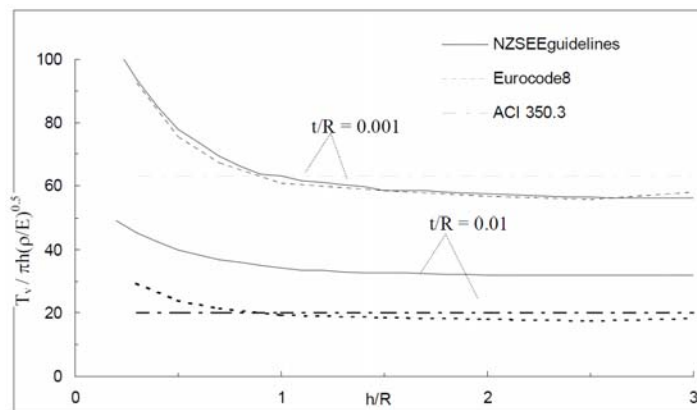


Fig. 2.2.6.1: Comparison of vertical time period coefficient (after [28]).

Distribution of hydrodynamic pressure due to vertical excitation also gets influenced by wall flexibility. For tanks with rigid wall, it is linearly distributed, i.e. hydrodynamic pressure is distributed same as hydrostatic pressure. From the expressions given in Table 2.2.6.2, it is seen that ACI 350.3 and NZSEE guidelines use linear pressure distribution for flexible tanks, i.e. effect of wall flexibility on distribution is not considered. This approach was suggested by Veletsos (1984), [47]. EC8 however, has incorporated the effect of wall flexibility on

distribution of hydrodynamic pressure. For flexible tanks, total pressure is sum of rigid component and a flexible component.

Code	Pressure component due to vertical seismic action
ACI 350.3	$p_v = \rho H b (1 - z/H) A_v(t)$ <i>b</i> is the ratio of vertical and horizontal acceleration, <i>b</i> should not be less than 2/3.
API 650	Distribution is not described.
NZSEE Guidelines	$p_v = \rho H (1 - z/H) A_v(t)$
Eurocode 8	For rigid tanks: $p_v = \rho H (1 - z/H) A_v(t)$ For flexible tanks: $p_v = \rho H (1 - z/H) A_v(t) + 0,815 f(\gamma) \rho H \cos\left(\frac{\pi z}{2H}\right) A_{vf}(t)$

Table 2.2.6.2: Expressions for time period of vertical mode in various codes.

API standards are extremely synthetic about the vertical seismic effect. Here, it is just said that vertical acceleration effects shall be considered in both upward and downward directions and combined with lateral acceleration effects by the SRSS rule. The maximum vertical seismic acceleration shall be taken as the 0.14S_{DS}, where S_{DS} is the design pseudo-acceleration corresponding to a period of 0.2 seconds. According to API 650, vertical seismic effects need not to be combined with the horizontal ones for determining loads, forces and resistances to overturning in the tank shell. Vertical seismic effects must be considered for determining shell hoop tensile stresses and shell membrane compression.

ACI 350.3 prescribe the use of the absolute (or direct) sum rule to combine vertical and horizontal seismic effects. According to Eurocode 8, when the response spectrum method is used, the peak combined pressure on the tank walls due to horizontal and vertical seismic actions may be obtained by applying the 30% rule (Figure 2.2.6.2). Then, the combined pressure should be added to the hydrostatic pressure on the wall at the one side of the tank (where the wall accelerates into the liquid) and subtracted as suction at the opposite.

- | |
|---|
| a) $E_{Edx} + 0,30 E_{E dy} + 0,30 E_{Edz}$
b) $0,30 E_{Edx} + E_{E dy} + 0,30 E_{Edz}$
c) $0,30 E_{Edx} + 0,30 E_{E dy} + E_{Edz}$ |
|---|

Fig. 2.2.6.2: 30% rule for combining the effects of the different earthquake components (after [12]).

2.2.7 A worked example

In this Section a worked example is reported. A steel tank, $E_s=2 \cdot 10^{11}$ N/m², $\rho_s=8000$ kg/m³, $f_y=275$ MPa, with a radius R of 10 m and total height of 9.6 m is fully anchored to a concrete mat foundation (Figure 2.2.7.1). The tank is filled with water, $\rho=1000$ kg/m³, to a height H of 8 m ($H/R = 0.8$). The tank wall is made of four courses, each 2.4 m high. The lower two courses are 1 cm thick and the upper two courses 0.8 cm thick. Let's determine the design seismic forces at ultimate limit states according to the Eurocode 8 simplified procedure of Section 2.2.4 and API 650 procedure of Section 2.2.5. Assumption: no vertical acceleration.

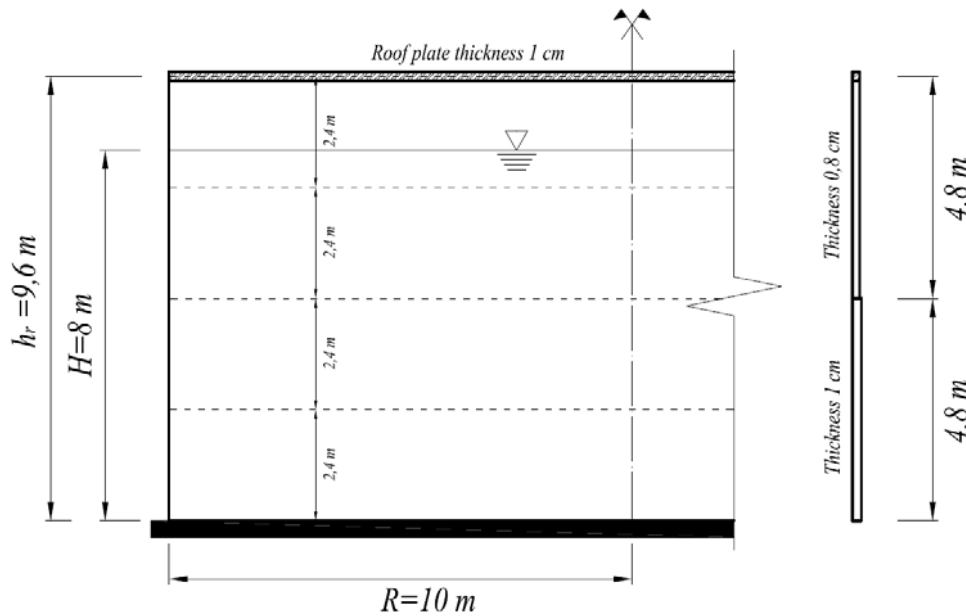


Fig. 2.2.7.1: Steel tank fully anchored to a concrete mat foundation.

$$\text{Liquid volume: } V_l = 8 \cdot (\pi 10^2) \cong 2510 \text{ [m}^3\text{]}$$

$$\text{Liquid mass: } m = \rho \cdot V_l = 1000 \cdot 2510 \cong 2,51 \cdot 10^6 \text{ [kg]}$$

$$\text{Cross sectional area in the bottom part of the tank: } A_{inf} = \pi(1000^2 - 999^2) \cong 6280 \text{ [cm}^2\text{]} = 0,63 \text{ [m}^2\text{]}$$

$$\text{Cross sectional area in the top part of the tank: } A_{sup} = \pi(1000^2 - 999,2^2) \cong 5025 \text{ [cm}^2\text{]} = 0,50 \text{ [m}^2\text{]}$$

$$\text{Tank wall volume } V_w = 4,8 \cdot (A_{sup} + A_{inf}) \cong 5,42 \text{ [m}^3\text{]}$$

$$\text{Tank wall mass: } m_w = \rho_s \cdot V_w = 8000 \cdot 5,42 \cong 43 \cdot 10^3 \text{ [kg]}$$

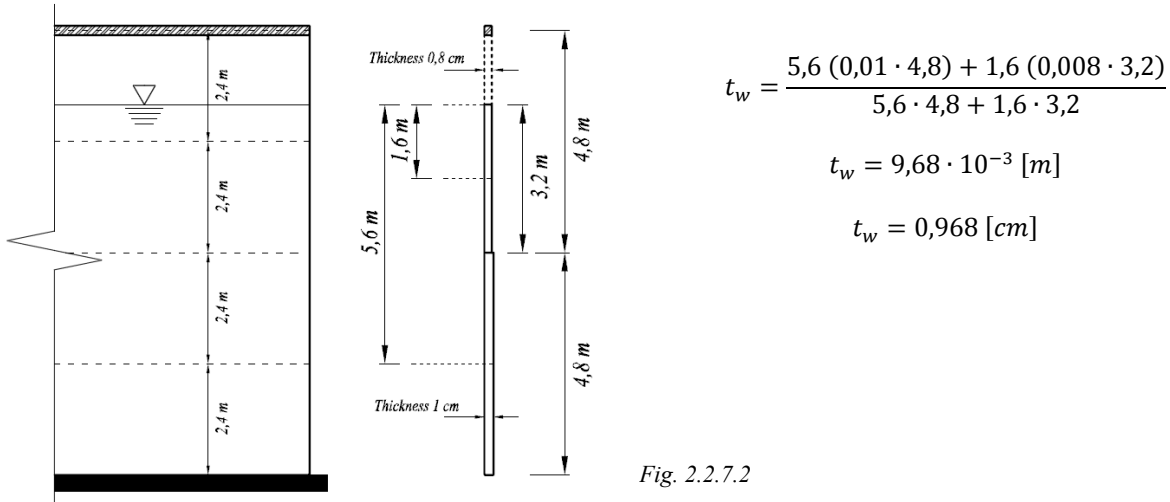
$$\text{Roof volume: } V_r = \pi r^2 \cdot t = \pi 10^2 \cdot 0,01 = 3,14 \text{ [m}^3\text{]}$$

$$\text{Roof mass: } m_r = \rho_s \cdot V_r = 8000 \cdot 3,14 \cong 25 \cdot 10^3 \text{ [kg]}$$

$$\text{Centroid of the wall: } h_w = \frac{240 \cdot (1 \cdot 480) + 720 \cdot (0,8 \cdot 480)}{(1 \cdot 480 + 0,8 \cdot 480)} \cong 453 \text{ [cm]} = 4,53 \text{ [m]}$$

$$\text{Centroid of the roof: } h_r = 9,6 \text{ [m]}$$

First, the equivalent uniform thickness t_w of the tank wall is calculated by the weighted average method, using weights equal to the distance from the liquid surface, Malhotra [30]. This method is derived from the rigorous procedure of Annex D of Eurocode 3 part 1-6, [11], for “Unstiffened cylindrical shells of stepwise variable wall thickness”.



• **Eurocode 8**

For $H/R=0.8$, $C_i=6,77$ and $C_c=1,57 \text{ s}/\sqrt{m}$ (Table 2.2.4.1). So the impulsive and convective periods are

$$T_i = C_i \frac{H\sqrt{\rho}}{\sqrt{t_w/R} \cdot \sqrt{E_s}} = 6,77 \frac{8\sqrt{1000}}{\sqrt{9,68 \cdot 10^{-3}/10} \cdot \sqrt{2 \cdot 10^{11}}} = 0,123 [s]$$

$$T_c = C_c\sqrt{R} = 1,57 \cdot \sqrt{10} = 4,965 [s]$$

For $H/R=0.8$, $m_i/m_1=0,459$ and $m_c/m_1=0,541$ (Table 2.2.3.1). Hence, the impulsive and convective masses are

$$m_i = 0,459 \cdot m = 0,459 \cdot 2,51 \cdot 10^6 \cong 1,15 \cdot 10^6 [kg]$$

$$m_c = 0,541 \cdot m = 0,541 \cdot 2,51 \cdot 10^6 \cong 1,36 \cdot 10^6 [kg]$$

Also, from Table 2.2.4.1, $h_i/H=0.404$, $h_c/H=0.583$, $h'_i/H=0.891$, $h'_c/H=0.954$. Hence, the impulsive and convective heights for the determination of the overturning moment above the base plate are

$$h_i = 0,404 \cdot H = 0,404 \cdot 8 = 3,23 [m]$$

$$h_c = 0,583 \cdot H = 0,583 \cdot 8 = 4,66 [m]$$

and the impulsive and convective heights for the determination of the overturning moment immediately below the base plate are

$$h'_i = 0,891 \cdot H = 0,891 \cdot 8 = 7,13 [m]$$

$$h'_c = 0,954 \cdot H = 0,954 \cdot 8 = 7,63 [m]$$

Assuming an importance factor $\gamma_I=1$ (tank containing drinking water, reliability class 2) and a reference peak ground acceleration $a_{gR}=1,962 \text{ m/s}^2$, the design peak ground acceleration is still $a_g=1,962 \text{ m/s}^2$. Assuming a soil type E, the soil factor S is 1,4 and the reference periods, in seconds, are $T_B=0.15$, $T_C=0.50$, $T_D=2.00$. So, the elastic response spectra can be plotted.

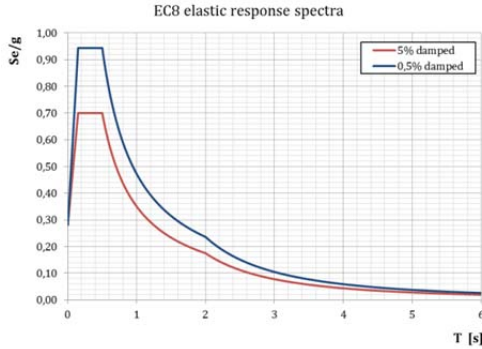


Fig. 2.2.7.3: Elastic response spectra.

The impulsive spectral acceleration for $T_i = 0.123 \text{ s}$, obtained from the 5% damped elastic response spectrum of Figure 2.2.7.3, is $S_e(T_i)=0.62g$. The convective spectral acceleration for $T_c= 4.960 \text{ s}$, obtained from the 0.5% damped response spectrum of Figure 2.2.7.3, is $S_e(T_c)=0.06g$.

The base shear is

$$\begin{aligned} Q &= (m_i + m_w + m_r) \cdot S_e(T_i) + m_c \cdot S_e(T_c) \\ &= (1,15 + 0,043 + 0,025) \cdot 10^6 \cdot 0,62 \cdot 9,81 + 1,36 \cdot 10^6 \cdot 0,06 \cdot 9,81 \cong 8,21 \text{ [MN]} \end{aligned}$$

The overturning moment above the base plate is

$$\begin{aligned} M &= (1,15 \cdot 3,23 + 0,043 \cdot 4,53 + 0,025 \cdot 9,6) \cdot 10^6 \cdot 0,62 \cdot 9,81 + 1,36 \cdot 10^6 \cdot 4,66 \cdot 0,06 \cdot 9,81 \\ &\cong 28,97 \text{ [MNm]} \end{aligned}$$

The overturning moment below the base plate is

$$\begin{aligned} M' &= (1,15 \cdot 7,13 + 0,043 \cdot 4,53 + 0,025 \cdot 9,6) \cdot 10^6 \cdot 0,62 \cdot 9,81 + 1,36 \cdot 10^6 \cdot 7,63 \cdot 0,06 \cdot 9,81 \\ &\cong 58,62 \text{ [MNm]} \end{aligned}$$

The maximum vertical displacement of the liquid surface due to sloshing is

$$\delta = R \frac{S_e(T_c)}{g} = 10 \cdot 0,06 = 0,6 \text{ [m]}$$

- **API 650**

For sake of simplicity, the same notation used above is maintained. However, the reference formula in the API 650 is always indicated in order to facilitate the reader.

Impulsive and convective periods (from API formulas E.4.5.1-1a and E.4.5.2a):

$$T_i = \frac{1}{\sqrt{2000}} C_i \frac{H\sqrt{\rho}}{\sqrt{t_w/D} \cdot \sqrt{E_s}} = \frac{1}{\sqrt{2000}} 6,7 \frac{8\sqrt{1000}}{\sqrt{9,68/20} \cdot \sqrt{210000}} = 0,119 \text{ [s]}$$

$$T_c = 1,8 \cdot K_s \cdot \sqrt{D} = 1,8 \cdot \frac{0,578}{\sqrt{\tanh\left(\frac{3,68 \cdot H}{D}\right)}} \cdot \sqrt{20} = 4,905 \text{ [s]}$$

Effective impulsive and convective masses (from API formulas E.6.1.1-1 and E.6.1.1-3):

$$m_i = \frac{\tanh\left(0,866 \frac{D}{H}\right)}{0,866 \frac{D}{H}} \cdot m = \frac{\tanh\left(0,866 \frac{20}{8}\right)}{0,866 \frac{20}{8}} \cdot 2,51 \cdot 10^6 \cong 1,13 \cdot 10^6 \text{ [kg]}$$

$$m_c = 0,230 \frac{D}{H} \tanh\left(\frac{3,67 H}{D}\right) \cdot m = 0,230 \frac{20}{8} \tanh\left(\frac{3,67 \cdot 8}{20}\right) \cdot 2,51 \cdot 10^6 \cong 1,30 \cdot 10^6 \text{ [kg]}$$

Impulsive and convective heights for the determination of the overturning moment above the base plate (from API formulas E.6.1.2.1-1 and E.6.1.2.1-3):

$$h_i = 0,375 \cdot H = 0,375 \cdot 8 = 3 \text{ [m]}$$

$$h_c = \left[1 - \frac{\cosh\left(\frac{3,67 H}{D}\right)}{\frac{3,67 H}{D} \sinh\left(\frac{3,67 H}{D}\right)} \right] \cdot H = 4,59 \text{ [m]}$$

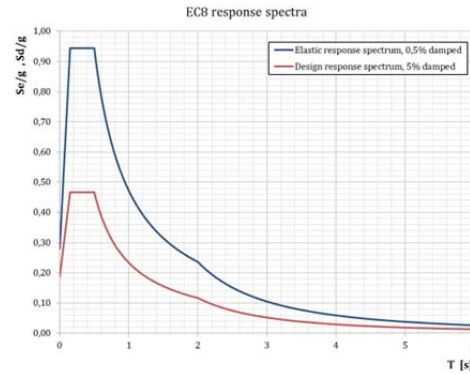
Impulsive and convective heights for the determination of the overturning moment immediately below the base plate (from API formulas E.6.1.2.2-1 and E.6.1.2.2-3):

$$h'_i = 0,375 \cdot \left[1 + 1,333 \left(\frac{0,866 \frac{D}{H}}{\tanh\left(0,866 \frac{D}{H}\right)} - 1 \right) \right] \cdot H = 7,89 \text{ [m]}$$

$$h'_c = \left[1 - \frac{\cosh\left(\frac{3,67 H}{D}\right) - 1,937}{\frac{3,67 H}{D} \sinh\left(\frac{3,67 H}{D}\right)} \right] \cdot H = 7,08 \text{ [m]}$$

Following the regulations for regions outside the USA specified at paragraph E.4.3, the impulsive and convective response accelerations (A_i and A_c in the API notation) are determined from the 5% and 0,5% damped design spectrum (Figure 2.2.7.4), respectively. The design response spectrum for the determination of the impulsive acceleration is obtained by applying a behavior factor $q=1,5$ to the 5% damped elastic spectrum. The value of the behavior factor is not taken from the API standards but from the Eurocode, because in the API standards only the values for the “allowable stress design method” are given (see Table 2.5.2.1 of Section 2.5.2). No dissipation of energy is associated to the convective component, so the design response spectrum for the determination of the convective acceleration is essentially the 0.5% damped elastic spectrum.

Fig. 2.2.7.4: Design and elastic response spectrum.



$$A_i = S_d(T_i) = 4,01 \text{ [m/s}^2\text{]} = 0,41g$$

$$A_c = S_e(T_c) = 0,59 \text{ [m/s}^2\text{]} = 0,06g$$

Now, the design seismic forces can be computed according to the SRSS combination rule.

The base shear (from API formula E.6.1-1) is:

$$\begin{aligned} Q &= \sqrt{[(m_i + m_w + m_r) \cdot A_i]^2 + [m_c \cdot A_c]^2} \\ &= \sqrt{[(1,13 + 0,043 + 0,025) \cdot 10^6 \cdot 0,411 \cdot 9,81]^2 + [1,30 \cdot 10^6 \cdot 0,039 \cdot 9,81]^2} \cong 5,58 \text{ [MN]} \end{aligned}$$

The overturning moment above the base plate (from API formula E.6.1.5-1) is:

$$\begin{aligned} M &= \sqrt{[(m_i h_i + m_w h_w + m_r h_r) \cdot A_i]^2 + [m_c h_c \cdot A_c]^2} \\ &= \sqrt{[(1,15 \cdot 3 + 0,043 \cdot 4,53 + 0,025 \cdot 9,6) \cdot 10^6 \cdot 0,411 \cdot 9,81]^2 + [1,30 \cdot 10^6 \cdot 4,59 \cdot 0,039 \cdot 9,81]^2} \\ &\cong 18,90 \text{ [MNm]} \end{aligned}$$

The overturning moment below the base plate (from API formula E.6.1.5-2) is:

$$\begin{aligned} M' &= \sqrt{[(m_i h'_i + m_w h_w + m_r h_r) \cdot A_i]^2 + [m_c h'_c \cdot A_c]^2} \\ &= \sqrt{[(1,15 \cdot 7,89 + 0,043 \cdot 4,53 + 0,025 \cdot 9,6) \cdot 10^6 \cdot 0,411 \cdot 9,81]^2 + [1,30 \cdot 10^6 \cdot 7,08 \cdot 0,039 \cdot 9,81]^2} \\ &\cong 43,03 \text{ [MNm]} \end{aligned}$$

The maximum vertical displacement of the liquid surface due to sloshing (from API formula E.7.2-1) is:

$$\delta = 0,5 D A_f = 1,24 \text{ [m]}$$

where:

$$A_f = K S_{DI} I \frac{4}{T_{con}^2} = 0,124g$$

$K = 1,5$ (coefficient to adjust the spectral acceleration from 5% - 0,5%)

$I = 1$ (importance factor coefficient set by the seismic use group, assumed I)

$S_{DI} = Q F_v S_1 = 0,5g$ (the design, 5% damped, spectral response acceleration parameter at a period of one second)

$Q = 2/3$ (scaling factor from the maximum considered earthquake to the design level spectral acceleration)

$S_1 = 1,25 S_p = 1,25 \cdot 0,20g = 0,25g$ (mapped, maximum considered earthquake, 5% damped, spectral response acceleration parameter at one second)

$S_p = 0,20g$ (peak ground acceleration)

$F_v = 3$ (velocity based site coefficient, for soil type E)

- **Results summary**

	Eurocode 8	API 650	
Impulsive time period T_i	0,123	0,119	[s]
Convective time period T_c	4,965	4,905	[s]
Impulsive mass m_i	$1,15 \cdot 10^6$	$1,13 \cdot 10^6$	[Kg]
Convective mass m_c	$1,36 \cdot 10^6$	$1,30 \cdot 10^6$	[Kg]
Impulsive height h_i	3,23	3,00	[m]
Convective height h_c	4,66	4,59	[m]
Impulsive height h'_i	7,13	7,89	[m]
Convective height h'_c	7,63	7,08	[m]
Impulsive pseudo-acceleration A_i	0,62g	0,41g	[m/s ²]
Convective pseudo-acceleration A_c	0,06g	0,06g	[m/s ²]
Base shear Q	8,21	5,58	[MN]
Overturning moment above the base plate M	28,97	18,90	[MNm]
Overturning moment below the base plate M'	58,62	43,03	[MNm]
Sloshing wave height δ	0,60	1,24	[m]

Table 2.2.7.1: Comparison between the results obtained using the Eurocode 8 and the API 650 prescriptions.

From Table 2.2.7.1 it is possible to note that:

- The impulsive and convective periods, masses and heights calculated according to the Eurocode and the API standards are almost the same. In fact, the formulas used for all these quantities are derived from the same simplified theory, the one presented in Section 2.2.1. The small differences in the numerical values are due to the small differences in the tabulated coefficients entering the above mentioned formulas. These coefficient are calculated for the SI units system in the Eurocode and for the US Customary units system in the API standards;
- The impulsive pseudo-acceleration calculated using the Eurocode is higher than the one of the API standards. This is due to the fact that in the Eurocode it is derived from an elastic 5% damped response spectrum, while the API suggest to use a design 5% damped spectrum which must include the effects of site amplification, importance factor and response modification.
- The convective pseudo-acceleration calculated according the two standards is exactly the same. In fact, it is derived from the same elastic 0,5% damped response spectrum;

- The fact that the impulsive pseudo-acceleration calculated using the Eurocode is higher than the one of the API standards is directly reflected on the design seismic forces. In fact, they are higher according to the Eurocode, which seems to be more conservative in the evaluation of such quantities;
- Another reason of the discrepancy in the seismic forces values lays in the fact that the two standards use different combination rules for the impulsive and the convective effects (see Section 2.5.3). The absolute sum used by the Eurocode 8 results in higher values of the seismic forces than the one calculated with the SRSS rule used by the API. However, this fact is much less influent than the difference in the impulsive acceleration values. In fact, if we use the same impulsive acceleration in the two standards, for example 0,41g, the seismic forces are:

	Eurocode 8	API 650	
Base shear Q	5,70	5,58	[MN]
Overturning moment above the base plate M	20,42	18,90	[MNm]

Table 2.2.7.2: Comparison between the results obtained using the Eurocode 8 and the API 650 prescriptions. $A_i=0,41g$ and $A_c=0,06g$.

From Table 2.2.7.2 it is evident that the absolute sum rule results in an overestimation of the seismic forces. However, the difference is not so big if compared to the difference arising from the use of two different response spectra (elastic and design) for the evaluation of the impulsive component;

- Finally, the sloshing wave height is slightly different in the two standards. This is due to the fact that they use two different empirical formulations for the estimation of this quantity. In particular, in the API standards the sloshing wave height results 60 cm higher than the Eurocode one.

2.3 Anchored vs Unanchored tanks

2.3.1 Eurocode 8: unanchored tanks

The impulsive and convective natural periods, masses and effective heights are calculated for an anchored tank, following the simplified procedure for fixed-base cylindrical tanks by Malhotra (Section 2.2.4) or the rigorous methods of Sections 2.2.2 and 2.2.3. If applicable, the impulsive natural period and damping are increased by taking into account the inertial soil-structure interaction (SSI) effects. Appendix A.7 of Eurocode 8 gives the corresponding formulas. With these increased values, the overturning moments above and below the base plate

are calculated, again according to Section 2.2.4. In most cases, the effects of uplift and of the accompanying rocking motion on the magnitude of the pressures is disregarded. For most purposes this is conservative, as rocking increases the flexibility of the system and shifts the period into a range of less dynamic amplification of forces. Once the peak hydrodynamic pressures are known, whether determined ignoring or considering uplift and SSI, calculation of the stresses in the tank is a matter of static structural analysis.

In Eurocode 8-Appendix A.9, three graphs in are used to calculate the uplift width, uplift height and axial compressive stress in the tank wall as functions of normalized overturning moment (Figures 2.3.1.1, 2.3.1.2 and 2.3.1.3). These figures are based on purely static finite element analyses performed by Scharf in [41]. Therefore, they do not account for an increase in the fundamental natural period of the impulsive mode due to uplifting, which, for most practical cases, leads to a significant decrease in the overturning moment. For fixed roofs, the values in Figure 2.3.1.1 are on the safe side, since they have been calculated assuming that the underlying soil to be quite stiff (Winkler springs with a subgrade reaction $k=4000 \text{ MN/m}^3$) which is unfavorable for vertical membrane forces).

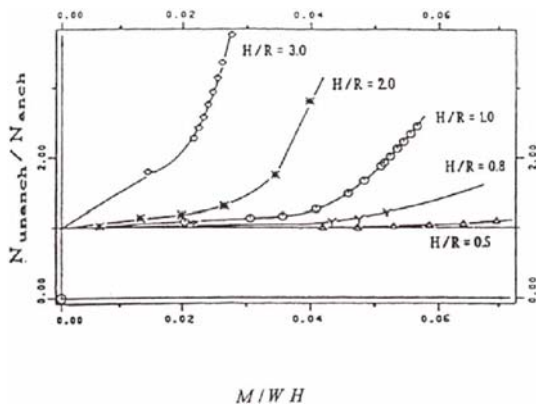


Fig. 2.3.1.1: Ratio of maximum compressive axial membrane force for fixed-roof unanchored cylindrical tanks on ground versus overturning moment (W =total weight of liquid). Figure A.11 in EC8 (after [13]).

From Figure 2.3.1.1 it can be seen that the maximum compressive axial force is strongly sensitive to the slenderness ratio H/R . In particular, for slender tanks the increase with respect to the anchored case is very significant. More or less the same trend can be observed in Figure 2.3.1.2 for the uplift height.

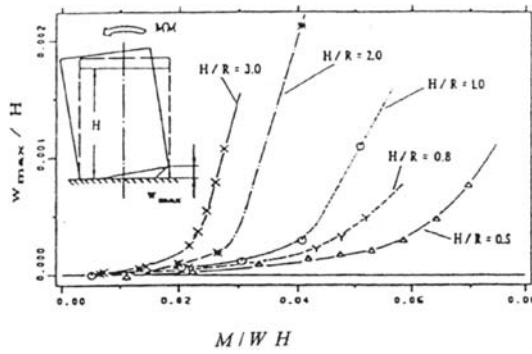


Fig. 2.3.1.2: Maximum vertical uplift of fixed-roof unanchored cylindrical tanks on ground versus overturning moment (W =total weight of liquid). Figure A.12 in EC8 (after [13]).

The plastic rotation θ in the base plate is calculated from the uplift height w and uplift width L and it must not exceed the estimated rotation capacity of 0.20 radians. The uplift width L can be obtained from Figure 2.3.1.3. Note that the uplifted length L seems to grow linearly with the uplift height w .

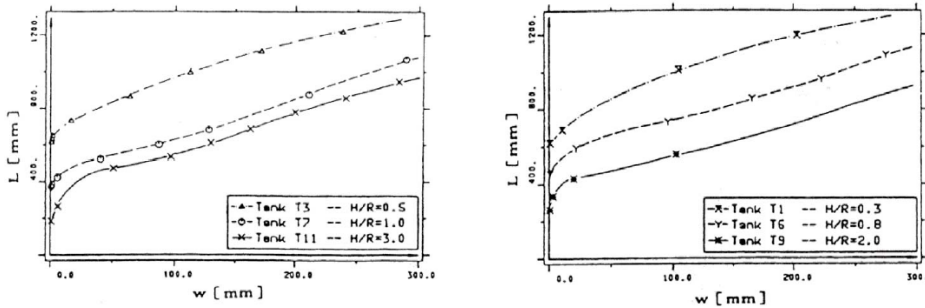


Fig. 2.3.1.3: Length of the uplifted part of the base in fixed-roof unanchored cylindrical tanks on ground as a function of the vertical uplift at the edge. Figure A.13 in EC8 (after [13]).

For the radial membrane stresses in the base plate only an empirical formulation is given and for more precise evaluations the use of a finite element model is suggested.

2.3.2 API 650: self-anchored steel tanks

In API 650 standards anchored and unanchored tanks are named “mechanically anchored” and “self-anchored tanks”. For self-anchored tanks a portion of the contents may be used to resist overturning. The overturning resisting force shall be determined by equation 2.3.2.1 (equation E.6.2.1.1-1a of API 650):

$$w_L = 99t_a \sqrt{f_y H \rho} \tag{2.3.2.1}$$

where in the specific gravity of the liquid ρ should be included also the effect of vertical acceleration, if any. t_a is the thickness of the bottom plate. Equation 2.3.2.1 is obtained from a translational equilibrium equation.

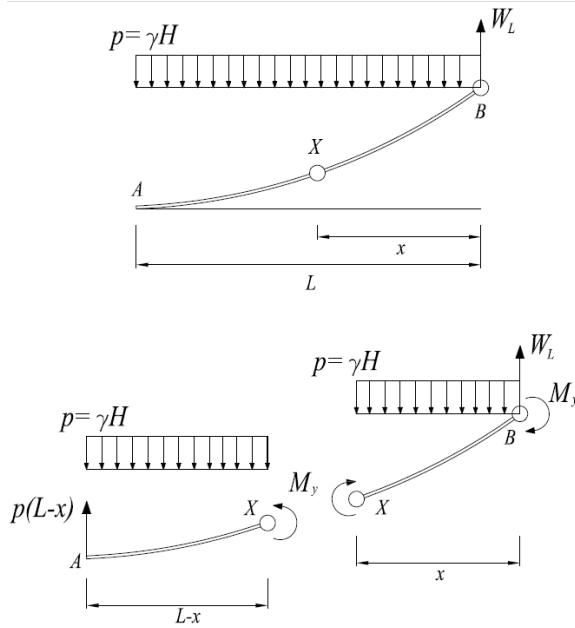


Fig. 2.3.2.1: Model for the uplifting force and uplifted length calculation, Wozniak and Mitchell (1978).

From the rotational equilibrium of the portion X-B of the beam of Figure 2.3.2.1 it is possible to calculate the position x of the inner plastic hinge.

$$\frac{px^2}{2} - 2M_y = 0 \tag{2.3.2.2a}$$

$$x = \sqrt{\frac{4M_y}{p}} \tag{2.3.2.2b}$$

Note that the position x of the inner plastic hinge depends on the hydrostatic pressure $p = \rho H$ and on the plastic bending moment $M_y = f_y \cdot w_p$, where $w_p = t_a^2/4$ is the plastic section modulus. As already mentioned in Section 1.3.2, the beam considered is a unitary strip of the bottom plate. Substituting p and M_y into equation 2.3.2.2b:

$$x = \sqrt{\frac{f_y t_a^2}{\rho H}} \tag{2.3.2.2c}$$

Now, considering the translational equilibrium of the portion X-B, it is possible to calculate the uplifting force:

$$w_L = px \tag{2.3.2.3a}$$

$$w_L = t_a \sqrt{f_y \cdot \rho \cdot H} \tag{2.3.2.3b}$$

Note that equation 2.3.2.3b coincides with equation 2.3.2.1; the coefficient 99 in equation 2.3.2.1 is due to the fact that in the API formula t_a is in mm, f_y is in MPa and γ in t/m^3 . Finally, from the

rotational equilibrium of the portion A-X, it is possible to compute the uplifted length L. A quadratic equation must be solved, but all the passages are omitted here.

$$\frac{p(L-x)^2}{2} - 2M_y = 0 \quad (2.3.2.4a)$$

$$L = 1,7 t_a \sqrt{\frac{f_y}{\rho H}} \quad (2.3.2.4b)$$

Equation 2.3.2.4b coincides with equation E.6.2.1.1.2-1a of API 650; the coefficient 1.7 is different because of the units system imposed by API.

Only empirical formulations are given for the estimation of the tank uplift, function of the uplifted length and the material yield strength. See equation E.7.3.1-1a in API 650.

For the calculation of the maximum vertical compressive stress σ_c the API standards are extremely synthetic. In fact they give only three different formulas according to the calculated anchorage ratio J (equation E.6.2.1.1.1-1), function of the overturning moment. If $J < 0,785$ the tank is self-anchored (no uplift) and the shell compression is given by equation E.6.2.2.1-1a; if $0,785 < J < 1,54$ the tank is uplifting but it is stable for the design load providing the shell compression is verified. In this case the shell compression is given by equation E.6.2.2.1-2a. If $J > 1,54$ the tank is not stable and a mechanical anchorage is needed; in this last case the shell compression is given by equation E.6.2.2.2-1a. Then, the so calculated maximum vertical compressive stress σ_c must be compared with the allowable compression stress F_c of equations (E.6.2.2.3-1a)-(E.6.2.2.3-2a).

As regards the hoop forces, different applicative formulas are given, according to the slenderness parameter D/H. Both the impulsive and convective effects, N_i and N_c , must be computed and then combined according to the SRSS rule. Finally, the hydrostatic effect N_h must be added. So, the hoop tensile stress, neglecting the effect of vertical acceleration, becomes

$$\sigma_T = \frac{N_h \pm \sqrt{N_i + N_c}}{t_w} \quad (2.3.2.5)$$

and it must be less than the yielding stress of the shell material.

2.3.3 ACI 350.3: uplifting in concrete tanks

The type of base on which tank is resting influences the time period of the tank itself. Some of the codes deal with tanks with different types of base supports. For example, ACI 350.3

mention about anchored, unanchored, flexible and unconstrained type of base supports, as shown in Figure 2.3.3.1. Whereas, API 650 and EC8 guidelines do not describe such base support.

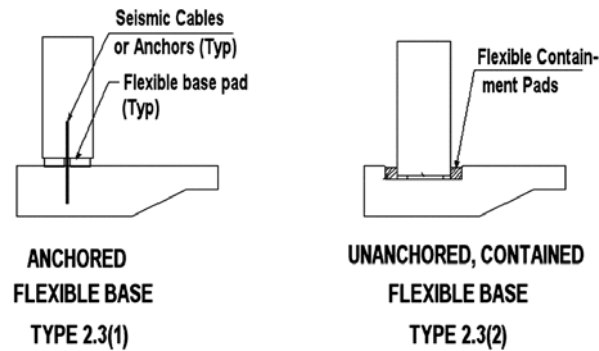


Fig. 2.3.3.1: Types of ground-supported, liquid-containing structures classified on the basis of their wall-to-footing connection (after [1]).

From an analysis point of view the fact that the tank is anchored or not does not make difference in ACI 350.3. For example, tanks of type 2.3(1) and 2.3(2) are calculated with the same method. In ACI 350.3 formulas to estimate the uplifting height, uplifting width or uplifting force are not present. This is due to the fact that in concrete tanks the uplifting phenomenon occurs in a totally negligible way, probably because of the weight of these structures, certainly bigger than the weight of steel tanks. Furthermore, common dimensions of concrete tanks involves low height to radius ratios. So, for such broad structures, the global stability with respect to overturning needs not to be verified. The most important issue when dealing with concrete tanks is the cracking phenomenon; in fact, for liquid-storage structures it is important to limit the cracks width in order to avoid liquid losses. Due to this reason, prestressed concrete is often used. However, apart from the cracking verifications, the structural elements (walls and foundations) must be verified with the usual calculations for reinforced concrete sections at ultimate limit states.

2.3.4 A worked example

In this Section a worked example is reported. The same steel tank of Section 2.2.7 is considered, but now it is not fully anchored to a concrete mat foundation but it is left unanchored. The thickness of the bottom plate is $t_a=7\text{mm}$. Assumption: $A_v=0$, no vertical acceleration. Let's study the uplifting phenomenon according to the Eurocode 8 method of Section 2.3.1 and API 650 procedure of Section 2.3.2.

- **Eurocode 8**

The first step to determine the internal forces of the tank according to the EC8, is the evaluation of the dimensionless quantity:

$$\frac{M}{WH} = \frac{28,97 \cdot 10^6}{2,51 \cdot 10^7 \cdot 8} = 0,145$$

where W is the total weight of the stored liquid.

It is immediate to note that this value is too high for the tabular method suggested by EC8 and presented here in Section 2.3.1. In fact, it is “out of tables” (see Figures 2.3.1.1 and 2.3.1.2). So, the design process according to EC8 cannot be carried out.

- **API 650**

For sake of simplicity, the notation used in this thesis is maintained. However, the reference formula in the API 650 is always indicated in order to facilitate the reader.

Weight of the tank roof and tank walls, distributed over the perimeter:

$$w_r = \frac{W_r}{2\pi R} = \frac{250}{2\pi \cdot 10} = 3,98 \text{ [kN/m]}$$

$$w_w = \frac{W_w}{2\pi R} = \frac{430}{2\pi \cdot 10} = 6,84 \text{ [kN/m]}$$

Weight of the fluid content that resists overturning (from API formula E.6.2.1.1-1a):

$$w_L = 99t_a \sqrt{f_y \rho H} = 99 \cdot 7 \sqrt{275 \cdot 1 \cdot 8} = 32,51 \text{ [kN/m]}$$

In order to define the seismic behavior of the tank let's define the anchorage ratio (from API formula E.6.2.1.1.1-1):

$$J = \frac{M}{D^2(w_r + w_w + w_L)} = 1,09$$

$0,785 < J < 1,54$. So, according to API Table E-6 the tank is uplifting, but it is stable for the design load. The tank is self-anchored.

Uplifted length (from API formula E.6.2.1.1.2-1a):

$$L = 0,01723t_a \sqrt{f_y / \rho H} = 0,01723 \cdot 7 \sqrt{275 / (1 \cdot 8)} = 0,71 \text{ [m]}$$

Estimation of the tank uplift (from API formula E.7.3.1-1a):

$$w = \frac{12,10 f_y L^2}{t_a} = \frac{12,10 \cdot 275 \cdot 0,71^2}{7} \cong 240 \text{ [mm]}$$

Maximum longitudinal shell-membrane compression stress (from API formula E.6.2.2.1-2a):

$$\sigma_c = \left(\frac{w_r + w_w + w_L}{0,607 - 0,18667 \cdot J^{2,3}} - w_L \right) \frac{1}{1000 t_w} = \left(\frac{3980 + 6840 + 32510}{0,607 - 0,18667 \cdot 1,09^{2,3}} - w_L \right) \frac{1}{1000 \cdot 9,68} \cong 8,44 \text{ [MPa]}$$

Dynamic hoop forces (from API formulas E.6.1.4-1a and E.6.1.4-4a):

$$N_i = 8,48 A_i \rho D H \left[\frac{y}{H} - 0,5 \left(\frac{y}{H} \right)^2 \right] \tanh \left(0,866 \frac{D}{H} \right) = 8,48 \cdot 0,41 \cdot 1 \cdot 20 \cdot 8 \left[\frac{7,7}{8} - 0,5 \left(\frac{7,7}{8} \right)^2 \right] \tanh \left(0,866 \frac{20}{8} \right) \\ \cong 270,53 \text{ [kN/m]}$$

$$N_c = \frac{0,98 A_c \rho D^2 \cosh \left[\frac{3,68(H-y)}{D} \right]}{\cosh \left(3,68 \frac{H}{D} \right)} = \frac{0,98 \cdot 0,06 \cdot 1 \cdot 20^2 \cosh \left[\frac{3,68(8-7,7)}{20} \right]}{\cosh \left(3,68 \frac{8}{20} \right)} \cong 19,39 \text{ [kN/m]}$$

where y is the distance from liquid surface to analysis point. If we analyze a section 30 cm above the base (which is often the most critical, see Section 3.1.2), then $y=H-0.3=7.7$ m.

Static hoop force:

$$N_h = \rho y R = 10 \cdot 8 \cdot 10 = 770 \text{ [kN/m]}$$

Dynamic hoop tensile stress (from API formula E.6.1.4-6):

$$\sigma_T = \frac{N_h + \sqrt{N_i^2 + N_c^2}}{t_w} = \frac{770 + \sqrt{152,01^2 + 19,39^2}}{9,68} \cong 107,56 \text{ [MPa]}$$

2.4 Rigidly supported vs Flexibly supported tanks

2.4.1 Simplified model and its application to Eurocode 8

For tanks founded on relatively deformable soils, the base motion can be significantly different from the free-field motion, for the reasons explained in Section 1.3.4. In general the translational component is modified and there is also a rocking component. Moreover, for the same input motion, as the flexibility of the ground increases, the fundamental period of the tank-fluid system and the total damping increase, reducing the peak force response. The increase in the period is more pronounced for tall, slender tanks, because the contribution of the rocking component is greater. The reduction of the peak force response, however, is in general less for tall tanks, since the damping associated with rocking is smaller than that associated with horizontal translation. A simple procedure, proposed for buildings by Veletsos (1977) and consisting of an increase of the fundamental period and of the damping of the structure, which is considered to rest on a rigid soil and subjected to the free-field motion, has been extended to the impulsive (rigid and flexible) components of the response of tanks in [17], [49], [51] by

Habenberger, Veletsos et al. The convective periods and pressures are assumed not to be affected by soil-structure interaction. A good approximation can be obtained through the use of an equivalent simple oscillator with parameters adjusted to match frequency and peak response of the actual system. The properties of this substitute oscillator are given by Habenberger, Veletsos et al. in [17], [51] in the form of graphs, as functions of the ratio H/R , for fixed values of the wall thickness ratio t_w/R , the initial damping, etc.

Here, the key points of the method are reported. To investigate the influence of the foundation flexibility on the seismic response of tanks the mechanical model developed by Veletsos and Tang (1992) is used. This model is based on the substructure method. Due to this method the shell-liquid-soil system is divided into two independent subsystems: the foundation-soil system and the tank-liquid system. The former can be modeled by spring-dashpot elements, and the latter can be idealized by single-degree-of-freedom oscillators, Haroun and Housner (1981), see Section 1.3.1. The coupling between the two subsystems is provided by interactive forces having equal amplitudes and opposite direction of action. This leads to a mechanical model of the coupled system which is shown in Figure 2.4.1.1a.

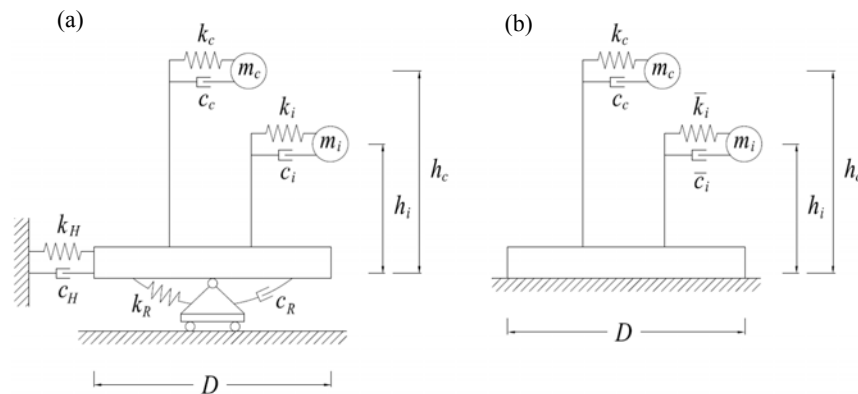


Fig. 2.4.1.1: Mechanical models for the soil-tank-liquid coupled system. (a) Coupled system. (b) Equivalent decoupled system.

The spring-dashpot elements k_H , c_H , k_R , c_R are frequency-dependent. Therefore, it may be appropriate to perform the analysis in the frequency domain.

However, for engineering application and design purposes the use of the response spectra method is always convenient. Because of the strong damping of the mechanical system of Figure 2.4.1.1, the modal decoupling is very complicated. So, Veletsos and Tang (1992) suggest an approximate decoupling using the transfer function of the coupled system, providing the base for response spectra calculations. The reliability and capability of the suggested engineering approach could be proved by comparison with more refined finite element calculations, see

Section 2.5.5. From the transfer function the adapted damping value and frequency value for system of Figure 2.1.1.2 can be determined. These adapted values are given by Habenberger in [17] in graphical form.

The described SDOF-system can be applied to the current version of the EC8 to consider the flexibility of the liquid tank basemat. The overall damping behavior of the replacement system is:

$$\bar{\xi}_i = \xi_R + \xi_m \beta^3 \tag{2.4.1.1}$$

where ξ_m is the structural damping of the tank. Damping values ξ_R and frequency ratios β are given in Figure 2.4.1.2, depending on the tank slenderness H/R and for different shear velocities of the subsoil v_s .

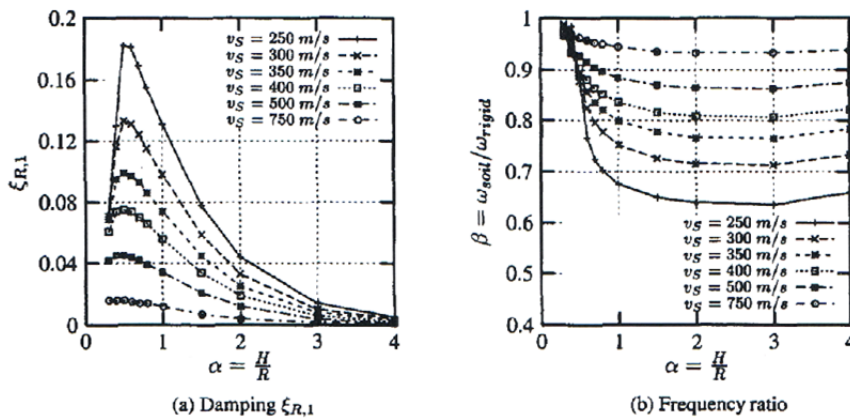


Fig. 2.4.1.2: Dynamic coefficients for the 1st mode of the impulsive horizontal vibration of the equivalent system with flexible foundation (after [17]).

2.4.2 A more rough procedure from NZSEE

In addition to the method of Section 2.4.1, Eurocode 8 also suggests a further simplified procedure, taken from Priestley [38]. The procedure operates by changing separately the frequency and the damping of the impulsive rigid and the impulsive flexible pressure contributions of Sections 2.2.1 and 2.2.2. In particular, for the rigid impulsive pressure components, whose time-histories are given by the free-field horizontal acceleration $A_g(t)$, consideration of soil-structure interaction effects amounts to replacing these time-histories with the response acceleration histories of a single degree of freedom oscillator having natural period and damping as specified below.

‘Rigid tank’ impulsive effect

$$T_i^* = 2\pi \sqrt{\frac{m_i + m_0}{k_x \alpha_x} + \frac{m_i h_i'^2}{k_\theta \alpha_\theta}} \quad (2.4.2.1)$$

‘Deformable tank’ impulsive effect

$$T_f^* = T_f \sqrt{1 + \frac{k_f}{k_x \alpha_x} + 1 + \frac{k_x h_f^2}{k_\theta \alpha_\theta}} \quad (2.4.2.2)$$

where m_0 is the mass of the foundation, m_{tot} is the total mass of the filled tank (including the foundation), k_f is the stiffness of the deformable tank, k_x is the horizontal stiffness of the foundation ($= 4\pi^2 m_f / T_f^2$), k_θ is the rocking stiffness of the foundation and α_x, α_θ are frequency dependent factors converting static stiffnesses into dynamic ones, Veletsos and Tang [51].

The general expression for the effective damping ratio of the tank foundation stiffness is:

$$\xi = \xi_s + \frac{\xi_m}{(T^* + T)^3} \quad (2.4.2.3)$$

where ξ_s is the radiation damping in the soil and ξ_m is the material damping in the tank. Both ξ_s and ξ_m depend on the specific vibration mode. In particular for ξ_s :

for the horizontal impulsive ‘rigid tank’ mode:

$$\xi_s = 2\pi^2 \frac{a}{T_i^*} \left(\frac{\beta_x}{\alpha_x} + \frac{k_x h_i'^2 \beta_\theta}{k_\theta \alpha_\theta} \right) \quad (2.4.2.4)$$

for the horizontal impulsive ‘deformable tank’ mode:

$$\xi_s = \frac{2\pi^2 m_f}{T_f^{*2}} a \left(\frac{\beta_x}{\alpha_x} + \frac{k_x h_f^2 \beta_\theta}{k_\theta \alpha_\theta} \right) \quad (2.4.2.5)$$

where a is the dimensionless frequency function ($= 2\pi R / v_s T$) and β_x, β_θ are frequency dependent factors providing radiation damping values for horizontal and rocking motions, [51].

2.4.3 ACI 350.3: the importance of the base connection

As already mentioned in Section 2.1, in ACI 350.3 methods to study the soil-structure interaction are not present. The flexibility of the base support involves only the type of base connection. In fact, for concrete tanks the base concrete mat may be assumed always rigid with respect to the supporting soil. So, the flexibility at the base totally lies in the fact that the walls can slide with respect to the base mat. This is the reason why, in ACI 350.3, “non-flexible” or “flexible” base connection may be also interpreted as “non-sliding” or “sliding” base connection.

The type of base on which tank is resting influences the time period of the tank itself. Some of the codes deal with tanks with different types of base supports. API 650 and EC8 guidelines do not describe such base support.

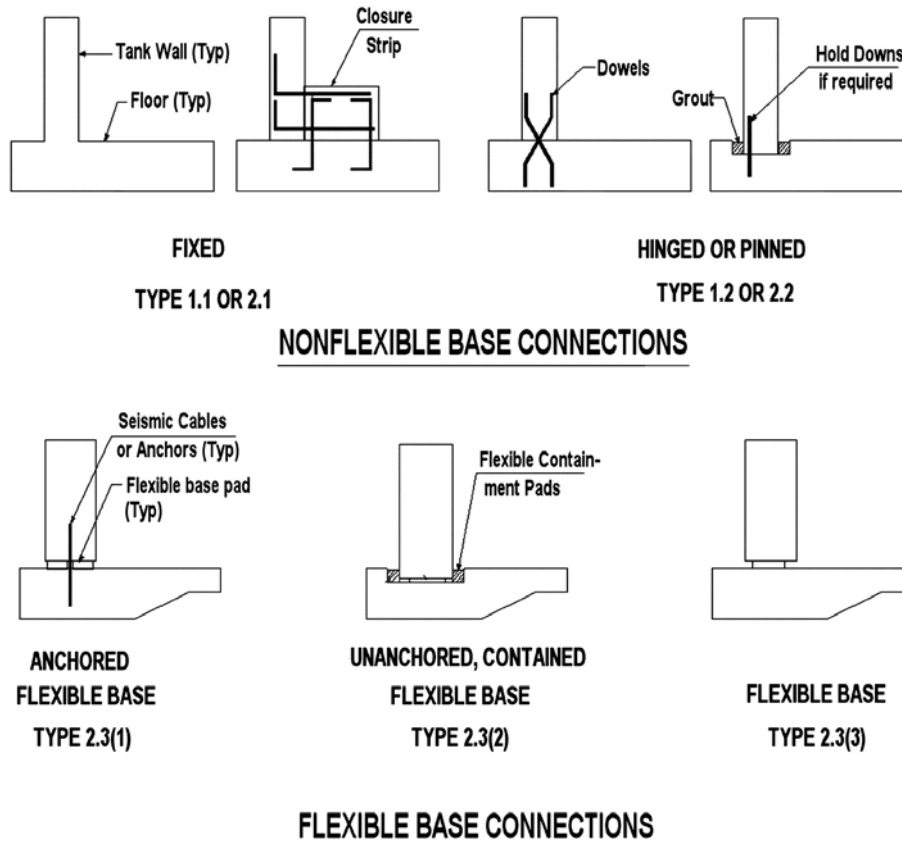


Fig. 2.4.3.1: Types of ground-supported, liquid-containing structures classified on the basis of their wall-to-footing connection (after [1]).

From Figure 2.4.3.1 note that tanks with a non-sliding connection are all anchored, whereas tanks with a sliding base connection may be either anchored or unanchored. The method employed to calculate the seismic forces is based on the mechanical analogue for rigid tanks, see Sections 1.2.2 and 2.2.4. What really changes is the formula to compute the impulsive period. In fact, it is different for non-sliding (ACI formula 9.25 and equation 2.2.4.3 of Section 2.2.4) and sliding base tanks (ACI formula 9.26). Furthermore, for sliding base tanks an upper bound of 1.25 seconds is suggested, in order to prevent excessive deformations.

In order to better understand the importance of the base connection on the impulsive period, a numerical example is reported in what follows. Let's consider a concrete tank containing drinking water with the following geometrical and mechanical characteristics:

Internal radius: $R = 10 [m]$

Height: $H = 8 [m]$

Height of stored liquid: $H_L = 7 [m]$

Wall thickness: $t_w = 25 [cm]$

Roof plate thickness: $t_r = 1,5 [cm]$

Concrete Young modulus: $E_c = 30000 [MPa]$

Reinforcing steel Young modulus: $E_s = 210000 [MPa]$

Concrete mass density: $\rho_c = 2,4 [kN/m^3]$

Now, let's compute the impulsive period T_i in the following two cases:

(a) non-sliding base connection, Type 2.2 in Figure 2.3.3.1;

(b) sliding base connection, Type 2.3(1) in Figure 2.3.3.1.

- **Case (a): non-sliding base connection**

Coefficients for determining the fundamental frequency of the tank-liquid system: C_I, C_W

$$C_W = 9.375 \cdot 10^{-2} + 0.2039 \cdot H_L/D - 0.1034 \cdot (H_L/D)^2 - 0.1253 \cdot (H_L/D)^3 + 0.1267 \cdot (H_L/D)^4 - 3.186 \cdot 10^{-2} \cdot (H_L/D)^5 = 0,149$$

$$C_I = C_W \cdot \sqrt{t_w/(10R)} = 0,235$$

$$\text{Fundamental frequency: } \omega_i = \frac{C_I}{H_L} \sqrt{\frac{t_w}{10R}} = 118,84 [rad/s]$$

$$\text{Fundamental impulsive period: } T_i = \frac{2\pi}{\omega_i} = 0,05 [s]$$

- **Case (b): sliding base connection**

Weight of the tank wall: $W_w = \rho_c \cdot (\pi \cdot (R + t_w)^2 - \pi \cdot R^2) \cdot H \cong 305,36 [kN]$

Weight of the tank roof (including snow load): $W_r = \rho_c \cdot (\pi \cdot (R + t_w)^2 \cdot t_r) + 1.2 \cdot \pi \cdot (R + t_w)^2 \cong 407,96 [kN]$

Weight of the stored liquid: $W_L = \pi \cdot R^2 \cdot H_L \cdot 10 \cong 21991,15 [kN]$

Equivalent weight of the impulsive component of the stored liquid: $W_i = \frac{\tanh(0,866 D/H_L)}{0,866 D/H_L} W_L \cong 8762,87 [kN]$

Cross sectional area of base cable (1φ16): $A_s = 201,06 [mm^2]$

Angle of base cable with horizontal: $\alpha = 90^\circ$

Effective length of base cable: $L_s = 600 [mm]$

Center-to-center spacing between base cables: $S_s = 300 [mm]$

Shear modulus of elastomeric bearing pad: $G_p = 0,0272 [MPa]$

Width of elastomeric bearing pad (in radial direction): $w_p = 250 [mm]$

Length of individual elastomeric bearing pad: $L_p = 250 [mm]$

Thickness of elastomeric bearing pads: $t_p = 40 [mm]$

Center-to-center spacing of elastomeric bearing pads: $S_p = 300 [mm]$

Spring constant of the tank wall support system: $k_a = 10^3 \left[\left(\frac{A_s E_s \cos^2 \alpha}{L_s S_s} \right) + \left(\frac{2 G_p w_p L_p}{t_p S_p} \right) \right] = 283,33 [kPa]$

Fundamental impulsive period: $T_i = \sqrt{\frac{8\pi(W_w+W_r+W_i)}{g D k_a}} = 2,07 [s]$

As expected, the fundamental impulsive period is much longer in case of a flexible base connection, case (b); in particular, it is two seconds longer. Note that, according to ACI 350.3, an impulsive period of 2.07 seconds is not admissible; so, for the tank of this example, one possibility is to increase the stiffness of the base connection. For example, one can increase the dimensions of the elastomeric pads, but more effective is to position the base cables with a certain inclination, in order not to vanish the steel contribution in the expression of k_a . For an inclination $\alpha = 60^\circ$, the impulsive period becomes $T_i=0.14$ s.

The spring constant k_a essentially represents the stiffness of the base connection with respect to horizontal traslation. It involves the contribution of the base cable with its axial stiffness k_s and the contribution of the bearing pad with its shear stiffness k_p (assuming small angular variations for the cable and a shear correction factor $\chi=2$ for the bearing pad).

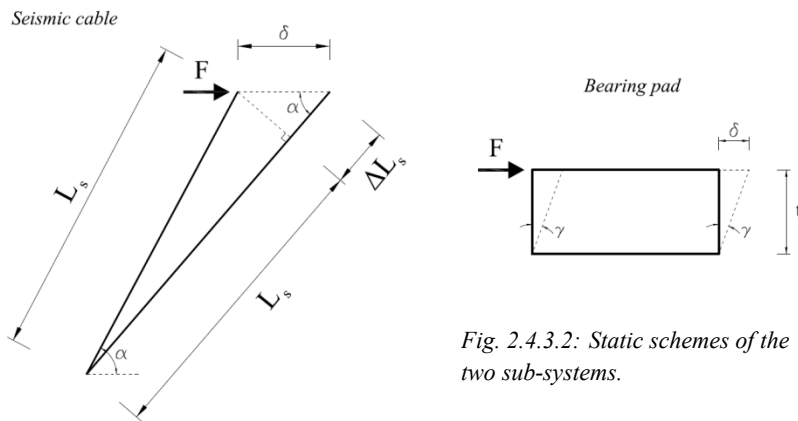


Fig. 2.4.3.2: Static schemes of the two sub-systems.

Seismic cable

$$\Delta L_s = \frac{F}{\cos \alpha} \cdot \frac{L_s}{E_s A_s}$$

$$\delta = \frac{\Delta L_s}{\cos \alpha} = \frac{F \cdot L_s}{E_s A_s \cos^2 \alpha}$$

$$k_s = \frac{F}{\delta} = \frac{E_s A_s \cos^2 \alpha}{L_s}$$

Bearing pad

$$\gamma = \frac{F}{\chi G_p A_p}$$

$$\delta = \gamma t_p = \frac{F}{\chi G_p A_p} t_p$$

$$k_p = \frac{F}{\delta} = \frac{\chi G_p A_p}{t_p}$$

2.5 Assessment of codes guidelines

2.5.1 Seismic design loads

If we want to make a direct comparison between the Eurocode and the US standards, we must consider the simplified design procedure given by the Eurocode itself (Section 2.2.3). In

fact, the rigorous procedure is based on a different and more sophisticated analogue (Sections 2.2.1 and 2.2.2). The great difference between the Eurocode simplified method and the US Standards methods is that in the former the pseudo-accelerations are obtained from the elastic response spectrum, while in the latter they are obtained from a design spectrum, which is the elastic one suitably reduced by a behavior factor. This fact leads to lower seismic forces in the US Standards than in the Eurocode, which seems to be the most conservative. One of the most important consequence of this fact lays in the impossibility to carry out the uplift analysis according to the EC8 tabular method.

Furthermore, the seismic force levels and response modification factors included in API 650 and ACI 350.3 provide results at allowable stress level. So, when comparing these provisions with other documents defining seismic forces at strength levels, the seismic forces obtained according to API or ACI should be increased by the applicable factors to derive comparable forces at strength levels.

Another reason of the Eurocode higher loads is in the adopted combination rule, the absolute sum, in contrast to the SRSS rule adopted by API 650 and ACI 350.3. But this point is better discussed in 2.5.3.

One important point about the simplified design method adopted by the various code and based on the Malhotra's work [30], is that the overturning moments are always determined using the analogue for rigid anchored tanks, also in the API 650 where only steel tanks (which are very flexible) are referred to. Then, in API 650, a lateral force coefficient is specified to represent the amplified tank acceleration as a ratio of the gravity acceleration g ; it does not take into account explicitly the effects of shell flexibility, site conditions or support conditions. Each of these factor may individually amplify or reduce the tank acceleration. When the value of a "moment parameter" (the so called anchorage ratio) exceeds 1.54 the tank is deemed to have overturned, and accordingly, it must be anchored.

2.5.2 Damping ratios and behavior factors

As regards the structural damping (i.e. the one associated with the impulsive component), if the damping values are not obtained from specific information, the following values should be used in linear analysis according to the Eurocode 8:

– damage limitation state:

Reinforced Concrete	5%
Steel and Prestressed r.c.	2%

- ultimate limit state: 5%

For the contents damping (i.e. the one associated with the convective component):

- water or other liquid: 0,5%
- granular materials: 0,10%

The global average damping of the whole system should account for the contributions of the different elements. Procedures to determine it are presented in EN 1998-2:2005, 4.1.3(1) and in EN 1998-6:2005 Annex B. This weighted damping must be used to enter the elastic spectra in the damage limitation state verifications. In the US standards just two values of the damping ratio are given: 5% for the impulsive component (both for steel and concrete tanks, 0.5% for the convective component). This is due to the fact that US standards do not make difference between damage and ultimate limit states, being these two codes based on the “allowable stress design method”.

In the same way that the dynamic response associated with the two pressure components is characterized by different damping ratios, it may also be associated with different hysteretic energy dissipation mechanisms. According to the Eurocode, no energy dissipation can be associated with the convective response of the liquid, whereas some hysteretic energy dissipation may accompany the response due to the impulsive pressure and the inertia of the tank walls, arising from the tank itself and the way it is supported on (or anchored to) the ground. If energy dissipation is taken into account through modification of the elastic spectrum by the behavior factor q , a different value of q should be used in the derivation of the action effects of the two components: according to the Eurocode $q=1.0$ (no energy dissipation) for the action effects of the convective pressure and $q=1.5$ for the action effects of the impulsive pressure and of the inertia of the tank walls. Use of q factors greater than 1.5 in ultimate limit state verifications is only allowed, provided that the sources of energy dissipation are explicitly identified and quantified and the capability of the structure to exploit them through appropriate detailing is demonstrated.

Since API 650 and ACI 350.3 provide results at allowable stress level, the behavior factors (or response modification factors) given by these two standards are higher than the Eurocode ones. In Tables 2.5.2.1a-b the values of API and ACI response modification factors are reported.

Anchorage system	R_{dir} (impulsive)	R_{vc} (convective)
Self-anchored	3.5	2
Mechanically-anchored	4	2

(a)

(b)

Type of structure	R_{wi} on or above grade	Buried*	R_{wc}
(a) Anchored, flexible-base tanks	4.5	4.5†	1.0
(b) Fixed- or hinged-base tanks	2.75	4.0	1.0
(c) Unanchored, contained, or uncontained tanks‡	2.0	2.75	1.0
(d) Elevated tanks	3.0	—	1.0

Table 2.5.2.1: Response modification factor. (a) API 650.3, steel tanks. (b) ACI 350.3, concrete tanks, (after [1]-[2]).

In general, the behavior factor mimics the nonlinear response of the tank and it accounts for ductility, damping and over-strength. All these factors contribute to a force reduction. The ductility reduction is to account for the force reduction associated with a more flexible response. The damping reduction is to account for the force reduction associated with increased system damping. The over-strength reduction is to account for the fact that the actual strength is higher than the calculated strength. The convective response is generally so flexible (periods between 2 and 10 seconds) that any increased flexibility due to non-linearity has negligible influence on the convective period and damping. It is, therefore, not justified to apply the ductility and damping reductions to the convective response. However, the over-strength reduction can still be applied. In the absence of raw data, NEHRP Technical Subcommittee 13 - Non-building Structures proposed a reduction factor for the convective forces $R_{wc}=2$ (Table 2.5.2.1a).

However, to the opinion of the author, there is the need for more research works about behavior factors and damping ratios, since all the codes do not say where their prescribed values come from. This is especially true for behavior factors.

2.5.3 Combination of impulsive and convective effects

In a time-history analysis the total pressure, considering only the first impulsive and convective modes, is the sum of the following two time-histories:

- the impulsive one being driven by $A_{i1}(t)$ (including the inertia of the walls) and;
- the convective one driven by $A_{c1}(t)$.

$A_{i1}(t)$ and $A_{c1}(t)$ are the pseudo-acceleration functions corresponding to the first impulsive and convective mode, respectively.

If, as it is customary in design practice, the response spectrum approach is used for the calculation of the maximum dynamic response, the maxima of the two time-histories of seismic action effects given by the response spectrum should be suitably combined. Except Eurocode 8, all the codes suggest SRSS (square root of sum of square) rule to combine impulsive and convective forces. Eurocode 8 suggests use of absolute summation rule; in fact, due to the generally wide separation between the dominant frequencies in the ground motion and the sloshing frequency, the “square root of the sum of squares” rule may be un-conservative, so that the alternative, upper bound, rule of adding the absolute values of the two maxima may be preferable in design. Each of these two maxima will be derived for the value of q and of the damping ratio considered appropriate for the corresponding component.

Unlike the Eurocode 8, both ACI 350.3 and API 650 use the SRSS combination rule. A very interesting motivation about the use of SRSS method is given by the New Zealand standard NZS 3106. Here is what C2.2.9.4 (Commentary) of that standard says:

“The impulsive and convective responses are generally wide separated, the impulsive period being much shorter than the convective period. When responses are widely separated, near-simultaneous occurrence of peak values could occur. However, the convective response takes much longer to build up than the impulsive response, consequently the impulsive component is likely to be subsiding by the time the convective component reaches its peak. It is thus recommended that the combined impulsive and convective responses be taken as the square root of the sum of the squares of the separate components.”

A numerical study was undertaken by the NEHRP Technical Subcommittee 13 – Non-building Structures to investigate the relative accuracy of direct (or absolute) sum and SRSS methods for combining the impulsive and convective responses. In this study:

- The impulsive period was varied between 0.05 seconds and 1 second;
- The convective period was varied between 1 second and 20 seconds;
- The impulsive and convective masses were assumed equal;
- Eight different ground motions from Northridge and Landers earthquake data were used.

While the SRSS modal combination rule does not provide the worst possible loading, it provides the most likely loading. It has been shown that this rule is suitable for combining the impulsive and the sloshing responses in tanks. Furthermore, it should be remembered that different portions of a site response spectrum are not controlled by the same event. Whereas, the short-period spectral values, which determine the impulsive response, are controlled by the closer earthquakes, the long-period spectral values, which determine the convective response, are controlled by distant, larger earthquakes. Therefore, there is already some conservatism inherent in assuming that the impulsive and convective responses will occur simultaneously.

2.5.4 Enhancement of uplift analysis in current standards

Three remarks must be made on the Eurocode 8 prescriptions about unanchored tanks. First, the EC 8, Appendix A.8 allows an increase in the fundamental natural period (thus a decrease in the overturning moment) due to uplifting; however, this is restricted to the range of parameter values for which design charts are available in Haroun [21], and the user has to refer to the original publication; no formulas or graphs are given in EC8. Second, EC8, Appendix A.7,

does not mention any reduction of the effective seismic load due to SSI; however, SSI can lead to a significant reduction of the effective seismic excitation. Third, the worked example of Section 2.3.4 shows that for common tank dimensions, sometimes it is not possible to carry out the uplift analysis, because the normalized overturning moment falls out of tables. This is a direct consequence of the fact that seismic forces, being calculated using the elastic spectra, are always overestimated in EC8. So, it can be concluded that the method proposed by EC8 to estimate the uplift is of very limited applicability.

It is very interesting to spend some words on the work done in [29] by Koller and Malhotra in order to evaluate the appropriateness of the simplified seismic calculations of unanchored cylindrical liquid storage tanks according to EC8. To this aim, the results of calculations according to EC8 were compared with results of a more sophisticated method, i.e. a nonlinear pushover analysis by Malhotra. Seven existing unanchored cylindrical oil storage tanks in Switzerland were investigated. None of them was designed to resist earthquake. All tanks were calculated “according to EC8” and five of them were also calculated “according to Malhotra”.

*Table 2.5.4.1: Main characteristics of investigated tanks. height H , radius R , volume V , thickness of the lowest courses t_{lc} , equivalent thickness of the mantle t_{eq} , yield stress of the mantle f_{ym} , thickness of the base plate t_{bp} , yield stress of the base plate f_{yb} . The tanks marked with * were only calculated according to EC8 (after [29]).*

Name of tank	Year of construction	H/R [-]	H [m]	R [m]	V [m ³]	t_{lc} [mm]	t_{eq} [mm]	f_{ym} [MPa]	t_{bp} [mm]	f_{yb} [MPa]
St-Triphon	1951	1.12	16.2	14.5	10'700	24	17.7	235	10	235
Mellingen	1967	1.14	25.0	22.0	38'000	27	20.1	295	27	235
*Niederhasli 43	1976	1.52	20.0	13.13	10'800	12	9.0	355	8.0	355
*Niederhasli 3	1958	1.67	20.0	12.0	9'050	23	16.1	235	10	235
Rümlang	1975	1.75	26.3	15.0	18'600	16	11.8	355	7.0	355
Birsfelden 4	1955	2.16	19.4	9.0	5'000	16	11.9	235	10	235
Vernier	1995	3.48	20.0	5.75	2'080	7.0	6.9	235	7.0	235

All tanks were calculated for identical soil conditions; in particular, a relatively stiff soil, such that the effects of SSI (soil structure interaction) remained moderate. For the calculations “according to Malhotra”, an initial local foundation stiffness (Winkler coefficient) of $4 \cdot 10^7$ N/m³ was assumed. For all calculations, the EC8 response spectrum of type 1 for ground class B, with peak ground acceleration of 1m/s^2 was used. An importance factor of 1.0 was adopted. For all the details about the pushover analysis method see Malhotra [29]. Here only the results are commented. The stresses and plastic rotations resulting from both methods of calculation were compared with admissible values given in EC8. The following verifications were undertaken:

- Plastic rotation in the base plate;
- Elastic buckling of the shell (mantle);
- Elephant footing (elastic-plastic collapse).

Assuming a maximum allowable steel strain of 5% and a length of the plastic hinge of two times thickness of the base plate, the maximum allowable rotation according to EC8 is 0.20

radians (11.5 degrees). It turned out that plastic rotation was the controlling parameter in all cases. Only in the case of the tank “Vernier” elephant footing was nearly as critical as the plastic rotation. Therefore, only the plastic rotation is shown in the following. This quantity is presented versus a slenderness parameter in Figure 2.5.4.1a and versus liquid volume in Figure 2.5.4.1b.

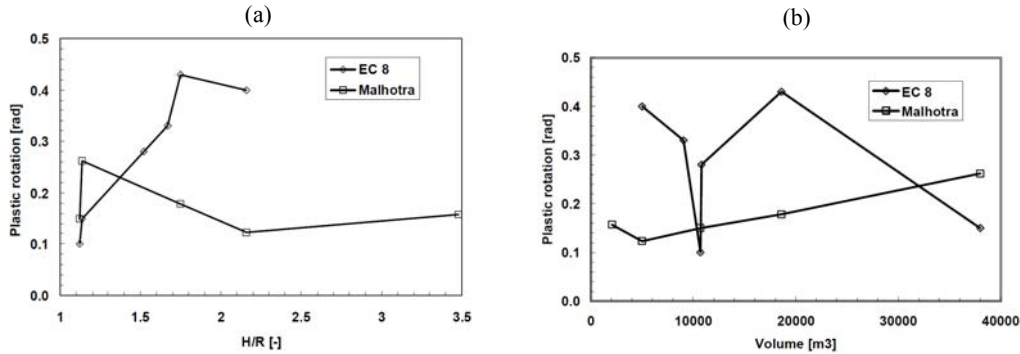


Fig. 2.5.4.1: (a) Plastic rotation vs Slenderness H/R, (b) Plastic rotation vs volume, (after [29]).

Figure 2.5.4.1a confirms the strong trend of increasing plastic rotation with increasing H/R ratio for the EC8 results. This trend appears very clearly although the results for tanks with very different volumes are drawn in Figure 2.5.4.1a. Any possible influence of the absolute volume onto the plastic rotation must be small. This is indeed confirmed by Figure 2.5.4.1b, where no clear trend can be seen, the low values of plastic rotation corresponding to the two very squat tanks, irrespective of their volumes. The situation is very different, however, for the results according to Malhotra. Here, no clear trend as a function of H/R is visible in Figure 2.5.4.1a. On the contrary, two tanks (“St-Triphon” and “Mellingen”) with nearly identical H/R ratios, but very different volumes, show significantly different plastic rotations. In Figure 2.5.4.1b, a trend of increasing plastic rotation with increasing fluid volume can be seen. Except for the particularly slender tank “Vernier” ($V = 2100 \text{ m}^3$), this trend is nearly perfectly linear. It can be concluded from these observations that the influence of the volume onto the plastic rotation is much stronger than the influence of the slenderness ratio H/R.

For the squat tanks “St-Triphon” and “Mellingen” ($H/R = 1.12$ and 1.14), whether the volume is moderate or large ($V = 10.700 \text{ m}^3$ and 38.000 m^3), the calculation according to EC8 leads to a significantly smaller plastic rotation than the calculation according to Malhotra, by a factor of 1.5 to 1.7. Two concurrent aspects can qualitatively explain this discrepancy: on one hand, partial uplifting increases the fundamental natural period less for squat than for slender tanks. This means that the EC8 calculation, neglecting this effect, is less penalized for squat than for slender tanks. On the other hand, the influence of SSI, taken into account by the EC8 calculation, but neglected in the calculation according to Malhotra, is more important for squat than for slender tanks. For squat tanks, the translational horizontal motion with respect to the surrounding

soil is dominating the SSI, and this motion is highly damped, whereas for slender tanks, SSI is dominated by rocking, with a much lower damping. SSI is therefore much more “beneficial” in the case of squat tanks. For $H/R > 1.5$, the EC8 leads to larger plastic rotations. Again, the same aspects as before can qualitatively explain this trend. Firstly, for slender tanks, as indicated above, the importance of the SSI, neglected by Malhotra, is less pronounced than for squat tanks. Secondly, neglecting the lengthening of the fundamental natural period by the EC8 calculation, as was done in the present study, as well as neglecting the hysteretic damping due to cyclic plastic deformations in the base plate, strongly penalizes the results according to EC8. In fact, as can be seen from Figure 2.3.1.2 of Section 2.3.1, which is based on purely static considerations, the partial uplift as a function of the overturning moment is extremely sensitive with respect to the slenderness ratio H/R . It is therefore very important to take into account the lengthening of the fundamental natural period, since this decreases the overturning moment.

As a conclusion, since both methods neglect “beneficial” physical effects (EC8: lengthening of the fundamental natural period and the damping due to cyclic plastic rotation in the base plate; Malhotra: the SSI effects), a small Swiss expert team assumed that both methods would “probably be conservative”. They concluded that it would be acceptable to consider a tank as earthquake safe if it was safe either according to EC8 or according to Malhotra (with the judgment of plastic rotation and stresses still according to EC8). This opinion was strongly influenced by the fact that the results found in the present study seem to be on the safe side in the light of the statistical investigation on damaged tanks published by O'Rourke and So (2000).

For practitioners, it is interesting to know that a calculation according to EC 8, as presented in this paper, seems to be overly conservative for tanks with slenderness ratios $H/R > \sim 1.5$. This might be of little importance for the design of new tanks, as the additional cost of an overdesign may remain small. However, this aspect can become very important for the re-evaluation of existing tanks, where unnecessary margins of conservatism might lead to significant, but unnecessary expenses. For tanks with a slenderness ratio $H/R > \sim 1.5$, therefore, it is strongly recommended to take into account at least the lengthening of the fundamental natural period of the “impulsive” motion – by any appropriate method, in order to eliminate unnecessary margins of conservatism.

As regards the API 650 provisions, the resistance to overturning is provided by the weight of the tank shell and by the weight of a portion of the tank content which depends on the width of the bottom plate (or ring beam) that lifts off the foundation. To determine this width, an elementary strip of the bottom plate perpendicular to the shell that can be lifted off the ground is considered. It is noted that in such a model neither the deformability of the tank wall nor the

flexibility of the underlying soil are considered. In addition, only small deformation behavior of the bottom plate is taken into account. At higher level of ground excitation, the capability of the plate to resist the applied loads would be fully accounted for, leading to conclusions of global instability (overturning). One other discrepancy noted in the procedure is that the overturning moment at the tank base and the uplift force are independent of each other which is unrealistic as the the overturning moment produces the uplift force! API 650 suggest an increase in the axial force in the tank wall which remains in contact with the ground during uplift. However, this increase is independent of the magnitude of uplift and this is not always conservative.

The Austrian design guidelines provide the most comprehensive regulations for assessign the increase in the axial force as a function of the magnitude of the uplift displacement. However, the design charts are limited to a narrow range of tank thickness and soil stiffness. Furthermore, it can be used in the presence of vertical excitation with only one horizontal earthquake component. The EC8 guidelines are based on the Austrian procedure and have the same limitations.

Based on comparison between the results of advanced finite element analyses of tank uplift, supported in part by observations from past earthquakes, and the procedure currently adopted in seismic standards, the following possible areas of enhancement of seismic standards as related to uplifted tanks are identified, Haroun [21]:

- develop formulas for accurate estimation of hydrodynamic overturning moments exerted on unanchored tanks, which are consistent with engineering intuition. In fact, at the state-of-art the overturning moments are computed from a mechanical analogue that applies only to rigid anchored tanks;
- employ reliable models for the uplift mechanism which include the effect of membrane stresses in the base plate;
- moderately tall unanchored tanks may have reserve strength against overturning over what predicted by current standards, leading to cost effective construction;
- global overturning moment in relatively broad tanks is not meaningful.

2.5.5 Soil-structure interaction

As already mentioned provisions for consideration of SSI are provided only in NZSEE guidelines and Eurocode 8. US standards do not consider the soil effects on the seismic response of tanks.

In addition to what explained in Section 2.5.4, regarding the method of analysis of unanchored tanks in EC8, another important point highlighted by Malhotra in [29] is the sensitivity study with respect to foundation stiffness. The nonlinear pushover analysis performed by Malhotra is sensitive with respect to the “local” foundation stiffness. This means that it makes a difference whether the tank is supported by a rigid concrete mat, a concrete ring or simply compacted soil. Therefore, a sensitivity study was carried out for the tank “Rümlang”, for three values of the foundation stiffness: $1 \cdot 10^7 \text{ N/m}^3$ (“soft”), $4 \cdot 10^7 \text{ N/m}^3$ (“moderately stiff”), and $4 \cdot 10^8 \text{ N/m}^3$ (“very stiff”). Table 2.5.5.1 presents the results that were obtained.

Physical quantity	Foundation stiffness		
	$\kappa = 1 \times 10^7 \text{ N/m}^3$ ("soft")	$\kappa = 4 \times 10^7 \text{ N/m}^3$ ("moderat. stiff")	$\kappa = 4 \times 10^8 \text{ N/m}^3$ ("very stiff")
Hysteretic damping	10 %	7.2 %	6.2 %
Plastic rotation	0.125 rad	0.178 rad	0.202 rad
Uplifting height	5.7 cm	7.3 cm	8.3 cm
Contact angle	230°	160°	96°
"Length" of uplifted part	22 cm	42 cm	55 cm
Axial compressive stress	6.4 MPa	11 MPa	20 MPa
Hoop compressive stress	49 MPa	95 MPa	112 MPa

Table 2.5.5.1: Results of calculations according to Malhotra for different values of foundation stiffness for the tank “Rümlang”(after [29]).

It can be seen from Table 2.5.5.1 that an increase of the foundation stiffness beyond the generic value used in this study seems to have little effect on plastic rotation ($\approx 10\%$ increase in plastic rotation for a 10-fold increase in foundation stiffness). Furthermore, it seems that an overestimation of the foundation stiffness leads to results on the safe side. It has to be kept in mind, though, that for a soft foundation (with low shear wave velocity of the underlying soil), the seismic excitation might be significantly stronger due to local site effects. The local foundation stiffness cannot be varied easily for the calculations according to EC8; a rigid foundation mat is always assumed. Therefore, no corresponding sensitivity study was performed for the calculations according to EC8. Note, however, that the rigid mat is assumed to lay on a viscoelastic soil, which gives rise to SSI effects.

To verify the reliability and capability of the simplified method adopted by EC8 and explained here at Section 2.4.2, let’s present the results of comparative calculations with the finite element method carried out by Wunderlich et al. (2000). The finite element model uses special boundary conditions to consider the radiation damping properties of the infinite half-space. Figure 2.5.5.1a shows the finite element model and Figure 2.5.5.1b gives the tank, liquid and soil parameters used for the specific case. The examined tank is excited by the vertical and horizontal acceleration time-histories of Figures 2.5.5.2.

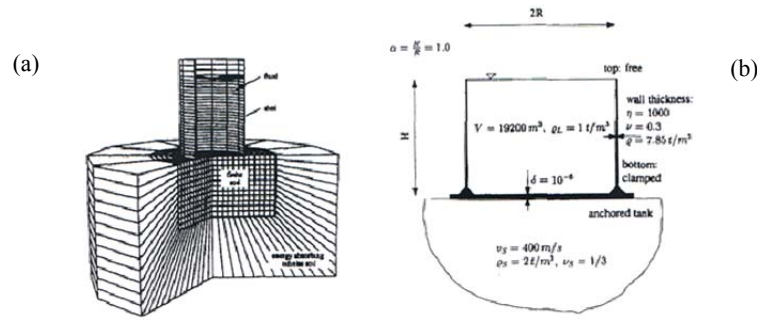


Fig. 2.5.5.1: (a) Finite element model, (b) Geometry and system of the tank example, (after [17]).

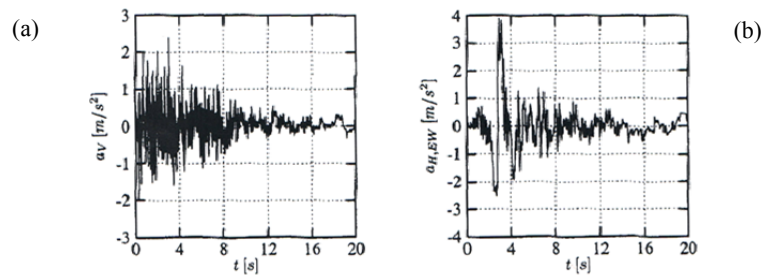


Fig. 2.5.5.2: Time-histories of the Erzincan earthquake 1992. (a) Vertical component, (b) East-west component, (after [17]).

The finite element calculation were carried out in the time domain, whereas the calculation with the simplified approach uses the FFT and DFT techniques in the frequency domain. The time-histories of normalized activated liquid masses induced by pressure on the tank bottom and the tank wall indicate only minor differences between FEM and the improved mechanical model. Figures 2.5.5.3 give the liquid masses M_V and M_H (normalized by the weight of the tank liquid M_L) resulting from the hydrodynamic pressure acting on the tank bottom and on the tank wall, respectively.

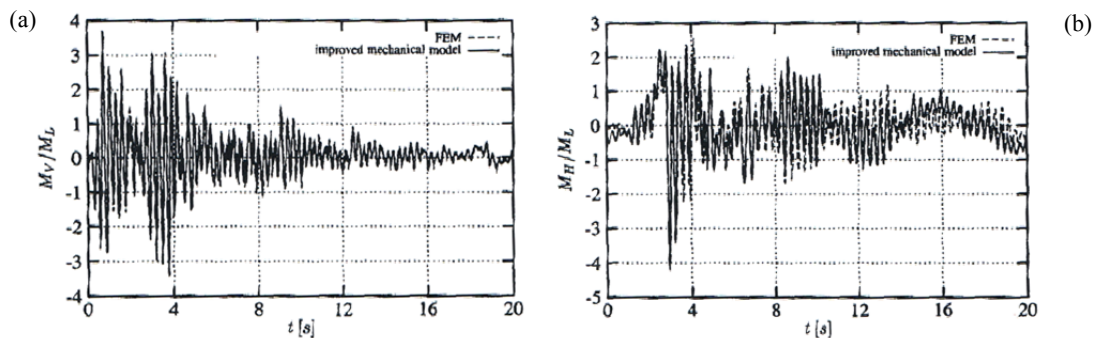


Fig. 2.5.5.3: (a) Time-history of normalized activated liquid masses induced by pressure on the tank bottom, (b) Time-history of normalized activated liquid masses induced by pressure on the tank wall, (after [17]).

Furthermore, the finite element calculations confirm that consideration of the foundation flexibility leads to a decrease of the resonance frequency of tall tanks ($H/R > 0.8$) and to a decrease of the radiation damping of broad tanks ($H/R < 0.5$).

2.5.6 Combined action of horizontal and vertical earthquake components

A very interesting contribution to the issue of combined horizontal and vertical ground motion may be given by Fischer et al. (1991) in [15]. The response of a steel tank ($H=24$ m, $R=12$ m) subjected to the horizontal and vertical earthquake component of the 1976 Friuli earthquake was evaluated by direct time integration method. The results in terms of the time histories of the individual contribution to the dynamically activated pressures at the bottom edge of the tank in the $\vartheta=0$ position are shown in Figure 2.5.6.1. They are the pressure due to the individual action of the horizontal and vertical excitation \hat{p}_H and \hat{p}_V , respectively, as well as the pressure due to the simultaneous horizontal and vertical excitation. Furthermore, the results of the application of the response spectrum method for the unidirectional excitations p_H and p_V are indicated in Figure 2.5.6.1.

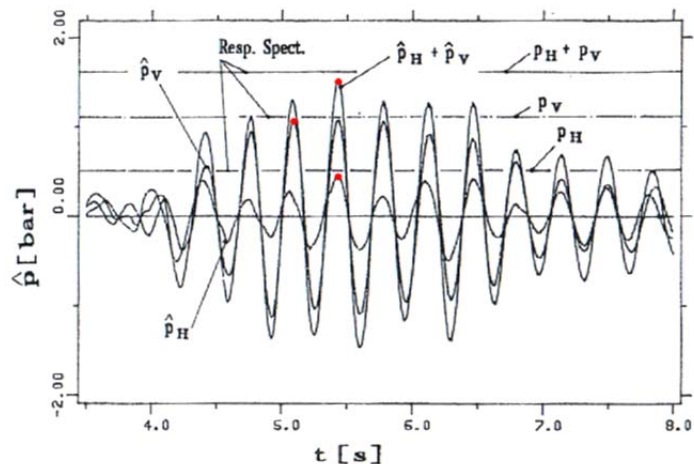


Fig. 2.5.6.1: Maximum pressure at the tank bottom due to horizontal and vertical excitation (after [15]).

This investigation shows that the response spectrum method gives a good estimate for the maximum activated pressures. Additionally, the following conclusions can be made:

- the situation in which the maximum dynamically activated pressure due to the horizontal excitation and the minimum dynamically activated pressure due to the vertical excitation appear at the same time, is really possible. This combination is the most dangerous for elastic buckling;
- the situation which is the most dangerous for elastic-plastic buckling (“elephant footing”), namely the simultaneous appearance of the maximum pressure due to horizontal and due to vertical excitation, is possible, too;

- hence, a simple SRSS superposition of the response due to horizontal and vertical excitation (the one adopted by API standards) would underestimate the risk of damage to such structures.

This is a justification for the proposal that a linear addition or a linear subtraction of the individual pressure contributions has to be considered. Figure 2.5.6.2 shows three different possibilities of superposition of the contributions of the static pressure p_{STAT} , the pressure due to the horizontal earthquake component $p_{H,2D}$ and the pressure due to the vertical earthquake component p_V , which are most critical with respect to the individual buckling mode.

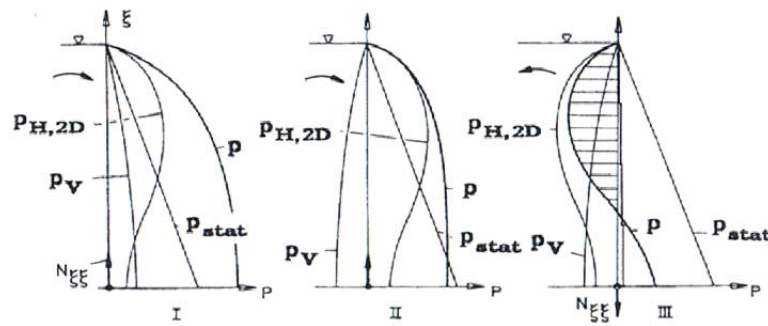


Fig. 2.5.6.1: Schematic presentation of different possible superpositions of the maximum pressure contributions (after [15]).

Case I ($p = p_{STAT} + p_{H,2D} + p_V$)

causes the highest circumferential tensile stresses and leads, especially in the case of broad tanks, to plastic buckling (Section 3.1.2). This plastic collapse problem can be analysed, for example, by a finite element method taking into account geometrical and material nonlinearities. This is done in [39] and [42] by Seiler, Wunderlich et al. They also investigated the influence of the vertical acceleration on the collapse load through a quasistatic approach. The vertical acceleration can reduce the ultimate load up to 40-50% in broad tanks.

Case II ($p = p_{STAT} + p_{H,2D} - p_V$)

is the most dangerous with respect to “shell crippling”, i.e. the elastic buckling due to axial compression force (Section 3.1.1). The stabilizing effect of the internal pressure is reduced by subtracting the dynamic pressure caused by the vertical earthquake component.

Case III ($p = p_{STAT} - p_{H,2D} - p_V$)

may lead to regions of low pressure mainly near the top of the tank where the wall is rather thin, and buckling due to external pressure as well as cavitation may occur (secondary buckling effects, Section 3.1.3).

2.6 Concluding remarks and future deepenings

Although it is a very simple matter to deal with the design provisions, it is a difficult or even an impossible task to understand the applied formulas and to gain further knowledge about their background. This statement is especially true for the API standard. Eurocode 8 gives more insight into its background, but leaves many uncertainties to the user in questions of applicability.

Review of various codes revealed that ACI 350.3, which is the most recent code, is quite comprehensive and simple to use. As in the API standards, in this code parameters of mechanical model are evaluated using rigid tank model. The flexibility of tank is just considered in the evaluation of impulsive time period. In contrast to this, Eurocode 8 uses separate models to find parameters of rigid and flexible tanks. Such an approach makes this code more cumbersome to use, without achieving any significant improvements in the values of parameters. Effect of vertical ground acceleration is considered in various codes with varying degree of details. Eurocode 8 suggests the more rational approach to obtain hydrodynamic pressure due to vertical acceleration, which is evaluated based on time period of breathing mode of vibration.

As regards the uplifting phenomenon, this is not treated by ACI 350.3 because it is totally negligible for concrete tanks. On the contrary, for steel tanks it represents one of the most important issue in the analysis of such structures. The tabular method proposed by the Eurocode 8 is very simple to use but of very limited applicability. In API 650, the model used to estimate the uplift is based on a too old and rough method, even it is the simplest to be understood from a theoretical viewpoint.

Eurocode 8 is the most advanced in the soil-structure interaction study; it proposes two different procedures. In API, SSI is totally absent and in ACI 350.3 the flexibility at the base involves the type of base connection and not the soil properties; in fact, for concrete tank the foundation is represented by a concrete mat, which can be always considered to be rigid with respect to the supporting soil.

As regards verification criteria, they must be differentiated for concrete and steel tanks. For concrete tanks, a designer can use the classical criteria of reinforced concrete sections at ultimate limit states for strength requirements, but it is very important also to check the cracking phenomenon for serviceability requirements. For steel tanks, the material strength is never a real problem. So, all the codes address their verifications criteria to the complicated issue of buckling. These are the reasons why in the present work the verifications criteria for concrete tanks are not covered (the reader is assumed to know them) and the ones for steel tanks are included in chapter 3, entirely devoted to the buckling problem.

A common feature to all current codes is that there is not a minimum explanation on where the prescribed values of damping ratios and behavior factors come from. So, an interesting deepening could be on this subject. In particular, a possible work could be the development of rational methods to estimate correct values for such quantities which, at present, seem to be only “magic numbers”. This is especially true for behavior factors, while the main problem with damping ratios is the difficulty in finding the original documents and sources in which the reasons of the values prescribed by the codes are explained.

Buckling of steel tanks

3.1 Buckling modes

3.1.1 Elastic buckling

This type of buckling is due to the axial compression forces developed at the generic meridian line, due to the self-weight of the tank walls and roof in addition to the increment given by the seismic action. Figures 3.1.1.1 and 3.1.1.2 show the “diamond shape” buckles of a destroyed wine tank.

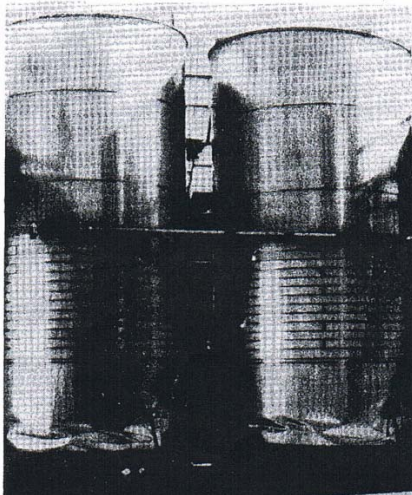
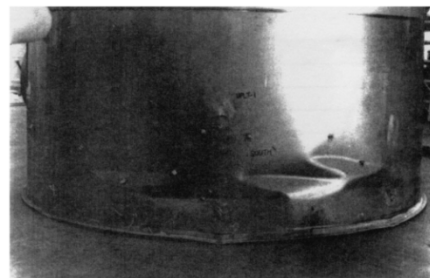


Fig. 3.1.1.1: “Diamond shape” buckles of a wine tank destroyed during an earthquake (after [16]-[18]).



The axial membrane stress needed to induce elastic buckling in a shell depends on the internal pressure, circumferential variation of the axial stress and amplitude of imperfections in the shell. The latter tend to decrease the buckling stress to a fraction of the classical buckling stress. The internal pressure reduces the effective imperfection amplitude and therefore increases the buckling stress. Circumferential variation of the axial stress reduces the probability of coincidence of the maximum stress and the maximum imperfection, again increasing the buckling stress.

Most investigations of axially pressurized cylinders dealing with uniformly distributed loads had been carried out in order to find a proper elastic buckling criterion. According to Peek (1988a), if a typical length scale for the non-uniformity is large compared to the wavelength of

the critical buckling mode, the effect of the non-uniformity on the buckling load can be expected to be small. Current codes such as API design recommendations use critical axial loads based on investigations of uniformly loaded tanks. A comprehensive comparison of elastic buckling criteria was given by Peek (1988a), who compared current codes with experimental data from model tanks under earthquake-like loads. Peek argued that the selection of the most suitable criterion for elastic buckling is a rather debatable issue because of the problem of imperfections and the effect of non-uniformity in the pre-buckling stresses. Hence he is of the opinion that the proposal for estimating the stability of cylinders in bending included in ECCS recommendations, [14], is a first step in the right direction. Fisher and Rammerstorfer (1982) drew the same conclusions and proposed the classical relation for the theoretical critical axial compression stress of perfect thin cylindrical shells with a proper knockdown factor, taking into account imperfections sensitivity of the bent cylindrical shell. The critical Euler's axial compressive stress for an axially loaded, perfect elastic cylinder in which a pure state of uniform membrane stresses exists before buckling and whose edges are immovable in both the radial and circumferential directions during buckling is:

$$\sigma_{c1} = \frac{E_w}{\sqrt{3(1-\nu_w^2)}} \cdot \frac{t_w}{R} = 0,605 \frac{E_w t_w}{R} \quad (3.1.1.1)$$

It should be emphasized that the result of a correct elastic or elastic-plastic bifurcation buckling calculation performed by means of a perfectly valid computer program is liable to grossly overestimate the actual carrying capacity of a shell. This is apt to be the case when shape imperfections are not allowed for in the computation, and also when the assumed boundary conditions or the assumed manner of introduction of the loads into the shell do not reflect reality. For example: a theoretically adequate computer calculation for an axially loaded elastic cylinder will predict the same critical load as equation 3.1.1.1, whereas the actual buckling load of an imperfect cylinder may be 3, 5, 7 times lower. Due to this reason, typically a proper knockdown factor $\hat{\alpha}$ is introduced and the allowable knocked-down vertical membrane stress f_{mb} can be expressed as:

$$f_{mb} = \hat{\alpha} \sigma_{c1} = \hat{\alpha} 0,605 \frac{E_w t_w}{R} \quad (3.1.1.2)$$

The stabilizing effect of internal pressure (due to smoothening of imperfections) should be considered when determining $\hat{\alpha}$, that may be defined as a "pressure-dependent knockdown factor". M.A. Haroun in [20] suggests a conservative value of 0.2, while API standards adopt 0.33 (see Section 3.2.1).

However, it is necessary to have high values of vertical compression forces, associated with low values of hoop forces induced by hydrostatic and hydrodynamic pressures, to reach the elastic buckling failure mode. This situation is very rare, so that the most common failure mode is the elastic-plastic collapse.

3.1.2 Elastic-plastic buckling

The bottom of the shell is normally subjected to a biaxial stress state consisting of hoop tension and axial compression. Moreover, radial deformations under the internal pressure create additional eccentricity, tending to induce the commonly observed “elephant’s foot” buckling as shown in Figures 3.1.2.1 and 3.1.2.2.



Fig. 3.1.2.1: “Elephant’s foot” buckling in a tank, Pisco earthquake, Peru, 2007.



Fig. 3.1.2.2: “Elephant’s foot” caused by the movement of water in a large steel storage tank during San Fernando, California, earthquake (February 1971).

The bulge formation results from the high circumferential tensile stresses due to the internal pressures (hydrostatic and hydrodynamic due to vertical excitation), in combination with the axial membrane stresses due to the overturning moment caused by horizontal earthquake excitation. More precisely, when the hoop tension reaches the yield limit, the annular strips cannot sustain any load increment and so the structural scheme resisting to a further vertical load increment is represented by a plate of height H and few millimetres thick. It is immediate to understand how this element can reach quickly a buckling failure. The biaxial stress state on a small portion of the tank walls and the diagrams of hoop tension and vertical compression along the tank height are shown in Figures 3.1.2.3 and 3.1.2.4.

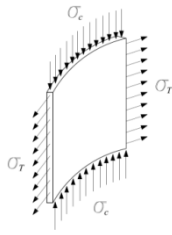


Fig. 3.1.2.3: Biaxial stress state on a portion of the tank walls.

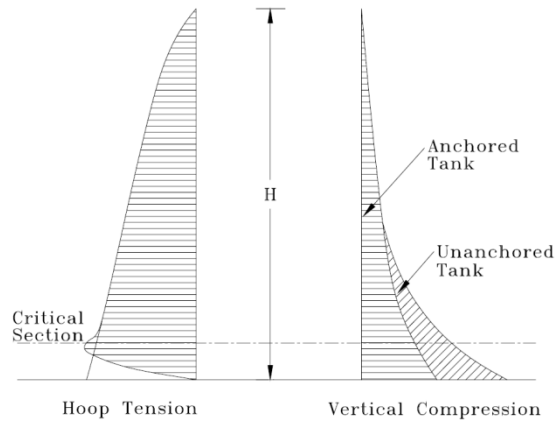


Fig. 3.1.2.4: Hoop tension and vertical compression forces for anchored and unanchored tanks (after [20]).

From Figure 3.1.2.4 note that the most critical section is typically located 30 cm above the tank bottom. Due to the phenomenon mentioned above this critical section is not able to carry any further vertical compressive force, since the annular strips that stiffen it are yielded.

The “elephant’s foot” mode is considered in various standards for the design of tanks (NZS 2654 and Eurocode 8 are the most important), all of which use the empirical equations developed by Rotter (1987) to cope with this situation. These equations are based on nonlinear elastic-plastic calculations for an isotropic shell under axisymmetric loading. The “elephant’s foot” buckling strength falls below the Von Mises failure criterion applied to the membrane theory. New Zealand guidelines assume a quadratic reduction of the classical buckling stress depending on the factor $(PR/t_w f_y)$ where P is the total internal pressure (equation 3.1.2.1). This factor essentially represents the effect of shell yielding in the circumferential direction due to internal pressure on the buckling capacity of the shell. The limit case is when the internal pressure is so high as to produce yielding in the circumferential direction, namely $PR/t_w = f_y$. In this case the buckling capacity of the shell f_{pb} vanishes at all.

$$f_{pb} = \sigma_{c1} \left[1 - \left(\frac{PR}{t_w f_y} \right)^2 \right] \tag{3.1.2.1}$$

A successive development of equation 3.1.2.1 is represented by the Rotter and Seide (1990) formula, equation 3.1.2.2.

$$f_{pb} = \sigma_{c1} \left[1 - \left(\frac{PR}{t_w f_y} \right)^2 \right] \left(1 - \frac{1}{1,12 + s^{1,15}} \right) \left(\frac{s + f_y/250}{s + 1} \right) \tag{3.1.2.2}$$

with P and f_y in MPa. Since equation 3.1.2.2 is adopted by Eurocode 8 to calculate the buckling strength, the new terms appearing in this formulation with respect to equation 3.1.2.1 will be better discussed in Section 3.2.4. Here, some results coming from its application are just commented. For example, in a study performed by Scharf (1990), he investigated real anchored tanks, chosen to be typical for the current practice in the petrochemical industry, with regard to tank wall instability under the assumption of a vertical to horizontal free field acceleration ratio of 0.5. The excitation was based on the Friuli 1976 earthquake. Figure 3.1.2.5 shows the computed critical earthquake intensity, characterized by the critical horizontal free field acceleration in units of g ($A_{H,crit}$ in the Figure), for different modes of tank wall instability.

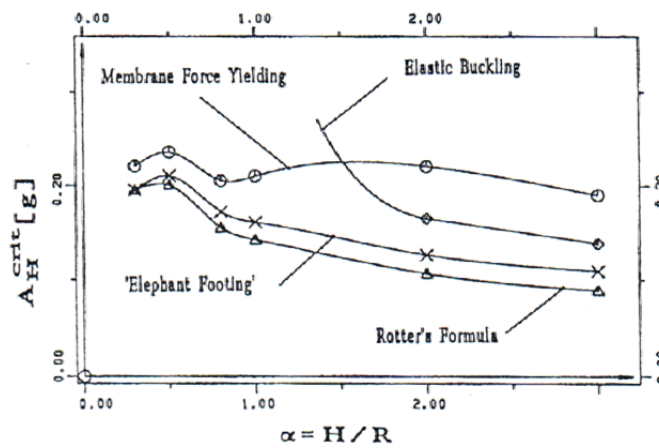


Fig. 3.1.2.5: Critical horizontal free field acceleration of anchored tanks for different modes of tank wall instability, function of the tanks slenderness (after [16]).

It is possible to note that, under the assumptions described above, elastic-plastic buckling is a potential failure mode for all, and especially for broad, anchored tanks. Furthermore, it can be seen that Rotter and Seide (1990) is a useful approach for elastic-plastic buckling.

As a conclusion for this Section, two possible methods of mitigation of “elephant’s foot” bulge formation are mentioned. The first one use hybrid fiber reinforced polymer laminates, as shown in Figures 3.1.2.6. In fact, in order to relief the shell from excessive hoop stresses, Haroun M.A. in [20] suggested to apply hybrid fiber reinforced polymer laminates, with the fibers aligned along the circumference of the shell. The combined system of carbon and glass fibres must circumvent the galvanic reaction with steel, in addition to exhibiting thermal balance and appropriate durability properties. It has been demonstrated theoretically that a hybrid FRP system can effectively increase the buckling capacity of the tank shell by participating in carrying the excessive hoop stress in the steel shell which causes “elephant’s foot” bulging. The number of laminates needed to resist the effective hoop stress resulting from the hydrodynamic pressures can be determined based on the required percentage increase in the elastic-plastic

buckling stress. However, the proposed system must undergo experimental verification tests before it is actually recommended in engineering practice. There are two sets of experimental tests that must be carried out: the first pertains to the performance of the hybrid FRP system alone, and the second evaluates the performance of the retrofitted tanks. The former set of tests is underway to determine the durability properties of the hybrid system, and in particular, determine its environmental reduction factors. In addition, the combined system of glass and carbon must be thermally balanced, and for this a sandwich-type laminate system is recommended. Once the properties of the hybrid FRP system are accurately predicted, a set of shake table tests on retrofitted tanks filled with liquid and subjected to earthquake time histories will be carried out to confirm and calibrate the theoretical findings of this study. Even if it is still subjected to experimental verifications, the proposed FRP retrofit scheme is promised to be structurally efficient as well as cost effective. For analytical and modeling aspects of this innovative system see [20].

A second type of strengthening system against “elephant’s foot” buckling was studied by Chen J.F., Rotter J.M. and Teng J.G. in [7]. Here it is suggested to use a light ring stiffener at a critical location. The strengthening effect is shown to be sensitive to the size of the ring stiffener, with rings that are too small and rings that are too large both causing lower strength than the optimal ring size. Also the effect of placing the ring at different locations was explored. The analytical solution of a system composed by the tank shell and the ring stiffener (Figure 3.1.2.7) is obtained starting from the shell bending equation and enforcing the compatibility condition between shell and ring. For all the detailed mathematical manipulations see [7]. The main conclusions of this work are that the location and size of the ring must be chosen with care, and that a very light ring is generally sufficient to produce a significant improvement. This is, therefore, an interesting example of structural behavior in which the provision of a larger amount of material than the optimum leads to reduced strength.



Fig. 3.1.2.6: Examples of tanks wrapped with FRP laminates.

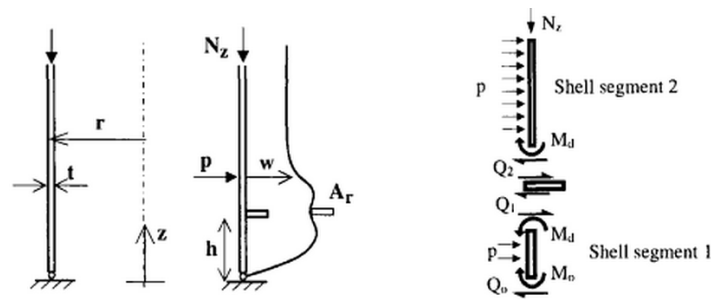


Fig. 3.1.2.7: Analytical model for the shell-ring interaction (after [7]).

3.1.3 Secondary buckling

The buckling behavior of steel tanks under seismic excitation identified by means of experimental and computational studies is usually classified as elastic buckling and elastic-plastic buckling. The latter is associated with “elephant’s foot” buckling, as explained in Section 3.1.2. “Diamond shape” buckling at the bottom of the tank has been described as elastic buckling in Section 3.1.1. However, elastic buckling sometimes includes also buckling at the top part of the tank (Figures 3.1.3.1). In this Section a deeper insight is given to this second kind of elastic buckling, even if it is not covered by current standards.

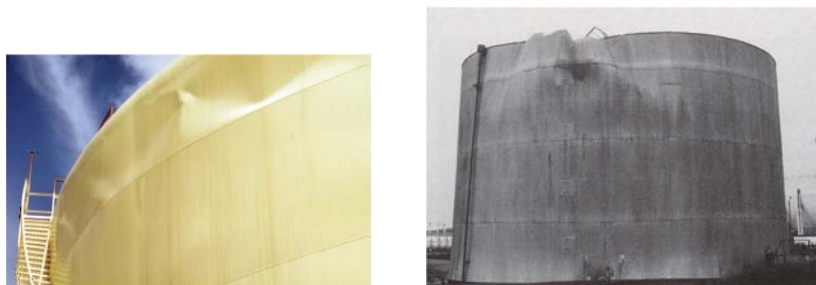


Fig. 3.1.3.1: Examples of elastic buckling at the top of the tank.

The buckling at the top of a tank has frequently been attributed to the sloshing component of the hydrodynamic response of the tank–liquid system. However, both Natsiavas and Babcock (1987) and Morita et al. (2003) proved that this buckling mode arises mostly from the impulsive action of the hydrodynamic response of the liquid; the sloshing action may contribute to the occurrence of this type of buckling, but it is not the main cause.

To the opinion of the author, a very interesting study of the phenomenon may be found in the work by Virella et al., [52]. Here, they investigated dynamic buckling of aboveground steel tanks with conical roofs and anchored to the foundation, subjected to horizontal components of real earthquake records. The study attempts to estimate the critical horizontal peak ground acceleration (Critical PGA), which induces elastic buckling at the top of the cylindrical shell, for

the impulsive hydrodynamic response of the tank-liquid system (the sloshing component is not included in the analysis). Three dimensional finite elements models of three cone roof tanks clamped at the base, with height to diameter ratios (H/D) of 0.40, 0.63 and 0.95, and with a liquid level of 90% of the height of the cylinder were used in this study. The tank models were named A, B and C and were subjected to accelerograms recorded during the 1986 El Salvador and 1966 Parkfield earthquakes. Dynamic buckling computations include material and geometric nonlinearity. Plasticity was included in the analysis to identify whether the buckling at the top of the cylindrical shell of the tank occurs before or after yielding. The procedure for obtaining the dynamic buckling loads can be divided into three steps. First, the model of the tank-liquid system is defined; second, an earthquake accelerogram is selected in order to perform the dynamic buckling simulations; and third, dynamic buckling is identified by means of a buckling criterion. The Budiansky and Roth criterion, which has been used extensively in the literature to determine the dynamic buckling load of structures, is employed in this case. According to this criterion, different analyses of the structure for several load levels need to be done, and the value for which there is a significant jump in the response for a small increase in the load indicates that the structure passes from a stable state to a critical state. For seismic stability analyses, there is a problem with this criterion due to the cyclic nature of the earthquake loading. As the direction of loading is not maintained for long enough to produce a very high jump in the displacements without loading in the opposite direction, it is sometimes difficult to identify the occurrence of buckling.

The results of the dynamic buckling analysis are that: for the El Salvador accelerogram, the critical PGA for buckling at the top of the cylindrical shell decreased with the H/D ratio of the tank (Figure 3.1.3.2a), while similar critical PGAs regardless of the H/D ratio were obtained for the tanks subjected to the Parkfield accelerogram (Figure 3.1.3.2b). From Figures 3.1.3.2 also emerges that elastic buckling at the top occurred as a critical state for the medium height (Model B) and tallest model (Model C) regardless both of the accelerogram considered, because plasticity was reached for a PGA larger than the critical PGA. For the shortest model (Model A), depending on the accelerogram considered, plasticity was reached at the shell before buckling at the top of the shell.

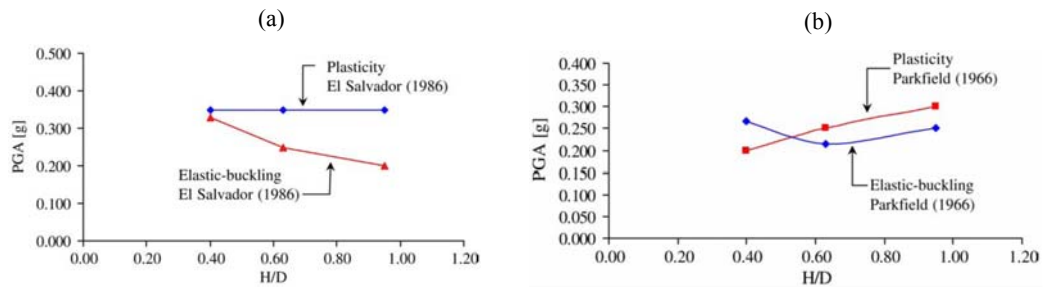


Fig. 3.1.3.2: Peak ground accelerations for elastic buckling modes and plasticity for the three tank models for the (a) 1986 El Salvador accelerogram, (b) 1966 Parkfield accelerogram, (after [52]).

As regard plasticity, the Von Mises stresses for the three models and the first yielded zones are highlighted in Figures 3.1.3.3 and 3.1.3.4.

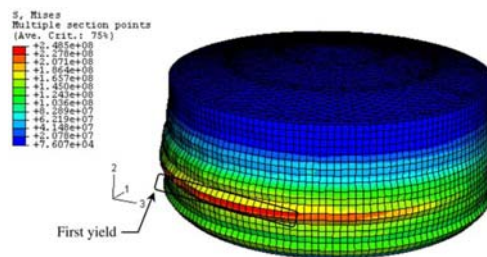


Fig. 3.1.3.3: Von Mises stresses for Model A subjected to the 1966 Parkfield accelerogram with $PGA=0.20g$, showing that the first yield occurs at the bottom of the shell, (after [52]).

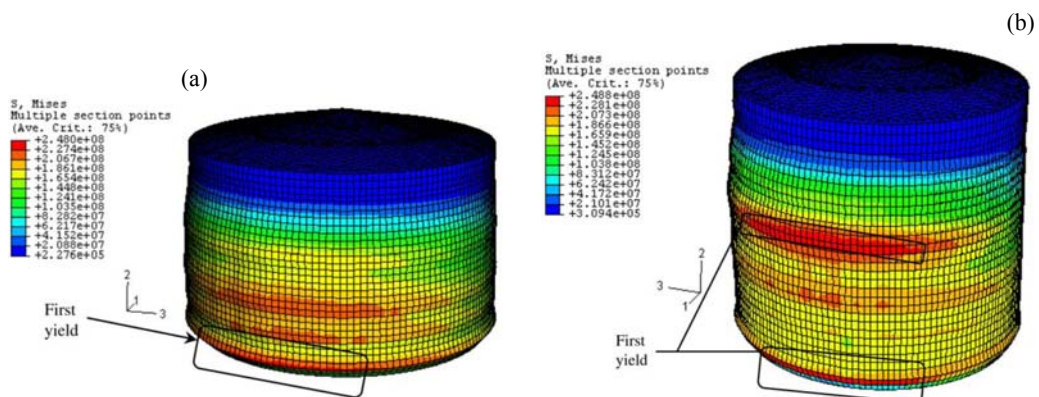


Fig. 3.1.3.4: Von Mises stresses for tanks subjected to the 1986 El Salvador accelerogram with $PGA=0.35g$, showing the first yield at loads higher than elastic buckling (Critical PGA) (a) Model B, (b) Model C, (after [52]).

In Figures 3.1.3.5 the deformed shapes at the critical PGAs for models A and C is reported. The elastic buckling at the top is evident.

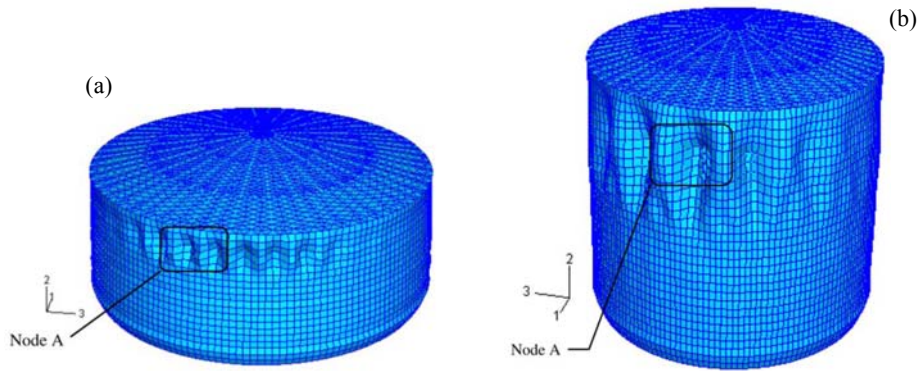


Fig. 3.1.3.5: Deformed shape for tank (a) Model A, (b) Model C, subjected to the 1986 El Salvador accelerogram, (after [52]).

It is important to discuss the actual mechanism of dynamic buckling for the tank–liquid systems considered in this paper. Natsiavas and Babcock (1987) have shown that the dynamic pressure in the fluid may induce a negative resultant pressure in the tank close to the free surface of the fluid, where the hydrostatic pressure is small. This negative resultant pressure ($P_{hyd} - P_{imp}$, in Figure 3.1.3.6) induces local compressive hoop stresses that may lead to local buckling of the tank.

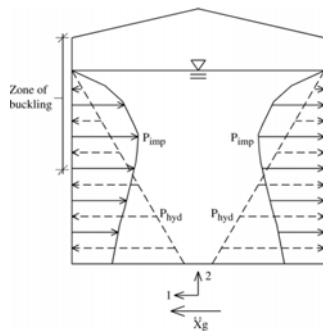


Fig. 3.1.3.6: Illustration of the buckling zone at the tank shell (after [52]).

The elastic buckling modes for the tanks considered in this study affect the top of the tank along the main direction of the excitation, where the impulsive component of the hydrodynamic pressures have their maximum values and the shell thicknesses are smallest. This buckling was produced by the negative (inward) resultant pressure $P_{hyd} - P_{imp}$ near the free surface of the fluid, which induced large compressive stresses sufficient to buckle the shell. Figure 3.1.3.7 presents the hoop, vertical and shear maximum stresses for a critical element at the buckling zone of tank Model A. This figure shows that the circumferential compressive membrane stresses are much larger than the vertical membrane stresses and shear stresses in the buckling region and thus are responsible for inducing local buckling in the tank shell. The maximum Von Mises stresses in the buckling zone are about 88 MPa (35% of the yield stress), so that the steel remains elastic at the onset of dynamic buckling. A similar behavior was obtained for the other tank–liquid systems.

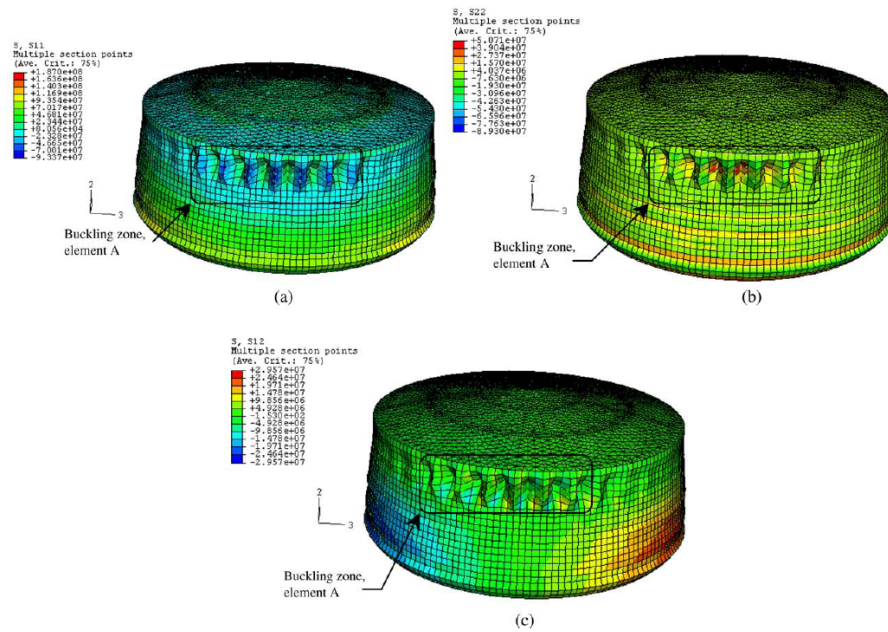


Fig. 3.1.3.7: Model A stresses at the critical PGA. (a) hoop stresses, (b) vertical stresses, (c) shear stresses, (after [52]).

Elastic dynamic buckling states for tank–liquid systems under horizontal earthquake excitation in which the buckling mode has deflections at the top of the cylindrical part of the shell have been obtained for critical values of PGA in the range between 0.25g and 0.35g, so that this failure mode should be of great concern to the designer and should be included in international codes provisions. The geometry of the tank, as reflected by the aspect ratio H/D, has some influence on the critical PGA, but no clear trend was observed for all the earthquakes considered. It is concluded that buckling at the top of the shell is caused by a negative (inward) net pressure at the zone in the tank where the impulsive hydrodynamic pressure induced by the earthquake excitation exceeds the hydrostatic pressure. This negative net pressure induces membrane compressive circumferential stresses which buckle the shell. This agrees with previous observations made by Natsiavas and Babcock (1987), whose main conclusion was that buckling at the top caused by external pressure is really a potential failure mode for very flexible model tanks rocking on an elastic soil.

Even if this possible failure mode is not covered by the codes specific for the analysis and design of tanks, a first attempt to evaluate analytically the critical buckling stress for this buckling mode can be made using the EC3 part 1-6 provisions for unstiffened cylindrical shells (Appendix D), [11]. Here, the critical Euler’s circumferential buckling stress (formula D.21 in EC3) is defined as:

$$\sigma_{\theta,c1} = 0,92 \left(\frac{E_w t_w}{R} \right) \left(\frac{C_{\theta}}{\omega} \right) \tag{3.1.3.1}$$

where ω is a dimensionless length parameter,

$$\omega = \frac{H}{R} \sqrt{\frac{R}{t_w}} = \frac{H}{\sqrt{R t_w}} \tag{3.1.3.2}$$

and the factor C_ϑ should be taken from table 3.1.3.1 (Table D.3 in EC3), with a value that depends on the boundary conditions, summarized in Table 3.1.3.2 and Figure 3.1.3.8 (Table 5.1 and Figure 8.1 in EC3).

Case	Cylinder end	Boundary condition	Value of C_ϑ
1	end 1 end 2	BC 1 BC 1	1,5
2	end 1 end 2	BC 1 BC 2	1,25
3	end 1 end 2	BC 2 BC 2	1,0
4	end 1 end 2	BC 1 BC 3	0,6
5	end 1 end 2	BC2 BC3	0
6	end 1 end 2	BC 3 BC 3	0

Table 3.1.3.1: Buckling factors for medium-length cylinders (after [11]).

Boundary condition code	Simple term	Description	Normal displacement w	Meridional displacements u	Meridional rotation β_ϑ
BC1r	Clamped	radially restrained meridionally restrained rotation restrained	$w = 0$	$u = 0$	$\beta_\vartheta = 0$
BC1f		radially restrained meridionally restrained rotation free	$w = 0$	$u = 0$	$\beta_\vartheta \neq 0$
BC2r		radially restrained meridionally free rotation restrained	$w = 0$	$u \neq 0$	$\beta_\vartheta = 0$
BC2f	Pinned	radially restrained meridionally free rotation free	$w = 0$	$u \neq 0$	$\beta_\vartheta \neq 0$
BC3	Free edge	radially free meridionally free rotation free	$w \neq 0$	$u \neq 0$	$\beta_\vartheta \neq 0$

NOTE: The circumferential displacement v is closely linked to the displacement w normal to the surface, so separate boundary conditions are not identified for these two parameters (see (4)) but the values in column 4 should be adopted for displacement v .

Table 3.1.3.2: Boundary conditions for shells (after [11]).

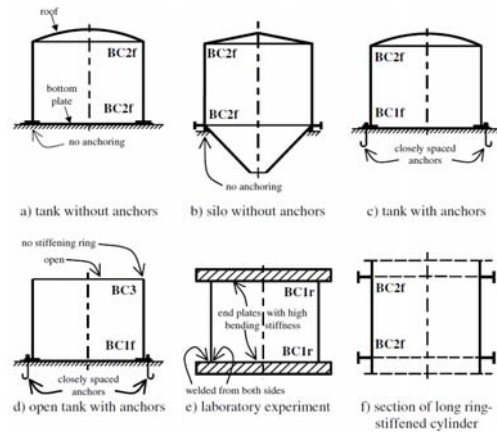


Fig. 3.1.3.8: Schematic examples of BCs for buckling limit state (after [11]).

Finally, it must be noted that EC3 provisions about shell buckling design apply in case of axisymmetric pressure distribution. However, they can be used also for different pressure configuration provided that there is a method to convert the generic pressure distribution into an equivalent axisymmetric one. For example, this is done in EC3 for the wind pressure (Figure 3.1.3.9, Figure D.2 in EC3), but not for the earthquake-induced hydrodynamic pressure. The value of the coefficient k_w is in the range $0.65 < k_w < 1$:

$$k_w = 0,46 \left(1 + 0,1 \sqrt{\frac{C_\vartheta}{\omega} \cdot \frac{R}{t_w}} \right) \tag{3.1.3.3}$$

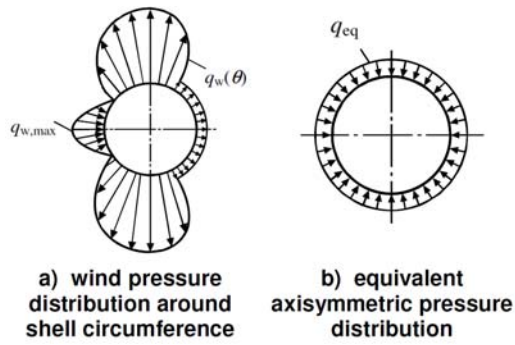


Fig. 3.1.3.9: Transformation of typical wind external pressure load distribution (after [11]).

3.2 Buckling in current standards

3.2.1 API 650

In this US standards the different buckling modes of Section 3.1 are not mentioned. Only allowable stresses for a uni-directional stress states are specified. According to API 650, verifications must be performed separately in the two directions, vertical and circumferential. Even if the buckling problem is never mentioned, it is possible to demonstrate that it is in some way hidden behind the verifications of the longitudinal membrane compression stress and of the hoop stress.

Regardless the allowable longitudinal shell-membrane compression stress f_{mb} (F_c in API notation), it is differentiated for two cases. If $\rho HD^2/t_w^2 > 44$ then

$$f_{mb} = 83 \frac{t_w}{D} \quad (3.2.1.1)$$

while if $\rho HD^2/t_w^2 < 44$ then

$$f_{mb} = 83 \frac{t_w}{2,5 D} + 7,5 \sqrt{\rho H} < 0,5 f_y \quad (3.2.1.2)$$

Remember that these formulas must be used with prescribed units of measure: t_w in mm, H and D in m, ρ in t/m^3 . If we focus the attention on the discriminant term $\rho HD^2/t_w^2$, it is possible to do the following very useful consideration: this term comes from the ratio of the hoop stress σ_p induced by internal pressure $p_{stat} = \rho H$ (neglecting the contribution of the vertical earthquake component) to the theoretical critical axial compression stress of perfect thin cylindrical shell σ_{c1} (Euler's formula). In fact,

$$\frac{\sigma_p}{\sigma_{c1}} = \frac{p_{stat} R / t_w}{0,6 \frac{E_w t_w}{R}} = \frac{\rho H R^2}{0,6 E_w t_w^2} \quad (3.2.1.3a)$$

and introducing in equation 3.1.1.3a the units of measure prescribed by API 650, it can be rewritten as follows:

$$\frac{\rho HR^2}{0,6E_w t_w^2} = \frac{10^4 \rho \left[\frac{N}{m^3} \right] HD^2 [m^3]}{0,6 \cdot 2 \cdot 10^5 \left[\frac{N}{mm^2} \right] t_w^2 [mm^2]} = \frac{1}{48} \frac{\rho HD^2}{t_w^2} \quad (3.2.1.3b)$$

Finally, from equations 3.1.1.3a and 3.1.1.3b we have obtained:

$$\frac{\sigma_p}{\sigma_{c1}} = \frac{1}{48} \frac{\rho HD^2}{t_w^2} \quad (3.2.1.4a)$$

or

$$\frac{\rho HD^2}{t_w^2} = 48 \frac{\sigma_p}{\sigma_{c1}} \quad (3.2.1.4b)$$

So, we can state that the discriminant term $\rho HD^2/t_w^2$ is strictly connected to the hoop stress. In particular, it reveals if the hoop stress induced by internal pressure σ_p had reached the buckling stress σ_{c1} (first case, $\rho HD^2/t_w^2 > 44$) or not (second case, $\rho HD^2/t_w^2 < 44$). In the first case, $\rho HD^2/t_w^2 > 44$ or $\sigma_p > \sigma_{c1}$, the allowable longitudinal shell-membrane compression stress f_{mb} comes directly from the expression of σ_{c1} .

$$f_{mb} = \sigma_{c1} = 0,6 \frac{E_w t_w}{R} = 1,2 \frac{E_w t_w}{D} \quad (3.2.1.5a)$$

Again, introducing in equation 3.1.1.5a the units of measure prescribed by API 650 it can be rewritten as follows:

$$f_{mb} = \sigma_{c1} = 1,2 \frac{E_w t_w}{D} = 1,2 \frac{2 \cdot 10^5 \left[\frac{N}{mm^2} \right] t_w [mm]}{10^3 D [mm]} = 240 \frac{t_w}{D} \quad (3.2.1.5b)$$

Then, a knockdown factor equal to 1/3 is probably adopted by API 650 and so the allowable knocked-down stress is:

$$f_{mb} = \frac{240}{3} \frac{t_w}{D} \cong 83 \frac{t_w}{D} \quad (3.2.1.6)$$

In the second case, $\rho HD^2/t_w^2 < 44$ or $\sigma_p < \sigma_{c1}$, the allowable longitudinal compression stress f_{mb} is lower, since the low internal pressure does not provide the beneficial effect explained in Section

3.1.1. In particular, f_{mb} is the sum of two terms: a first one, set equal to 2/5 of f_{mb} in the first case (equation 3.1.1.6), and a second one which can give a small increment.

$$f_{mb} = 83 \frac{t_w}{2,5 D} + 7,5 \sqrt{\rho H} \quad (3.2.1.7)$$

However, f_{mb} in this second case must not exceed half of the yielding stress f_y .

It can be noted that API 650 do not mention any type of buckling, but actually elastic buckling is accounted for in verifications of longitudinal compression stresses. Here, also the beneficial effect of internal pressure are taken into account: in fact in the first case anular strips undergo a good level of tension and so they can offer a good stiffness to the meridian lines. Also, an high pressure prevents buckling towards the internal. In the second case, when the hydrostatic pressure remains below a certain value and the imperfections are still present, the resistance is lower.

Since the verification of the longitudinal compression stresses follows an elastic buckling criterion, API 650 also prescribe limitations on the hoop stresses, in order to avoid elastic-plastic buckling. In particular, hoop stress (including both hydrostatic and hydrodynamic contribution) must not exceed the lesser of:

- the basic allowable membrane stress for the shell material, increased by 33%;
- 90% of the yielding stress, times the joint efficiency factor E.

These limitations aim to avoid the yielding of anular strips, which is the main cause of “elephant’s foot” buckling, as explained in Section 3.1.2.

Finally, we can conclude that API standards aim to avoid an elastic-plastic collapse by keeping the hoop stresses below the yielding threshold. Then, on the basis of the value of the internal pressure, also the longitudinal compression stresses are limited in order to avoid an elastic buckling failure. This approach is very easy to apply but also very rough and approximate. In fact, it specifies limits for uni-directional stress states depending on the value of a discriminant term strictly connected to the internal pressure. But actually the elastic-plastic collapse is due to a bi-axial stress state. That is to say that vertical compression stress and hoop stress alone do not cause the elastic-plastic buckling, but the real cause is the combination of the two, not considered by API 650. In this standard, in the expression of the allowable longitudinal compression stress f_{mb} , the hoop stress does not appear. This stress is limited separately from other conditions.

3.2.2 A worked example

In this Section the API verification criteria are applied to the tank of Sections 2.2.7 and 2.3.4, in order to show how much easy and fast is to apply them to a real case.

The maximum longitudinal shell-membrane compression stress (from API formula E.6.2.2.1-2a), as computed in Section 2.3.4, is:

$$\sigma_c = \left(\frac{w_r + w_w + w_L}{0,607 - 0,18667 \cdot J^{2,3}} - w_L \right) \frac{1}{1000 t_w} = \left(\frac{3980 + 6840 + 32510}{0,607 - 0,18667 \cdot 1,09^{2,3}} - w_L \right) \frac{1}{1000 \cdot 9,68} \cong 8,44 \text{ [MPa]}$$

For the case under consideration $\rho H D^2 / t_w^2 = 34.15 < 44$, so the allowable longitudinal shell-membrane compression stress f_{mb} is (F_c from API formula E.6.2.2.3-2a):

$$f_{mb} = \frac{83 t_w}{2,5 D} + 7,5 \sqrt{\rho H} = \frac{83 \cdot 9,68}{2,5 \cdot 20} + 7,5 \sqrt{1 \cdot 8} \cong 37,28 \text{ [MPa]}$$

$\sigma_c < f_{mb}$. Shell compression is verified!

The hoop tensile stress, including hydrostatic and hydrodynamic contribution due to horizontal excitation, (from API formula E.6.1.4-6), as computed in Section 2.3.4, is:

$$\sigma_T = \frac{N_h + \sqrt{N_t^2 + N_c^2}}{t_w} = \frac{770 + \sqrt{152,01^2 + 19,39^2}}{9,68} \cong 107,56 \text{ [MPa]}$$

The maximum allowable hoop tension membrane stress for the combination of hydrostatic product and dynamic membrane hoop effects shall be the lesser of:

- the design allowable stress of steel, increased by 33%. $160 \cdot 1,33 = 212.8$ [MPa];
- $0.9 \cdot f_y$ times the joint efficiency. Assuming $E=1$, $0.9 \cdot f_y = 0.9 \cdot 275 = 247.5$ [MPa].

$\sigma_T > 212.8$. Hoop tension is verified!

3.2.3 ECCS recommendations

In this Section the ECCS (European Convention for Constructional Steelwork) provisions are presented. Such provisions are collected in [14], *Buckling of Steel Shells-European Recommendations* and deal with the elastic buckling phenomenon. They are very detailed and represent the basis for the criteria adopted by Eurocode 8 for the elastic buckling load calculation. This is the reason why it was considered important to include them in the present thesis.

First of all, it must be said that recommendations apply only if the boundary conditions are such that radial and tangential displacements of both edges of the shell are precluded and when

the cylinder is not too long, $\frac{H_w}{R} < 0.95 \sqrt{\frac{R}{t_w}}$, nor too short, $\frac{H_w}{R} < \frac{1,411}{\sqrt{\alpha_0}} \sqrt{\frac{t_w}{R}}$ (α_0 is the knockdown

factor in case of pure axial compressive load). If these conditions are fulfilled, the axial buckling load is almost independent of the length of the cylinder H_w and the other boundary conditions. One of the possible way of preventing radial and tangential displacements is the use of end rings; ECCS also gives criteria to design such elements. The buckling load is much lower for cylinders whose edge is movable in the radial or circumferential direction. For long cylinders both the length and the boundary conditions affect the buckling behavior because column buckling comes into play. It may be said that a perfect cylinder is a long one when the circumferential wave number changes from $n=2$ to $n=1$. For imperfect cylinders the shell buckling modes may interact dangerously with the column buckling mode. Therefore the length limitation has been chosen to coincide with the transition from $n=3$ to $n=2$ (from here comes the condition $\frac{H_w}{R} < 0.95 \sqrt{\frac{R}{t_w}}$). Very short cylinders fails by plate buckling which depends on the length H_w of the cylinder, rather than by shell buckling, and meridian lines of the cylinder wall buckle like bars having a wide and thin cross section. Since bars have moderate imperfection sensitivity, the knockdown factor for short cylinder in the elastic range may be taken equal to one. However, since common tank dimensions fall down the “not too long cylinders” category, short cylinders are not discussed further in the present work.

According to ECCS, the ultimate buckling stress (σ_u in ECCS notation) can be computed as follows. If $\hat{\alpha}\sigma_{c1} \leq f_y/2$,

$$f_{mb} = \frac{\hat{\alpha}\sigma_{c1}}{\gamma} \quad (3.2.3.1a)$$

and if $\hat{\alpha}\sigma_{c1} \geq f_y/2$,

$$f_{mb} = f_y \left[1 - 0,4123 \left(\frac{f_y}{\hat{\alpha}\sigma_{c1}} \right)^{0,6} \right] \quad (3.2.3.1b)$$

where $\hat{\alpha}$ is the knockdown factor already mentioned in Section 3.1.1 (α in ECCS notation) and $\gamma=4/3$ is an additional safety factor taking into account the unfavorable post-buckling behavior (snap-back branch in the load-displacement curve) of cylindrical shells subjected to meridional compressive stresses (Figure 3.2.3.1). In fact, for some structures, the loss of stiffness after buckling is so great that the buckled equilibrium configuration can only be maintained by returning to an earlier level of loading. Classical examples of this type are buckling of thin cylindrical shells under axial compression and buckling of complete spherical thin shells under uniform external pressure. This phenomenon is named “finite-disturbance buckling”. The reason for the name is that in such structures a finite disturbance during the quasi-static application of

the load can force the structure to pass from an unbuckled equilibrium configuration to a buckled one before the critical load is reached. In Figures 3.2.3.2 the difference between “finite-disturbance buckling” of cylindrical shells or spheres and “classical or bifurcation buckling” of columns and plates is highlighted.

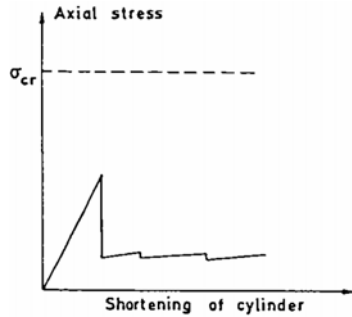


Fig. 3.2.3.1: Experimental diagram for an axially loaded cylinder. $\sigma_{cr}=\sigma_{cl}$ (after [14]).

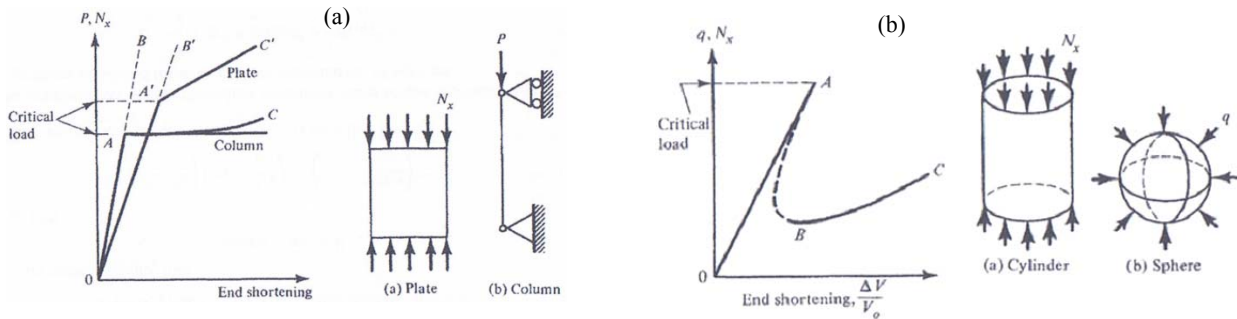


Fig. 3.2.3.2: (a) Classical buckling (b) Finite-disturbance buckling (after [43]).

Introducing the parameter $\lambda = \sqrt{f_y / \hat{\alpha}\sigma_{c1}}$, equations 3.2.3.1a-b become: if $\lambda \geq \sqrt{2}$,

$$\frac{f_{mb}}{f_y} = \frac{0,75}{\lambda^2} \tag{3.2.3.2a}$$

and if $\lambda \leq \sqrt{2}$,

$$\frac{f_{mb}}{f_y} = 1 - 0,4123 \cdot \lambda^{1,2} \tag{3.2.3.2b}$$

The relationship between $\hat{\alpha}\sigma_{c1}$ and f_{mb} is represented graphically in Figure 3.2.3.3, for a yielding stress $f_y=275$ MPa.

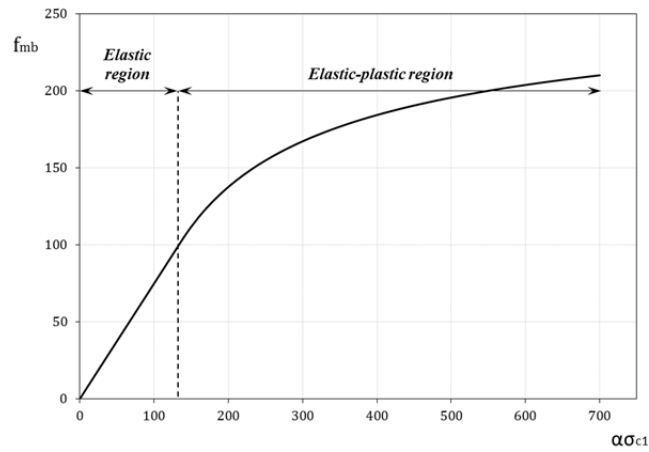


Fig. 3.2.3.3: Elastic buckling strength vs critical buckling stress.

The empirical limit $\lambda=\sqrt{2}$ separating the range of validity of expression 3.2.3.2a from 3.2.3.2b (or the empirical limit $\hat{\alpha}\sigma_{c1}=f_y/2$ separating the range of validity of expression 3.2.3.1a from 3.2.3.1b) has been so chosen that comparison of experimental results with predictions obtained by means of equations 3.2.3.1a to 3.2.3.2b shows these predictions to be reasonably safe. In Figure 3.2.3.3 it can be seen that when the theoretical buckling stress $\hat{\alpha}\sigma_{c1}$ is below the empirical limit $f_y/2=138$ MPa, the buckling stress f_{mb} coincides with $\hat{\alpha}\sigma_{c1}$ (excluding the additional safety factor γ). Here the behavior of the material is still fully elastic, that is to say that the material crisis does not interfere with the buckling failure and so the structure can reach the full theoretical buckling stress, calculated taking into accounts the second order effects but assuming the material to be perfectly elastic. On the contrary, when $\hat{\alpha}\sigma_{c1}$ overcomes $f_y/2$, the two types of crises interfere; in particular, approaching the yield stress of the material does not allow the complete development of the theoretical buckling stress and so we cannot assume the full $\hat{\alpha}\sigma_{c1}$ as the effective buckling stress. The interaction between the two failure modes (material yielding and buckling) can be seen in Figure 3.2.3.3 by the fact that in the elastic-plastic region f_{mb} does not grow linearly with $\hat{\alpha}\sigma_{c1}$. It is possible to conclude that f_{mb} may be defined as the critical buckling stress with regard to the elastic buckling limit state, and it takes into account also the effect of material plasticizations.

Regardless the knockdown factor, in [14] it is defined as follows:

“The reduction factor is the lower limit of the ratio of the experimental buckling load, with buckling assumed to occur in the elastic range, to the theoretical critical load of the perfect cylinder, calculated with pure membrane stresses at the pre-buckling stage. It accounts for the detrimental effect of shape imperfections, residual stresses and edge disturbances. It depends on the imperfections, on the geometry and on the type of loading.”

ECCS gives different values of the knockdown factor for four cases:

$$\hat{\alpha} = \alpha_0 \quad \text{pure axial compressive load}$$

$$\hat{\alpha} = \alpha_b \quad \text{pure bending}$$

$$\hat{\alpha} = \alpha_p = \alpha_0 + (1 - \alpha_0) \frac{\phi}{\phi + 0,007} \quad \text{axial compressive load combined with internal pressure}$$

$$\hat{\alpha} = \frac{\alpha_0 \sigma_0 + \alpha_b \sigma_b}{\sigma_0 + \sigma_b} \quad \text{axial compressive load combined with bending}$$

where σ_0 and σ_b are the uniform compressive stress due to the design axial load and the maximum compressive stress due to the design bending moment, respectively. $\phi = \frac{PR\sqrt{R}}{E_w t_w \sqrt{t_w}}$ is the normalized internal pressure P. In Figures 3.2.3.4 and 3.2.3.5 values of α_0 , α_b and α_p are plotted.

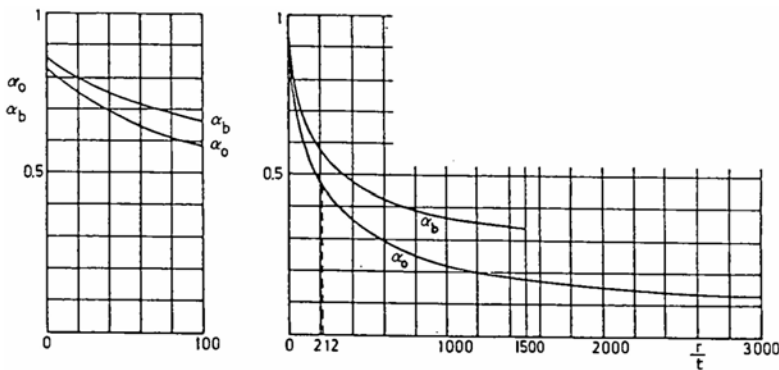


Fig. 3.2.3.4: Evaluation of α_0 and α_b (after [14]).

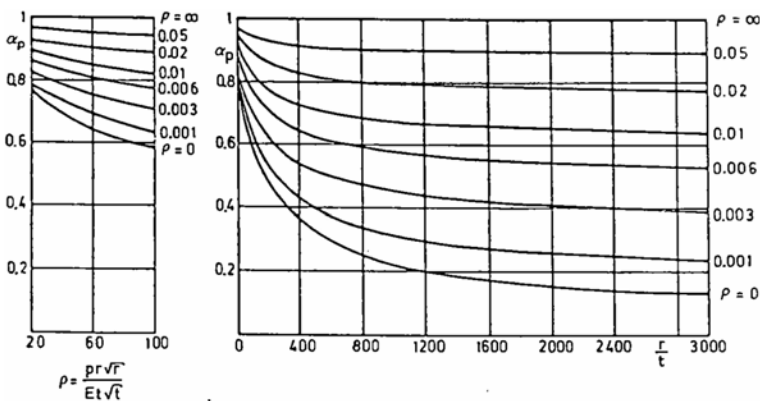


Fig. 3.2.3.5: Evaluation of α_p . ϕ is equal to ρ in the figure (after [14]).

It is important to note that the curves in Figures 3.2.3.3 and 3.2.3.4 have been established as the lower bound of scatter bands of numerous experimental points obtained from tests on plastic and metal cylinders performed over many years by a number of researchers. Hence the equations for α_0 , α_b and α_p are not derived from theory, but are curve-fitting formulas. The values given for $\hat{\alpha}$ are overconservative for very short cylinder. For such cylinders different formulas are suggested in [14].

3.2.4 Eurocode 8

Eurocode 8 offers a more thorough discussion of the buckling problem than API 650. In EC8, provisions regarding the two main buckling modes (elastic and elastic-plastic) are differentiated and treated explicitly. Formulas to calculate the maximum vertical membrane stresses f_{mb} and f_{pb} are given for the two cases; the lowest one must be greater than the maximum vertical compressive stress σ_c in the tank walls (σ_m in the Eurocode notation). So, the tank is safe from a buckling point of view if:

$$\sigma_c \leq \min\{f_{mb}; f_{pb}\} \quad (3.2.4.1)$$

- **Elastic buckling**

EC8 states that this form of buckling has been observed in those parts of the shell where the thickness is reduced with respect to the thickness of the base and/or the internal pressure (which has a stabilizing effect) is also reduced with respect to the maximum value attained at the base. Therefore, for tanks of constant or varying wall thickness, the verification for elastic buckling should take place at the base as well as in the wall above the base where both the shell thickness and the hydrodynamic pressure are smaller than the corresponding ones at the base of the tank. Indeed, this is often observed as “diamond shape” buckling in steel tanks. Due to the stabilizing effect of the internal pressure, the verification should be based on the minimum possible value of the interior hydrodynamic pressure (the hydrostatic one is constant) in the seismic design situation. According to EC8, when checking against elastic buckling, the contribution of the vertical component of the earthquake motion to the internal pressure should be ignored. The elastic critical buckling stress with regard to the elastic buckling limit state is (from EC8 equation A.62):

$$f_{mb} = 0,19 \cdot \sigma_{c1} + 0,81 \cdot \sigma_d \quad (3.2.4.2)$$

where σ_{c1} is the theoretical critical axial compression stress of perfect thin cylindrical shell (equation 3.1.1.1, Euler’s formula) and σ_d (σ_p in EC8 notation) can be computed as follows:

$$\sigma_d = \sigma_{c1} \sqrt{1 - \left(1 - \frac{\bar{p}}{5}\right)^2 \left(1 - \frac{\sigma_0}{\sigma_{c1}}\right)^2} \leq \sigma_{c1} \quad (3.2.4.3)$$

In equation 3.2.4.3, \bar{p} is the ratio between hoop stress induced by internal pressure σ_p and the theoretical critical axial compression stress σ_{c1} :

$$\bar{p} = \frac{\sigma_p}{\sigma_{c1}} = \frac{PR}{t_w \sigma_{c1}} < 5 \quad (3.2.4.4a)$$

and if $\lambda^2 = \frac{f_y}{\hat{\alpha} \cdot \sigma_{c1}} \leq 2$ then the buckling stress parameter σ_0 is:

$$\sigma_0 = f_y \left(1 - \frac{\lambda^2}{4} \right) \quad (3.2.4.4b)$$

while if $\lambda^2 = \frac{f_y}{\hat{\alpha} \cdot \sigma_{c1}} > 2$ then the buckling stress parameter σ_0 is:

$$\sigma_0 = \hat{\alpha} \cdot \sigma_{c1} \quad (3.2.4.4c)$$

with $\hat{\alpha}$ ($\bar{\sigma}$ in EC8 notation) that can be computed as follows:

$$\hat{\alpha} = 1 - 1,24 \frac{\delta}{t_w} \left[\sqrt{1 + \frac{2}{1,24 \frac{\delta}{t_w}}} - 1 \right] \quad (3.2.4.5)$$

The ratio δ/t_w denotes the ratio of maximum imperfection amplitude to the wall thickness, and can be computed as follows:

$$\frac{\delta}{t_w} = \frac{0,06}{b} \sqrt{\frac{R}{t_w}} \quad (3.2.4.6)$$

where b is a parameter indicating the quality of the construction: $b=1$ for normal construction, $b=1.5$ for quality construction, $b=2.5$ for very high quality construction. It is noted that equations 3.2.4.4b-c do exactly coincide with equations 3.2.3.2a-b if $f_{mb}=\sigma_0$ and the additional safety factor $\gamma=4/3$ is omitted. In this case equations 3.2.3.2a-b can be rewritten as:

$$\frac{\sigma_0}{f_y} = 1 - \frac{\lambda^2}{4} \quad (3.2.4.7a)$$

$$\frac{\sigma_0}{f_y} = \frac{1}{\lambda^2} \quad (3.2.4.7b)$$

and equation 3.2.4.7b is exactly equation 3.2.4.4c:

$$\sigma_0 = \frac{f_y}{\lambda^2} = \hat{\alpha} \cdot \sigma_{c1} \quad (3.2.4.7c)$$

This means that the quantity σ_0 of Eurocode provisions plays the role of the quantity f_{mb} of ECCS provisions. So, it is possible to state that EC8 represents a further developments of ECCS in the buckling load assessment. What really changes between the two documents is that the knockdown factor $\hat{\alpha}$ in Eurocode takes into account only the buckling stress reduction due to imperfections, while in ECCS it takes into account also the type of loadings and the effect of internal pressure. In EC8 the reduction due to internal pressure is taken into account through another term of equation 3.2.4.3.

From equation 3.2.4.2 emerges that the critical buckling stress with regard to the elastic buckling limit state f_{mb} is a percentage of the ideal critical buckling stress σ_{c1} , composed of a fixed portion (19%) plus another portion (81%) depending on σ_d , in turn dependent on σ_{c1} . From relationships 3.2.4.2 to 3.2.4.6 it is possible to note how f_{mb} is influenced by three factors:

- the amount of imperfections, which tends to reduce the limit stress;
- the internal pressure, which reduces the imperfections thus increasing the limit stress;
- the gap between critical buckling stress σ_{c1} and yielding stress σ_y .

The maximum value that f_{mb} can attain is equal to σ_{c1} . This happens when $\sigma_d = \sigma_{c1}$. To have this condition it is necessary to zero the two terms in round brackets of equation 3.2.4.2. The first one, $(1 - \bar{p}/5)$, is zero when $\bar{p} = 5$, that is when the hoop stress σ_p induced by the internal pressure P is 5 times the critical buckling stress. To zero the second term $(1 - \sigma_0/\sigma_{c1})$ two conditions must be fulfilled. First, it is necessary to have no imperfections, that is to have a knockdown factor $\hat{\alpha} = 1$ so that $\sigma_0 = \sigma_{c1}$. Second, the yielding stress f_y must be greater than $2\sigma_{c1}$. In practice, the above described situation is very difficult to reach for real cases. This is why f_{mb} is always less than the Euler's critical buckling stress σ_{c1} .

Equation 3.2.4.2 adopted by EC8 reflects the increase in the critical buckling stress due to the axial stresses being induced by bending action rather than uniform axial load. It can be seen from the above discussions that EC8 provides a rational approach to determine the critical buckling stress with regard to the elastic buckling limit state of tanks. In fact, the EC8 approach takes into account imperfections, internal pressure and non-uniform axial stress. This is based on the New Zealand code, which first adopted this approach, but also on ECCS provisions. All the other codes account for the effects of internal pressure, while ignoring the effects of bending.

Finally, it must be noted that criteria to calculate the critical buckling stress are also given in [11], EC3 part 1-6. A quick comparison between EC8 and EC3 shows that the bases are

identical. In practice, EC8 shows the same procedure of EC3, but each formula is specified for cylinders having the typical dimensions of liquid-storage tanks.

- **Elastic-plastic buckling**

This form of buckling (denoted by the formation of an “elephant’s foot” bulge) normally occurs close to the base of the tank, due to a combination of vertical compressive stresses and tensile hoop stresses inducing an inelastic bi-axial state of stress. In tanks with variable wall thickness, verification for this mode of buckling should not be limited to the section close to the base of the tank, but should extend to the bottom section of all parts of the wall which have constant thickness.

As already shown in Section 3.1.2, the empirical equation developed by Rotter and Seide (1990) to calculate the critical buckling stress with regard to the elastic-plastic buckling limit state f_{pb} is:

$$f_{pb} = \sigma_{c1} \left[1 - \left(\frac{PR}{t_w f_y} \right)^2 \right] \left(1 - \frac{1}{1,12 + s^{1,15}} \right) \left(\frac{s + f_y/250}{s + 1} \right) \quad (3.2.4.8)$$

where s is a dimensionless factor given by $R/(t_w \cdot 400)$ and the last term is to generalize the formula to all kind of steel, since it was originally calibrated for a steel with $f_y=250$ MPa. P and f_y must be included in MPa. It is not very clear the meaning of the second term in brackets.

In contrast to the case of elastic buckling, the effect of the internal pressure in equation 3.2.4.8 is to reduce the critical buckling stress. In fact, as already mentioned in Section 3.1.2, this failure mode happens for high value of hoop stresses (steel must be yielded) and equation 3.2.4.8 shows that when annular strips are yielded ($PR/t_w=f_y$) all load-carrying capacities are lost ($f_{pb}=0$). So, in this case, to get a conservative design, the value of P must be the maximum possible in the seismic design situation. It must include hydrostatic pressure and hydrodynamic pressures due to all the components of the earthquake excitation.

It is important to note that equation 3.2.4.8 is based on nonlinear elastic-plastic calculations for an isotropic shell under axisymmetric loading and it was originally developed for pinned boundary conditions at the tank base. However, fixed boundary conditions result in a higher buckling strength. Furthermore, Eurocode 8 suggest to check the buckling stress at the tank base as well as at the boundary between two shell courses with different thickness, and here conditions close to a fixed tank base prevail. Therefore the above equation may be used for all these cases.

Using the Eurocode's formulations to compute the elastic and elastic-plastic critical buckling stresses (equations 3.2.4.2 and 3.2.4.8 in this thesis), it is possible to obtain a “strength domain” with respect to buckling failure. This is what is represented in Figure 3.2.4.1 for different thickness to radius ratios t/R . From this Figure it is very easy to note that, for a fixed value of t/R , the elastic buckling is the most dangerous for low values of circumferential stress (and so of internal pressure), whereas elastic-plastic buckling is the most dangerous for high values of circumferential stress (and so of internal pressure). These “strength domains” highlight in a very simple and efficient way the influence of internal pressure on the buckling strength. Furthermore, from a very fast handmade calculation, it is possible to assess that the maximum buckling strength decreases by 72% for a thickness reduction from $t/R=3,5\%$ to $t/R=0,5\%$. For example, for a tank with radius $R=10$ m, the maximum buckling strength is 180 MPa for a thickness $t=35$ mm and 50 MPa for a thickness $t=5$ mm.

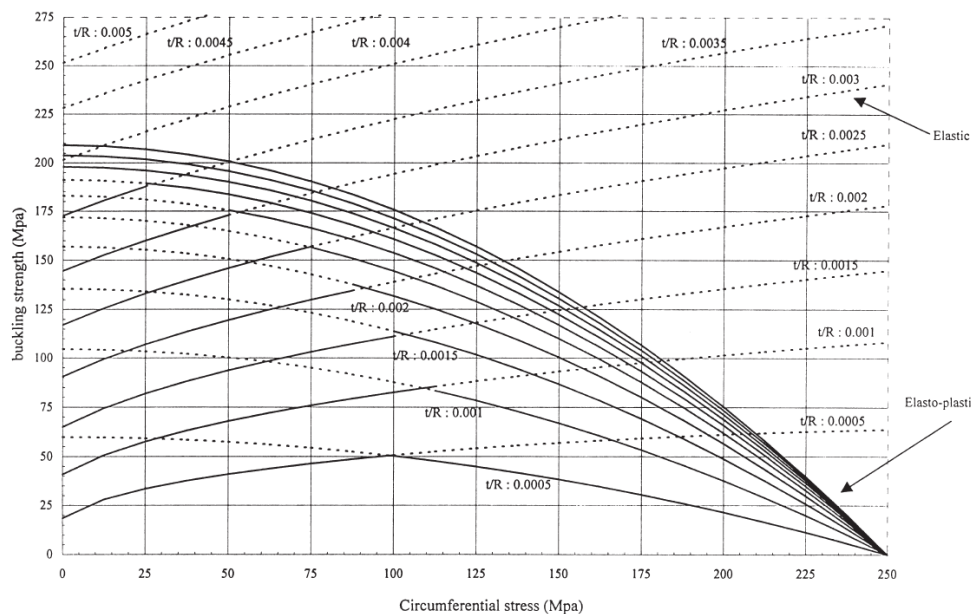


Fig. 3.2.4.1: Elastic and elasto-plastic buckling strengths of anchored steel cylindrical tanks (after [18]).

3.3 Design of a new tank shell for seismic loads

The thickness t_w of the tank shell plays a dominant role in determining the shell buckling capacity. It is primarily evaluated from considerations of allowable hoop stress under hydrostatic pressure p_{stat} , and therefore, it is dependent on tank radius R , liquid height H , yield stress of steel f_y , and the factor of safety SF . In equation 3.3.1 the hoop stress induced by the hydrostatic

pressure is set equal to the yield stress, suitably reduced by the factor of safety in order to provide the allowable hoop stress:

$$\frac{p_{stat} R}{t_w} = \frac{f_y}{SF} \quad (3.3.1)$$

and so, the equation for calculating the thickness is:

$$t_w = \frac{p_{stat} \cdot R \cdot SF}{f_y} \quad (3.3.2)$$

and the factor of safety SF can be expressed as:

$$SF = \frac{f_y t_w}{p_{stat} R} \quad (3.3.3)$$

Shell membrane buckling limits the design at low total liquid pressure but the effect of elastic-plastic buckling becomes apparent with the increase of earthquake acceleration accompanied by higher H/R values. High dynamic pressures cause the elastic-plastic buckling stress f_{pb} to dip below the knocked-down membrane buckling stress f_{mb} . Therefore, the problem arising from such a low elastic-plastic buckling stress can be controlled by selecting an appropriate reduction factor that ensures the elastic-plastic buckling does not limit the design. This is satisfied if:

$$f_{pb} \geq f_{mb} \quad (3.3.4)$$

Now, let's work through expression 3.3.4 in order to find a condition on the reduction factor SF. Using equations 3.1.1.2 and 3.1.2.1 for f_{pb} and f_{mb} expression 3.3.4 can be rewritten as:

$$\sigma_{c1} \left[1 - \left(\frac{PR}{t_w f_y} \right)^2 \right] \geq \hat{\alpha} \sigma_{c1} \quad (3.3.5a)$$

$$1 - \left(\frac{PR}{t_w f_y} \right)^2 \geq \hat{\alpha} \quad (3.3.5b)$$

$$\left(\frac{PR}{t_w f_y} \right)^2 \leq 1 - \hat{\alpha} \quad (3.3.5c)$$

$$\left(\frac{\frac{P}{p_{stat}} p_{stat} R}{t_w f_y} \right)^2 \leq 1 - \hat{\alpha} \quad (3.3.5d)$$

Now, using equation 3.3.3, the inequality 3.3.5d becomes:

$$\left[\frac{\left(\frac{P}{p_{stat}} \right)}{SF} \right]^2 \leq 1 - \hat{\alpha} \quad (3.3.5e)$$

Solving for SF:

$$SF \geq \frac{1}{\sqrt{1 - \hat{\alpha}}} \frac{P}{p_{stat}} \quad (3.3.5f)$$

For example, assuming a knockdown factor $\hat{\alpha} = 0,2$ (M.A. Haroun), inequality 3.3.5f becomes:

$$SF \geq 1,12 \frac{P}{p_{stat}} \quad (3.3.5g)$$

So, for a reduction factor that fulfills condition 3.3.5f one can use equation 3.3.2 to design the thickness. However, it should be noted that using this procedure does not guarantee a safe design, but it ensures that elastic-plastic buckling is controlled especially at higher earthquake accelerations.

Graphically, the procedure involves entering the graph of Figure 3.2.4.1 with the circumferential stress and select the first curve whose point of maximum is to the left of the input data. For example, for an input circumferential stress of 75 MPa, the optimal thickness according to this procedure is $t=0.003R$, as shown in Figure 3.1.1.

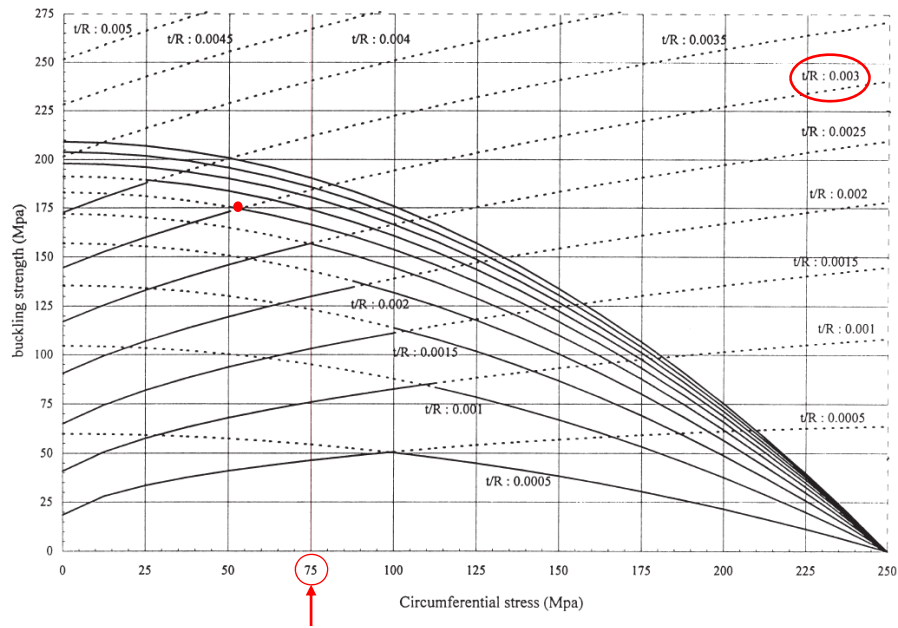


Fig. 3.3.1: Graphical method to select the optimal thickness.

P/p_{stat} is the total to hydrostatic pressure ratio, evaluated at the tank base:

$$\frac{P}{p_{stat}} = \frac{p_{stat} + p}{p_{stat}} = 1 + \frac{p}{\rho H} \tag{3.3.6}$$

where p is the hydrodynamic pressure, including the impulsive component due to horizontal excitation (the convective one may be neglected) and the pressure component due to vertical excitation. These two pressure components are combined with the SRSS rule:

$$p = \sqrt{p_i^2 + p_v^2} \tag{3.3.7}$$

A very fast and efficient way to evaluate the impulsive pressure for flexible tank is suggested by Haroun in [20]:

$$p_i = q_0 \rho H A_i \frac{a_g}{g} \tag{3.3.8}$$

where A_i is the normalized design spectral acceleration corresponding to the impulsive fundamental period T_i , a_g is the horizontal PGA and the coefficient q_0 is plotted in Figure 3.3.1 versus the height to radius ratio. From this graph it is immediate to note how much influence the slenderness parameter H/R has on the hydrodynamic pressure. In fact, for slender tanks hydrodynamic pressures are quite low, while for broad tanks they assume higher values.

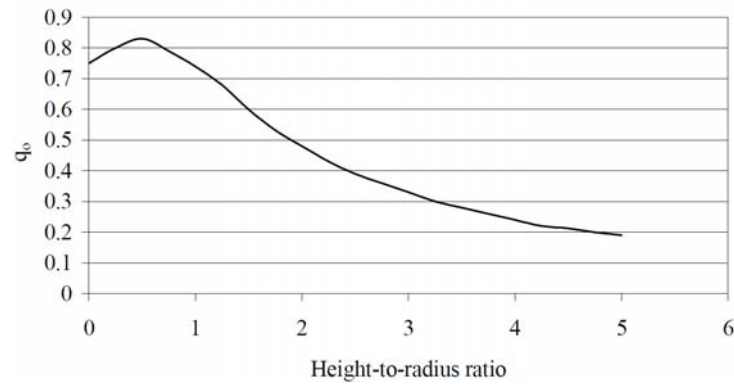


Fig. 3.3.1: Pressure coefficient q_0 (after [20]).

Regardless the pressure component due to vertical excitation, according to Haroun it can be evaluated from:

$$p_v = \rho H A_{vf} \frac{a_{vg}}{g} \quad (3.3.8)$$

where A_{vf} is the normalized design spectral acceleration corresponding to the vertical fundamental period T_v and a_{vg} is the vertical PGA.

For example, assuming that the vertical PGA is half of the horizontal one ($a_{vg}=0.5a_g$), the ratio p/p_{stat} of equation 3.3.6 becomes:

$$\frac{P}{p_{stat}} = 1 + \frac{a_g}{g} \sqrt{(q_0 A_i)^2 + (0,5A_{vf})^2} \quad (3.3.9)$$

3.4 Concluding remarks and possible enhancements

Review of API 650, ECCS and EC8 provisions revealed that Eurocode 8 offers the most thorough discussion of the buckling problem because the two main buckling modes (elastic and elastic-plastic) are differentiated and treated explicitly. Formulas to calculate the maximum vertical membrane stresses f_{mb} and f_{pb} are given for the two cases. On the other side, in API 650, verifications are only performed separately in the two directions, vertical and circumferential and it is possible to demonstrate that the two buckling modes are in someway hidden behind this verifications. However, the API approach, even if it is the easiest to apply, it is very rough; in fact, it specifies limits for uni-directional stress states depending on the value of a discriminant term strictly connected to the internal pressure. But actually the elastic-plastic collapse is due to a bi-axial stress state. On the contrary, the European standards also consider the bi-axial stress state at the base of the tank walls; here, the interaction between vertical and hoop stresses is

explicitly reported in the equations. For these reason a possible enhancement of API 650 could be, for example, the adoption of the proven Rotter's formula (equation 3.1.2.2) for elastic-plastic buckling to minimize the occurrence of such damage in future seismic events.

In the present thesis methods for “elephant's foot” mitigation are suggested, taking a cue from Haroun et al., [7]-[20]; because these methods involve quite innovative techniques that still need further developments, there is the need to carry out more specific tests on them and to set up more refined models.

Regardless elastic buckling, ECCS gives a very detailed method to calculate the critical stress and Eurocode 8 offers an extended version of that method. The most important difference between the two is that in ECCS provisions the effect of the type of loading, internal pressure and shell imperfections are all included in the “experimental” knockdown factors, while in EC8 the empirical formulation for the knockdown factor takes into account only shell imperfections. The effect of internal pressure and of bending are taken into account through other terms. Also in this case API standard are the most approximate. In fact, it accounts for the effects of internal pressure and imperfections, while ignoring the effects of bending, namely the API critical axial load is based on investigations of uniformly loaded tanks. So, a first possible step in the right direction for API 650 could be the adoption of the ECCS method, less expensive than the EC8 one from a computational point of view. However, it is necessary to have high values of vertical compression forces, associated with low values of hoop forces induced by hydrostatic and hydrodynamic pressures, to reach the elastic buckling failure mode . This situation is very rare, so that the most common failure mode is the elastic-plastic collapse.

Finally, both API 650 and Eurocode 8 do not mention the secondary buckling effect which may develop at the top part of the tank. But it must be said that, at present, any analytical formula for this type of elastic buckling exists. As shown in Section 3.1.3, this failure mode should be of great interest to the designers because it appears at not so high PGA values. However, is not yet completely clear the influence of the tank geometry and of the temporal characteristics of the base excitation on the critical PGA. Due to these reasons, there is the need to give a deeper insight into the phenomenon with the aim of finding an analytical expression for the buckling load and of generalizing the problem from a “response spectrum viewpoint”, much more useful than results coming from time-history analyses for design purposes. A first attempt to evaluate analytically the buckling strength for this buckling mode can be made using the EC3 part 1-6 provisions, provided that it is found and validated a method to convert the cosine-distributed earthquake-induced hydrodynamic pressure into an equivalent axisymmetric one.

PART II

**NUMERICAL MODELING AND
DYNAMIC ANALYSES OF A
CLAMPED STEEL TANK**

Finite element model

4.1 Tank model

4.1.1 Geometry, material and boundary conditions

In order to investigate the nonlinear dynamic behavior of steel tanks anchored to the foundation a finite element model is set up. The geometric characteristics of the tank under investigation are shown in Figure 4.1.1.1. Experience from past earthquakes has shown that tanks that are completely filled with liquid are more prone to suffer damage, Virella [52], thus this study considers a liquid level of 90% of the height of the tank with a 10% freeboard. The contained liquid is drinking water ($\rho=1000 \text{ Kg/m}^3$). In accordance with [52] the tapered thickness for the tank considered was designed for this study using the API 650 provisions for serviceability conditions. No seismic design considerations were taken into account. The tank is initially assumed without a roof structure. The total mass of the cylinder is 83 tons. Since a fully base anchorage is considered and our primary interest is in the buckling of the cylinder shell, the model has clamped conditions at the base.

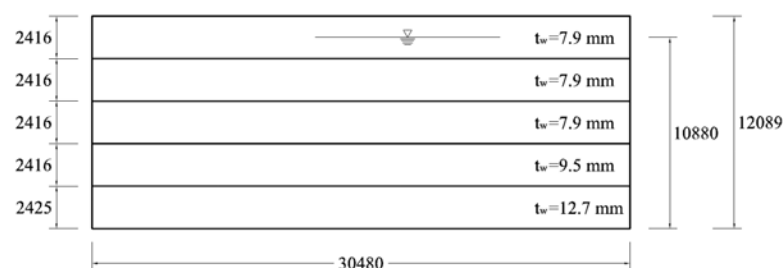


Fig. 4.1.1.1: Geometric characteristics of the tank (in millimeters), $H/D=0.40$.

As regard the tank material, steel S 275 is assumed, with the following mechanical properties:

- Mass density 7850 Kg/m^3
- Yield strength 275 MPa
- Ultimate strength 430 MPa

- Elastic modulus 210000 MPa
- Poisson's ratio 0,30
- Strain hardening modulus 3888 MPa

The finite element analysis package ABAQUS, [23]-[24]-[25], was used to carry out all the computations. Figure 4.1.1.2 shows the model in ABAQUS. The model was prepared by using an input file, created in MATLAB and then imported and run in ABAQUS. Several input files were created for different purposes (see Appendices C and D).

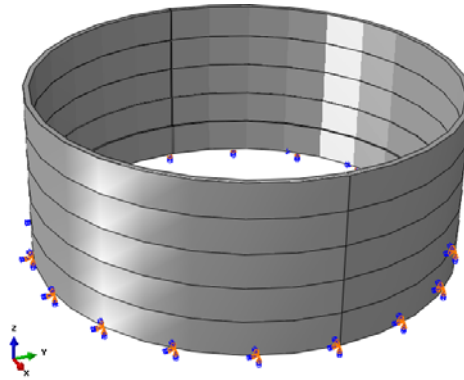


Fig. 4.1.1.2: Tank model, from ABAQUS.

4.1.2 Mesh details

Since the objective here is to find a mesh capable of correctly reproducing the behavior of the structure especially in the nonlinear field, only material nonlinearities are considered. Geometric nonlinearities can be neglected for this special purpose. The structure is pushed into the nonlinear range through the application of the impulsive pressure only, derived considering the tank as rigid. Any vertical acceleration is considered. According to Veletsos at al. [48], the impulsive pressure due to horizontal excitation can be written as:

$$p_i(\zeta, \vartheta, t) = c_i(\zeta)\ddot{x}_g(t)\rho R \cos \vartheta \quad (4.1.2.1)$$

where $\ddot{x}_g(t)$ is the ground-acceleration time history. In expression (4.1.2.1) the function $c_i(\zeta)$ describes the variation along the tank's height and may be determined as follows:

$$c_i(\zeta) = 1 - \sum_{n=1}^{\infty} c_{cn}(\zeta) \quad (4.1.2.2)$$

where $c_{cn}(\zeta)$ are the coefficients describing the axial variation of the n^{th} convective component:

$$c_{cn}(\zeta) = \frac{2}{\lambda_n^2 - 1} \frac{\cosh(\lambda_n H/R \zeta)}{\cosh(\lambda_n H/R)} \quad (4.1.2.3)$$

λ_n stands for the n^{th} root of the first derivative of the Bessel function of the first kind and first order. The first three of these roots are: $\lambda_1=1.841$, $\lambda_2=5.311$, $\lambda_3=8.536$. For the broad tank under investigation, $H=10.88$ m and $R=15.24$ m. Note that in the expressions given by Veletsos H is intended to be the height of the stored liquid. So:

$$c_{c1}(\zeta) = 0,4154 \cdot \cosh(1,841 z/15,24) \quad (4.1.2.4a)$$

$$c_{c2}(\zeta) = 0,0032 \cdot \cosh(5,311 z/15,24) \quad (4.1.2.4b)$$

$$c_{c3}(\zeta) = 0,0001 \cdot \cosh(8,536 z/15,24) \quad (4.1.2.4c)$$

The second and third convective component give a very low contribution, so they can be neglected and:

$$c_i(z) = 1 - \sum_{n=1}^{\infty} c_{cn}(z) \cong 1 - c_{c1}(z) = 1 - 0,42 \cdot \cosh(1,841 z/15,24) \quad (4.1.2.5)$$

Finally, the ground-acceleration time history of equation 4.1.2.1 is replaced by the peak ground acceleration, in units of g . So, equation 4.1.2.1 takes the form

$$p_i(\zeta, \vartheta, t) = PGA \cdot g \cdot \rho R \cos \vartheta \cdot [1 - 0,42 \cdot \cosh(1,841 z/15,24)] \quad (4.1.2.6)$$

and the analysis is carried out for linearly increasing values of the PGA, from $0g$ to $1.5g$. Obviously, in addition to the earthquake induced pressure, also the hydrostatic pressure and the self-weight of the tank are included in the model.

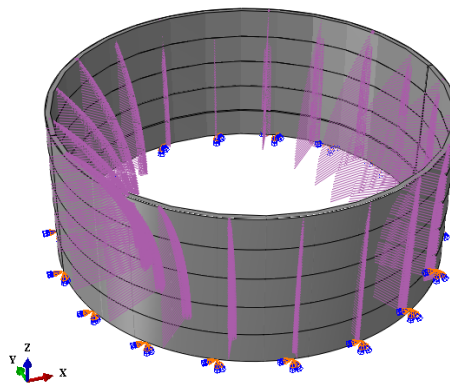


Fig. 4.1.2.1: Tank model loaded by the impulsive pressure, from ABAQUS.

The ABAQUS shell element library provides elements that allow the modeling of curved, intersecting shells that can exhibit nonlinear material response and undergo large overall motions (translations and rotations). The library is divided into three categories consisting of general-

purpose, thin, and thick shell elements. Thin shell elements provide solutions to shell problems that are adequately described by classical (Kirchhoff) shell theory, thick shell elements yield solutions for structures that are best modeled by shear flexible (Mindlin) shell theory, and general-purpose shell elements can provide solutions to both thin and thick shell problems. All shell elements use bending strain measures that are approximations to those of Koiter-Sanders shell theory (Budiansky and Sanders, 1963). For the present case the general-purpose shell elements are considered the best choice, since they are available both in ABAQUS/Standard and in ABAQUS/Explicit. The general-purpose elements provide robust and accurate solutions in all loading conditions for thin and thick shell problems. Thickness change as a function of in-plane deformation is allowed in their formulation. They do not suffer from transverse shear locking, nor do they have any unconstrained hourglass modes. With the exception of the small-strain elements S4RS, S3RS and S4RSW, all of these elements consider finite membrane strains. No hourglass control is required for the axisymmetric general-purpose shells, nor in the bending and membrane response of the fully integrated element S4. The membrane kinematics of S4 are based on an assumed-strain formulation that provides accurate solutions for in-plane bending behavior.

In geometrically nonlinear analyses in ABAQUS/Standard the cross-section thickness of finite-strain shell elements changes as a function of the membrane strain based on a user-defined “effective section Poisson’s ratio,” . In ABAQUS/Explicit the thickness change is based on the “effective section Poisson’s ratio” for all shell elements in large-deformation analyses, unless the user has specified that the thickness change should be based on the element material definition.

In order to choose a good finite element mesh, a first analysis is performed using quadrilateral shell elements S8R, Figure 4.1.2.2a. The S8R is an eight-node, doubly curved shell element with reduced integration, characterized by quadratic shape functions. The element size is the smallest as possible with such elements, so that the solution of this analysis may be considered as the reference solution in terms of accuracy. Then, several analysis using linear element S4R (Figure 4.1.2.2b) are carried out in order to find the element size that allow to approach the reference solution. The S4R is a four-node, doubly curved shell element with reduced integration, hourglass control and finite membrane strain formulation. The objective is to reach a good compromise between computational efficiency, time saving and results accuracy.

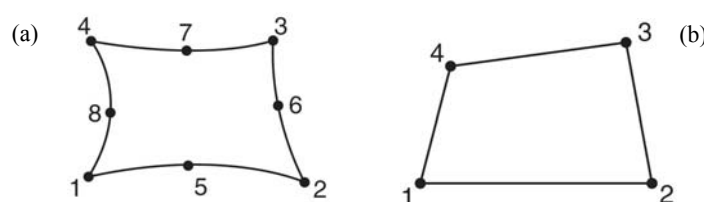


Fig. 4.1.2.2: (a) Eight-node element S8R, (b) Four-node element S4R.

For each analysis the results are presented in terms of equivalent plastic strains and Von Mises stresses, at different load level. Since ABAQUS gives the possibility to subdivide the analysis into steps and the steps into increments, from the step time it is possible to go back to the value of the PGA(g), knowing how the PGA(g) grows during the step. For the current case only one step of the duration of one is used. The self weight and hydrostatic pressure are kept constant during the step. Conversely, the PGA(g), and so the impulsive pressure, grows linearly during the step, from 0 at the step time $t=0$ to 1.5 at the step time $t=1$, Figure 4.1.2.3.

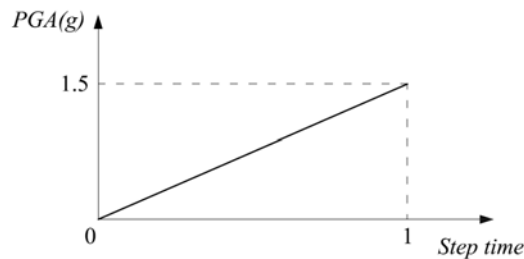


Fig. 4.1.2.3: Variation of the impulsive pressure during the analysis step, $PGA(g)=1.5 \cdot \text{Step time}$.

- **Analysis 1: Esize:600 - Elements S8R (reference solution)**

The first plasticization is at an height of 2720 millimeters from the tank base, at the step time 0.72, for a value of the PGA=1.08g.

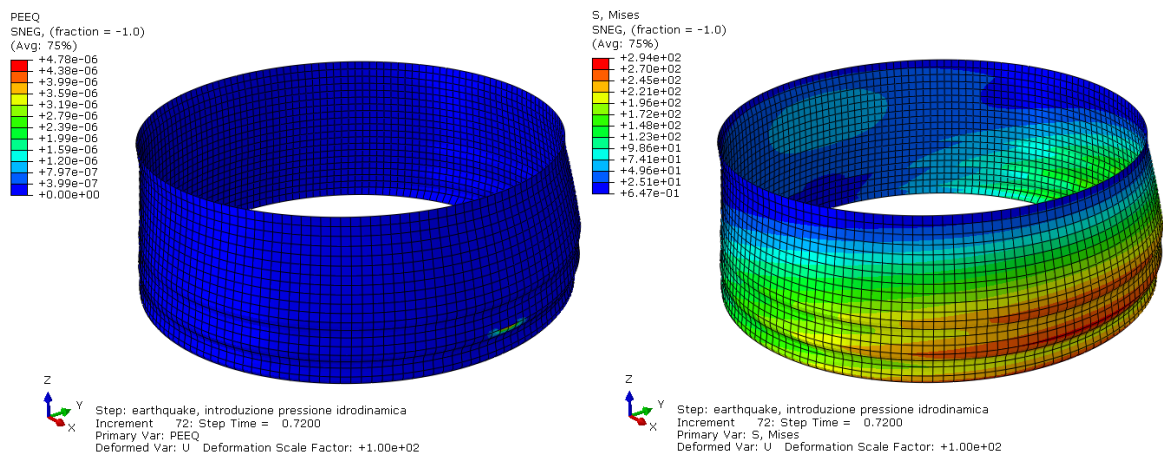


Fig. 4.1.2.4: Equivalent plastic strains and Von Mises stresses for PGA=1.08g.

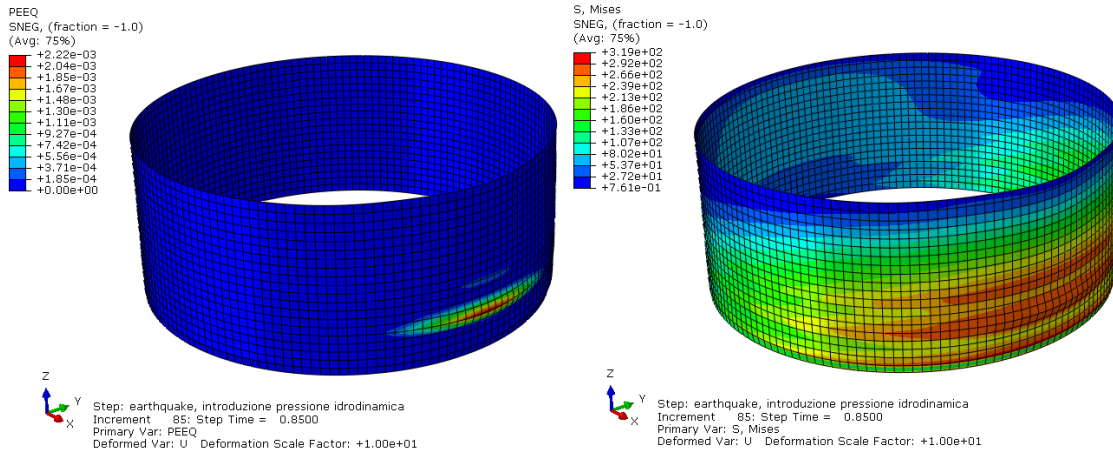


Fig. 4.1.2.5: Equivalent plastic strains and Von Mises stresses for $PGA=1.275g$.

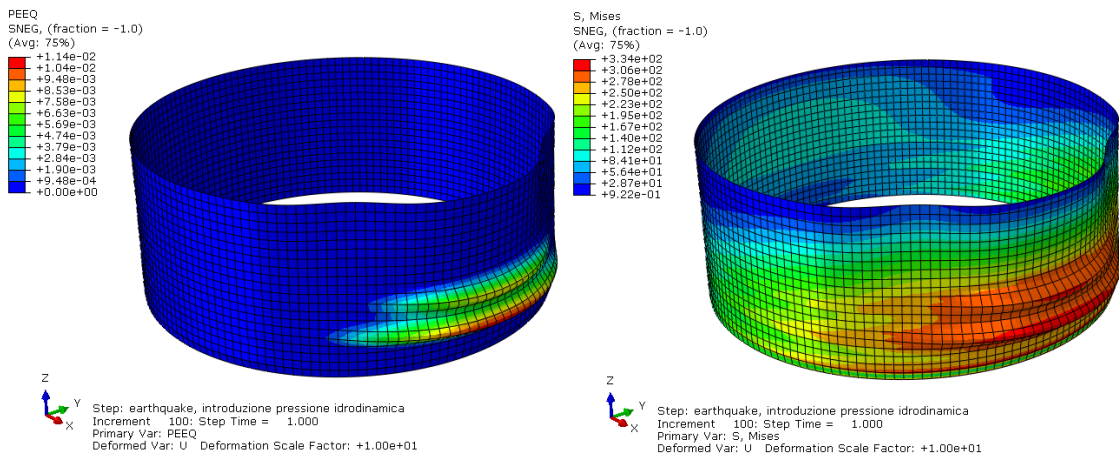


Fig. 4.1.2.6: Equivalent plastic strains and Von Mises stresses for $PGA=1.5g$.

- **Analysis 2: Esize:600 - Elements S4R**

The first plasticization is at an height of 600 millimeters from the tank base, at the step time 0.66, for a value of the $PGA=0.99g$.

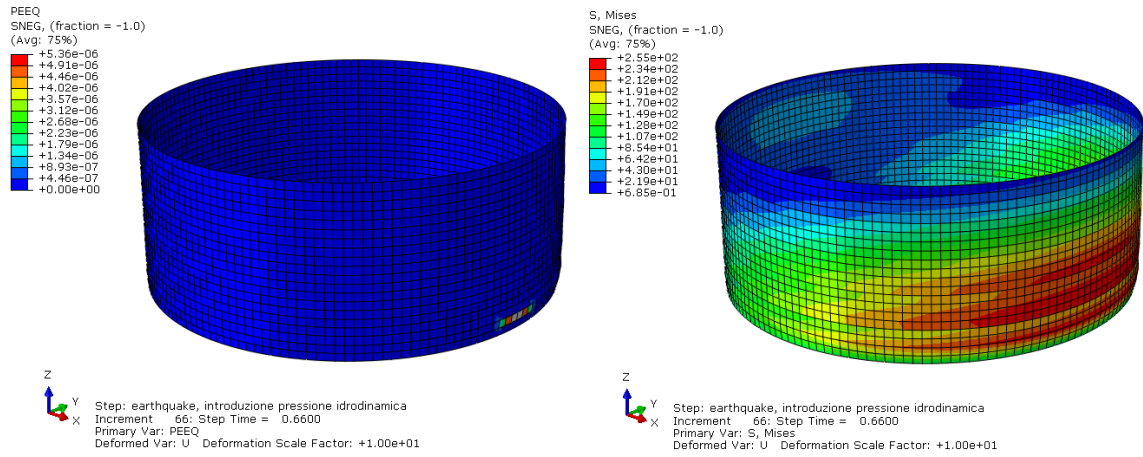


Fig. 4.1.2.7: Equivalent plastic strains and Von Mises stresses for $PGA=0.99g$.

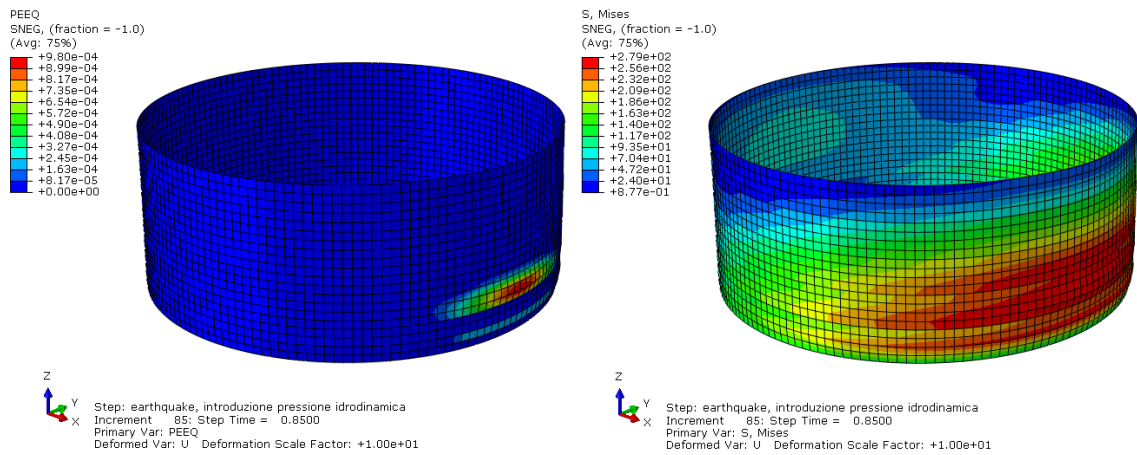


Fig. 4.1.2.8: Equivalent plastic strains and Von Mises stresses for $PGA=1.275g$.

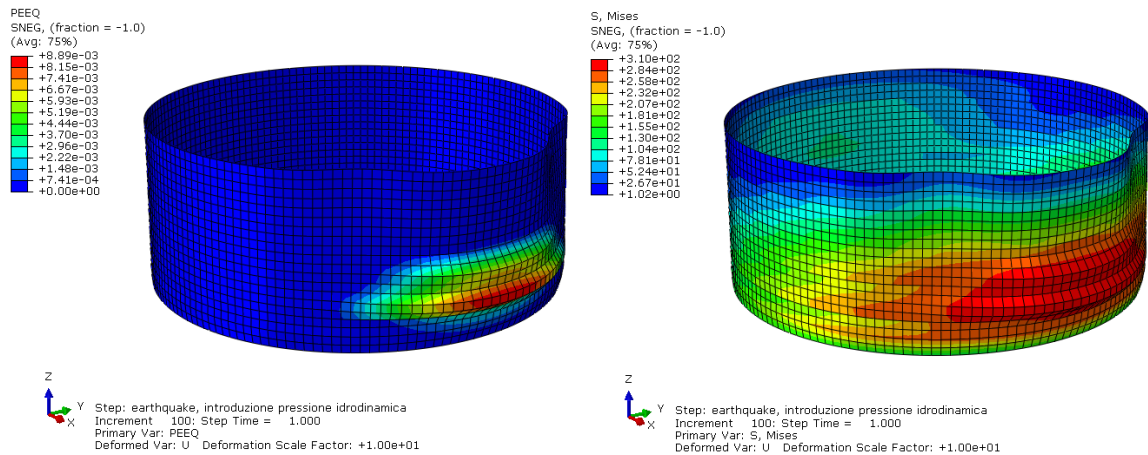


Fig. 4.1.2.9: Equivalent plastic strains and Von Mises stresses for $PGA=1.5g$.

• **Analysis 3: Esize:500 - Elements S4R**

The first plasticization is at an height of 2819 millimeters from the tank base, at the step time 0.73, for a value of the PGA=1.095g.

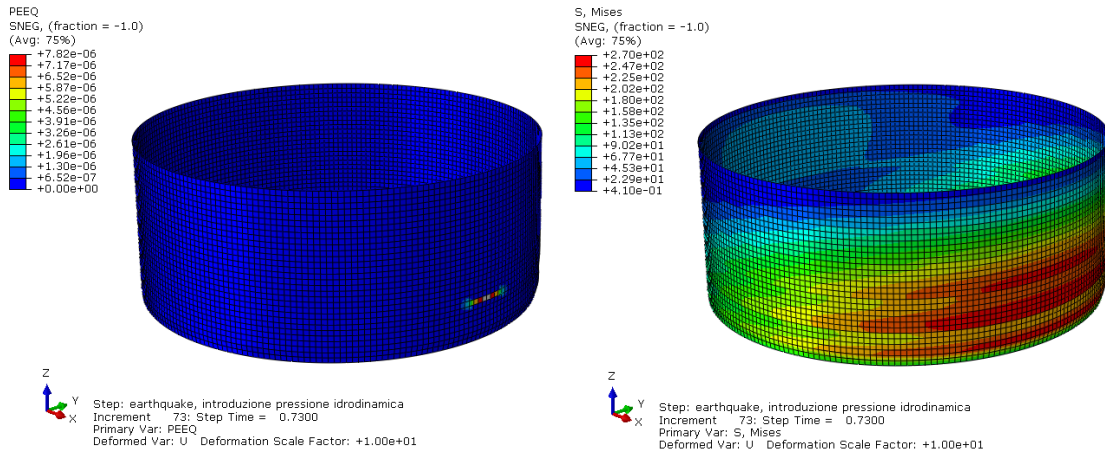


Fig. 4.1.2.10: Equivalent plastic strains and Von Mises stresses for PGA=1.095g.

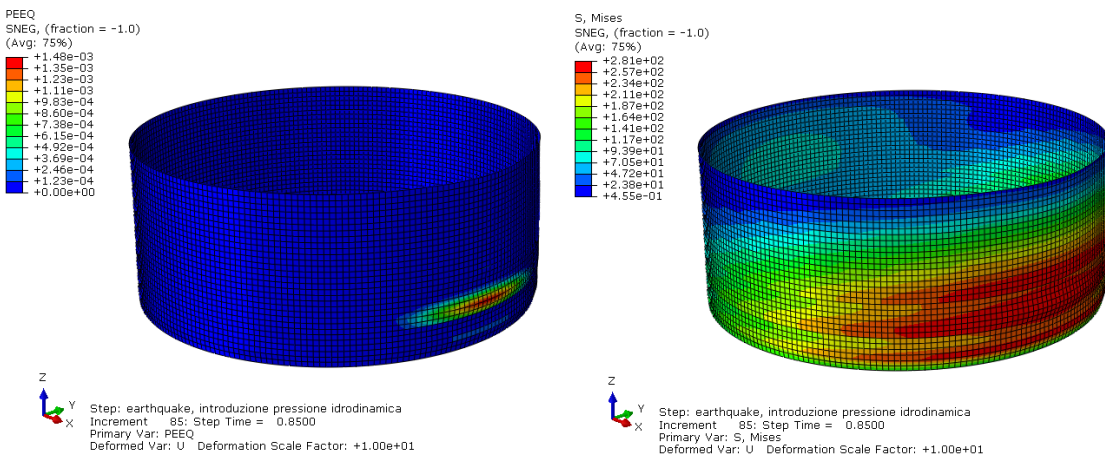


Fig. 4.1.2.11: Equivalent plastic strains and Von Mises stresses for PGA=1.275g.

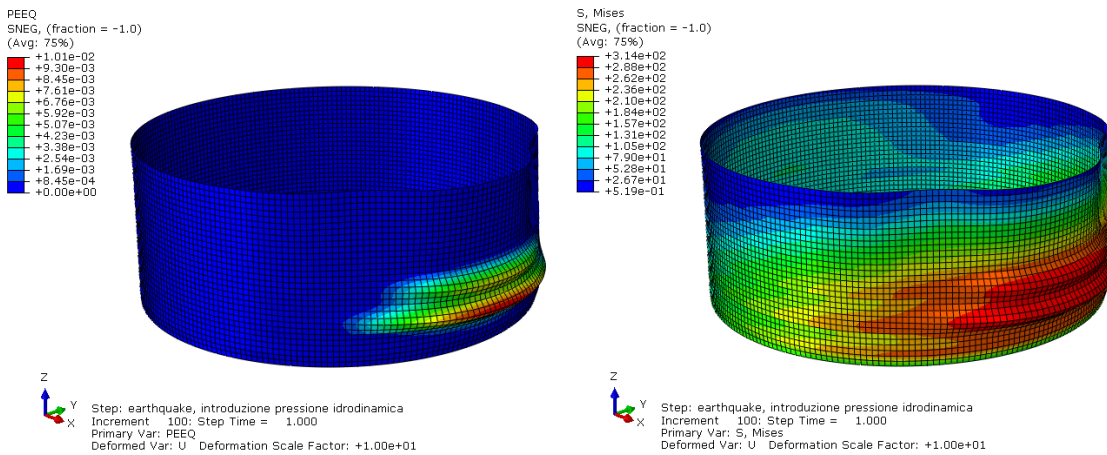


Fig. 4.1.2.12: Equivalent plastic strains and Von Mises stresses for PGA=1.5g.

As expected, if we maintain the same element size and we just switch from quadratic to linear elements, the results are quite different. This is what happens in the analysis two, where the region of the first yielding does not coincide with that of analysis one, which is assumed to be the reference solution. So, if we want to use linear elements it is necessary to further refine the mesh. Assuming an element size of 500 millimeters in the third analysis, the results show a good agreement with those of reference. The region of the first yielding and the PGA that produce it are more or less the same and the Von Mises stresses at the different step times differ only by a 6-12%. So, the results of analysis three are considered acceptable to study the nonlinear response of the structure, even if in a design process they must not be take in their absolute value but they must be always compared to the values given by the codes. The great advantage of using linear elements S4R is to obtain a solution in a smaller time than the time required by quadratic elements S8R. In fact, analysis three converges in a time equal to half of analysis one. The details of the final mesh adopted are:

- Element type: S4R
- Element size: 500 mm
- Total number of elements: 7080
- Total number of nodes: 7316

4.2 Liquid model

4.2.1 The added mass model

In the present work the dynamic interaction between the fluid and the structure is modeled using the “added mass method”. As already mentioned in Section 1.3.3 this method is particularly correct for broad tank ($H/D < 0.5$). The added mass model is obtained from a pressure distribution for the impulsive mode of the tank-liquid system, with a cosine distribution around the tank cylinder. The convective component is neglected. The impulsive pressure distribution is obtained from the horizontal rigid body motion of a rigid tank-liquid system [48], and is described as

$$p_i(\zeta, \vartheta, t) = c_i(\zeta)\ddot{x}_g(t)\rho R \cos \vartheta \quad (4.2.1.1)$$

where $\ddot{x}_g(t)$ is the ground-acceleration time history and the function $c_i(\zeta)$ describes the variation along the tank’s height and may be determined as explained in Section 4.1.2.

The liquid mass added to the tank shell is calculated from the pressure distribution in equation 4.2.1.1. In particular, the lumped mass at each node of the finite element mesh is

computed using the tributary area and dividing by the reference normal acceleration $a_n = \ddot{x}_g(t) \cos \vartheta$. For interior nodes, the expression of the lumped mass becomes

$$m_i = \frac{p_i Esize^2}{a_n} = c_i(\zeta) \cdot \rho R \cdot Esize^2 \tag{4.2.1.2}$$

For the nodes at the liquid surface and at the tank bottom, the expression of the lumped mass becomes

$$m_i = \frac{p_i Esize^2}{2 a_n} = \frac{1}{2} c_i(\zeta) \cdot \rho R \cdot Esize^2 \tag{4.2.1.3}$$

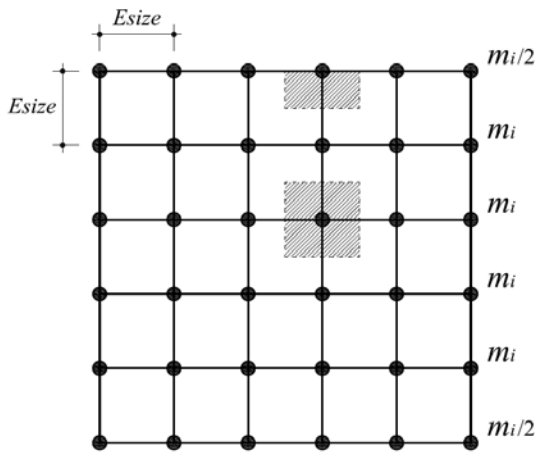


Fig. 4.2.1.1: Added masses attached to the nodes of the finite element mesh, and their tributary area.

It is immediate to note that the added mass have the same vertical variation as the impulsive pressure distribution from which they are derived, and they have a uniform distribution around the circumference.

Because the added mass is the liquid mass that moves together with the tank, it acts normal to the cylindrical shell, and so it must be implemented in the model in such a way that it only add inertia in the radial direction. To do this in ABAQUS, a particular class of connector elements is used, named MPC type LINK. This type of elements provides a pinned rigid link between two nodes to keep the distance between the nodes constant, as shown in Figure 4.2.1.2. The displacements of the first node are modified to enforce this constraint. The rotations at the nodes, if they exist, are not involved in this constraint. In practice, they work exactly like truss elements, with the great advantage from a computational point of view that they do not have mass and they are not deformable. Finally, these links must be constrained in the vertical and tangential direction by means of simple support constraints oriented in those directions, as shown in Figure 4.2.1.4.

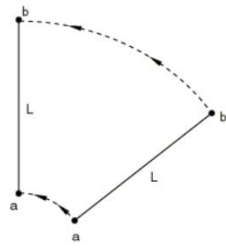


Fig. 4.2.1.2: Multi Point Constraint type LINK.

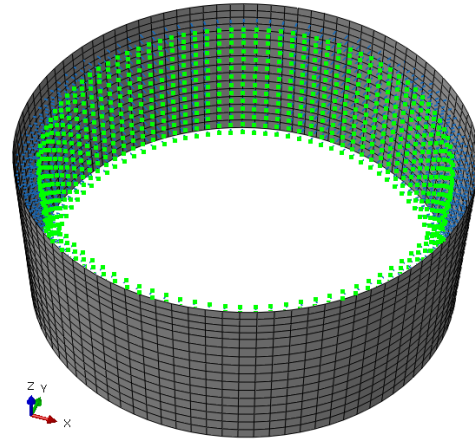


Fig. 4.2.1.3: Finite element model with added masses attached to the shell nodes by means of MPC type LINK elements.

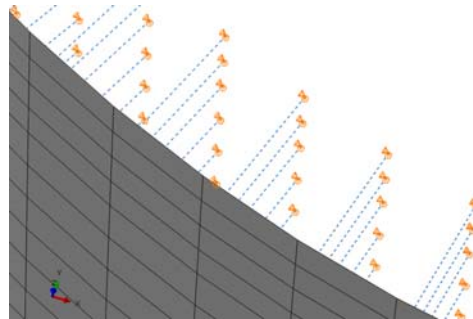
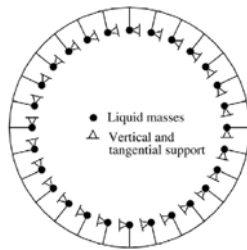


Fig. 4.2.1.4: Model with added mass constrained around the circumference.

4.2.2 Added mass calculation

The calculation of the added masses is performed in MATLAB, for all the code details see Appendix B. For an element size of 500 mm the distribution of the added masses along a meridian line is shown in Figure 4.2.2.1.

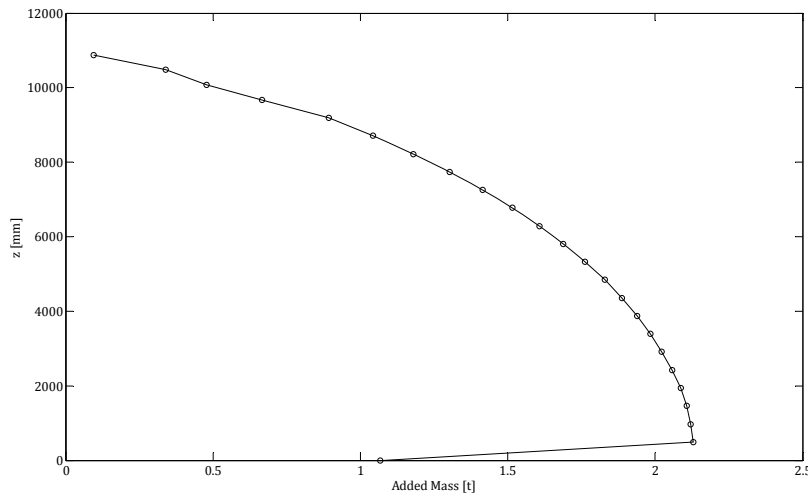


Fig. 4.2.2.1: Added mass along a meridian line.

The total added mass along a meridian line is $m_{mer}=35,21$ t. The total added mass of the model is 6725 t. The impulsive mass excited by horizontal excitation can be computed as the mass free to move in the horizontal direction. To compute such a quantity the added mass must be projected in the horizontal direction. Since the mass is derived from the impulsive pressure, it follows the same distribution. So, the horizontal component of the mass has a circumferential variation of the form

$$m_h = m \cos \vartheta \tag{4.2.2.1}$$

where $m=m_{mer}\cos\vartheta$. In terms of pressures it is equivalent to say that the horizontal component of the pressure P_h can be expressed as

$$P_h = P \cos \vartheta \tag{4.2.2.2}$$

where $P=P_{max}\cos\vartheta$ and P_{max} is the pressure at $\vartheta=0$, Figure 4.2.2.2.

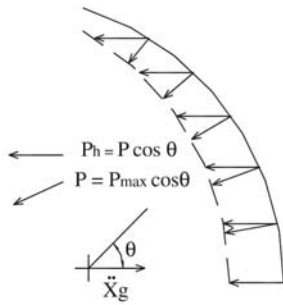


Fig. 4.2.2.2: Pressure component in the direction of the excitation.

The expression for the total impulsive mass that considers the pressure in the direction of the excitation, along with the cosine distribution of the pressure along the tank circumference is

$$M_i = 4R \int_0^{\pi/2} m_h d\vartheta \tag{4.2.2.3}$$

Substituting expression 4.2.2.1 into expression 4.2.2.3 and integrating

$$M_i = 4Rm_{mer} \int_0^{\pi/2} \cos^2 \vartheta d\vartheta = \pi Rm_{mer} \tag{4.2.2.4}$$

Note that in equation 4.2.2.4 m_{mer} must be expressed in mass per unit length. So, for the tank under investigation, m_{mer} is obtained as the sum of the added masses distributed along a meridian line, each one divided by the element size. The results is

$$m_{mer} = 0,0683 [t/mm] \tag{4.2.2.5}$$

and so

$$M_i = \pi Rm_{mer} = \pi \cdot 15240 \cdot 0,0683 = 3270 [t] \tag{4.2.2.6}$$

Finally, the so called impulsive mass ratio can be defined as

$$M_{ir} = \frac{M_i}{m} \quad (4.2.2.7)$$

where m is the total mass of the stored liquid. For the present case, equation 4.2.2.7 results as

$$M_{ir} = \frac{3270}{7939} = 0,42 \quad (4.2.2.8)$$

The impulsive mass ratio of equation 4.2.2.8 can be compared with the impulsive mass ratio calculated according to the formula proposed by Housner (1963) in [26]:

$$M_{ir} = \frac{\tanh\left(1,7 \frac{R}{H}\right)}{1,7 \frac{R}{H}} \quad (4.2.2.9)$$

For the present case,

$$M_{ir} = \frac{\tanh\left(1,7 \frac{15240}{10880}\right)}{1,7 \frac{15240}{10880}} = 0,41 \quad (4.2.2.10)$$

Since the impulsive mass ratio calculated according to equation 4.2.2.7 shows good agreement with the one proposed by Housner, it is possible to conclude that the added mass model represents correctly the dynamic behavior of the tank-liquid system.

4.3 Systems nonlinearities

4.3.1 Material nonlinearity

The first source of nonlinearity is the material nonlinearity. For the present case, steel with an elasto-hardening behavior is considered, as already mentioned in Section 4.1.1. ABAQUS offers several models for metal plasticity analysis. The main options are a choice between rate-independent and rate-dependent plasticity, a choice between the Mises yield surface for isotropic materials and Hill's yield surface for anisotropic materials, and for rate-independent modeling a choice between isotropic and kinematic hardening. For the present case rate-independent plasticity is used and isotropic hardening is select. Rate-independent plasticity is used mostly in modeling the response of metals and some other materials at low temperature (typically below half the melting temperature on an absolute scale) and low strain rates. The rate-independent

metal plasticity model uses associated flow. Isotropic hardening means that the yield function is written as

$$f(\sigma) = \sigma^0(\varepsilon^{pl}, T) \quad (4.3.1.1)$$

where σ^0 is the equivalent (uniaxial) stress, ε^{pl} is the work equivalent plastic strain, defined by

$$\sigma^0 \varepsilon^{pl} = \boldsymbol{\sigma}^0 : \boldsymbol{\varepsilon}^{pl} \quad (4.3.1.2)$$

and T is the temperature. Isotropic hardening is generally considered to be a suitable model for problems in which the plastic straining goes well beyond the incipient yield state where the Bauschinger effect is noticeable. Therefore, this hardening theory is used for such applications as dynamic problems involving finite strains and manufacturing processes, any process involving large plastic strain and in which the plastic strain does not continuously reverse direction sharply.

4.3.2 Geometric nonlinearity

The second source of nonlinearity is related to changes in the geometry of the structure during the analysis. Geometric nonlinearity occurs whenever the magnitude of the displacements affects the response of the structure. This may be caused by:

- Large deflections or rotations.
- “Snap through.”
- Initial stresses or load stiffening.

ABAQUS/Standard defaults to small displacement geometry, while ABAQUS/Explicit defaults to nonlinear geometry. This can be overridden in the initial step or any subsequent step using the command *STEP, NLGEOM=ON or OFF, except that once *STEP, NLGEOM=ON has been issued, it cannot be turned back off for the rest of the analysis. In a small-displacement analysis, geometric nonlinearity is ignored in the element calculation, i.e. the kinematic relationships are linearized. This means that the element stiffness matrices are formulated using the initial geometry of the elements, while in a geometrically nonlinear analysis, they are formulated using the geometry in the most recently completed increment.

Almost all FE codes, including ABAQUS, use the stiffness (also called the displacement) method of solution, in which the equation $\mathbf{K}\mathbf{u} = \mathbf{f}$ is solved for \mathbf{u} . Thus, the fundamental FE solution is nodal displacements; strains and stresses are calculated from these displacements. Strain is calculated using the matrix \mathbf{B} of shape function relationships between strain and the

nodal displacements: $\boldsymbol{\varepsilon} = \mathbf{B}\mathbf{u}^{\text{elem}}$. Stress is then calculated from strain using the constitutive equation. When nonlinear geometry is turned on the stiffness matrix of the system becomes

$$\mathbf{K}_T = \mathbf{K} + \mathbf{K}_G \quad (4.3.2.1)$$

where \mathbf{K} is the usual stiffness matrix but formulated with respect to the current configuration and \mathbf{K}_G is the geometric or stress stiffness matrix.

$$\mathbf{K} = \sum_{j=1}^N \mathbf{K}_e^j = \sum_{j=1}^N \int_{V_e^j} \mathbf{B}_t^T \mathbf{D}_t \mathbf{B}_t dV \quad (4.3.2.2a)$$

$$\mathbf{K}_G = \sum_{j=1}^N (\mathbf{K}_G)_e^j = \sum_{j=1}^N \int_{V_e^j} \mathbf{G}_t^T \boldsymbol{\sigma}_t \mathbf{G}_t dV \quad (4.3.2.2b)$$

where:

N = total number of elements in the FE model;

V_e^j = domain for element j ;

\mathbf{B}_t = strain-displacement matrix with respect to the current configuration;

\mathbf{D}_t = stress-strain matrix with respect to the current configuration;

$\boldsymbol{\sigma}_t$ = current Cauchy stress matrix in the global coordinate system;

\mathbf{G}_t = derivative matrix of the shape functions.

Dynamic analyses

5.1 Modal analysis

5.1.1 Effect of pre-stress states on the impulsive modes of vibration

Prior to the nonlinear time-history analyses, the dynamic properties of the structure are investigated by means of a modal analysis. In Section 5.1.2 the significant mode shapes and natural periods with respect to horizontal motion for the added mass model of the broad tank are computed. In this Section the influence of hydrostatic pressure and self weight loads (pre-stress state) on the natural periods and mode shapes of the broad tank is studied.

In ABAQUS, a frequency extraction analysis is performed using the Lanczos solver. The frequency extraction procedure:

- performs eigenvalue extraction to calculate the natural frequencies and the corresponding mode shapes of a system;
- will include initial stress and load stiffness effects due to preloads and initial conditions if geometric nonlinearity is accounted for in the base state, so that small vibrations of a preloaded structure can be modeled;
- is a linear perturbation procedure. It means that the response is a linear perturbation response about a base state. The base state is the current state of the model at the end of the last general analysis step prior to the linear perturbation step. If the first step of the analysis is a perturbation step, the base state is determined from the initial conditions.

The eigenvalue problem for the natural frequencies of an undamped finite element model is

$$(-\omega^2 \mathbf{M} + \mathbf{K})\boldsymbol{\phi} = \mathbf{0} \quad (5.1.1.1)$$

where \mathbf{M} is the mass matrix (which is symmetric and positive definite), \mathbf{K} is the stiffness matrix (which includes initial stiffness effects if the base state included the effects of nonlinear geometry) and $\boldsymbol{\phi}$ is the modal matrix (the matrix containing the eigenvectors).

The first thirty natural periods and mode shapes of the tank-liquid system are determined by neglecting and including the pre-stress state caused by the hydrostatic pressure and the self-weight of the tank. In Table 5.1.1.1 only the odd natural periods are listed because, due to the symmetry of the structure, duplicated natural periods are obtained. Therefore, the second mode is the same as the first and the fourth the same as the third, ad so forth.

Mode	PRE-STRESS INCLUDED			PRE-STRESS NEGLECTED		
	T [s]	n	m	T [s]	n	m
1	0.964	8	1	2.744	14	1
3	0.962	9	1	2.703	15	1
5	0.930	10	1	2.694	13	1
7	0.921	7	1	2.599	16	1
9	0.887	11	1	2.542	12	1
11	0.839	12	1	2.464	17	1
13	0.827	6	1	2.324	18	1
15	0.793	13	1	2.307	11	1
17	0.750	14	1	2.190	19	1
19	0.710	15	1	2.068	20	1
21	0.693	5	1	2.023	10	1
23	0.673	16	1	1.956	21	1
25	0.639	17	1	1.850	22	1
27	0.607	18	1	1.749	23	1
29	0.577	19	1	1.723	9	1

Table 5.1.1.1: Natural periods including and neglecting the pre-stress state. *n* and *m* indicate the number of circumferential and axial waves, respectively.

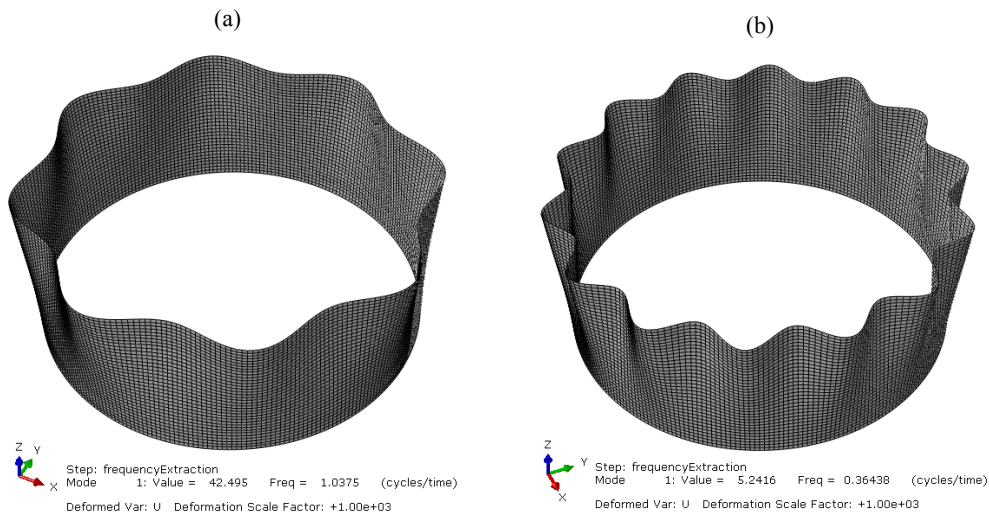


Figure 5.1.1.1: Mode 1, (a) Pre-stress included, (b) Pre-stress neglected.

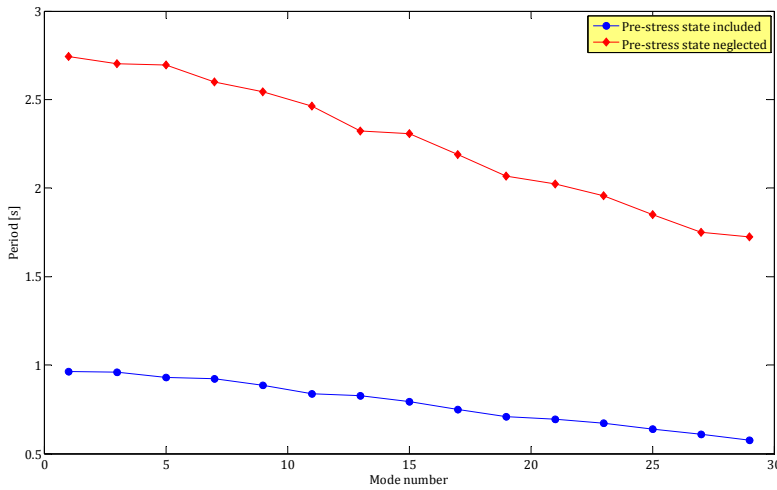


Figure 5.1.1.2: Natural period vs Mode number.

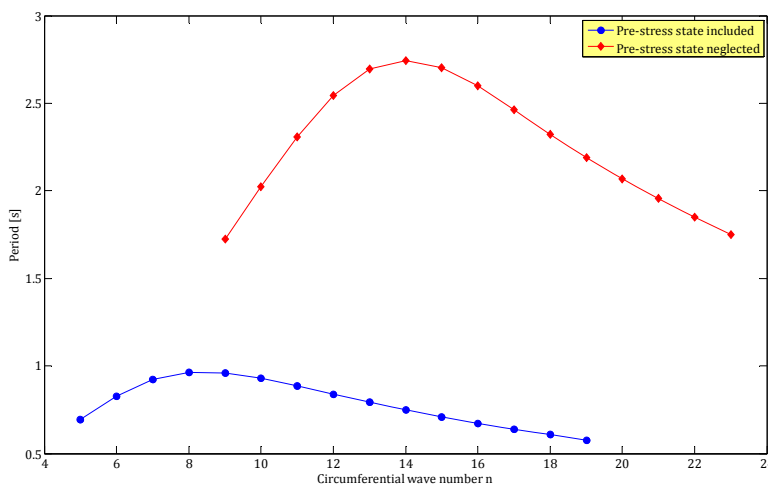


Figure 5.1.1.3: Natural period vs Circumferential wave number.

This study has shown that the pre-stress state caused by the hydrostatic pressure and the self-weight has a strong influence on the natural periods and mode shapes of anchored steel tanks partially filled with water. In particular, the presence of the pre-stress state tends to lower the natural periods, that is to stiffen the structure. From Figure 5.1.1.3 it is possible to note that the differences between the natural periods when the pre-stress state was neglected and included are smaller for those modes characterized by low circumferential wavenumbers (e.g. $n < 10$). However, it must be noted that the study deals only with the first thirty modes extracted by ABAQUS, which extracts modes in decreasing order of natural period. Probably these first thirty modes are not the most significant with respect to horizontal motion. Typically the most important modes, those with the highest participation factor, have only one circumferential wave ($n=1$) and so for these mode the influence of the pre-stress state on the natural period is quite low and can be neglected.

5.1.2 Fundamental mode shapes

To compute the natural periods and mode shapes for the added mass model of the tank-liquid system, the hydrostatic pressure and the self-weight of the tank are initially applied, i.e. they are modeled as a pre-stress state, even if their effect is expected to be small, for the reasons explained in Section 5.1.1.

With a finite element size of 500 millimeters the number of degrees of freedom of the model is extremely large. So, due to time reasons, it is not convenient to ask ABAQUS the extraction of all the mode shapes. The Lanczos solver used by ABAQUS in the frequency extraction analysis allows to search for all the natural frequencies and mode shapes within a specified range of frequencies. So, it is much more convenient to start with a coarse mesh, ask for all the mode shapes until the cumulated effective mass is higher than 85% of the mass of the model, and individuate the range of fundamental frequencies. Then, the frequency extraction analysis on the model with the finer mesh is performed only within that range of frequencies, a little bit enlarged to account for the fact that refining the mesh leads to an increase in flexibility of the structure.

A frequency extraction analysis on a model with finite element size of 900 millimeters is performed. The natural periods and mode shapes are computed until the ratio α_x of the horizontal component EM_x of the cumulated effective mass to the total mass of the system projected in the x-direction is larger than 0,85.

$$\alpha_x = \frac{EM_x}{M_i + M_{tank}} = \frac{EM_x}{3353} \geq 0,85 \tag{5.1.2.1}$$

With such a model 900 mode shapes need to be extracted in order to meet condition 5.1.2.1, as shown in Figure 5.1.2.1.

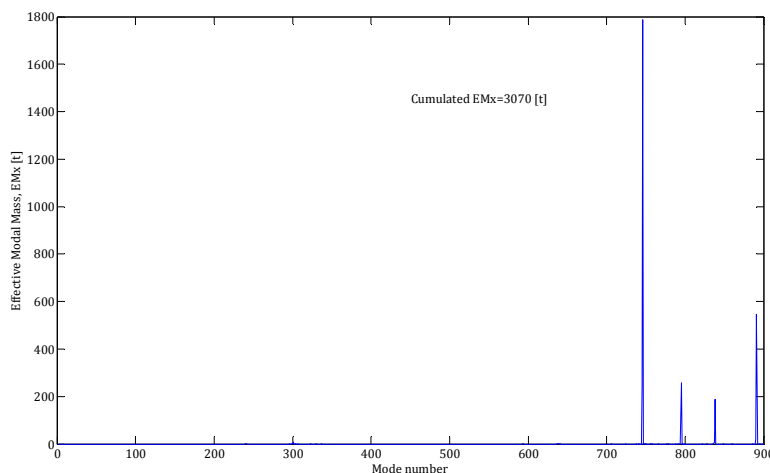


Figure 5.1.2.1: Effective modal mass vs Mode number, Esize 900.

Condition 5.1.2.1 is met considering only the contribution of mode shapes number 745, 890, 794, 746, 837, whose cyclic frequency are 4.56, 5.32, 4.72, 4.56, 4.89 Hz, respectively. So, if we name these five modes as fundamental modes, the range of fundamental frequencies goes from 4.56 to 5.32 Hz.

Now, the frequency extraction analysis can be performed on the refined model (Esize 500 millimeters); in particular, 700 mode shapes are requested within the frequency range that goes from 4 to 6 Hz.

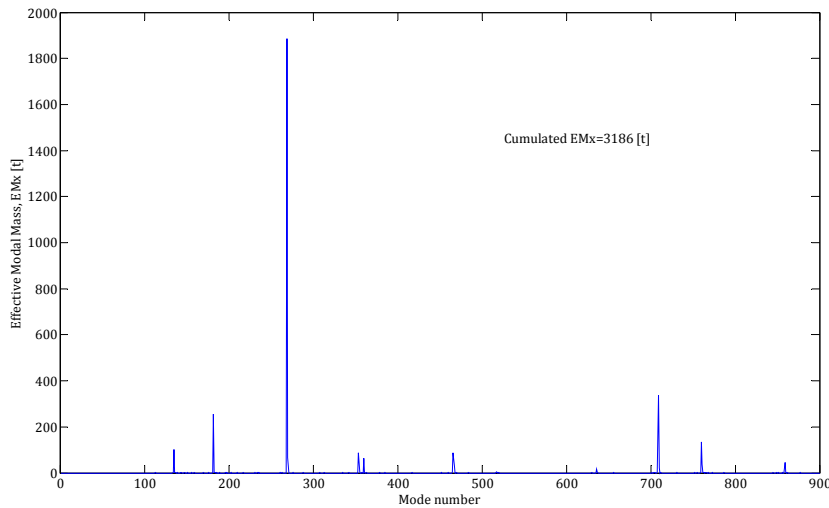


Figure 5.1.2.2: Effective modal mass vs Mode number, Esize 500.

The fundamental mode shapes, those that contribute to meeting equation 5.1.2.1, are 269, 709, 182, 760, 135, 466 and 354 which for convenience are renamed 1,2,3,4,5,6 and 7 respectively. All the details about these seven fundamental mode shapes are reported in Table 5.1.2.1.

Mode	f [Hz]	ω [rad/sec]	T [s]	α_x	m	n
1	4.613	28.984	0.217	0.562	1	1
2	5.483	34.451	0.182	0.101	>1	1
3	4.458	28.010	0.224	0.077	>1	1
4	5.615	35.280	0.178	0.040	>1	1
5	4.389	27.577	0.228	0.031	>1	1
6	4.970	31.227	0.201	0.026	>1	1
7	4.756	29.883	0.210	0.026	>1	1

Table 5.1.2.1: Numerical details about the fundamental mode shapes. n and m indicate the number of circumferential and axial waves, respectively.

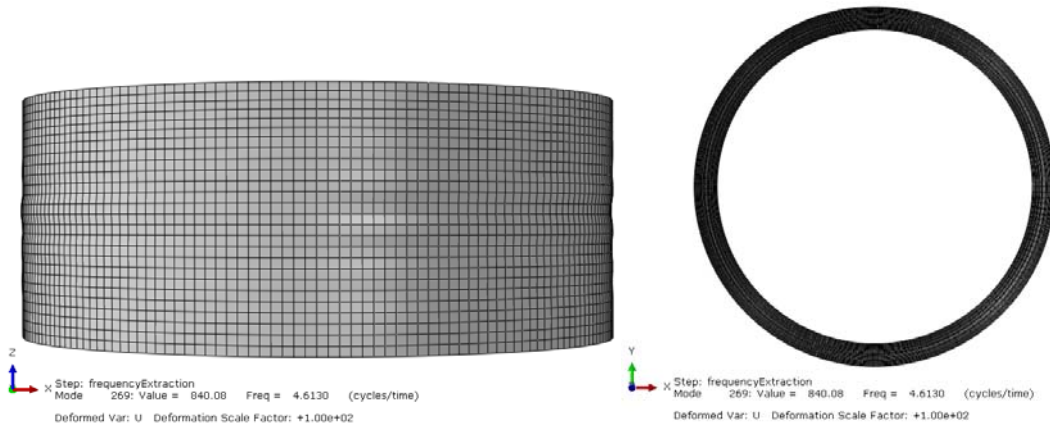


Figure 5.1.2.3:
Mode 1.

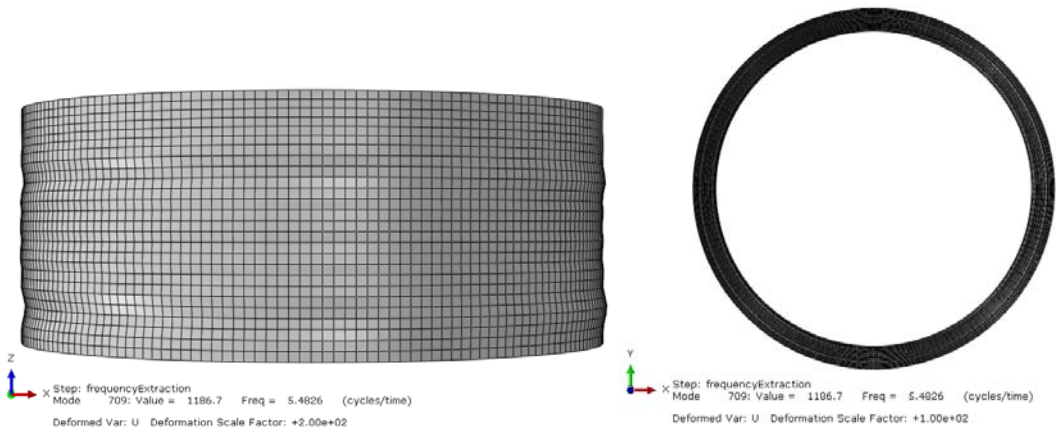


Figure 5.1.2.4:
Mode 2.

From Figures 5.1.2.3, 5.1.2.4 and from Table 5.1.2.1 it is possible to note that all the fundamental mode shapes are beam-type mode; in fact, they are characterized by the absence of cross-section distortions ($n=1$), typical of shell-modes. Furthermore, the results found are totally in agreement with the results of Virella et al. [54], in which tanks of similar proportions are studied.

5.2 Dynamic buckling analyses

5.2.1 Setting analysis

An initial analysis step is performed, loading the tank with the hydrostatic pressure and the self-weight and by including geometric nonlinearities so that the stiffness matrix of the system is modified by the presence of the initial static preloading. The dynamic analyses are carried out in a second step, including both material and geometric nonlinearities. The nonlinear equation of motion solved in the dynamic analyses has the form

$$\mathbf{m}\ddot{\mathbf{u}} + \mathbf{c}\dot{\mathbf{u}} + \mathbf{f}_s(\mathbf{u}, \dot{\mathbf{u}}) = -\mathbf{p}_{\text{eff}} \quad (5.2.1.1)$$

where \mathbf{u} , $\dot{\mathbf{u}}$, $\ddot{\mathbf{u}}$ are the displacement, velocity and acceleration vector; \mathbf{m} , \mathbf{c} are the mass and damping matrix; \mathbf{p}_{eff} is the vector of the effective earthquake forces. \mathbf{p}_{eff} can be expressed as the sum of two contributions:

$$\mathbf{p}_{\text{eff}} = \mathbf{m} \mathbf{r}_x \ddot{x}_g(t) \quad (5.2.1.2a)$$

$$\mathbf{p}_{\text{eff}} = \mathbf{m}_s \mathbf{r}_x \ddot{x}_g(t) + \mathbf{m}_i \mathbf{r}_x \ddot{x}_g(t) \quad (5.2.1.2b)$$

where \mathbf{r}_x is the vector of influence coefficients containing ones at the degrees of freedom in the direction of the applied earthquake $\ddot{x}_g(t)$; $\ddot{x}_g(t)$ is the horizontal acceleration record. The first contribution to the effective earthquake forces is given by the inertial forces that develop on the empty tank and the second one returns exactly the impulsive pressure. \mathbf{m}_s and \mathbf{m}_i are the mass matrix of shell elements and the mass matrix of point mass elements representing the fluid, written in the global reference system.

In the governing equation 5.2.1.1 the term $f_s(\mathbf{u}, \dot{\mathbf{u}})$ represents the resisting forces, which depend on the prior history of displacement and velocity, being the system inelastic. In fact, the force-displacement relation is no longer single-valued if the system is unloading or reloading; for displacement u at time t the resisting force f_s depends on the prior history of motion of the system and whether the displacement is currently increasing ($\dot{u} > 0$) or decreasing ($\dot{u} < 0$).

The main objective of the analysis performed herein is to estimate the dynamic buckling load, which in this case is represented by the peak ground acceleration that produce buckling, PGA_{cr} . To this aim the accelerograms are scaled and several analyses are performed for increasing value of the PGA. So, the PGA plays the role of the load factor.

$$\ddot{x}_g(t) = \text{PGA} \cdot f(t) \quad (5.2.1.3)$$

$f(t)$ is the time variation of the accelerogram. To obtain more generic results a set of seven accelerograms is used (see Section 5.2.3). For each accelerogram the analysis is performed for n increasing values of PGA, from 0.1g to 0.75g. At the end, a total of $7 \cdot n$ nonlinear dynamic analyses is performed in ABAQUS/Standard, using an implicit time integration technique (see Section 5.2.4).

In the finite element model, the earthquake excitation is introduced by accelerating the base nodes in the x-direction, Figure 5.2.1.1. So, one-directional earthquake is considered. Any acceleration is considered in the y or z-direction.

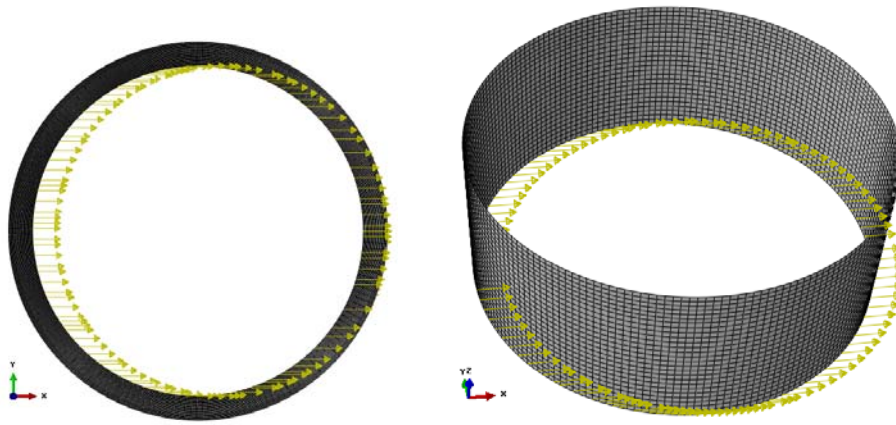


Figure 5.2.1.1: Horizontal acceleration (in the x-direction) to the base nodes of the model.

In conclusion, the procedure for obtaining the dynamic buckling load can be divided into three steps. First, the model of the tank-liquid system is defined (Chapter 4); second, a set of earthquake accelerograms is selected in order to perform the dynamic simulation (Section 5.2.3); and third, dynamic buckling is identified by means of a buckling criterion (Section 5.3.2).

For all the details about the MATLAB code use to set the dynamic buckling analyses see Appendix D.

5.2.2 Damping of the tank-fluid system

To introduce damping to the model, a Rayleigh damping matrix \mathbf{c} is used in the governing equation 5.2.1.1.

$$\mathbf{c} = \alpha \mathbf{m} + \beta \mathbf{k} \tag{5.2.2.1}$$

where α is the mass proportional coefficient and β is the stiffness proportional coefficient. The damping ratio for the n^{th} mode of such system is

$$\xi_n = \frac{\alpha}{2} \frac{1}{\omega_n} + \frac{\beta}{2} \omega_n \tag{5.2.2.2}$$

The coefficients α and β can be determined from specified damping ratios ξ_i and ξ_j for the i^{th} and j^{th} mode, respectively. Expressing equation 5.2.2.2 for these two modes leads to a system of two equations in the two unknowns α and β . Assuming $\xi_i = \xi_j = \xi$, the system has the form

$$\begin{cases} \xi = \frac{\alpha}{2} \frac{1}{\omega_i} + \frac{\beta}{2} \omega_i \\ \xi = \frac{\alpha}{2} \frac{1}{\omega_j} + \frac{\beta}{2} \omega_j \end{cases} \tag{5.2.2.3}$$

Solving the system for α and β results in

$$\alpha = \xi \frac{2\omega_i\omega_j}{\omega_i + \omega_j} \quad (5.2.2.4a)$$

$$\beta = \xi \frac{2}{\omega_i + \omega_j} \quad (5.2.2.4b)$$

In applying this procedure to practical problems, the modes i and j with specified damping ratios should be chosen to ensure reasonable values for the damping ratios in all the modes contributing significantly to the response. Typically ξ is specified for the modes with the highest and the lowest frequency, so that for all the other modes it will be somewhat smaller. For the present case it is assumed $\xi=2\%$ for the fifth ($\omega_{\min}=27.577$ rad/s) and the fourth mode ($\omega_{\max}=35.280$ rad/s). This assumption leads to the following Rayleigh coefficients:

$$\alpha = 0.02 \frac{2 \cdot 27,577 \cdot 35,280}{27,577 + 35,280} = 0,619100 \quad (5.2.2.5a)$$

$$\beta = 0.02 \frac{2}{27,577 + 35,280} = 0,000636 \quad (5.2.2.5b)$$

The so calculated coefficients are then assigned separately to the shell and mass elements in the ABAQUS model.

5.2.3 Selection of the earthquake accelerograms

According to Eurocode 8 [12], for nonlinear time-history analyses the time-dependent response of the structure may be obtained through direct numerical integration of its differential equation of motion, using response spectrum-compatible accelerograms. Criteria to verify the compatibility of an accelerogram with the response spectrum are specified in [12]. Also, if the dynamic response of the structure is obtained from at least seven nonlinear time-history analyses with spectrum-compatible accelerograms, the average of the response quantities from all these analyses should be used as a representative or design value.

Now a central concept in earthquake engineering, the response spectrum provides a convenient means to summarize the peak response (in terms of displacement, velocity and acceleration) of all possible linear single-degrees-of-freedom systems to a particular component of the ground motion. The response of the SDOF system to a base acceleration time history (Figure 5.2.3.1) is calculated by numerical integration of the equation of motion for a fixed value of the damping ratio and for a varying value of the stiffness (or period) of the structure. In a

response spectrum, the peak responses are typically plotted as a function of the natural vibration period.

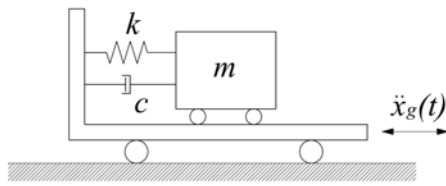


Figure 5.2.3.1: Damped SDOF system.

Assuming the tank as a SDOF system it is possible to calculate the acceleration response spectrum for each accelerogram belonging to a database of over 3500 accelerograms. Then, knowing the range of significant periods of the tank from Section 5.1.2, it is possible to select only those seven accelerograms whose response spectrum best fits the site-specific elastic spectrum in that range. The horizontal elastic response spectrum in terms of acceleration is calculated using the NTC'08 [34] prescriptions, starting from the following assumptions:

- Soil type A (assuming a rock soil with average shear wave velocity >800 m/s): $S=1$, $T_B=0.113$ s, $T_C=0.340$ s, $T_D=2.371$ s;
- Reference PGA $a_g=1.89$ m/s² (assuming the tank built in Milazzo, ME);
- Maximum spectral amplitude factor $F_0=2.46$ (assuming the tank built in Milazzo, ME);
- Damping ratio equal to 5%.

The use of the elastic response spectrum instead of the design one is justified by the fact that nonlinearity is already included in the model. The range of significant periods is (T_{min}, T_{max}) but actually common rule is to extend it to $(T_{min}, 2 \cdot T_{max})$ to account for the effect of nonlinearity, which tends to elongate the fundamental period. From Section 5.1.2 we know $T_{min}=0.178$ s and $T_{max}=0.228$ s. So, the seven best accelerograms are searched in the range $(0.178, 0.456)$, highlighted in Figure 5.2.3.2.

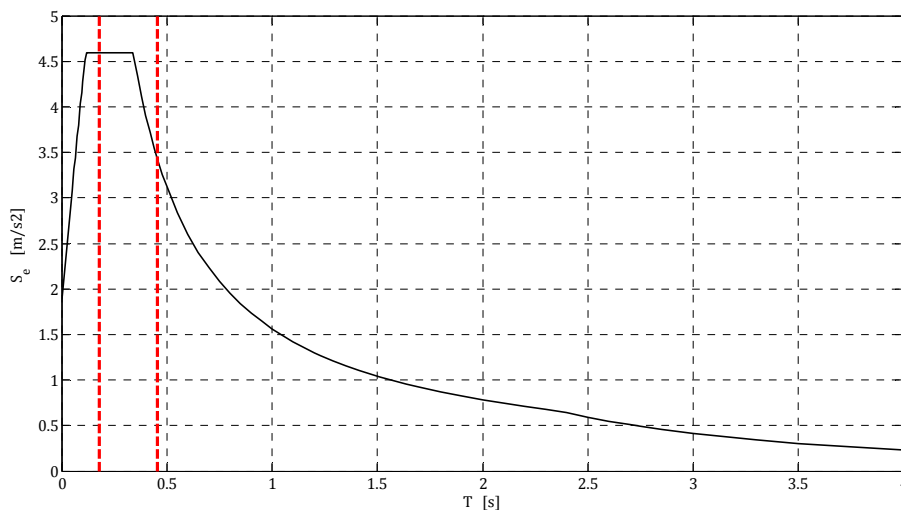


Figure 5.2.3.2: NTC'08 horizontal elastic response spectrum (5% damped). The two vertical red lines identify the range of periods for the detection of compatible accelerograms.

According to the EC8 prescriptions [12]:

“Recorded accelerograms, or accelerograms generated through a physical simulation of source and travel path mechanisms, may be used, provided that the samples used are adequately qualified with regard to the seismogenetic features of the sources and to the soil conditions appropriate to the site, and their values are scaled to the value of $a_g \cdot S$ for the zone under consideration.”

Therefore, all the recorded accelerograms belonging to the database have been scaled to the value of $a_g \cdot S = 1.89 \text{ m/s}^2$, as shown in Figure 5.2.3.3. Furthermore, the search of response spectrum-compatible accelerograms is made only among those earthquake records with a typical average shear wave velocity of a Soil type A ($v_{s,30} > 800 \text{ m/s}$).

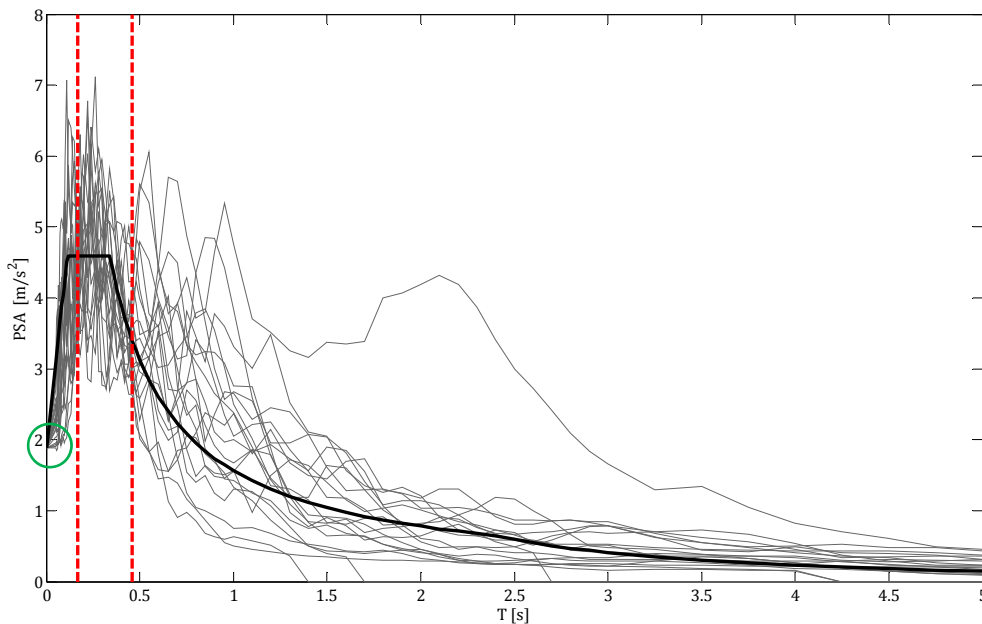


Figure 5.2.3.3: Response spectra of the recorded accelerograms (in gray), scaled to the value of $a_g \cdot S = 1.89 \text{ m/s}^2$. NTC'08 spectrum (in black) and significant range of periods (in red).

The seven accelerograms whose average response spectrum best fits the NTC'08 spectrum in the selected range of periods are plotted in Figure 5.2.3.4, together with the average spectrum. Their characteristics are reported in Table 5.2.3.1.

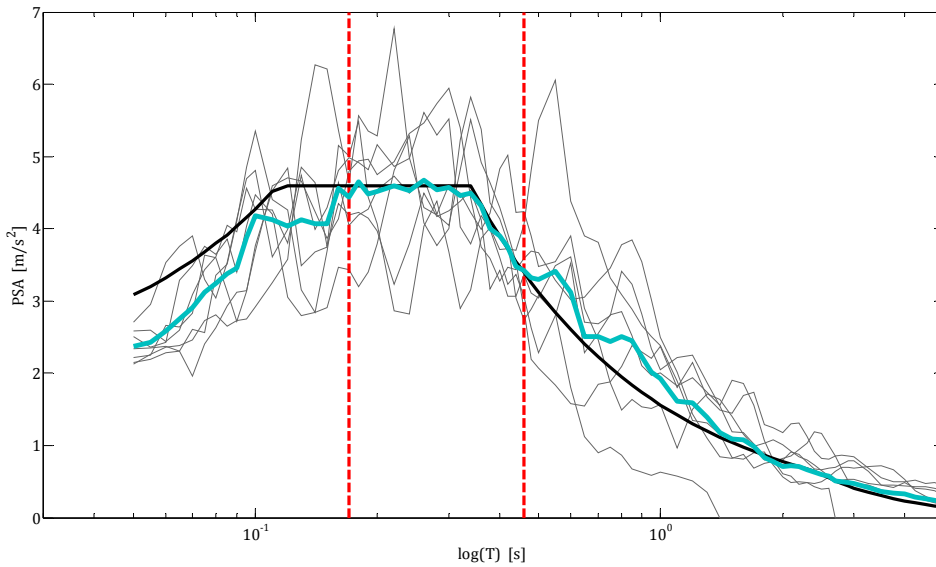


Figure 5.2.3.4: Search results. Response spectra of the 7 selected accelerograms (in gray) with their average spectrum (in blue) and matching with the NTC'08 spectrum (in black) in the selected range of periods (in red).

N°	Earthquake name	Station name	Duration [s]	PGA [g]	t_{PGA} [s]	M_W	R_{jb} [km]
1	Irpinia, Italy (1980), N-S comp.	Auletta	35	0.062	16.93	6.90	9.52
2	Northridge, LA (1994), E-W comp.	Pacoima Dam (downstr)	20	0.430	3.74	6.69	4.92
3	Irpinia, Italy (1980), E-W comp.	Auletta	35	0.058	16.67	6.90	9.52
4	Northridge, LA (1994), N-S comp.	Littlelock-Brainard Can	40	0.060	13.01	6.69	46.31
5	Denali, Alaska (2002), E-W comp.	R109	80	0.060	28.30	7.90	42.99
6	Whittier Narrows, LA (1987), N-S comp.	Pasadena-CIT Kresge Lab.	40	0.089	3.42	5.99	6.77
7	Irpinia, Italy (1980), E-W comp.	Bagnoli Irpinio	40	0.049	7.25	6.20	17.79

Table 5.2.3.1: Details about the seven selected accelerograms: earthquake and station name, duration, peak ground acceleration, time instant at which the PGA occurs, moment magnitude, Joiner-Boore distance.

As already mentioned in Section 5.2.1 all these accelerograms are assigned to the model in the x-direction. The original record of each accelerogram is plotted in Figures 5.2.3.5 to 5.2.3.11, but remember that for the purposes of dynamic buckling analysis the accelerograms will be scaled, so that only their temporal variation is maintained.

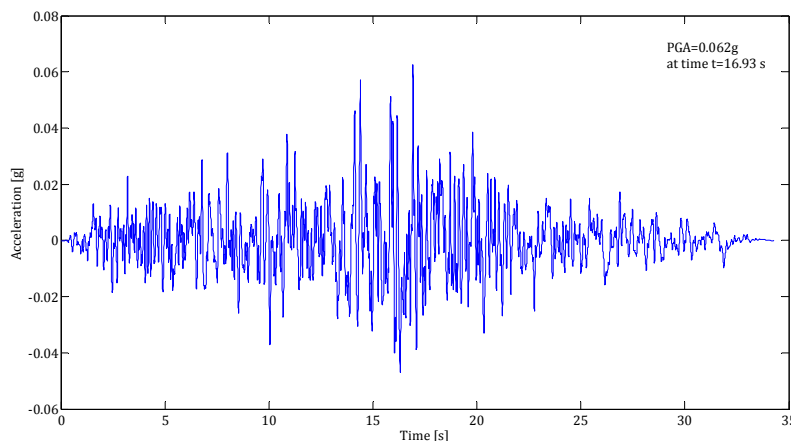


Figure 5.2.3.5: Accelerogram 1.

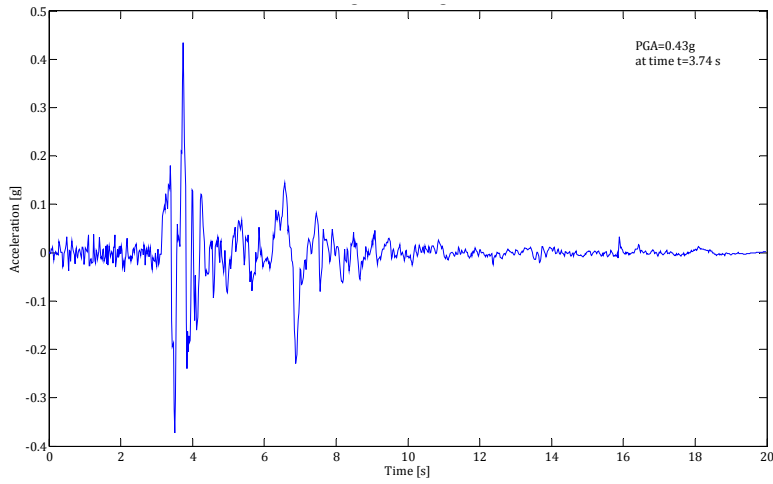


Figure 5.2.3.6: Accelerogram 2.

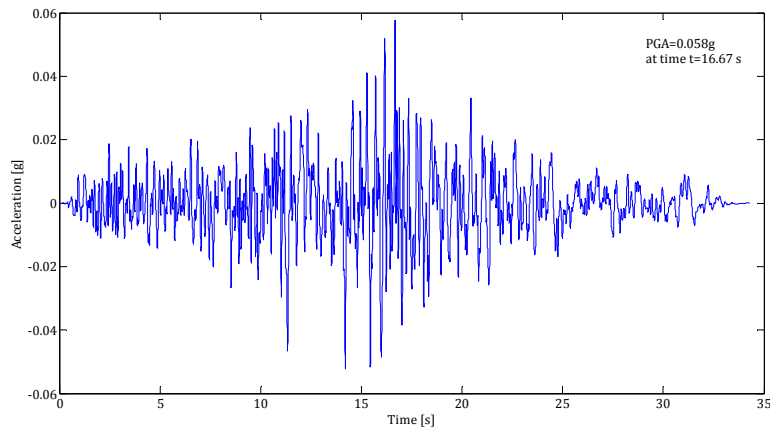


Figure 5.2.3.7: Accelerogram 3.

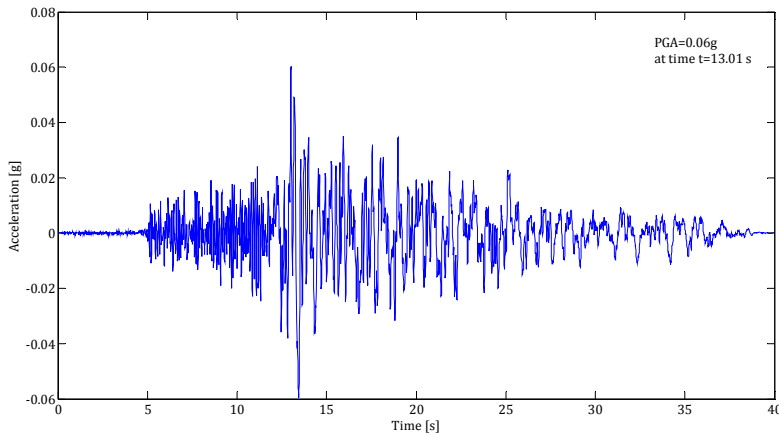


Figure 5.2.3.8: Accelerogram 4.

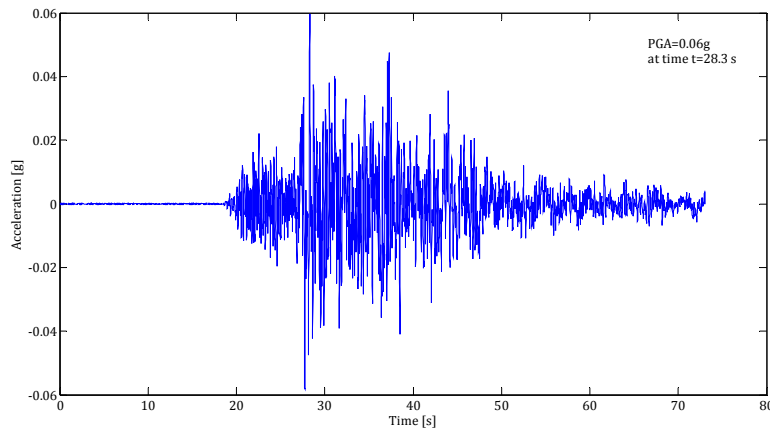


Figure 5.2.3.9: Accelerogram 5.

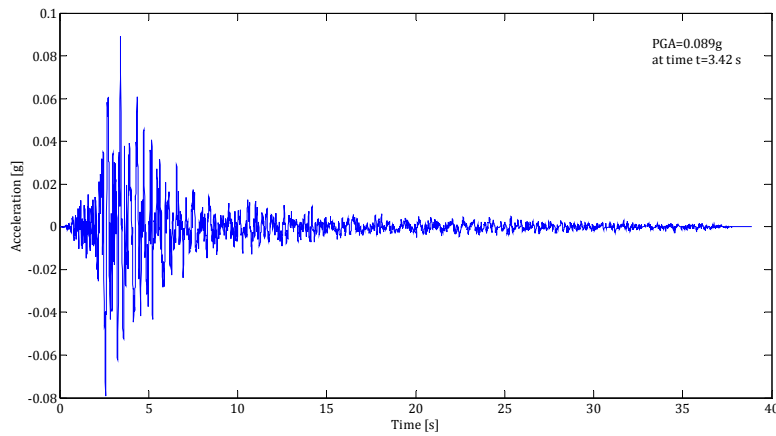


Figure 5.2.3.10: Accelerogram 6.

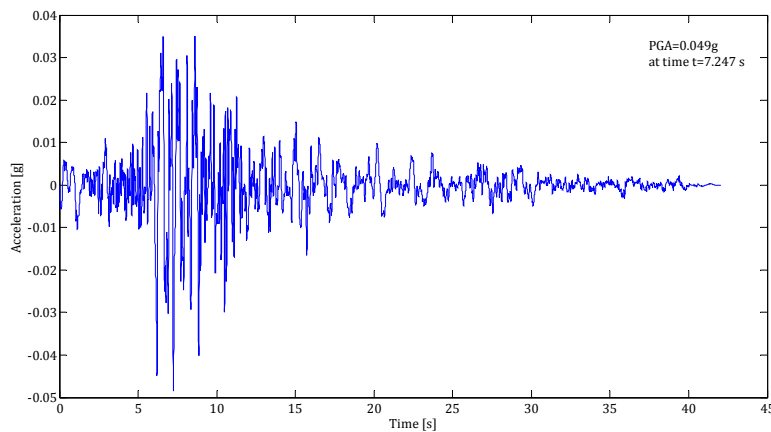


Figure 5.2.3.11: Accelerogram 7.

It is decided to perform the computations using just a portion of the earthquake records, with sufficient time to capture the peak of the original accelerogram. The reason of this lies in the fact that many analyses runs will be required to obtain the dynamic buckling load PGA_{cr} , so that reducing the computer time of the simulation is an essential part of the whole procedure. Also, accelerograms 2,4 and 5 contain some zeros at the beginning of the record; for these accelerograms, after removing the initial zeros, the times are reset.

Furthermore, the original sampling was increased in order to reduce the number of points of each accelerogram and therefore the number of analysis steps. Increasing the original sampling, the sampling frequency of the signal is reduced. Considering that sampling every x seconds corresponds to a sampling frequency of $1/x$ Hz, the maximum original sampling frequencies are those of accelerograms 1,3 and 7 ($1/0.0029=345$ Hz). After increasing the sampling, they become $1/0.0087=115$ Hz. At the end, the sampling frequencies of the base accelerations used for the computations are in the range 50-115 Hz. The resampling procedure does not change the structural response; in fact, for the Nyquist theorem, the maximum frequency that can be perceived by the structure corresponds to half that of sampling. So, working with sampling frequencies of 100 Hz the maximum frequency that can be perceived is

50 Hz and this is acceptable in lighth of the highest frequency of the structure, which is 5.6 Hz (from Section 5.1.2).

All the details about the modifications to the original earthquake records, with the aim of reducing the analysis time, are collected in Table 5.2.3.2 and the final modified records used for the computations are plotted in Figures 5.2.3.12 to 5.2.3.18.

Accel. N°	Original duration [s]	Reduced duration [s]	Original sampling [s]	Increased sampling [s]	Original frequency [Hz]	Reduced frequency [Hz]
1	0 - 35	0 - 25	0.0029	0.0087	345	115
2	0 - 20	0-10	0.0200	0.0200	50	50
3	0 - 35	0 - 25	0.0029	0.0087	345	115
4	0 - 40	5 - 30	0.0100	0.0100	100	100
5	0 - 80	18 - 55	0.0100	0.0100	100	100
6	0 - 40	0 - 10	0.0050	0.0100	200	100
7	0 - 40	0 - 20	0.0029	0.0087	345	115

Table 5.2.3.2: Details about modifications to the 7 records.

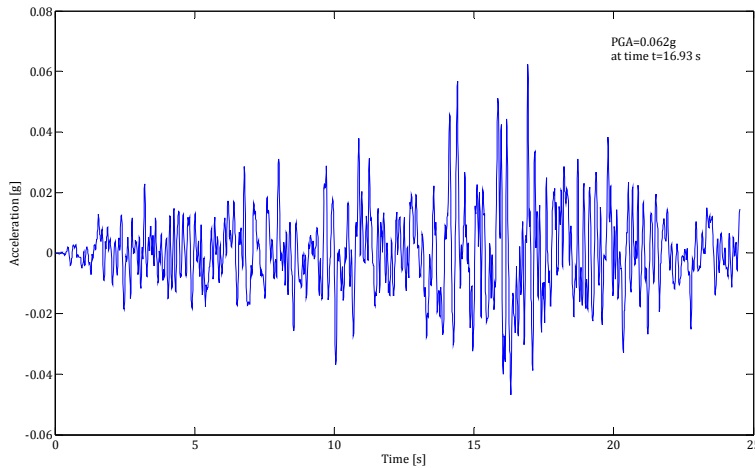


Figure 5.2.3.12: Accelerogram 1.

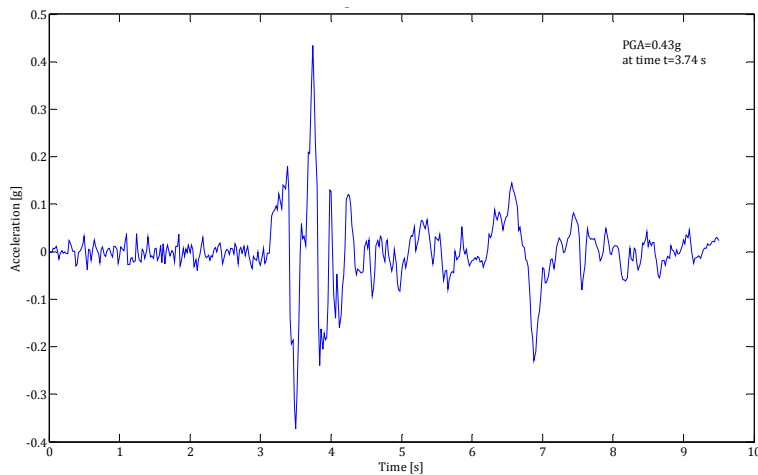


Figure 5.2.3.13: Accelerogram 2.

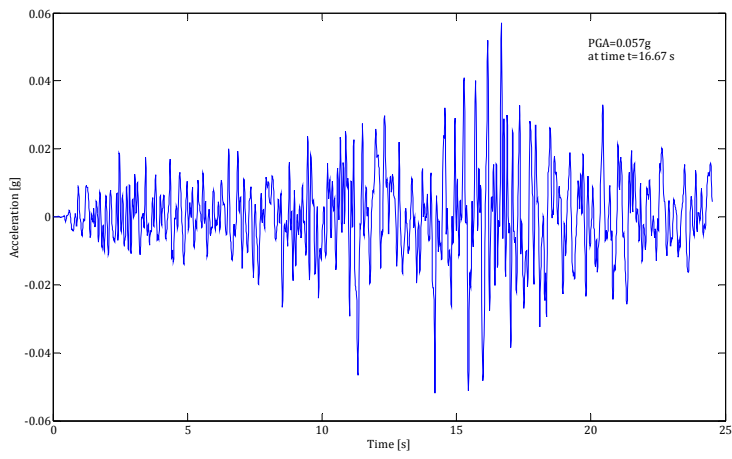


Figure 5.2.3.14: Accelerogram 3.

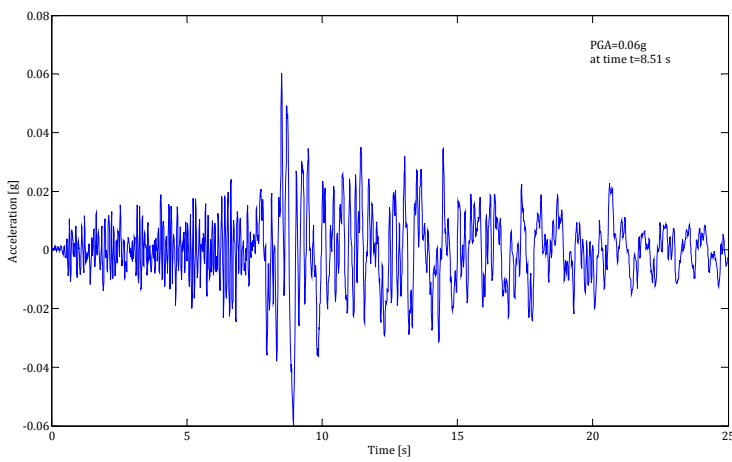


Figure 5.2.3.15: Accelerogram 4.

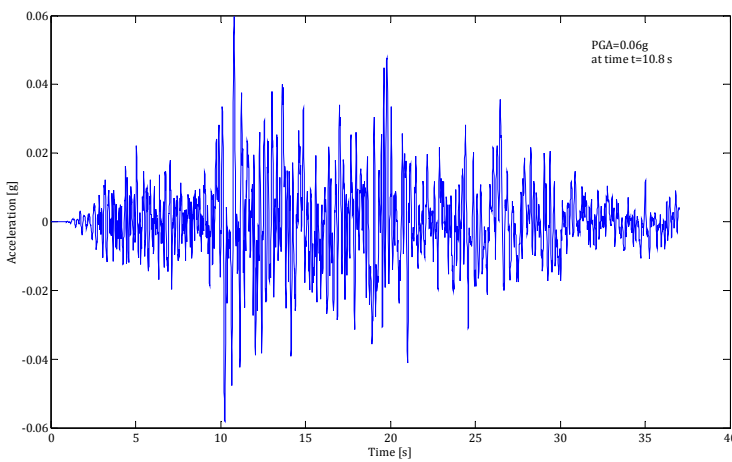


Figure 5.2.3.16: Accelerogram 5.

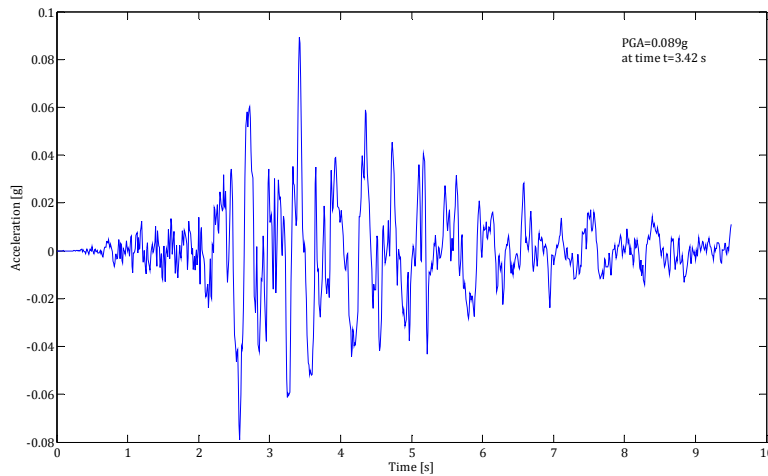


Figure 5.2.3.17: Accelerogram 6.

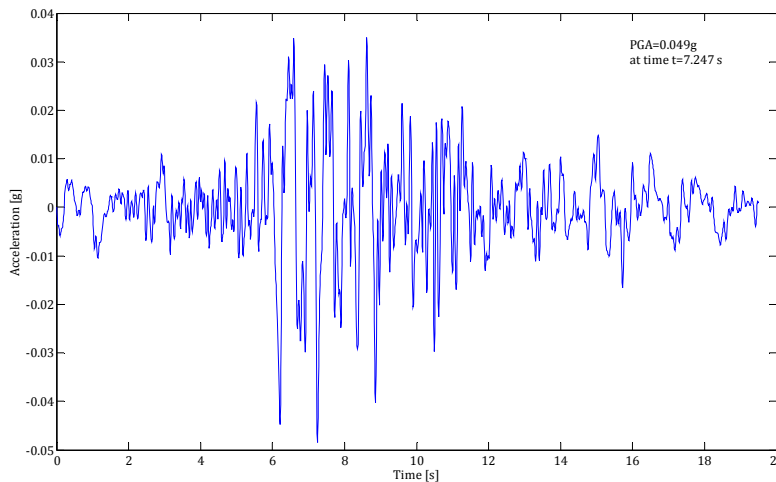


Figure 5.2.3.18: Accelerogram 7.

5.2.4 Implicit time integration method

When studying the nonlinear dynamic response of a structure, direct integration of the system's equation of motion must be used. In the present case, the nonlinear equation of motion solved in the dynamic analyses has the form

$$\mathbf{m}\ddot{\mathbf{u}} + \mathbf{c}\dot{\mathbf{u}} + \mathbf{f}_s(\mathbf{u}, \dot{\mathbf{u}}) = -\mathbf{p}_{\text{eff}} \quad (5.2.4.1)$$

where the meaning of each term was discussed in Section 5.2.1.

Dynamic integration methods are broadly characterized as implicit or explicit. Explicit schemes, as used in ABAQUS/Explicit, obtain values for dynamic quantities at $t+\Delta t$ based entirely on available values at time t . In an explicit dynamic analysis displacements and velocities are calculated in terms of quantities that are known at the beginning of an increment; therefore, the global mass and stiffness matrices need not be formed and inverted, which means that each increment is relatively inexpensive compared to the increments in an implicit integration scheme. However, the central difference operator, which is the most commonly used

explicit operator for stress analysis applications, is only conditionally stable, the stability limit being approximately equal to the time for an elastic wave to cross the smallest element dimension in the model. Implicit schemes remove this upper bound on time step size by solving for dynamic quantities at time $t+\Delta t$ based not only on values at t , but also on these same quantities at $t+\Delta t$. But because they are implicit, the integration operator matrix must be inverted and a set of nonlinear equilibrium equations must be solved at each time increment.

In structural problems implicit integration schemes usually give acceptable solutions with time steps typically one or two orders of magnitude larger than the stability limit of simple explicit schemes, but the response prediction will deteriorate as the time step size, Δt , increases relative to the period, T , of typical modes of response. In general, a maximum increment versus period ratio $\Delta t/T < 1/10$ is a good rule for obtaining reliable results. Thus, the relative economy of the two techniques of integration depends on the stability limit of the explicit scheme, the ease with which the nonlinear equations can be solved for the implicit operator, the relative size of time increments that can provide acceptable accuracy with the implicit scheme compared to the stability limit of the explicit scheme, and the size of the model.

In the present case, Equation 5.2.4.1 will be solved numerically using an implicit time-integration method available in ABAQUS/Standard, with the time increment equal to the sampling data of the recorded earthquakes. For this particular problem ABAQUS/Standard is considered computationally more effective than ABAQUS/Explicit because the ABAQUS/Explicit simulation would require a very large number of increments since the stable time increment is much smaller than the total duration of the selected earthquakes.

ABAQUS/Standard uses the Newmark β -method as time integration method. This method is fully based on the following equations for velocity and displacement:

$$\dot{u}_{i+1} = \dot{u}_i + [(1 - \gamma)\Delta t]\ddot{u}_i + (\gamma\Delta t)\ddot{u}_{i+1} \quad (5.2.4.2a)$$

$$u_{i+1} = u_i + (\Delta t)\dot{u}_i + [(0.5 - \beta)\Delta t^2]\ddot{u}_i + [\beta\Delta t^2]\ddot{u}_{i+1} \quad (5.2.4.2b)$$

where the parameters β and γ define the variation of acceleration over a time step and determine the stability and accuracy characteristics of the method. Typical selection for γ is $1/2$ and $1/6 < \beta < 1/4$ is satisfactory from all points of view, including that of accuracy. Equations 5.2.4.2, combined with the equilibrium equation at the end of the time step, provide the basis for computing u_{i+1} , \dot{u}_{i+1} and \ddot{u}_{i+1} at time $i+1$ from the known u_i , \dot{u}_i and \ddot{u}_i at time i . The Newmark β -method belong to the family of implicit methods; in fact, iteration is required to implement these computations because the unknown \ddot{u}_{i+1} appears in the right side of equations 5.2.4.2. At each time increment a set of simultaneous nonlinear dynamic equilibrium equations must be

solved. This is done iteratively with the Newton-Raphson method, which assumes that, over a small time step Δt , the secant stiffness could be replaced by the tangent stiffness, as shown in Figure 5.2.4.1. Actually, it is decided to use the modified Newton-Raphson method, in order to help the convergence of the analyses, since a strong nonlinear response is expected. The modified Newton-Raphson method uses always the initial tangent stiffness, so that it must not be recalculated at each time step.

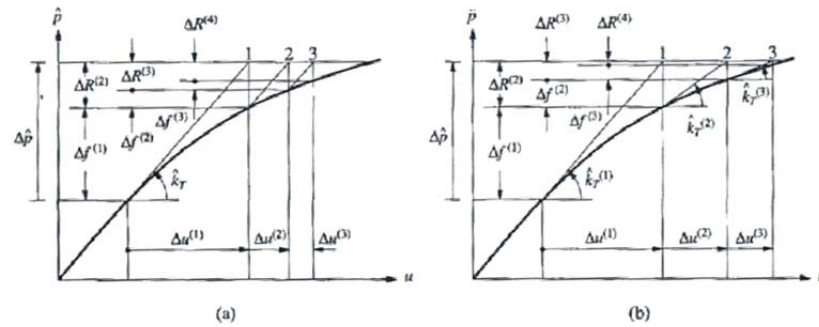


Figure 5.2.4.1: Iteration within a time step for nonlinear system. (a) Modified Newton-Raphson iteration, (b) Newton-Raphson iteration, (after [8]).

5.3 Results

5.3.1 Observed tank behavior

In this Section we intend to analyze and give a first qualitative assessment on the seismic response of the structure. To do that the results of the incremental dynamic analysis of the tank subjected to accelerogram seven are analyzed. However, the behavior is similar for the structure subjected to the other accelerograms. Essentially two types of phenomenon can be observed from Figures 5.3.1.1 to 5.3.1.3. The first one is the presence of local (or secondary) buckling at the upper-middle part of the shell. The second one is the formation of an elephant's foot bulge at the bottom of the tank. Local buckling occurs for PGA values higher than 0.40g, few second after the peak in the base acceleration. The elephant's foot bulge at the base develops for PGA values higher than 0.55g. Both secondary buckling and elephant's footing characterize the deformed shape of the structure subjected to each accelerogram. However, the elephant's foot may occur at different locations; in fact, the critical section could be the base (as for accelerogram seven) or at the mid-height where there is a drastic reduction in the thickness (as for accelerograms five and six), as shown in Figures 5.3.1.4 to 5.3.1.6. As explained in Part I - Section 3.1.2, the critical section of the shell is subjected to a biaxial stress state consisting of hoop tension and axial compression. The bulge formation results from the high circumferential

tensile stresses due to the internal pressures, in combination with the axial membrane stresses due to the overturning moment caused by horizontal earthquake excitation. More precisely, when the hoop tension reaches the yield limit, the annular strips cannot sustain any load increment and so the structural scheme resisting to a further vertical load increment is represented by a plate of height H and few millimetres thick. It is immediate to understand how this element can reach quickly a buckling failure. Due to the phenomenon mentioned above the critical section is not able to carry any further vertical compressive force, since the annular strips that stiffen it are yielded.

Accelerogram 7 scaled at PGA=0.45g

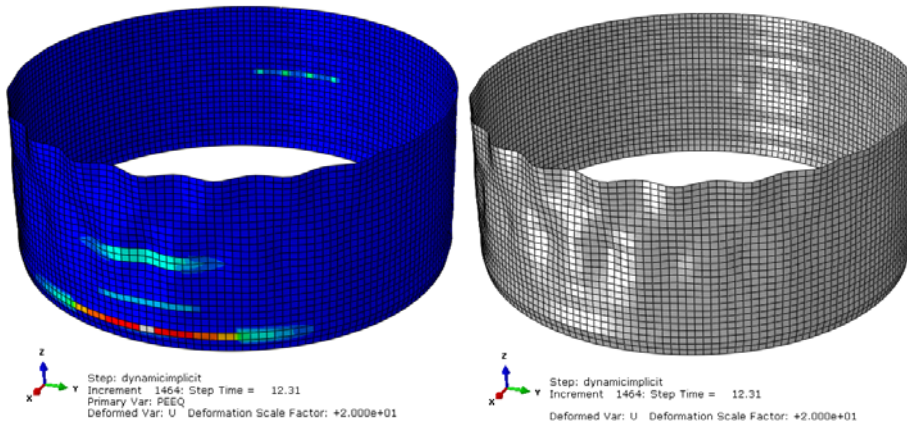


Figure 5.3.1.1: Equivalent plastic strain and deformed shape for the tank subjected to accelerogram 7, scaled at a PGA of 0.45g.

Accelerogram 7 scaled at PGA=0.55g

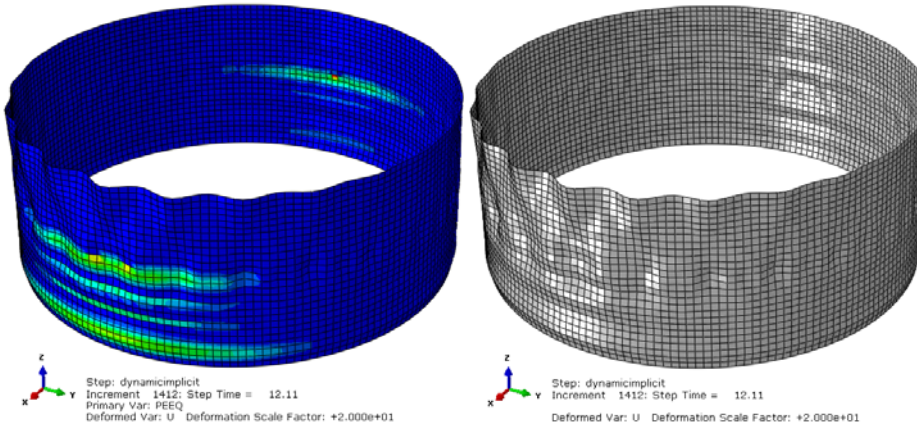


Figure 5.3.1.2: Equivalent plastic strain and deformed shape for the tank subjected to accelerogram 7, scaled at a PGA of 0.55g.

Accelerogram 7 scaled at PGA=0.75g

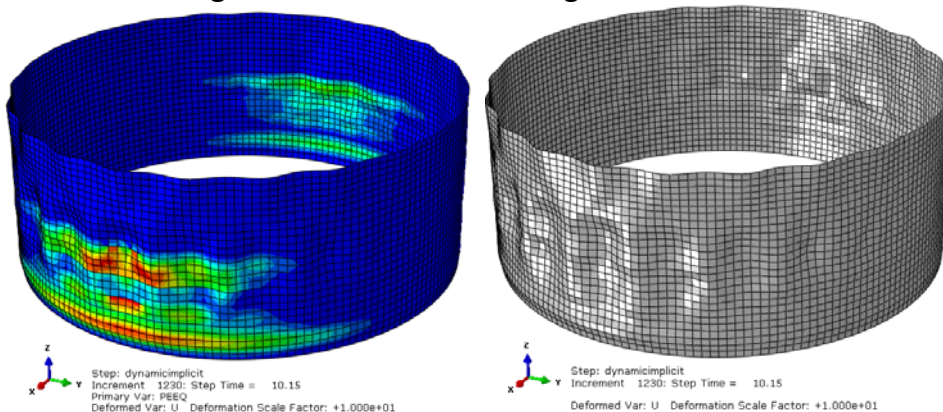


Figure 5.3.1.3: Equivalent plastic strain and deformed shape for the tank subjected to accelerogram 7, scaled at a PGA of 0.75g.

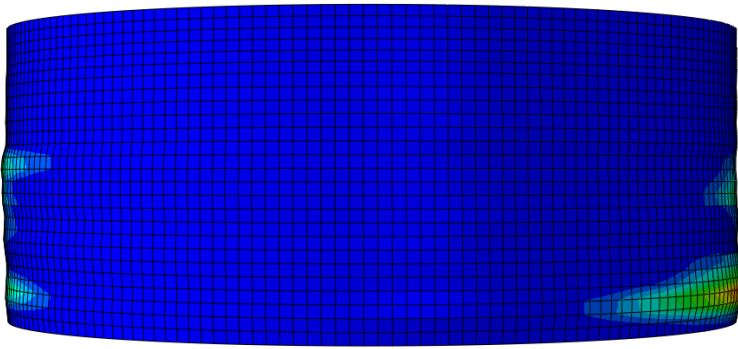


Figure 5.3.1.4: Elephant's foot bulge at the base of the tank subjected to the accelerogram 7 scaled at a PGA of 0.75g.

z
x
Step: dynamicimplicit
Increment: 1023; Step Time = 8.578
Primary Var: PEEQ
Deformed Var: U Deformation Scale Factor: +1.000e+01

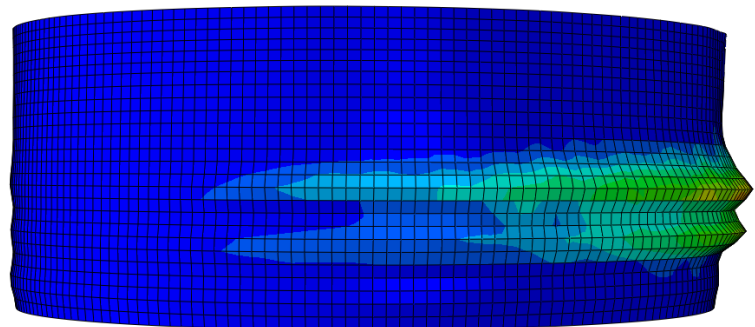


Figure 5.3.1.5: Elephant's foot bulge at the mid-height of the tank subjected to the accelerogram 2 scaled at a PGA of 0.75g.

z
x
Step: dynamicimplicit
Increment: 5895; Step Time = 47.00
Primary Var: PEEQ
Deformed Var: U Deformation Scale Factor: +1.000e+01

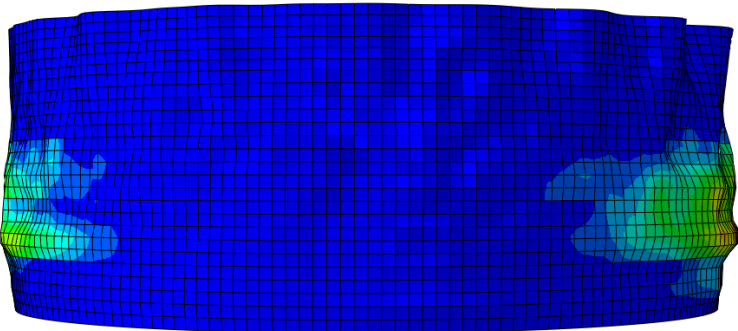


Figure 5.3.1.6: Elephant's foot bulge at the mid-height of the tank subjected to the accelerogram 5 scaled at a PGA of 0.75g.

z
x
Step: dynamicimplicit
Increment: 2790; Step Time = 19.46
Primary Var: PEEQ
Deformed Var: U Deformation Scale Factor: +1.000e+01

Since the elephant's foot buckling has been widely discussed in the literature and is fully covered by the actual regulations (see Part I - Section 3.2), our attention is mainly focused on the local buckling at the upper-middle part of the shell. This phenomenon is not covered in the actual regulations and studies on this type of buckling can be found only in Virella [52]. However, it is not yet clear if it is a pure elastic buckling or if, also in this case, material yielding plays a key role as for the elephant's foot buckling. A first step in understanding this is to perform some analyses assuming a linear-elastic behavior for the material. The results of such analyses on the tank subjected to the accelerogram six are presented in Figures 5.3.1.7.

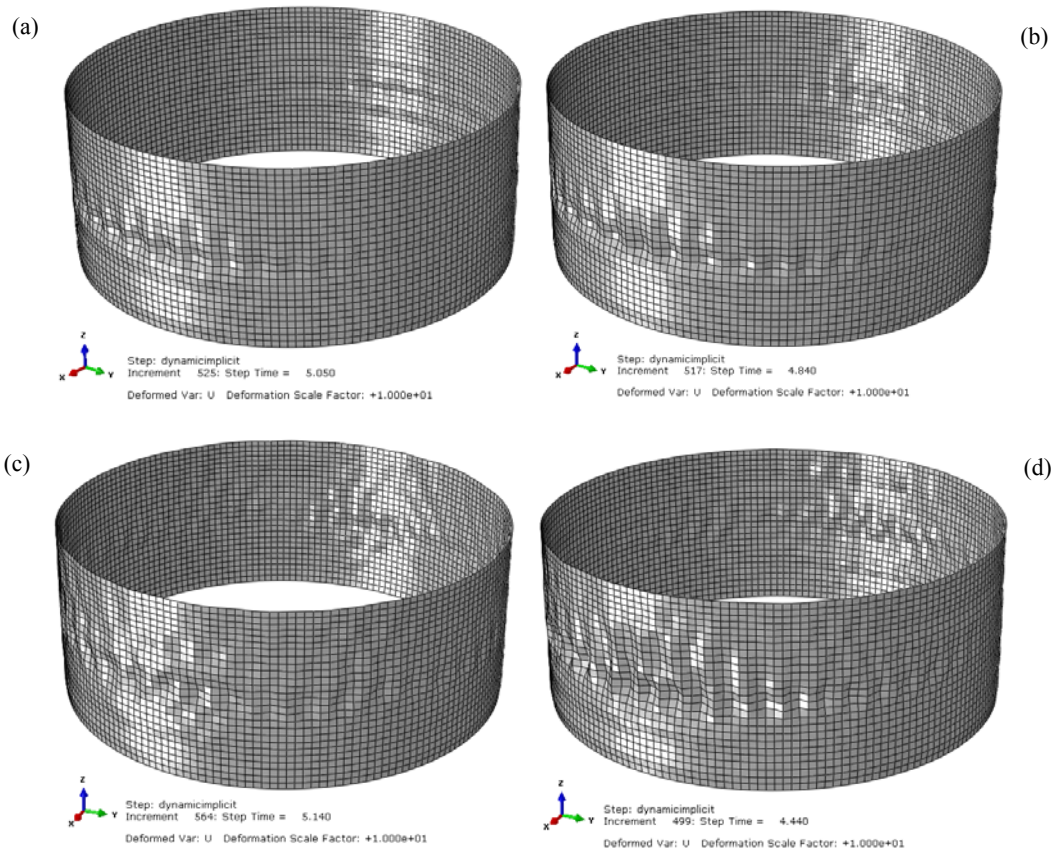


Figure 5.3.1.7: Results of linear-elastic analyses on the tank subjected to the accelerogram 6 scaled at a PGA of (a) 0.50g, (b) 0.55g, (c) 0.65g, (d) 0.75g.

From Figures 5.3.1.7 it is evident how the local buckling phenomenon occurs even in the linear-elastic case. So, we can define it as a pure elastic buckling (sometimes referred as secondary buckling, in order to distinguish it from the diamond shape buckling discussed in Part I – Section 3.1.1). The physical reasons of such behavior are those explained in Part I – Section 3.1.3 and briefly discussed here. The dynamic pressure in the fluid may induce a negative resultant pressure in the tank close to the free surface of the fluid, where the hydrostatic pressure is small. This negative resultant pressure ($P_{\text{hyd}} - P_{\text{imp}}$) induces local compressive hoop stresses that may lead to local buckling of the tank.

The reasons of the two types of buckling (elastic and elastic-plastic) are known if we consider them separately. However, in Section 5.3.4 a method to understand if there is interaction between the two mechanisms is set up. But before to study that interaction, in Section 5.3.2 a deeper insight is given into the elastic buckling mode; in particular a criterion to estimate the dynamic buckling load is presented. Then, is precisely from this criterion that the interaction with material nonlinearities will be analyzed.

5.3.2 Dynamic buckling criterion

The Budiansky and Roth criterion [45]-[52], which has been used extensively in the literature to determine the dynamic buckling load of structures, is employed in this work. According to this criterion, different analyses of the structure for several load levels need to be done, and the value for which there is a significant jump in the response for a small increase in the load indicates that the structure passes from a stable state to a critical state. When monitoring the system response through displacements of selected points for small values of the loading parameter, small oscillations are observed, the amplitudes of which gradually increases as the loading is increased. When the loading reaches its critical value, the maximum amplitude experiences a large jump. Therefore implementation of this criterion requires to solve the equations of motion for different values of the loading parameter, then plot the maximum displacement versus loading curve from which the critical loading value is determined.

The first step required by the Budiansky and Roth criterion is to monitor the transient responses of selected points of the structure. Criteria used to select the most representative node of the structure are discussed in Section 5.3.3. For now, with the sole purpose of illustrating the criterion, the attention is focused on the transient response of node 4680 (coordinates -1523.79, 250.658, 11283) of the tank subjected to the accelerogram six. It is important to underline that the results of this Section are those obtained from linear-elastic analyses. In fact, proceeding in this way, we avoid the interaction with material nonlinearity and we are sure that the final curves depend only on geometric nonlinearity, i.e. the critical PGA identifies the pure elastic buckling load. The influence of nonlinear material behavior on the dynamic buckling load will then be analyzed in Section 5.3.4. Figure 5.3.2.1 displays the transient response of node 4680 for different levels of excitation. From these Figure it is evident how a significant jump in the displacement field can be observed only for PGAs above 0.70g (red curves).

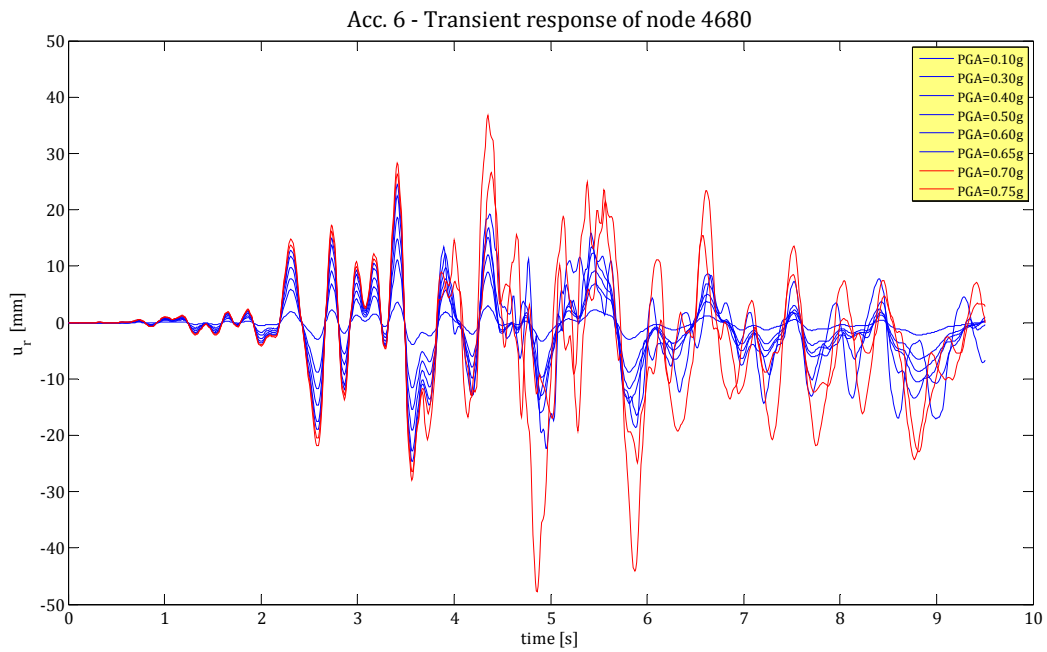
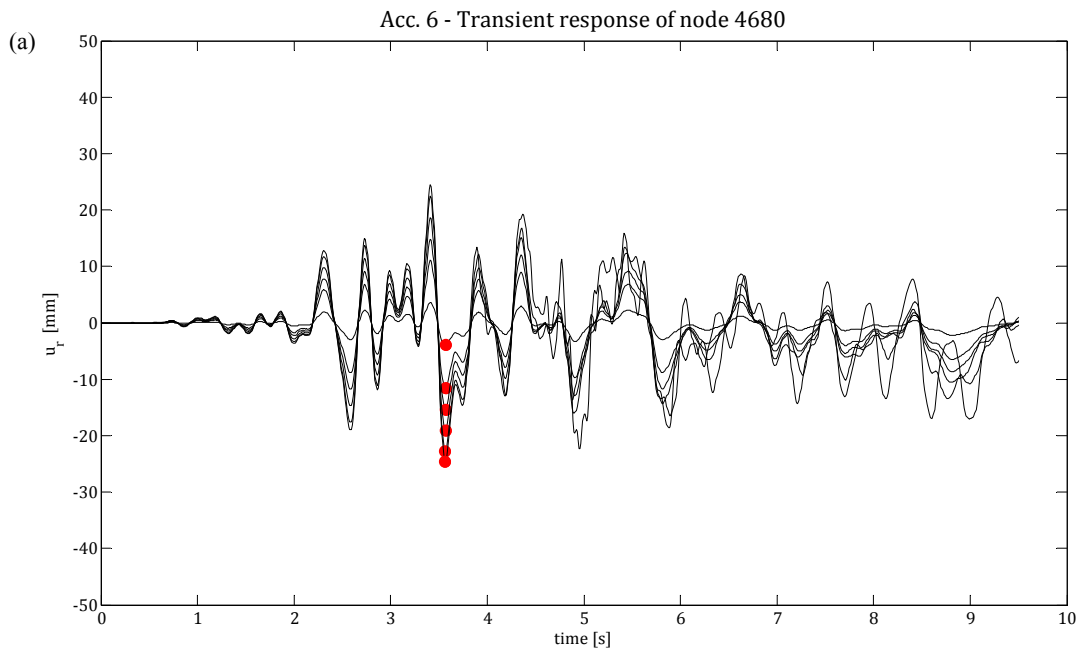


Figure 5.3.2.1: Time-history of the radial displacement of node 460. PGA from 0.10g to 0.75g

Now, the peaks in the transient responses are highlighted in Figures 5.3.2.2 (red dots) and are studied in detail in Figure 5.3.2.3 by plotting the PGA versus the absolute value of the maximum radial displacement at the node considered.



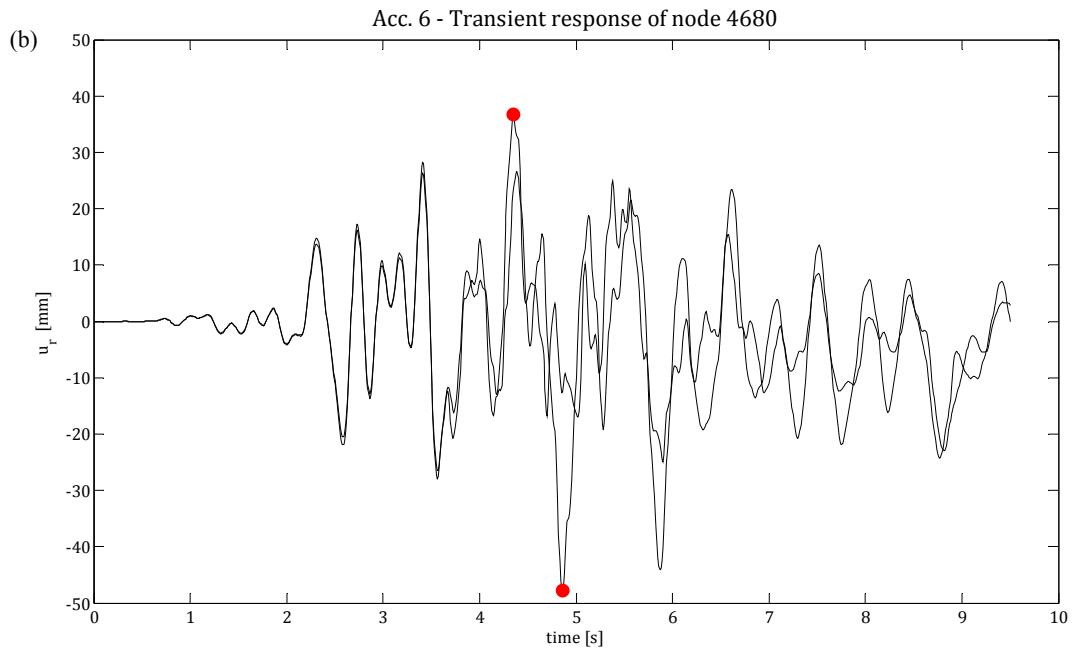


Figure 5.3.2.2: Time-history of the radial displacement of node 4680.

(a) PGA from 0.10g to 0.65g. (b) PGA from 0.70g to 0.75g.

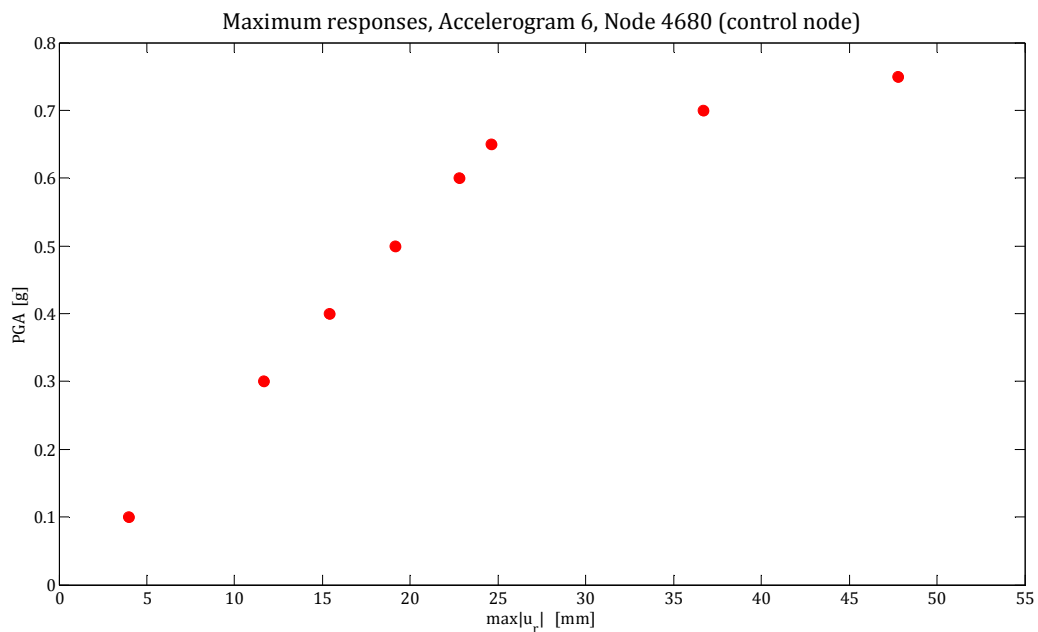


Figure 5.3.2.3: Peaks in the transient responses of node 4680 for different levels of excitation, in absolute value.

Finally, these points are fitted by means of a linear regression model, producing a sort of path, Figure 5.3.2.4. This is not an equilibrium path in the sense of static stability, but it is a useful plot to identify the nature of the nonlinear dynamic response as it evolves for different PGA levels. We shall refer to it as “pseudo-equilibrium path”. The pseudo-equilibrium path in 5.3.2.4 shows the systems approaching a maximum PGA, as the stiffness is progressively reduced. Two different responses can be identified from the pseudo-equilibrium path. At small displacements, the curve follows an initially stable path, with the slope corresponding to the initial stiffness of

the system. A second trend can be observed for higher PGA, associated with a reduction in the stiffness. The pseudo-equilibrium path, approximated by a bilinear trace, is very useful because the intersection of the two lines provides an estimate of the critical PGA, i.e. the excitation level at the transition from the initially stable to an unstable path. Furthermore, since we are dealing with the results of a linear-elastic analyses, we are sure that the reduction in stiffness is due solely to geometric nonlinearity. Any nonlinearity associated to the material is involved in the pseudo-equilibrium path of Figure 5.3.2.4. The linear regression used for the bilinear model produced a good fit, as the correlation coefficients of the regression were close to one.

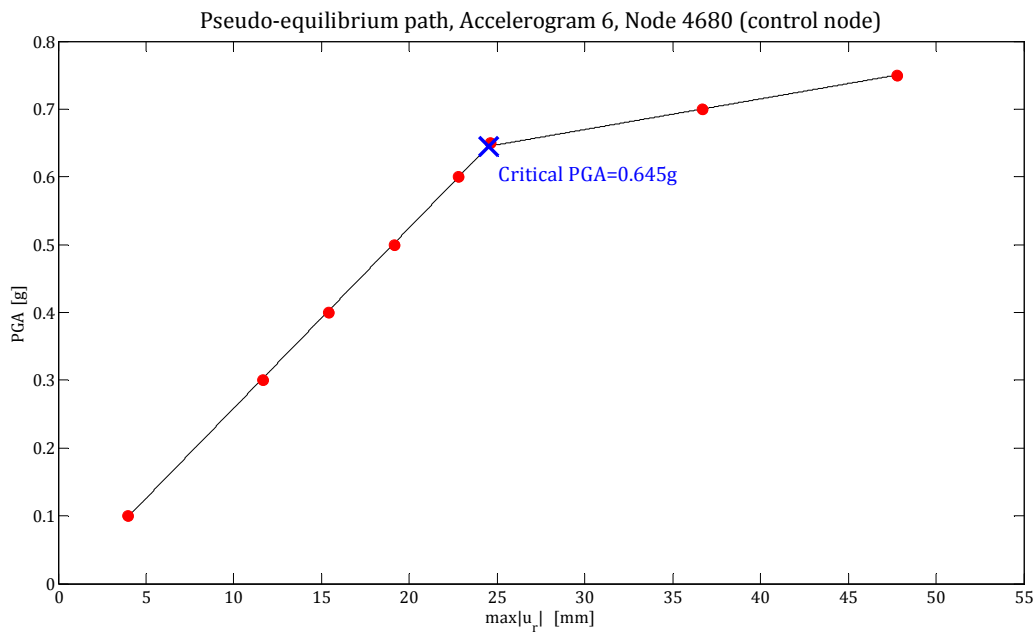


Figure 5.3.2.4: Node 4680, pseudo-equilibrium path.

The method used to perform the bilinear regression is the following: first, a linear regression is performed among all those points until the correlation coefficient r (equation 5.3.2.1) is smaller than 0.99. Then, the remaining points are fitted by means of a second linear regression, thus obtaining the bilinear trace. Points that are on the first line represent the linear response of the structure. The remaining points represent the nonlinear response. Given two stochastic variables x and y , the correlation coefficient (or Pearson’s index) is defined as the covariance to variances product ratio and it is a measure of the correlation between the two; the closer to one, the more x and y are related.

$$r = \frac{\sigma_{xy}}{\sigma_x \sigma_y} \tag{5.3.2.1}$$

The bilinear regression model has been implemented in MATLAB. For all the code details see Appendix E.

5.3.3 Control node selection

In order to study the possible interaction between material and geometric nonlinearities two grid points must be fixed in the most stressed parts of the structure, where the maximum deformations and plasticization are expected, Figure 5.3.3.1

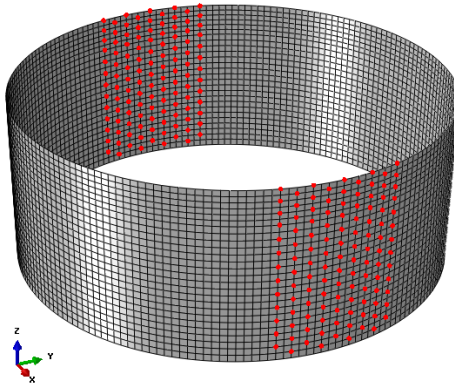


Figure 5.3.3.1: Grid points between which the control node is searched.

For each analysis, i.e. for the tank subjected to each accelerogram, the control node of the structure is the one that develops the lowest critical PGA. This implies that for each analysis, the pseudo-equilibrium path is built for each node of the grid according to what explained in Section 5.3.2. The only essential difference is that now also material nonlinearities are accounted for, i.e. the paths are developed from the results of elastic-plastic analyses. Then, the path with the lowest critical PGA identifies the control node. This is done automatically by the MATLAB code of Appendix E. Once the structure has its control node for each accelerogram, the different pseudo-equilibrium paths may be compared and discussed. This is what is done in Section 5.3.5. Search results of the control node are shown in Table 5.3.3.1 and Figures 5.3.3.2 to 5.3.3.5.

Accelerogram	Node	x [mm]	y [mm]	z [mm]	PGA _{cr} [g]
1	4967	15240	0	12089	0.541
2	2195	-15188.5	1251.94	5324.2	0.441
3	3057	15240	0	7740.2	0.106
4	2195	-15188.5	1251.94	5324.2	0.284
5	4967	15240	0	12089	0.132
6	4967	15240	0	12089	0.287
7	3065	14715.3	3964.58	7740.2	0.546

Table 5.3.3.1: Control nodes details.

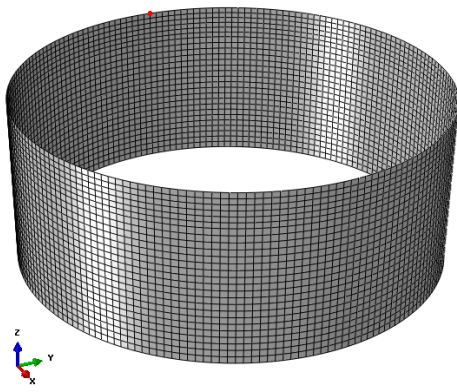


Figure 5.3.3.2: Accelerograms 1 and 3,
control node 5062.

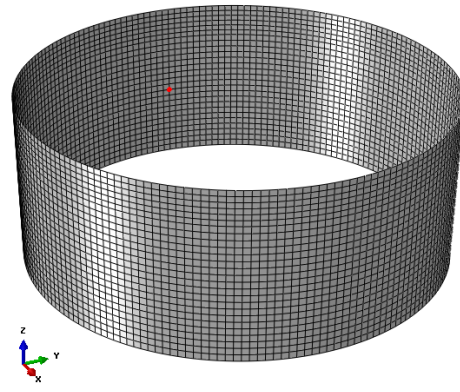


Figure 5.3.3.3: Accelerograms 2 and 4,
control node 2195.

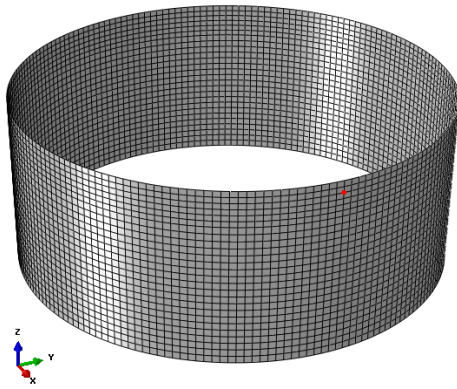


Figure 5.3.3.4: Accelerogram 6,
control node 4585.

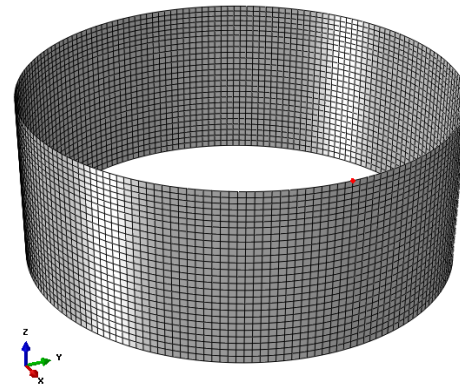


Figure 5.3.3.5: Accelerograms 5 and 7,
control node 4967.

5.3.4 The influence of plasticity

A first attempt to understand the influence of material yielding on the critical PGA for the structure is to compare the pseudo-equilibrium paths resulting from elastic and elastic-plastic analyses. This is done in Figure 5.3.4.1 for the sixth accelerogram. As expected, the elastic-plastic critical PGA is lower than the elastic one. In particular, a reduction of 40% is observed. So we can state that the pseudo-equilibrium paths are strongly influenced also by material yielding. Furthermore, the control node of the structure may change from the elastic to the elastic-plastic analysis; in fact, the elastic path is developed for node 4680, while the elastic-plastic one for node 4585. It is interesting to note that in the elastic-plastic analysis the control node 4585 remains in the elastic range (Figure 5.3.4.2). So, for the structure subjected to accelerogram six, the failure mode is still characterized by pure elastic buckling but the value of PGA at which this buckling occurs is dramatically reduced by plasticization in other parts of the structure. We can conclude that material yielding changes the global behavior of the structure.

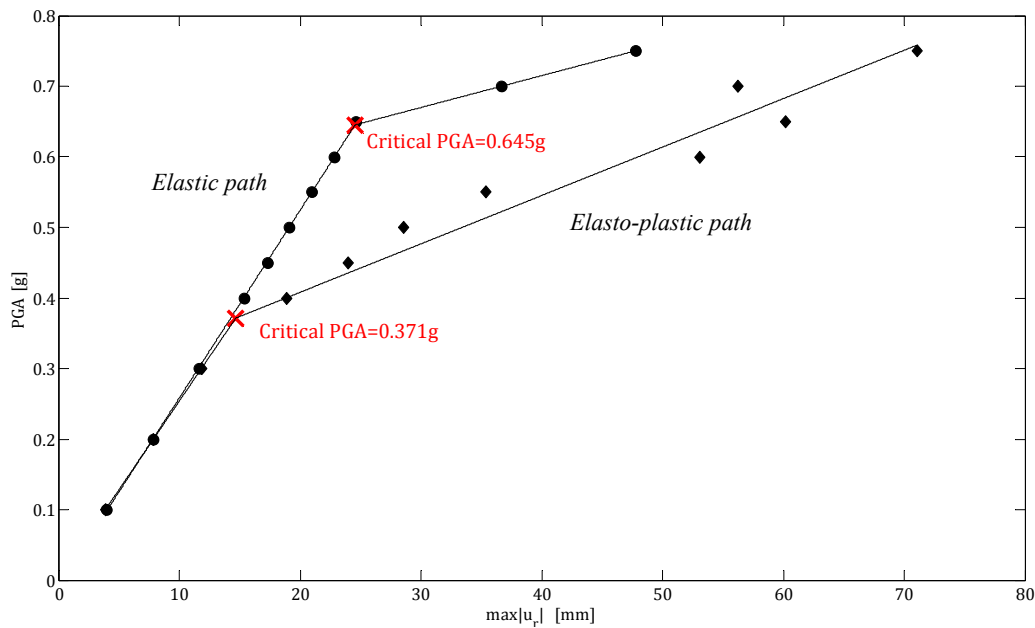


Figure 5.3.4.1: Accelerogram 6, elastic and elasto-plastic pseudo-equilibrium path.

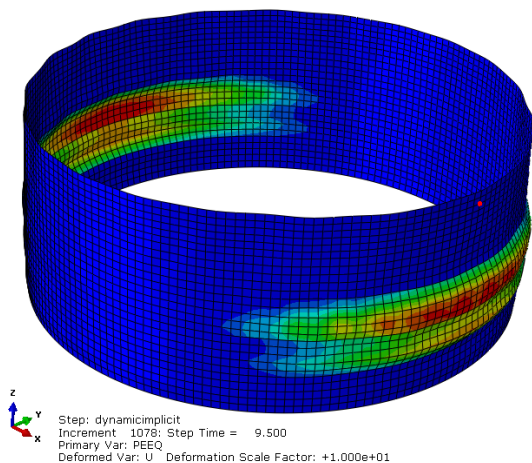


Figure 5.3.4.2: Equivalent plastic strain and node 4585.

Now we want to verify if plasticity has the same influence on the structure independently on the base accelerogram. But instead of comparing the results of elastic analyses with those of elastic-plastic analyses for each accelerogram, a faster and more approximate way to understand if the pseudo-equilibrium paths are influenced by material yielding, and so if there is interaction between material and geometric nonlinearities, is to compare the critical peak ground acceleration PGA_{cr} with the peak ground acceleration that produces the first yielding somewhere in the structure, PGA_y . The values of PGA_y are searched with a MATLAB code and the results are printed in Figure 5.3.4.3. The comparison with the values of PGA_{cr} emerges from Figures 5.3.4.4 to 5.3.4.10. Note that in these Figures the pseudo-equilibrium path, representing the failure of the structure, and the first yielding may be referred to different parts of the tank. In particular, a blue dashed line is used when the first yielding occurs in an another part with

respect to the control node and an orange dashed line is used when it occurs near the control node.

```

ACCELEROGRAM 1:
PGA=0.1g: any yielding is observed
PGA=0.2g: any yielding is observed
PGA=0.3g: the first yielding is observed at the element 1147 , after 19.74 sec.
-----
ACCELEROGRAM 2:
PGA=0.1g: any yielding is observed
PGA=0.2g: any yielding is observed
PGA=0.3g: the first yielding is observed at the element 2484 , after 23.09 sec.
-----
ACCELEROGRAM 3:
PGA=0.1g: any yielding is observed
PGA=0.2g: any yielding is observed
PGA=0.3g: the first yielding is observed at the element 1240 , after 18.496 sec.
-----
ACCELEROGRAM 4:
PGA=0.1g: any yielding is observed
PGA=0.2g: any yielding is observed
PGA=0.3g: the first yielding is observed at the element 2293 , after 11.85 sec.
-----
ACCELEROGRAM 5:
PGA=0.1g: any yielding is observed
PGA=0.2g: the first yielding is observed at the element 2102 , after 11.42 sec.
-----
ACCELEROGRAM 6:
PGA=0.1g: any yielding is observed
PGA=0.2g: any yielding is observed
PGA=0.3g: the first yielding is observed at the element 1234 , after 3.43 sec.
-----
ACCELEROGRAM 7:
PGA=0.1g: any yielding is observed
PGA=0.2g: any yielding is observed
PGA=0.3g: any yielding is observed
PGA=0.4g: the first yielding is observed at the element 383 , after 7.282 sec.
-----
    
```

Figure 5.3.4.3: Search results of the PGA that produces the first yielding somewhere in the tank.

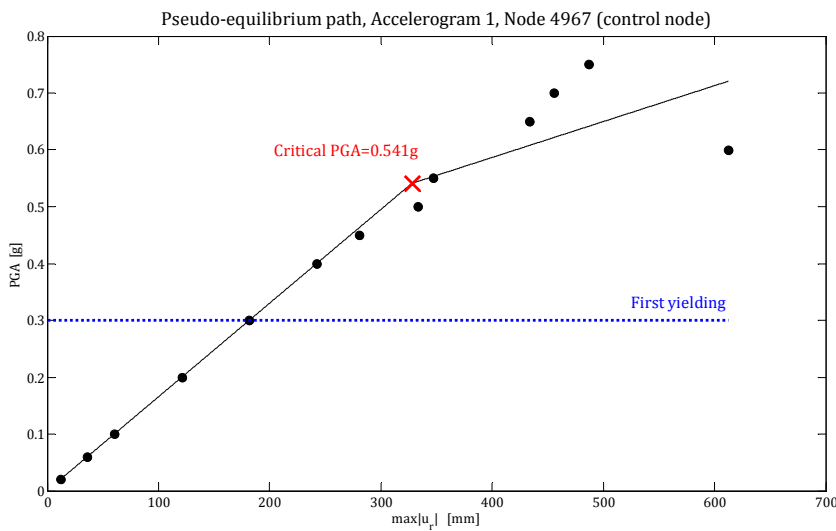


Figure 5.3.4.4: Pseudo-equilibrium path and first yielding of the tank subjected to accelerogram 1.

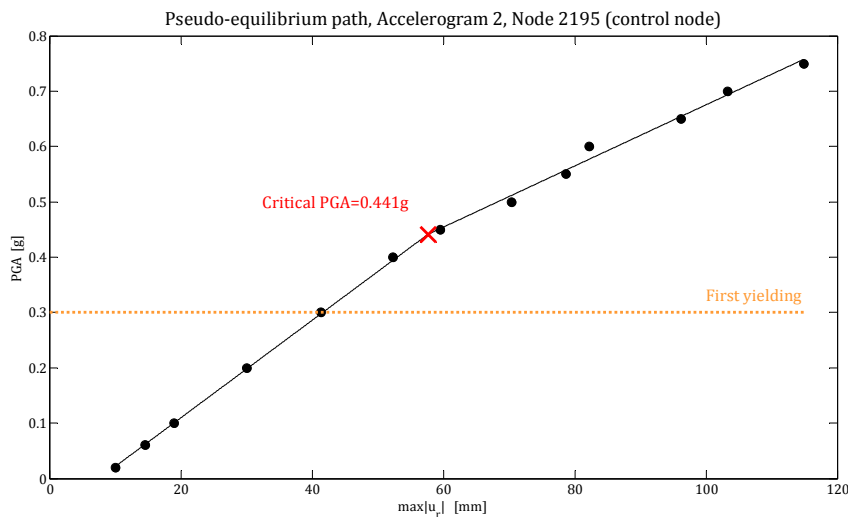


Figure 5.3.4.5: Pseudo-equilibrium path and first yielding of the tank subjected to accelerogram 2.

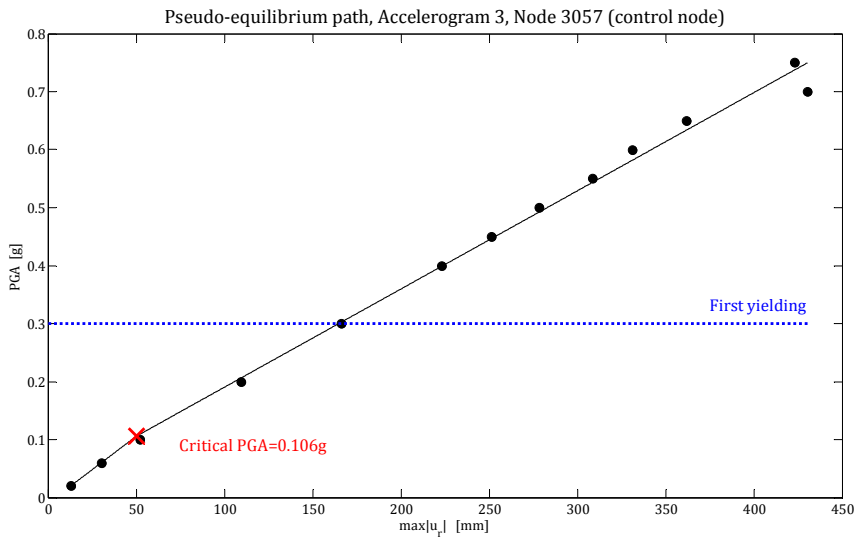


Figure 5.3.4.6: Pseudo-equilibrium path and first yielding of the tank subjected to accelerogram 3.

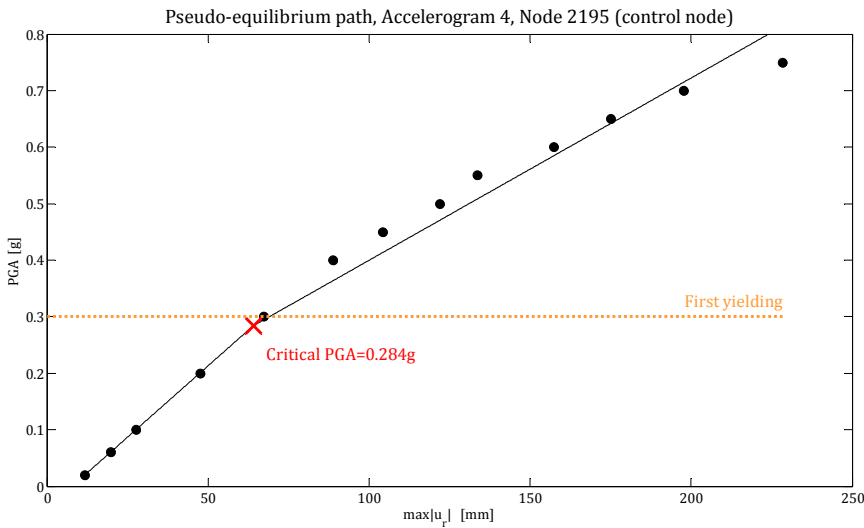


Figure 5.3.4.7: Pseudo-equilibrium path and first yielding of the tank subjected to accelerogram 4.

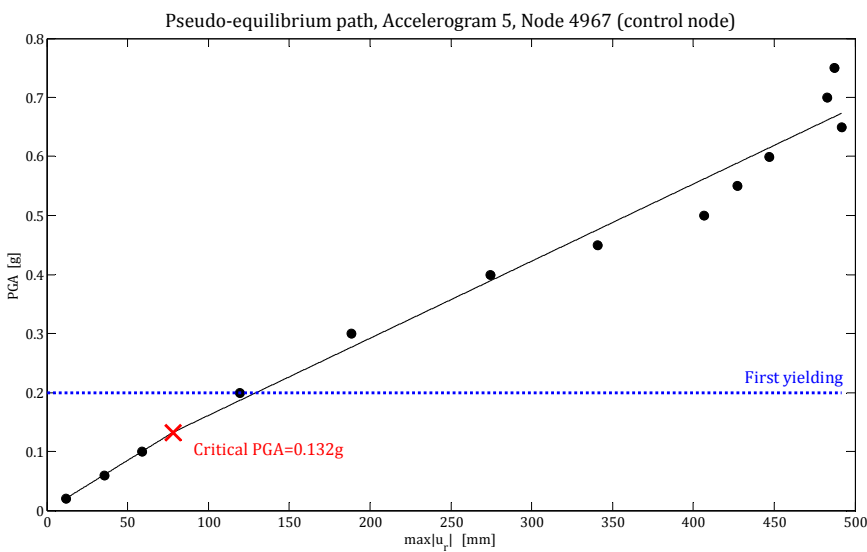


Figure 5.3.4.8: Pseudo-equilibrium path and first yielding of the tank subjected to accelerogram 5.

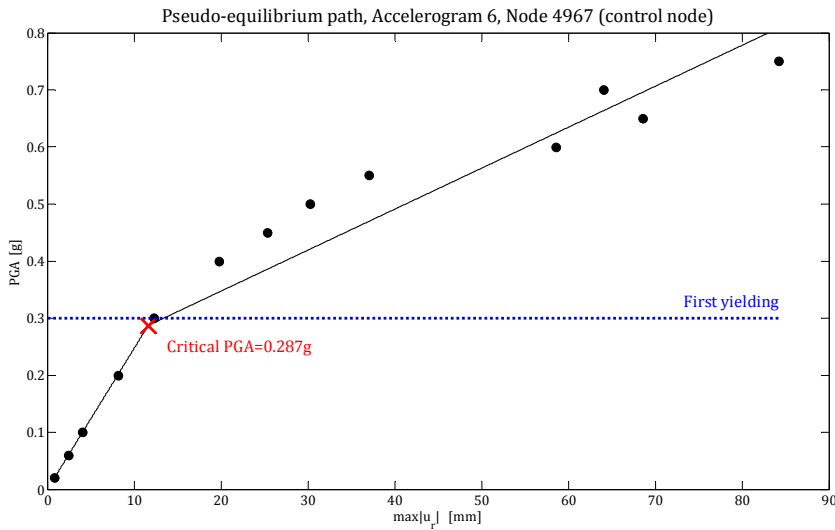


Figure 5.3.4.9: Pseudo-equilibrium path and first yielding of the tank subjected to accelerogram 6.

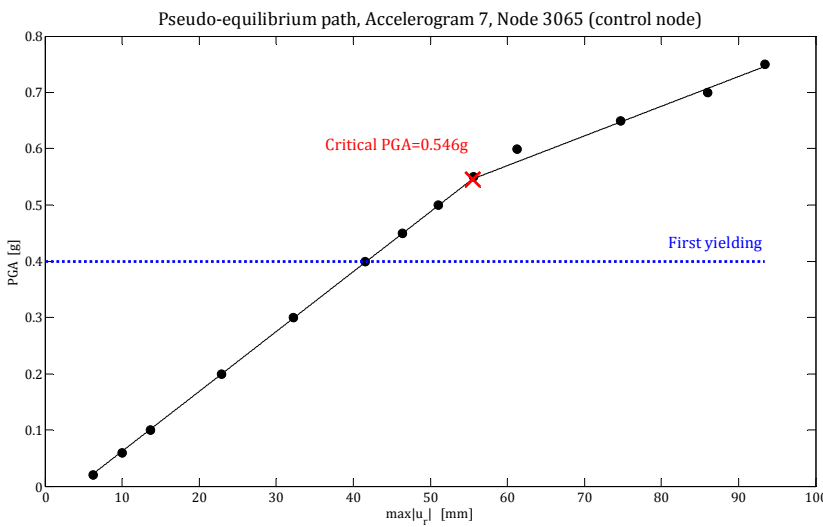


Figure 5.3.4.10: Pseudo-equilibrium path and first yielding of the tank subjected to accelerogram 7.

Except for the second and fourth accelerogram, the first yielding always occurs in a different region of the structure with respect to the control node of the pseudo-equilibrium curve. From Figures 5.3.4.4 to 5.3.4.10 it is evident how the structural failure is always influenced by the occurrence of plasticity somewhere in the structure, since PGA_y is always lower than PGA_{cr} , with the only exceptions of accelerogram three and five. In this cases the dynamic buckling load seems not to be influenced by plasticity; but since the change of slope is not so drastic, we are not sure that the critical PGA may be interpreted as the dynamic buckling load for this two cases. Due to this reason we can state that plasticity always modifies the structural behavior, drastically reducing the dynamic buckling load.

Finally, the average PGA_{cr} is computed in order to provide an estimate of the dynamic buckling load for the tank under consideration. This is possible since the Eurocode 8 states that if the dynamic response of the structure is obtained from at least seven nonlinear time-history

analyses with spectrum-compatible accelerograms, the average of the response quantities from all these analyses should be used as a representative or value.

$$\overline{PGA}_{cr} = \frac{0.541 + 0.441 + 0.106 + 0.284 + 0.132 + 0.287 + 0.546}{7} g = 0.334g \quad (5.3.4.1)$$

5.3.5 Failure modes

From the position of the control node and the plastic strain distribution along the tank it is possible to understand the nature of the failure mechanism. The contour plots of Figures 5.3.5.1 to 5.3.5.7 depict the plastic strain of the tank subjected to the accelerograms 1,2,4,6,7 scaled to a PGA of 0.75g. Figures 5.3.3.3 and 5.3.5.5 show the contour plots of the tank subjected to the accelerograms 3 and 5 scaled to PGA=0.3g, since for these accelerogram buckling seems to be independent from the first yielding. In these Figures is highlighted also the position of the control nodes, to which the pseudo-equilibrium paths of Section 5.3.4 are reported. The Figures refer to the time instant of the maximum radial displacement of the control node.

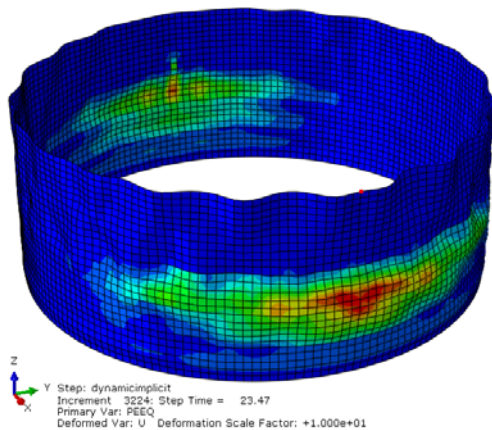
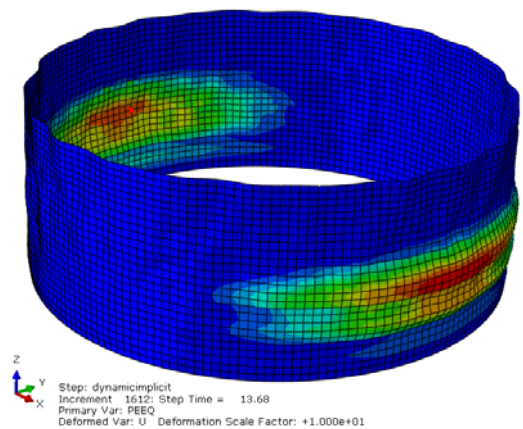


Figure 5.3.5.1: Equivalent plastic strain and control node of the tank subjected to accelerogram 1 (PGA=0.75g).

Figure 5.3.5.2: Equivalent plastic strain and control node of the tank subjected to accelerogram 2 (PGA=0.75g).



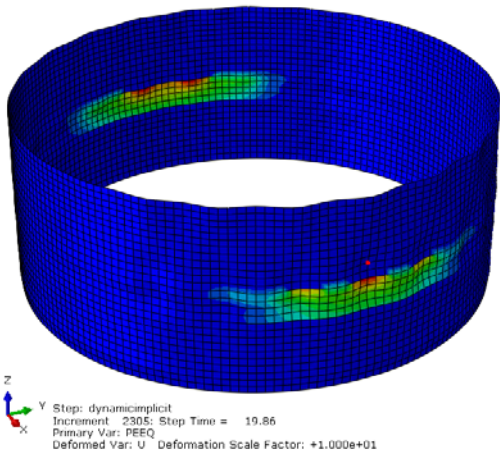


Figure 5.3.5.3: Equivalent plastic strain and control node of the tank subjected to accelerogram 3 (PGA=0.30g).

Figure 5.3.5.4: Equivalent plastic strain and control node of the tank subjected to accelerogram 4 (PGA=0.75g).

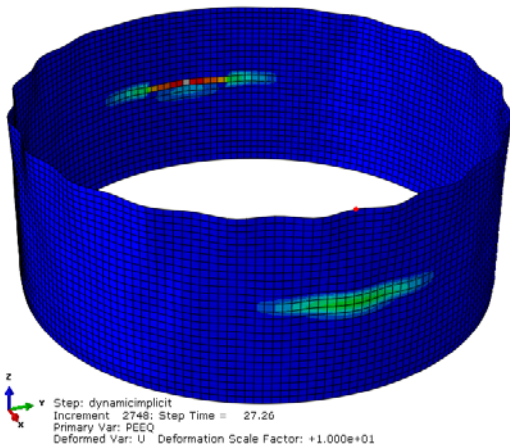
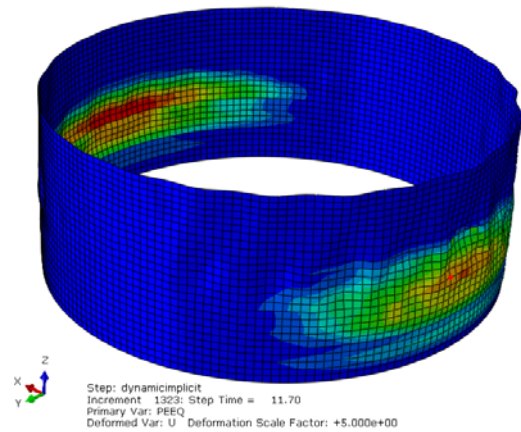
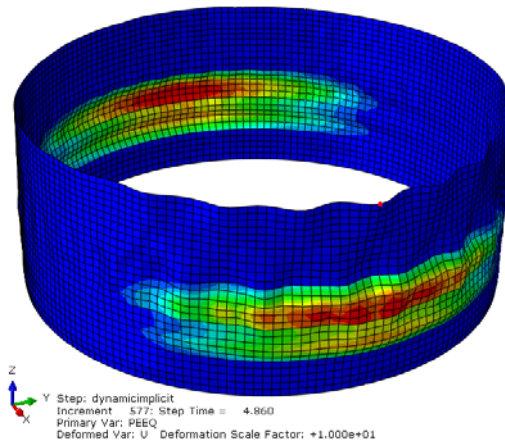


Figure 5.3.5.5: Equivalent plastic strain and control node of the tank subjected to accelerogram 5 (PGA=0.30g).

Figure 5.3.5.6: Equivalent plastic strain and control node of the tank subjected to accelerogram 6 (PGA=0.75g).



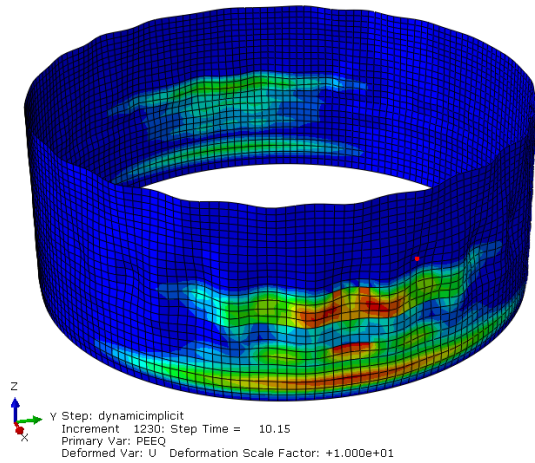


Figure 5.3.5.7: Equivalent plastic strain and control node of the tank subjected to accelerogram 7 (PGA=0.75g).

The Figures reveal that the control node is always in the upper-middle part of the structure, where no plasticity occurs even for the highest value of PGA analyzed, 0.75g. The only exceptions are represented by accelerograms two and four, for which the control node lies in a lower part of the tank. Only in this cases the failure mode is more similar to an elephant's foot buckling and may be referred as elastic-plastic buckling (Figure 5.3.5.8). In all the other cases the failure mode is characterized by secondary buckling at the upper-middle part of the structure, where the material is still elastic. We can conclude that the dominant failure mode is this secondary (or local) buckling, which is an elastic buckling mode. Nevertheless, in the light of what shown in Section 5.3.4, the dynamic buckling load is strongly influenced by the occurrence of plasticity in other parts of the structure, typically in the middle-low part.

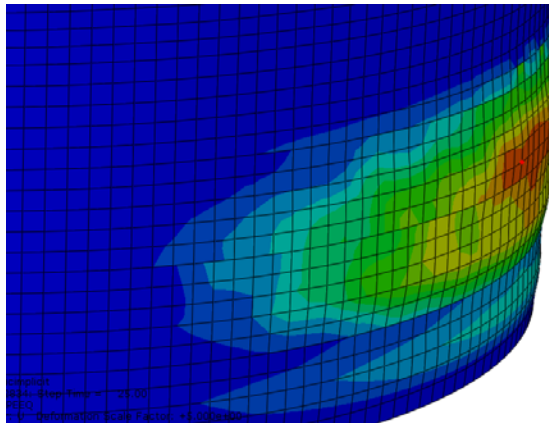


Figure 5.3.5.8: Elastic-plastic buckling of the tank subjected to accelerogram 4.

5.4 Fragility curves development

5.4.1 Generalities on fragility curves

In this Section, some considerations concerning the vulnerability of atmospheric storage tanks subjected to seismic actions are given. The seismic vulnerability is often characterized by a fragility curve (i.e., the probability of getting a specific limit state). Past studies dealing with seismic risk analysis and fragility curves development may be found in Iervolino [27], O'Rourke [35], Salzano [40] and Talaslidis [44].

The limit state considered herein is the dynamic buckling, and the probability of failure is intended to be the probability of having buckling for a fixed value of a certain ground motion intensity measure im , as expressed by equation 5.4.1.1:

$$p_f = P(IM_{cr} \leq im) \quad (5.4.1.1)$$

where IM_{cr} is the random variable representing those particular values of the intensity measure which produce buckling. The correct choice of an intensity measure (PGA, PGV, PSA, etc.) is of crucial importance in describing the structural response; studies on which is the best choice for liquid-storage tanks are carried out in Section 5.4.3. Equation 5.4.1.1 can be rewritten in terms of conditional probability as

$$p_f = P(\text{buckling} | IM = im) \quad (5.4.1.2)$$

The probability of failure of equation 5.4.1.1 is essentially the definition of the cumulative density function for the random variable IM_{cr} . Therefore it can be expressed as

$$p_f = F_{IM_{cr}}(im) \quad (5.4.1.3)$$

If we assume a log-normal distribution for IM_{cr} (see Cornell [9] and Talaslidis [44]), equation 5.4.1.3 becomes

$$p_f = \Phi \left[\frac{\ln(im) - \mu}{\sigma} \right] \quad (5.4.1.4)$$

where Φ is the standard normal CDF. Proceeding in this way, we are studying the seismic fragility of the tank with respect to dynamic buckling for the specific site where it is built (Milazzo). For this reason the ground motions adopted for the analysis were selected using information about the acceleration response spectrum at the site considered. Therefore even when PGA is used as intensity measure information about the spectra shape is implicitly taken into account.

The actual buckling probability in a given time interval can then be calculated by combining fragility with the seismic hazard function, H . This function essentially represents in the standard way the likelihood of various levels of future intense ground motions at the site, so it gives the probability that the ground motion intensity measure at the site will not be exceeded during a particular time period, as expressed by equation 5.4.1.5. In this particular function the uncertainties in earthquake position, earthquake size and ground motion parameter prediction are combined.

$$H(im) = P(IM \leq im) \quad (5.4.1.5)$$

Typically the hazard function is the result of a Poisson process, in which the Poisson distribution is used to calculate the probability of having one or more events N during the observation time interval t , given the mean occurrence rate λ .

$$P(N \geq 1) = 1 - e^{-\lambda t} \quad (5.4.1.6)$$

In this case, the hazard function H is

$$H = P(N \leq 1) = e^{-\lambda t} \quad (5.4.1.7)$$

An example of the so calculated hazard function is that of Figure 5.4.1.1, where the intensity measure is the PGA.

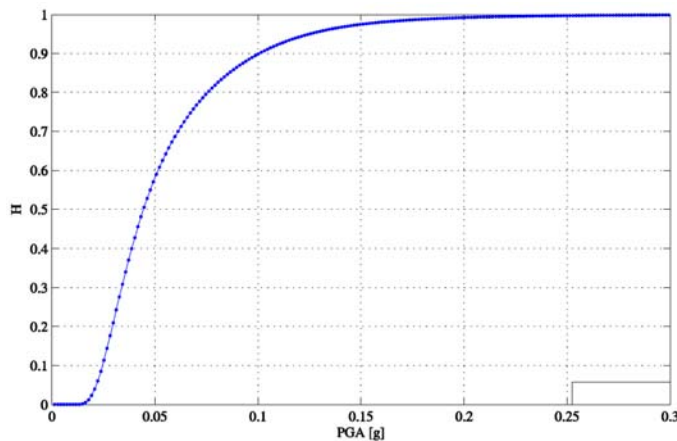


Figure 5.4.1.1: Hazard function.

Once the hazard function is known, the total probability theorem (Benjamim and Cornell, 1970) can be applied to find the probability of getting buckling P_{buck} during the observation time interval t at the site considered.

$$P_{buck} = \int_{-\infty}^{+\infty} P(buckling|IM = im) \cdot \frac{dH}{d(im)}(im)d(im) \quad (5.4.1.8)$$

5.4.2 New accelerograms and dynamic analyses

With the same criteria discussed in Section 5.2.3, a second group of response spectrum-compatible accelerograms is selected, in order to have more data to develop fragility curves. The search results are collected in Table 5.4.2.1 and plotted in Figures 5.4.2.1 to 5.4.2.7.

N ^o	Earthquake name	Station name	Duration [s]	PGA [g]	t _{PGA} [s]	M _W	R _{jb} [km]
8	Loma Prieta, California (1989), E-W comp.	Gilroy Array #1	40	0.410	3.43	6.93	8.84
9	San Fernando, LA (1971), N-S comp.	Old Seismo Lab	30	0.200	5.8	6.61	21.50
10	Whittier Narrows, LA (1987), E-W comp.	Pasadena-CIT Kresge Lab.	40	0.110	3.32	5.99	6.77
11	Northridge, LA (1994), E-W comp.	LA-Wonderland AVE	30	0.110	8.00	6.69	15.11
12	Irpinia, Italy (1980), N-S comp.	Sturnio	30	0.077	4.33	6.20	20.38
13	Northridge, LA (1994), N-S comp.	Pacoima Dam (downstr)	20	0.054	36.35	6.69	4.92
14	Northridge, LA (1994), N-S comp.	LA-Griffith Park Observatory	45	0.160	8.89	6.69	21.20

Table 5.4.2.1: Details about the seven selected accelerograms: earthquake and station name, duration, peak ground acceleration, time instant at which the PGA occurs, moment magnitude, Joiner-Boore distance.

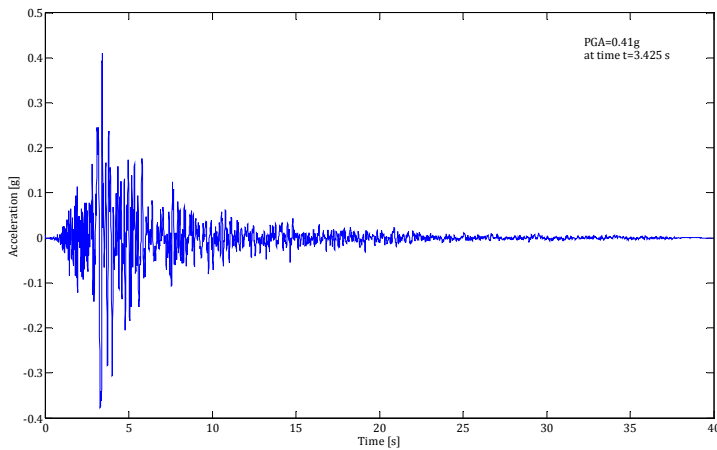


Figure 5.4.2.1: Accelerogram 8.

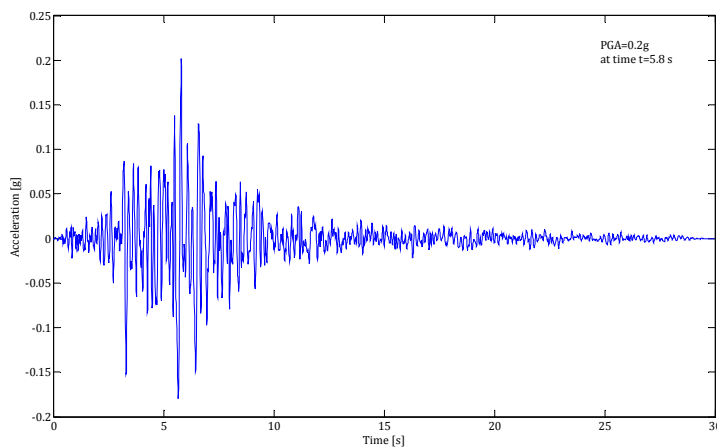


Figure 5.4.2.2: Accelerogram 9.

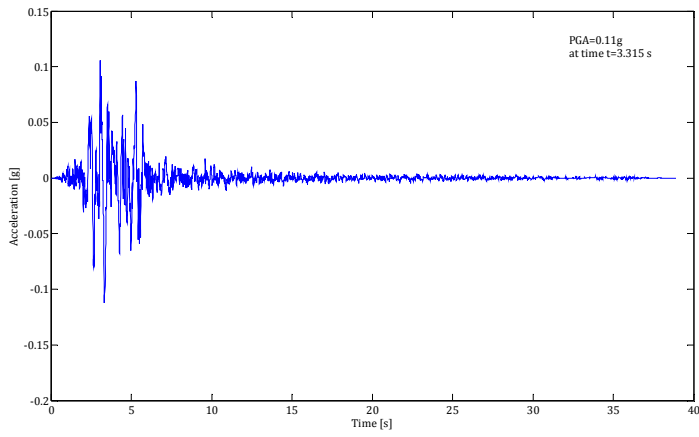


Figure 5.4.2.3: Accelerogram 10.

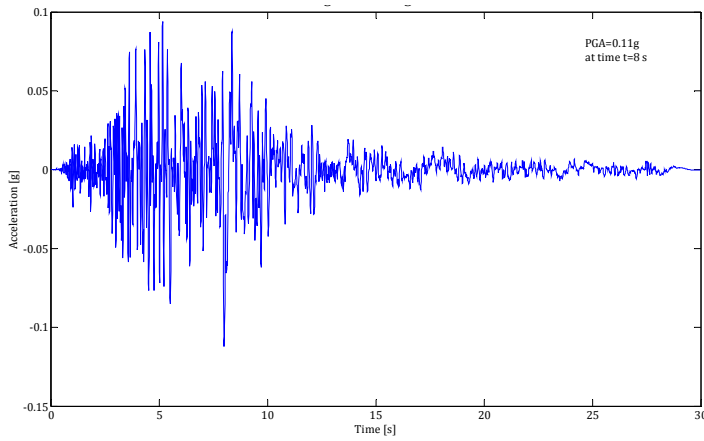


Figure 5.4.2.4: Accelerogram 11.

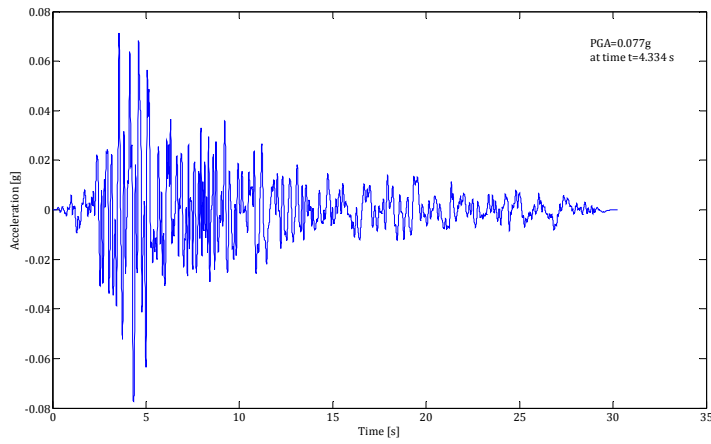


Figure 5.4.2.5: Accelerogram 12.

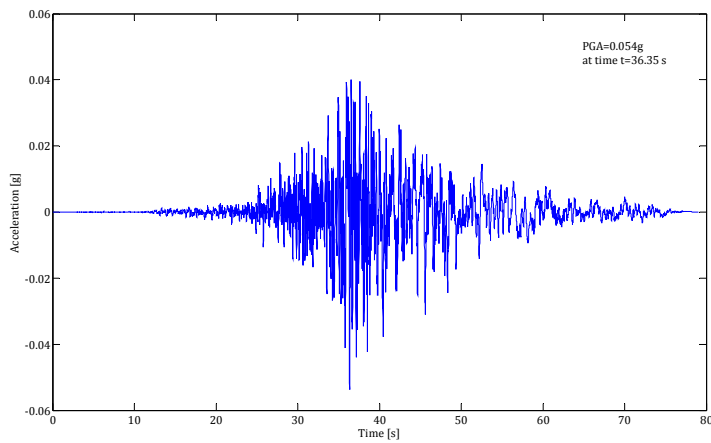


Figure 5.4.2.6: Accelerogram 13.

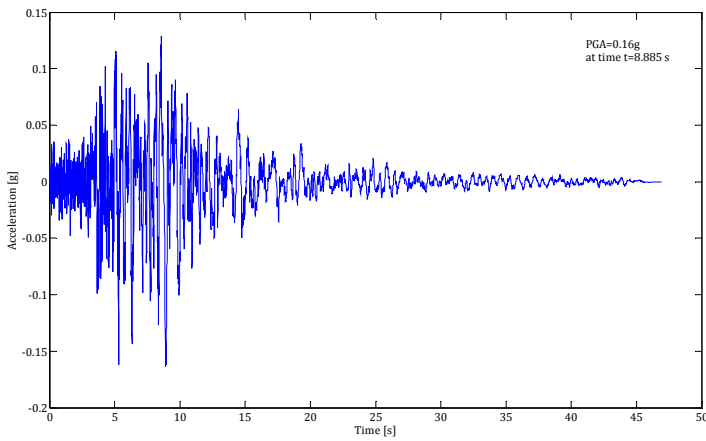


Figure 5.4.2.7: Accelerogram 14.

Each accelerogram is scaled and used for an incremental dynamic analysis, as already done for the first set of accelerograms. Then, the Budiansky-Roth criterion is used to calculate the dynamic buckling loads. The results are collected in Table 5.4.2.2, together with the results of the first group of accelerograms. The pseudo-equilibrium paths of the second group of accelerograms are plotted in Figures 5.4.2.8 to 5.4.2.14.

Accelerogram	PGA _{cr} [g]
1	0.541
2	0.441
3	0.106
4	0.284
5	0.132
6	0.287
7	0.546
8	0.307
9	0.412
10	0.589
11	0.393
12	0.216
13	0.431
14	0.183

Table 5.4.2.2: Buckling load for the tank subjected to all 14 accelerograms.

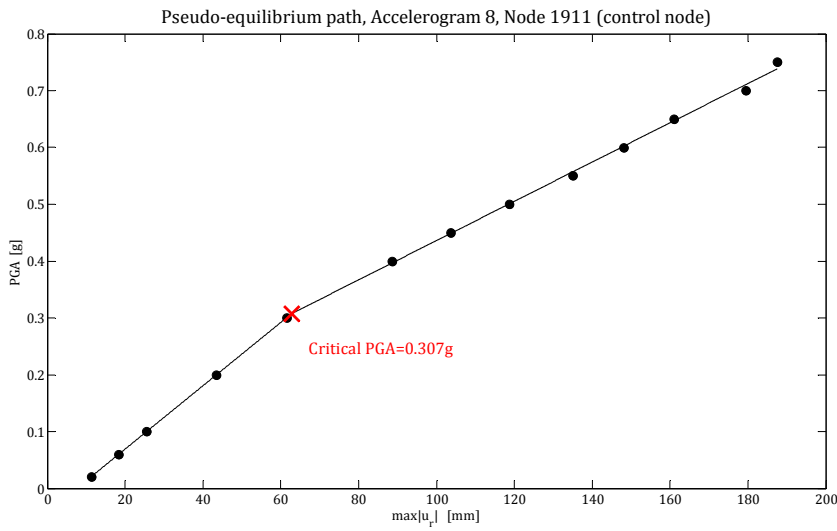


Figure 5.4.2.8: Pseudo-equilibrium path of the tank subjected to accelerogram 8.

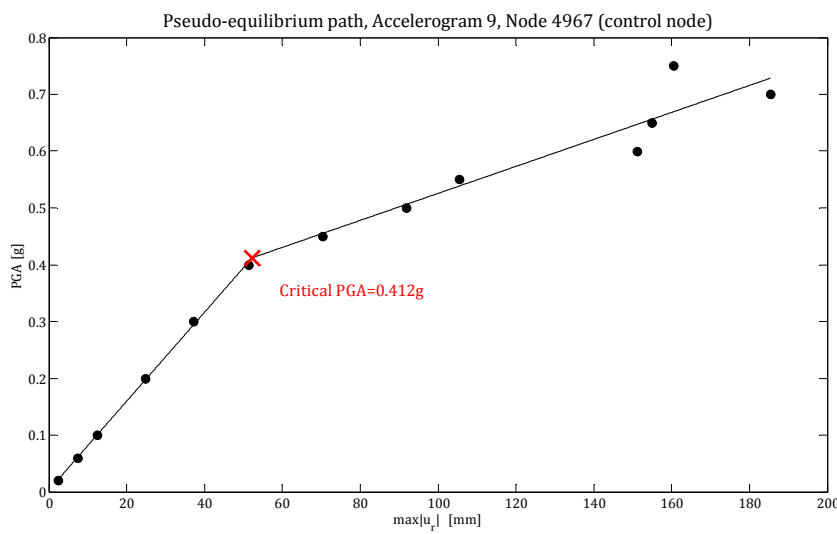


Figure 5.4.2.9: Pseudo-equilibrium path of the tank subjected to accelerogram 9.

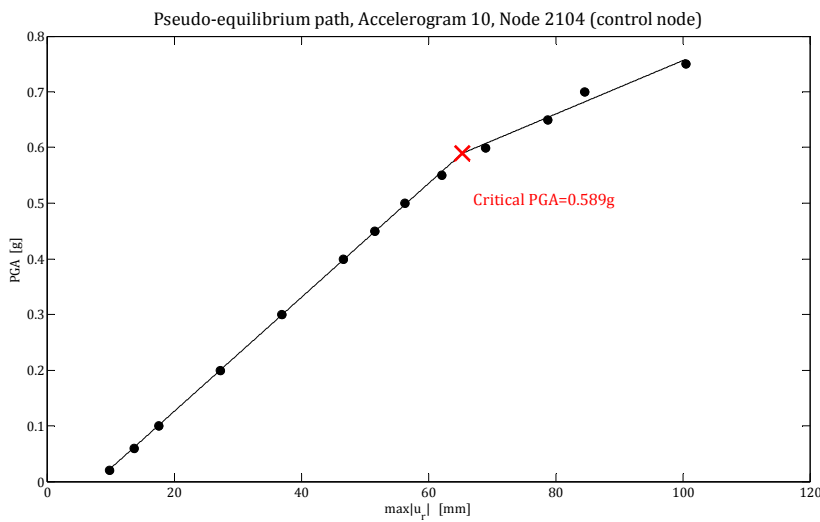


Figure 5.4.2.10: Pseudo-equilibrium path of the tank subjected to accelerogram 10.

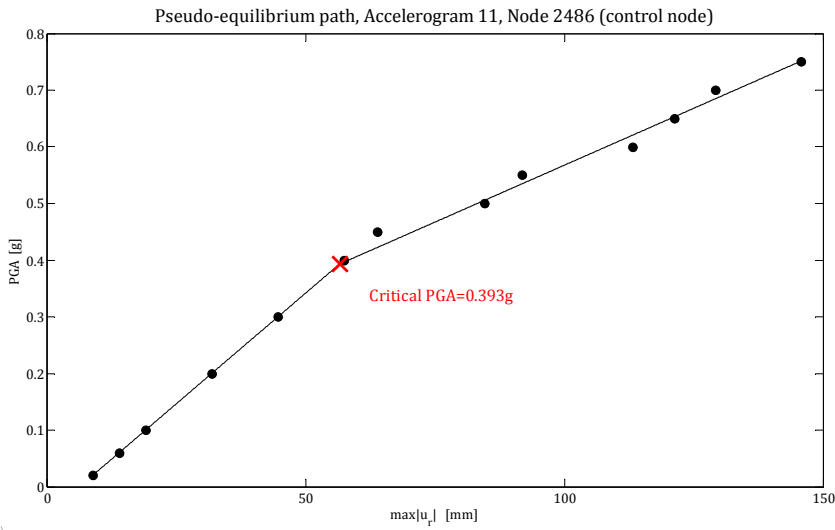


Figure 5.4.2.11: Pseudo-equilibrium path of the tank subjected to accelerogram 11.

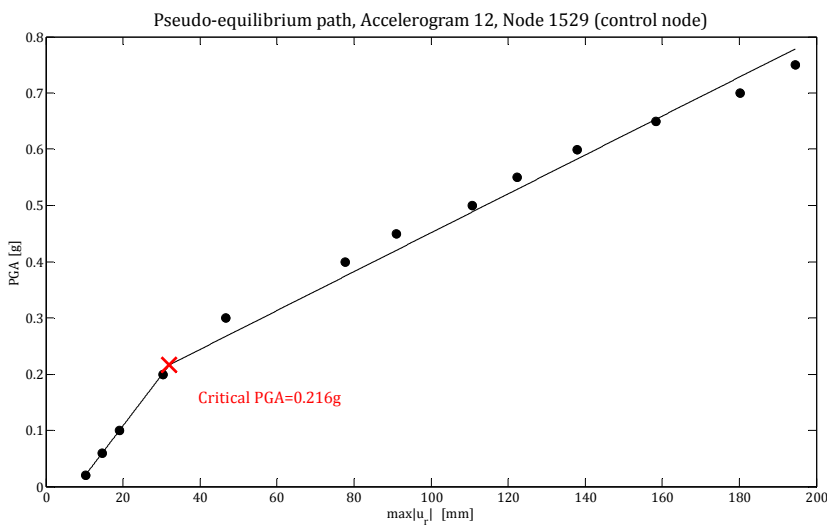


Figure 5.4.2.12: Pseudo-equilibrium path of the tank subjected to accelerogram 12.

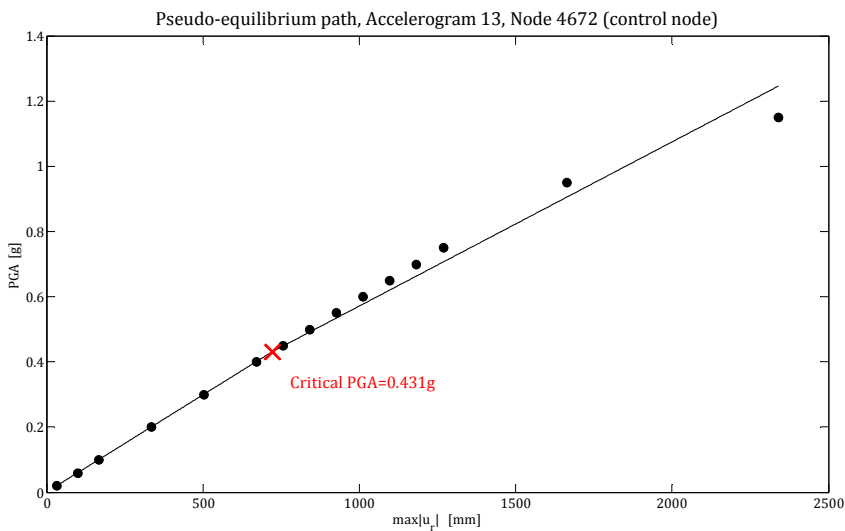


Figure 5.4.2.13: Pseudo-equilibrium path of the tank subjected to accelerogram 13.

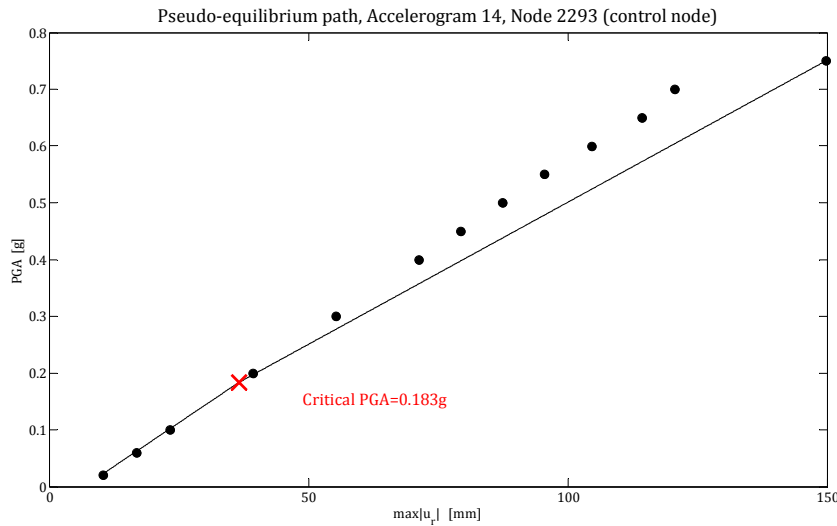


Figure 5.4.2.14: Pseudo-equilibrium path of the tank subjected to accelerogram 14.

5.4.3 Efficiency of ground motion intensity measures

According to Tothong [46], the ground motion intensity measure is, from the engineering perspective, the quantification of the characteristics of a ground motion that are important to the nonlinear structural response, e.g. the amplitude and frequency content, or spectral shape (response spectral ordinates at multiple periods), of the ground motion. Therefore, an IM that contains information about spectral shape, as well as information about the structure, can be expected to be preferable and to lead to more appropriate scale factors when scaling (in amplitude) ground motions to target values of the IM. Note that scaling earthquake records are often needed because, by definition, the rare earthquake events considered in structural design and evaluation are scarce, and therefore, few of them have been recorded by seismometers. From a seismology perspective, on the other hand, the IM is used to quantify the ground motion hazard at a site due to seismicity in the region; hence, the feasibility of computing this seismic hazard in terms of an IM must also be considered.

Geophysicists and structural engineers use to classify earthquakes on the basis of two classes of parameters such as “ground parameters” and “structural dynamic affecting factors” (Chopra, 1995). Ground parameters refer to the intensity measures characterising the ground motion: PGA or alternatively peak ground velocity PGV. Structural affecting factors usually refer to the dynamic amplification induced on a single degree of freedom system with the same period of the analysed structure (first mode spectral acceleration $PSA(T_1)$), although experimental investigations have shown that different parameters are needed if the effects of earthquake on structures would be accurately reproduced by structural analysis. For instance, in seismic analysis of piping system PGV is commonly used, whereas PGA is more useful when steel storage tanks are under investigation (Eidinger, 2001). But since for tanks, in contrast to

framed structures, there are not specific studies in literature about the efficiency of the different ground motion parameters, this Section tries to give a contribution to this subject.

Prior to study in detail the fragility with respect to the dynamic buckling, the correlation between the structural response in terms of radial displacement and the PGA or PSA is analyzed. To this purpose, the maximum radial displacements (i.e. the points that make up the fourteen pseudo-equilibrium paths) are now plotted in a logarithmic plane both in terms of PGA (Figure 5.4.3.1) and in terms of PSA (Figure 5.4.3.2), Baker [3]. Then they are fitted by means of a linear regression model, with the aim of finding a correlation between the radial displacement and the two ground motion parameters.

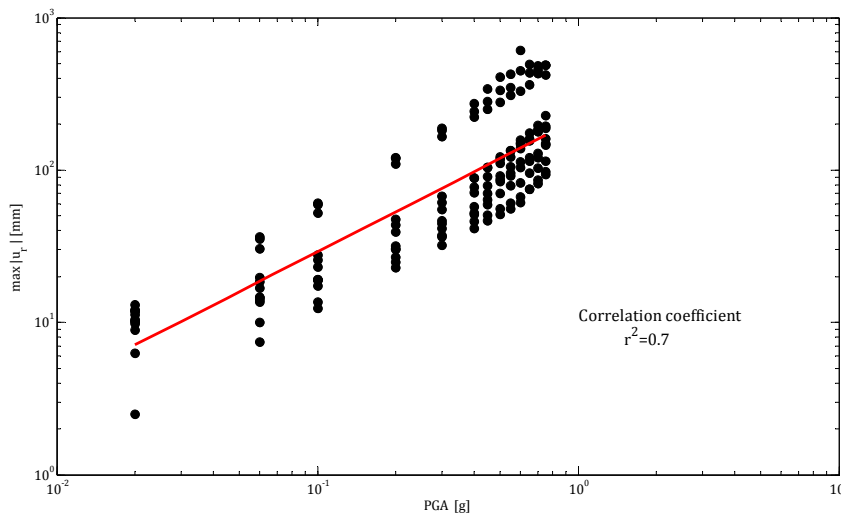


Figure 5.4.3.1: Maximum radial displacements vs PGA, log scale.

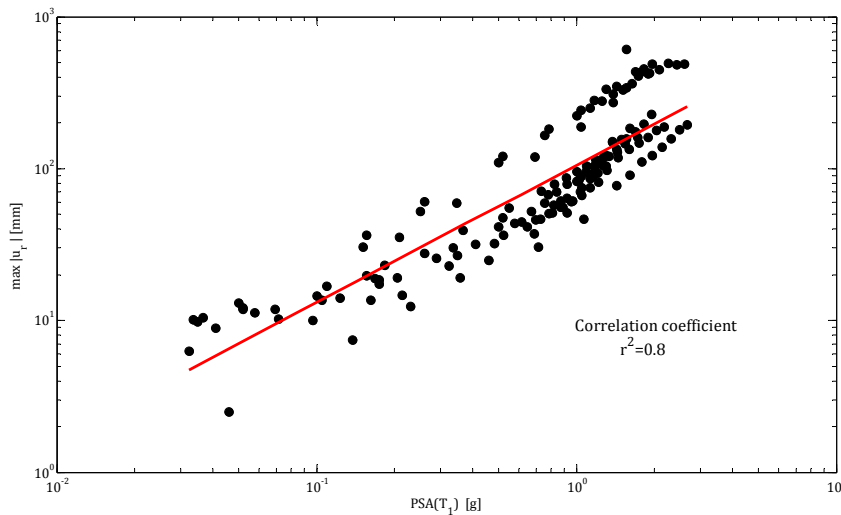


Figure 5.4.3.2: Maximum radial displacements vs PSA, log scale.

From Figures 5.4.3.1 and 5.4.3.2 we can conclude that the structural response seems to be better correlated with the PSA, and therefore PSA is more efficient than PGA when the maximum radial displacement is concerned.

5.4.4 Fragility curves

As already mentioned in Section 5.4.1, the fourteen values of critical PGA collected in Table 5.4.2.2 are used to find the first and second moment (mean μ and standard deviation σ) of a log-normal distribution. This is done automatically with the MATLAB command *normfit*. Note that, just because the distribution is log-normal, the natural logarithm of the PGA_{cr} values must be used. The results are:

$$\mu_{PGA} = 1.1727 \quad (5.4.4.1a)$$

$$\sigma_{PGA} = 0.5346 \quad (5.4.4.1b)$$

$$\delta_{PGA} = \sigma_{PGA}/\mu_{PGA} = 0.4559 \quad (5.4.4.1c)$$

Once the mean and the standard deviation are known it is possible to compute the CDF curve. This is done with the MATLAB command *normcdf*. The so computed curve is plotted in Figure 5.4.4.1 together with the empirical (or sampling) CDF.

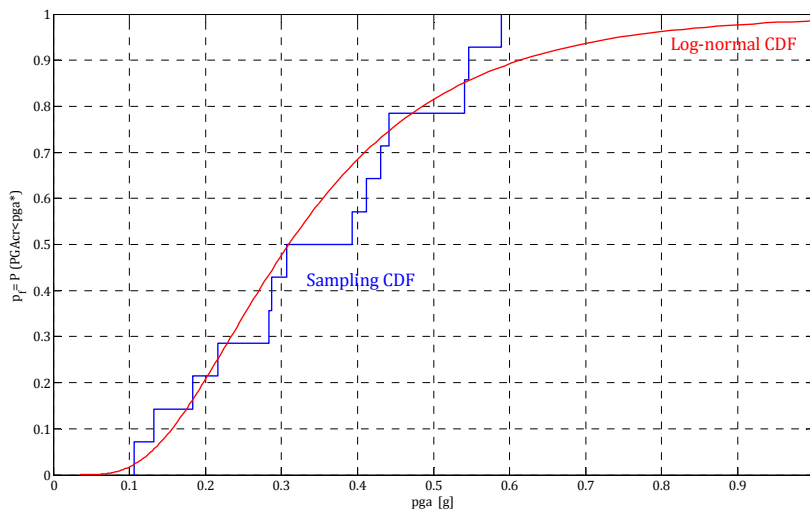


Figure 5.4.4.1: Fragility curve in terms of PGA.

The same plot can be obtained in terms of spectral acceleration. From Section 5.1.2 the fundamental period of the structure is $T_1=0.217$ seconds. The spectral accelerations corresponding to this period are calculated from the 5% damped response spectra of the fourteen accelerograms. The original values are collected in Table 5.4.4.1. Then, starting from the PGA_{cr} values, the original $PSA(T_1)$ are scaled in order to obtain the $PSA_{cr}(T_1)$ values, also reported in Table 5.4.4.1.

Accelerogram	PSA(T ₁) [g]	PSA _{cr} (T ₁) [g]
1	0.162	1.407
2	0.726	0.738
3	0.143	0.266
4	0.156	0.737
5	0.207	0.458
6	0.220	0.706
7	0.078	0.881
8	1.184	0.889
9	0.464	0.946
10	0.195	1.025
11	0.230	0.805
12	0.275	0.770
13	0.095	0.783
14	0.296	0.335

Table 5.4.4.1: Original and critical spectral accelerations corresponding to the first period of vibration of the tank.

As already done for the PGA_{cr}, also the PSA_{cr} is assumed to be a log-normally distributed random variable. The mean and standard deviation are computed from the natural logarithm of the PSA_{cr}(T₁) values. The results are:

$$\mu_{PSA} = 0.3437 \tag{5.4.4.2a}$$

$$\sigma_{PSA} = 0.4419 \tag{5.4.4.2b}$$

$$\delta_{PSA} = \sigma_{PSA} / \mu_{PSA} = 1.2857 \tag{5.4.4.2c}$$

The resulting fragility curve in terms of PSA is plotted in Figure 5.4.4.2 and the comparison with the curve in terms of PGA is highlighted in Figure 5.4.4.3.

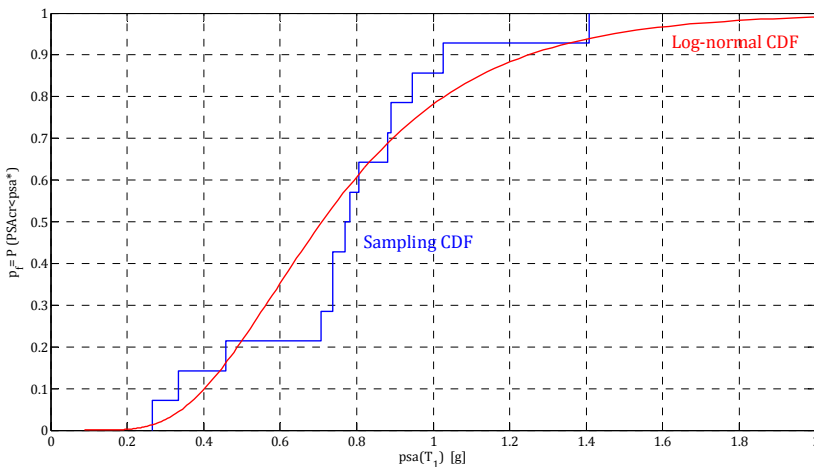


Figure 5.4.4.2: Fragility curve in terms of PSA.

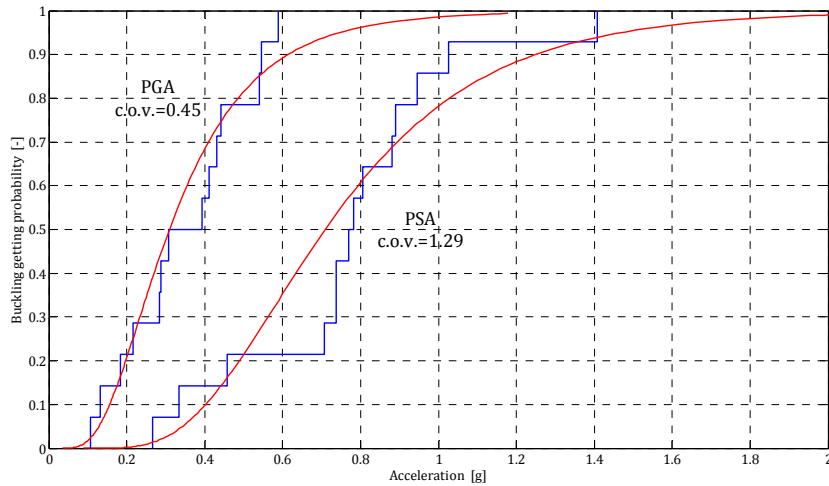


Figure 5.4.4.3: Fragility curves.

Figures 5.4.4.1 and 5.4.4.2 show that both for the PGA and PSA the analytical curve seems to fit quite well the sampling one; this implies that the log-normal distribution model is well suited to the buckling problem of liquid-storage tanks. Figure 5.4.4.3 shows that the buckling problem is better correlated and described by the PGA rather than the PSA. In fact, the fragility curve for the PGA covers a narrower range of acceleration values and its coefficient of variation is about one third compared to that of the PSA curve. For these reasons we can conclude that, in spite of the higher efficiency of PSA when considering maximum radial displacements (see Section 5.4.3), less uncertainty is associated to the buckling problem described by the PGA rather than the PSA.

Concluding remarks

6.1 Conclusions

The conclusions of this Section are related only to the second part of the thesis, as those on the topics covered in Part I have been reported chapter by chapter in that Part. The main conclusions resulting from the dynamic analyses carried out in Part II are:

- The added mass model for the tank considered provides results in full agreement with those found in the literature for tanks of similar proportions. We refer of course to the dynamic properties of the model (frequencies, periods, impulsive mass ratio, etc.).
- The modal analysis carried out at Section 5.1 shows that, contrary to what expressed by some studies in the literature, the effect of pre-stress states on the impulsive modes of vibration is negligible, at least for broad tanks. In fact, such effect starts to become significant for $n > 4$ (n =number of circumferential wave number). But for broad tanks the significant vibration modes are all characterized by $n=1$ (beam-type modes). Any shell modal form ($n \neq 1$) is among those fundamental for the structure.
- Dynamic simulations of Section 5.2 shows that the added mass model allow us to capture two types of buckling modes discussed in the first part of the thesis: elephant's foot buckling and secondary buckling. However, the dominant failure mode is the secondary buckling at the upper-middle part of the shell rather than the formation of the elephant's foot bulge at the middle-low part. The third type of buckling (diamond shape buckling) is not captured by our model, but this can be explained by the fact that it is typical of tanks in which the annular strips are subjected to low tension (limit case: empty tank subjected only to horizontal excitation). In this case the annular strips do not stiffen the vertical strips, which buckle due to the high compression generated by the overturning moment.
- The secondary buckling is an elastic buckling mode: this is proved by means of linear-elastic analyses. Conversely, the elephant's foot buckling is an elastic-plastic buckling mode. It always occurs in a yielded region of the structure, typically located at the mid-height where there is a drastic reduction in the thickness.

- Even if the secondary buckling is an elastic buckling mode it is strongly influenced by the occurrence of plasticity in other parts of the structure. This is proved by applying the Budiansky-Roth criterion to the results of elastic and elastic-plastic analyses. With such criterion an estimate of the dynamic buckling load, in terms of critical peak ground acceleration, is provided. The comparison between the pseudo-equilibrium paths obtained from elastic and elastic-plastic analyses reveal that the buckling load is strongly reduced by the occurrence of plasticity. Furthermore, the average dynamic buckling load corresponds to a PGA_{cr} of 0.33g, so that this mode of failure should be of great concern to the designer, although not yet explicitly covered by current standards.
- The most efficient ground motion intensity measure (i.e. the parameter better correlated with the structural response) is the pseudo-acceleration at the first natural frequency of the tank-fluid system. But despite this, the fragility curve associated with the PSA has an higher coefficient of variation than the curve in terms of PGA. Then we can conclude that, even if globally the structural response seems to be more correlated with the PSA, the uncertainties associated to the buckling phenomenon are less if this phenomenon is described in terms of PGA.

6.2 Future works

Possible future works may be divided into two categories: (a) improvements to this thesis and correction of possible errors and inaccuracies, (b) development and deepening of the results obtained in this thesis. To the first category belong:

- Model refinement. To make the model more realistic and similar to liquid-storage tanks commonly used in industrial plants, a roof structure must be added. In addition to this, also stiffening elements like roof rafters, ring beams and interior columns are sometimes employed. Also a base plate, or in general a foundation system, can be added. Alternatively, a possible way to account for the base plate, is to add rotational springs at the base; the stiffness of such springs can be computed as the flexural stiffness of a plate element.
- Extension of the seismic excitation to the tridimensional case. In particular, it should be interesting to include in the base excitation the vertical component of the ground motion since it may modify the failure mode of the structure. In fact, it will increase the hoop stresses, making the elephant's foot buckling the dominant failure mode.

Suggestions on the second category are:

- Verify how much the structural response depends on the base condition. As a first attempt, the base clamping may be replaced by a pinned constraint. But in this optic, the best thing would be to eliminate the constraint at the base and directly study the interaction with the underlying soil, creating also for the soil a finite element model with the correct mechanical properties. In this way the results obtained can be generalized for different soil categories.
- In the present work the added mass has been computed from pressure distributions of rigid tanks and it has been normalized with respect to the normal acceleration. Proceeding in this way the temporal variation disappears and the added mass does not vary during the simulation. As already mentioned in Section 1.3.3 this approach is particularly correct for broad tanks, where the pressure does not change much depending on whether the tank is assumed to be rigid or flexible. On the contrary, for slender tanks, the pressure distribution changes for rigid and flexible tanks. So, for this tank category, calculate the added mass from rigid impulsive pressure is an error because for flexible structures the added mass depends on the flexibility of the structure itself. So it should be correct to calculate it from the flexible pressure component but this implies to include the spectral acceleration in the expression of the added mass which therefore can not be normalized anymore with respect to the ground acceleration. Proceeding in this way the added mass varies with time and so it varies during a time-history analysis. In a finite element framework this leads to the need to implement a mass matrix that changes during the analysis.
- Compare the results obtained from incremental dynamic analyses on the added mass model of the tank with the results of a quasi-static analysis on the same tank, but in which pressure eigenforms are used as equivalent loads in order to model the fluid. This type of analysis may be easily carried out with the so called Riks method, implemented in ABAQUS/Standard. Such method belongs to the family of arc-length methods. In this case a quasi-static solution can be obtained only if the magnitude of the load does not follow a prescribed history; it must be part of the solution. So, the hydrodynamic loads are defined in their form and then they are increased proportionally during the analysis. By monitoring the load-displacement curve of some points of the structure it is possible to understand which is the load multiplier that produce buckling. This load, if interpreted in terms of PGA, can be compared to the critical PGAs obtained in this thesis by means of the Budiansky-Roth criterion.

Appendix A

The equation of motion for the fluid (equation 1.2.2.1) is a Laplace's equation. In mathematics, Laplace's equation is a second-order partial differential equation often written as:

$$\nabla^2 \phi = 0 \quad (\text{A.1})$$

in which ∇^2 is the Laplace operator. Equation A.1 may be written in spherical coordinates x, y, z

$$\frac{\partial^2 \phi}{\partial x^2} + \frac{\partial^2 \phi}{\partial y^2} + \frac{\partial^2 \phi}{\partial z^2} = 0 \quad (\text{A.2})$$

or in cylindrical coordinates r, ϑ, z

$$\frac{\partial^2 \phi}{\partial r^2} + \frac{1}{r} \frac{\partial \phi}{\partial r} + \frac{1}{r^2} \frac{\partial^2 \phi}{\partial \vartheta^2} + \frac{\partial^2 \phi}{\partial z^2} = 0 \quad (\text{A.3})$$

In mathematics, Bessel functions are canonical solutions $y(x)$ of Bessel's differential equation:

$$x^2 \frac{d^2 y}{dx^2} + x \frac{dy}{dx} + (x^2 - \alpha^2)y = 0 \quad (\text{A.4})$$

for an arbitrary real or complex number α (the order of the Bessel function); the most common and important cases are for α an integer or half-integer. Bessel functions are also known as cylinder functions or cylindrical harmonics because they arise also when finding separable solutions to Laplace's equation in cylindrical or spherical coordinates. Bessel functions are therefore especially important for many problems of wave propagation and static potentials. In solving problems in cylindrical coordinate systems, one obtains Bessel functions of integer order ($\alpha=n$); in spherical problems, one obtains half-integer orders ($\alpha=n+1/2$).

Bessel functions of the first kind, denoted as $J_\alpha(x)$, are solutions of Bessel's differential equation that are finite at the origin ($x = 0$) for integer α , and diverge as x approaches zero for negative non-integer α . It is possible to define the function by its Taylor series expansion around $x = 0$:

$$J_\alpha(x) = \sum_{m=0}^{\infty} \frac{(-1)^m}{m! \Gamma(m + \alpha + 1)} \left(\frac{1}{2}x\right)^{2m+\alpha} \quad (\text{A.5})$$

where $\Gamma(z)$ is the gamma function, a generalization of the factorial function to non-integer values. The graphs of Bessel functions (Figure A.1) look roughly like oscillating sine or cosine functions that decay proportionally to $1/\sqrt{x}$, although their roots are not generally periodic, except asymptotically for large x .

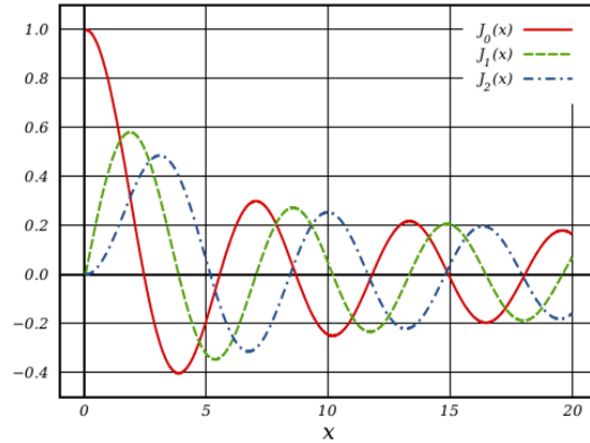


Fig. A.1: Plot of the Bessel function of the first kind, for integers order $\alpha=0,1,2$.

The Bessel functions are valid even for complex arguments x , and an important special case is that of a purely imaginary argument. In this case, the solutions to the Bessel equation are called the modified Bessel functions of the first kind and are defined as

$$I_\alpha(x) = i^{-\alpha} J_\alpha(ix) = \sum_{m=0}^{\infty} \frac{1}{m! \Gamma(m + \alpha + 1)} \left(\frac{1}{2}x\right)^{2m+\alpha} \tag{A.6}$$

The series expansion for $I_\alpha(x)$ is thus similar to that for $J_\alpha(x)$, but without the alternating $(-1)^m$ factor. Unlike the ordinary Bessel functions, which are oscillating as functions of a real argument, I_α is an exponentially growing function. Like the ordinary Bessel function J_α , the function I_α goes to zero at $x = 0$ for $\alpha > 0$ and is finite at $x = 0$ for $\alpha = 0$.

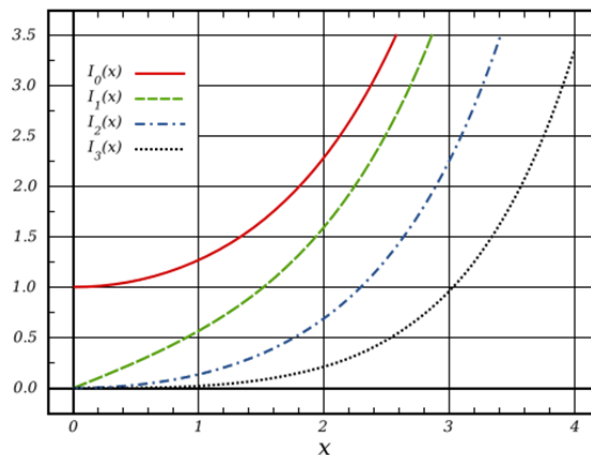


Fig. A.2: Plot of the modified Bessel function of the first kind, for integers order $\alpha=0,1,2$.

Appendix B

Here the MATLAB code used for the added mass calculation is reported. However, these code lines are also included in the Appendices C and D, where the codes used to generate the complete model for ABAQUS are reported.

```
%-----%
%                               EARTHQUAKE ENGINEERING                               %
%                               Added mass model of an anchored steel tanks           %
%                               Added mass calculation                               %
%-----%
densLiquido=1e-09;      % Mass density of the stored liquid [t/mm3]
densTank=7.85e-09;    % Mass density of the shell [t/mm3]
g=9810;               % gravity acceleration [mm/s2]
altezza=12089;        % Height of the tank walls [mm]
altezzaLiquido=10880; % Height of the stored liquid [mm]
raggio=15240;         % Tank radius [mm]
Esize=500;            % Initial finite element size [mm]
virole=[2425,12.7;
        4841,9.5;
        7257,7.9;
        9673,7.9;
        altezzaLiquido,7.9;
        altezza,7.9]; % Heights of the different tank strips (referred to
z=0) and their associated thickness [mm]

EsizeAlt=[];          % Effective finite element size in the vertical
direction [mm]
nDivisioni=ceil(virole (1,1)/Esize);
quote=linspace (0,virole(1,1),nDivisioni+1)';
EsizeAlt(1,1)=quote(2)-quote(1);
for i=2:size(virole,1)
    nDivisioni=ceil((virole(i,1)-virole(i-1,1))/Esize);
    tmpQuote=linspace (virole(i-1,1),virole(i,1),nDivisioni+1)';
    EsizeAlt(i,1)=tmpQuote(2)-tmpQuote(1);
    quote=[quote;tmpQuote(2:end)];
end
quoteMasse=quote(quote<=altezzaLiquido);
divAlt=length(quote)-1;
divCirc=ceil(2*pi*raggio/Esize);

cc1=2/(1.841^2-1)*cosh
(1.841*altezzaLiquido/raggio*quoteMasse/altezzaLiquido)/cosh(1.841*altezzaLiquido/raggio);
cc2=2/(5.311^2-1)*cosh
(5.311*altezzaLiquido/raggio*quoteMasse/altezzaLiquido)/cosh(5.311*altezzaLiquido/raggio);
cc3=2/(8.536^2-1)*cosh
(8.536*altezzaLiquido/raggio*quoteMasse/altezzaLiquido)/cosh(8.536*altezzaLiquido/raggio);
ci=1-(cc1+cc2+cc3);
```

```

primaQuota=1;
mi=zeros(size(quoteMasse));
for i=1:size(virole,1)-1
    ultimaQuota=find(quoteMasse==virole(i,1),1);
    miTmp=densLiquido*raggio*ci(primaQuota:ultimaQuota)*EsizeAlt(i)*Esize;
%[t]
    miTmp(1)=miTmp(1)/2;
    miTmp(end)=miTmp(end)/2;
    mi(primaQuota:ultimaQuota)=mi(primaQuota:ultimaQuota)+miTmp;
    primaQuota=ultimaQuota;
end

%-----%
%                               MASS PROPERTIES OF THE MODEL                               %
%-----%
V=pi*(raggio^2-(raggio-virole(1,2))^2)*(virole(1,1));
Mtank=densTank*V;
for i=2:length(virole)
    V=pi*(raggio^2-(raggio-virole(i,2))^2)*(virole(i,1)-virole(i-1,1));
    Mtank=Mtank+densTank*V;
end
Mtank                % total mass of the shell
mi_tot=sum(mi)*(divCirc-1) ; % total added mass
mres=sum(mi(2:end)./Esize); % added mass along a meridian [t/mm]
Mi=pi*raggio*mres    % horizontal component of the impulsive mass [t]
Mliq=pi*raggio^2*altezzaLiquido*densLiquido; % total liquid mass [t]
Mir=Mi/Mliq          % impulsive mass ratio
Mmodel=Mtank+mi_tot  % total mass of the model [t]
Mmodel_x=Mtank+Mi    % horizontal component of the mass of the model [t]

% plot
h1=figure(1);
set(gcf,'color',[1 1 1]); % colore sfondo bianco
box on
hold on
grid off
plot(mi,quoteMasse,'k-o')
%h2=title('ADDED MASS ALONG A MERIDIAN LINE');
%set(h2,'color','black','fontsize',20,'fontname','cambria');
h4=xlabel('Added Mass [t]');
set(h4,'color','black','fontsize',15,'fontname','cambria'); h5=ylabel('z
[mm]');
set(h5,'color','black','fontsize',15,'fontname','cambria');
set(gca,'fontsize',15,'fontname','cambria','LineWidth',1);
%gtext(['Cumulated EMx=',num2str(chop(CumulatedY1,4)), '
[t]'], 'FontName','cambria','FontSize',15)

```


Appendix C

Here the MATLAB code used for the complete model generation is reported. With this code it is possible to set three different analysis steps (or even just some of them): the static step, the frequency extraction step and the dynamic implicit one. If the dynamic step is switched on, it requires the definition of an accelerogram in an external *.txt* file, saved in the same folder of the MATLAB code. The *.inp* file can be imported and run in ABAQUS or directly run with ABAQUS-Command.

```
%-----%
%
%                               EARTHQUAKE ENGINEERING
%                               Added mass model of an anchored steel tanks
%                               Generation of an input text-file for ABAQUS/Standard
%-----%
outFileName='prova_STD.inp';
%-----%
%                               INPUT DATA
%-----%
aggiungiMasse=1;           %(1=yes,0=no)
StepStatico=1;            %(1=yes,0=no)
EigenvalueAnalysis=1;    %(1=yes,0=no)
ImplicitDynamicStep=1;   %(1=yes,0=no)
densLiquido=1e-09;       % Mass density of the stored liquid [t/mm3]
densTank=7.85e-09;      % Mass density of the shell [t/mm3]
g=9810;                  % gravity acceleration [mm/s2]
altezza=12089;           % Height of the tank walls [mm]
altezzaLiquido=10880;    % Height of the stored liquid [mm]
raggio=15240;            % Tank radius [mm]
Esize=500;               % Initial finite element size [mm]
virole=[2425,12.7;
        4841,9.5;
        7257,7.9;
        9673,7.9;
        altezzaLiquido,7.9;
        altezza,7.9]; % Heights of the different tank strips (referred to
z=0) and their associated thickness [mm]
alpha=0.619100;         % Mass proportional damping coefficient
beta=0.000636;          % Stiffness proportional damping coefficient

EsizeAlt=[];            % Effective finite element size in the vertical
direction [mm]
nDivisioni=ceil(virole (1,1)/Esize);
quote=linspace (0,virole(1,1),nDivisioni+1)';
EsizeAlt(1,1)=quote(2)-quote(1);
for i=2:size(virole,1)
    nDivisioni=ceil((virole(i,1)-virole(i-1,1))/Esize);
    tmpQuote=linspace (virole(i-1,1),virole(i,1),nDivisioni+1)';
    EsizeAlt(i,1)=tmpQuote(2)-tmpQuote(1);
    quote=[quote;tmpQuote(2:end)];
end
```

```

quoteMasse=quote(quote<=altezzaLiquido);

divAlt=length(quote)-1;
divCirc=ceil(2*pi*raggio/Esizer);
raggioTruss=raggio*0.9;
angoli=linspace(0,2*pi(),divCirc);
%%
outFile=fopen(outFileName,'w+');
fprintf(outFile,'*HEADING \n');
fprintf(outFile,'PROVA SERBATOIO \n');

close all
figure
hold on
%-----%
%                               TANK NODES                               %
%-----%
fprintf(outFile,'*NODE \n');
numNodo=1;
x=[];
y=[];
z=[];
for j=1:length(quote)
    fprintf(outFile,'*NODE, NSET=% s \n',['NODIANELLO',num2str(j)]);
    for i=1:length(angoli)-1
        x(numNodo,1)=raggio*cos(angoli(i));
        y(numNodo,1)=raggio*sin(angoli(i));
        z(numNodo,1)=quote(j);
        fprintf(outFile,'% d, % f, % f, % f
\n',numNodo,x(end),y(end),z(end));
        numNodo=numNodo+1;
    end
end
plot3(x,y,z,'.');

%-----%
%                               MASS NODES                               %
%-----%
if aggiungiMasse==1
    xTruss=[];
    yTruss=[];
    zTruss=[];
    numNodoTruss=1;
    for j=1:length(quoteMasse)
        for i=1:length(angoli)-1
            xTruss(numNodoTruss,1)=raggioTruss*cos(angoli(i));
            yTruss(numNodoTruss,1)=raggioTruss*sin(angoli(i));
            zTruss(numNodoTruss,1)=quoteMasse(j);
            if zTruss(end)~=0
                fprintf(outFile,'*NODE, NSET=% s
\n',['NODOMASSA',num2str(numNodoTruss)]);
                fprintf(outFile,'% d, % f, % f, % f
\n',numNodo,xTruss(end),yTruss(end),zTruss(end));
            end
            numNodo=numNodo+1;
            numNodoTruss=numNodoTruss+1;
        end
    end
end
plot3(xTruss,yTruss,zTruss,'.r');
end

```

```

%-----%
%
%                               TANK ELEMENTS
%-----%
fprintf(outFile,'*ELEMENT, TYPE=S4R, ELSET=SERBATOIO_F1 \n');
fascia=1;
numEle=1;
for i=1:divAlt
    for j=1:divCirc-1
        if j==(divCirc-1 )
            n1=(i-1)*(divCirc-1)+j;
            n2=(i-1)*(divCirc-1)+1;
            n3=i*(divCirc-1)+1;
            n4=i*(divCirc-1)+j;
        else
            n1=(i-1)*(divCirc-1)+j;
            n2=(i-1)*(divCirc-1)+j+1;
            n3=i*(divCirc-1)+j+1;
            n4=i*(divCirc-1)+j;
        end
        if z(n1)>=virole(fascia,1)
            fascia=fascia+1;
            fprintf(outFile,'*ELEMENT, TYPE=S4R, ELSET=% s
\n', ['SERBATOIO_F', num2str(fascia)]);
        end
        fprintf(outFile,'% d,\t% d,\t% d,\t% d,\t% d \n', numEle, n1, n2, n3, n4);
        numEle=numEle+1;
        plot3(x([n1, n2, n3, n4, n1]), y([n1, n2, n3, n4, n1]), z([n1, n2, n3, n4, n1]));
    end
end
%-----%
%
%                               MULTIPOINT CONSTRAINTS - LINKS
%-----%
if aggiungiMasse==1

    for i=1:length(quoteMasse)
        for j=1:divCirc-1
            n1=(i-1)*(divCirc-1)+j;
            n2=n1+length(x);
            if n1>=divCirc
                fprintf(outFile,'*MPC\nLINK, %d, %d\n', n1, n2);
            end
        end
    end
    plot3([x(n1), xTruss(n1)], [y(n1), yTruss(n1)], [z(n1), zTruss(n1)], 'r');
end

%-----%
%
%                               ADDED MASSES - Added masses positioning
%-----%
cntMassa=1;
for i=1:length(quoteMasse)
    for j=1:divCirc-1
        n1=(i-1)*(divCirc-1)+j;
        n2=n1+length(x);
        if n1>=divCirc
            fprintf(outFile,'*ELEMENT, TYPE=MASS, ELSET=% s
\n', ['MASSA', num2str(cntMassa)]);
            fprintf(outFile,'% d,\t% d \n', numEle, n2);
        end
        numEle=numEle+1;
        cntMassa=cntMassa+1;
    end
end

```

```

end
%-----%
%          ADDED MASSES - Added masses values and damping          %
%-----%
    cc1=2/(1.841^2-1)*cosh
(1.841*altezzaLiquido/raggio*quoteMasse/altezzaLiquido)/cosh(1.841*altezzaLiquido/raggio);
    cc2=2/(5.311^2-1)*cosh
(5.311*altezzaLiquido/raggio*quoteMasse/altezzaLiquido)/cosh(5.311*altezzaLiquido/raggio);
    cc3=2/(8.536^2-1)*cosh
(8.536*altezzaLiquido/raggio*quoteMasse/altezzaLiquido)/cosh(8.536*altezzaLiquido/raggio);
    ci=1-(cc1+cc2+cc3);

    primaQuota=1;
    mi=zeros(size(quoteMasse));
    for i=1:size(virole,1)-1
        ultimaQuota=find(quoteMasse==virole(i,1),1);

miTmp=densLiquido*raggio*ci(primaQuota:ultimaQuota)*EsizeAlt(i)*Esize;    %[t]
        miTmp(1)=miTmp(1)/2;
        miTmp(end)=miTmp(end)/2;
        mi(primaQuota:ultimaQuota)=mi(primaQuota:ultimaQuota)+miTmp;
        primaQuota=ultimaQuota;
    end

    cntMassa=1;
    for i=1:length(quoteMasse);
        valoreMassa=mi(i);
        for j=1:divCirc-1
            n1=(i-1)*(divCirc-1)+j;
            n2=n1+length(x);
            if n1>=divCirc
                fprintf(outFile, '*MASS,
ELSET=%s, alpha=%f\n', [ 'MASSA', num2str(cntMassa) ], alpha);
                fprintf(outFile, '% f, \n', valoreMassa);
            end
            numEle=numEle+1;
            cntMassa=cntMassa+1;
        end
    end

end
%-----%
%          MASS PROPERTIES OF THE MODEL          %
%-----%
V=pi*(raggio^2-(raggio-virole(1,2))^2)*(virole(1,1));
Mtank=densTank*V;
for i=2:length(virole)
    V=pi*(raggio^2-(raggio-virole(i,2))^2)*(virole(i,1)-virole(i-1,1));
    Mtank=Mtank+densTank*V;
end
Mtank                                % total mass of the shell
mi_tot=sum(mi)*(divCirc-1) ;          % total added mass
mres=sum(mi(2:end)./Esize);           % added mass along a meridian
Mi=pi*raggio*mres                     % horizontal component of the impulsive mass [t]
Mliq=pi*raggio^2*altezzaLiquido*densLiquido; % total liquid mass [t]
Mir=Mi/Mliq                           % impulsive mass ratio
Mmodel=Mtank+mi_tot                    % total mass of the model [t]
Mmodel_x=Mtank+Mi                      % horizontal component of the mass of the model [t]

```

```

%-----%
%                                     %
%                                     %
%-----%
    cntMassa=1;                        % Added masses constraints
    for i=2:length(quoteMasse)
        for j=1:divCirc-1
            idNodo=(i-1)*(divCirc-1)+j;
            fprintf(outFile,'*TRANSFORM, NSET=% s, TYPE=C
\n', ['NODOMASSA', num2str(idNodo)]);
            fprintf(outFile,'% f,\t% f,\t% f,\t% f,\t% f,\t% f
\n',0.0,0.0,0.0,0.0,0.0,1.0);
            fprintf(outFile,'*BOUNDARY \n');
            fprintf(outFile,'% d,\t2,\t3\n',idNodo+length(x));
            cntMassa=cntMassa+1;
        end
    end
end
fprintf(outFile,'** Name: incastro alla base Type: Displacement/Rotation\n');
% Encastre at the tank base
fprintf(outFile,'*Boundary\n');
fprintf(outFile,'NODIANELLO1, 1, 6\n');
%-----%
%                                     %
%                                     %
%-----%
fprintf(outFile,'*MATERIAL, NAME=STEEL \n');
fprintf(outFile,'*DENSITY \n');
fprintf(outFile,'7.85e-09,\n');
fprintf(outFile,'*ELASTIC, TYPE=ISO \n');
fprintf(outFile,'2.1E+5,\t0.3\n');
fprintf(outFile,'*PLASTIC, HARDENING=ISOTROPIC \n');
fprintf(outFile,'275,\t0\n');
fprintf(outFile,'430,\t0.039875\n');
fprintf(outFile,'*Damping,alpha=%f, beta=%f\n**\n',alpha,beta);

for i=1:size(virole,1)
    fprintf(outFile,'*SHELL SECTION, ELSET=% s,OFFSET=% f, MATERIAL=STEEL
\n', ['SERBATIOIO_F', num2str(i)],0.5);
    fprintf(outFile,'% f,\n',virole(i,2));
end
%-----%
%                                     %
%                                     %
%-----%
fprintf(outFile,'*Elset, elset=_SuperficieInternaCilindro_SNEG, generate \n
1, % d, 1\n',n1);
fprintf(outFile,'*Surface, type=ELEMENT, name=SuperficieInternaCilindro \n
_SuperficieInternaCilindro_SNEG, SNEG \n');

if StepStatico==1
fprintf(outFile,'** STEP: static\n** \n*Step, name=statico, nlgeom=yes \n
introduzione della pressione idrostatica \n*Static \n 1., 1., 1e-05,
1.\n**\n');
fprintf(outFile,'** LOADS\n**\n** Name: self weight Type: Gravity \n*Dload
\n, GRAV, % f, 0., 0., -1.\n** \n',g);
fprintf(outFile,'** Name: pressione idrostatica Type: Pressure \n*Dload \n
SuperficieInternaCilindro, HP, % f, % f,
0.\n**\n',densLiquido*altezzaLiquido*10^4,altezzaLiquido);
fprintf(outFile,'*End step \n');
end

if EigenvalueAnalysis==1
fprintf(outFile,'** STEP: frequency extraction \n**\n');
fprintf(outFile,'*Step, name=frequencyExtraction, perturbation \n');

```

```

fprintf(outFile, '*Frequency, eigensolver=Lanczos, acoustic coupling=off,
normalization=displacement \n');
fprintf(outFile, '700, 4, 6, , \n**\n');
fprintf(outFile, '*End step \n');
end

if ImplicitDynamicStep==1
fid=fopen('accelerogramma1.txt','r');
AAA=[];
while feof(fid)==0
BBB=fgets(fid);
pippo=str2num(BBB);
AAA=[AAA pippo];
end
fclose(fid);
time=[];
for i=1:2:length(AAA)
timetmp=AAA(i);
time=[time timetmp];
end
acceleration=[];
for i=2:2:length(AAA)
accelerationtmp=AAA(i);
acceleration=[acceleration accelerationtmp]; % base acceleration [m/s^2]
end
acceleration=acceleration*10^3; % base acceleration
[mm/s^2]
PGA=max(abs(acceleration)) % PGA [mm/s^2]
PGA_g=max(abs(acceleration./(10^3*9.81))) % PGA [g]
PGAtime=time(find(acceleration==PGA)) % Time instant at which the
PGA occurs [s]

fprintf(outFile, '*Amplitude, name=accelerogramma\n');
for i=1:length(time)
fprintf(outFile, '% f, % f\n', time(i), acceleration(i));
end

fprintf(outFile, '** STEP: dynamic implicit\n**\n');
fprintf(outFile, '*Step, name=dynamic implicit, nlgeom=YES, inc=2000\n');
fprintf(outFile, '*Dynamic\n');
fprintf(outFile, '0.02, %f, 1e-15, 0.02\n', time(end));
fprintf(outFile, '** Name: baseAcc Type: Acceleration/Angular
acceleration\n');
fprintf(outFile, '*Boundary, type=ACCELERATION, AMPLITUDE=accelerogramma\n');
fprintf(outFile, 'NODIANELLO1, 1, 1, 1.\n');
fprintf(outFile, '*End step \n');
end

fclose(outFile)

```

Appendix D

Here the MATLAB code used for the dynamic buckling analyses of the tank subjected to a specific accelerogram, scaled at different PGA, is reported. It is possible to run this code directly in MATLAB and the generated input files are solved by ABAQUS through the command “*system*”, which calls upon the operating system to execute the given command. The resulting status and standard output are returned. If n is the number of PGA values by which the accelerogram is scaled, with this code ABAQUS performs n dynamic analyses. The code requires the presence of the accelerogram in the same folder, saved as *.mat* files. The accelerogram is specified by the MATLAB variable *cntAccel*.

```
%------%
%                               EARTHQUAKE ENGINEERING           %
%           Added mass model of an anchored steel tanks         %
%           Incremental implicit dynamic analyses on 1 accelerogram %
%------%
for i=1:7;
load(['accelerogramma',num2str(i),'.mat'])
end
listAccel{1}=accelerogramma1;
listAccel{2}=accelerogramma2;
listAccel{3}=accelerogramma3;
listAccel{4}=accelerogramma4;
listAccel{5}=accelerogramma5;
listAccel{6}=accelerogramma6;
listAccel{7}=accelerogramma7;

PGA=[0.10,0.20,0.30,0.40,0.45,0.50];           % PGA in units of g

cntAccel=5;   % select the accelerogram you want to use

for cntPGA=1:length(PGA)
    time=listAccel{1,cntAccel}(:,1);
    acceleration=listAccel{1,cntAccel}(:,2);

SF(cntAccel,cntPGA)=PGA(cntPGA)/max(abs(acceleration./9.81)); % scale factor

outFileName=['Acc',num2str(cntAccel),'_PGA=',num2str(PGA(cntPGA)),'g.inp'];

%------%
%                               INPUT DATA                       %
%------%
aggiungiMasse=1;           % (1=yes,0=no)
StepStatico=1;             % (1=yes,0=no)
ImplicitDynamicStep=1;    % (1=yes,0=no)
densLiquido=1e-09;        % Mass density of the stored liquid [t/mm3]
```

```

densTank=7.85e-09;      % Mass density of the shell [t/mm3]
g=9810;                % gravity acceleration [mm/s2]
altezza=12089;         % Height of the tank walls [mm]
altezzaLiquido=10880; % Height of the stored liquid [mm]
raggio=15240;          % Tank radius [mm]
Esize=500;             % Initial finite element size [mm]
virole=[2425,12.7;
        4841,9.5;
        7257,7.9;
        9673,7.9;
        altezzaLiquido,7.9;
        altezza,7.9]; % Heights of the different tank strips (referred to
z=0) and their associated thickness [mm]
alpha=0.619100;       % Mass proportional damping coefficient
beta=0.000636;        % Stiffness proportional damping coefficient

EsizeAlt=[];          % Effective finite element size in the vertical
direction [mm]
nDivisioni=ceil(virole (1,1)/Esize);
quote=linspace (0,virole(1,1),nDivisioni+1)';
EsizeAlt(1,1)=quote(2)-quote(1);
for i=2:size(virole,1)
    nDivisioni=ceil((virole(i,1)-virole(i-1,1))/Esize);
    tmpQuote=linspace (virole(i-1,1),virole(i,1),nDivisioni+1)';
    EsizeAlt(i,1)=tmpQuote(2)-tmpQuote(1);
    quote=[quote;tmpQuote(2:end)];
end
quoteMasse=quote(quote<=altezzaLiquido);

divAlt=length(quote)-1;
divCirc=ceil(2*pi*raggio/Esize);
raggioTruss=raggio*0.9;
angoli=linspace(0,2*pi(),divCirc);
%%
outFile=fopen(outFileName,'w+');
fprintf(outFile,'*HEADING \n');
fprintf(outFile,'PROVA SERBATOIO \n');

figure(8)
hold on
%-----%
%                                TANK NODES                                %
%-----%
fprintf(outFile,'*NODE \n');
numNodo=1;
x=[];
y=[];
z=[];
for j=1:length(quote)
    fprintf(outFile,'*NODE, NSET=% s \n',['NODIANELLO',num2str(j)]);
    for i=1:length(angoli)-1
        x(numNodo,1)=raggio*cos(angoli(i));
        y(numNodo,1)=raggio*sin(angoli(i));
        z(numNodo,1)=quote(j);
        fprintf(outFile,'% d, % f, % f, % f
\n',numNodo,x(end),y(end),z(end));
        numNodo=numNodo+1;
    end
end
end
plot3(x,y,z, '. ');

```



```

%-----%
%
%                                MASS NODES
%-----%
if aggiungiMasse==1
    xTruss=[];
    yTruss=[];
    zTruss=[];
    numNodoTruss=1;
    for j=1:length(quoteMasse)
        for i=1:length(angoli)-1
            xTruss(numNodoTruss,1)=raggioTruss*cos(angoli(i));
            yTruss(numNodoTruss,1)=raggioTruss*sin(angoli(i));
            zTruss(numNodoTruss,1)=quoteMasse(j);
            if zTruss(end)~=0
                fprintf(outFile,'*NODE, NSET=% s
\n', ['NODOMASSA', num2str(numNodoTruss)]);
                fprintf(outFile,'% d, % f, % f, % f
\n', numNodo, xTruss(end), yTruss(end), zTruss(end));
            end
            numNodo=numNodo+1;
            numNodoTruss=numNodoTruss+1;
        end
    end
    plot3(xTruss, yTruss, zTruss, 'r');
end
%-----%
%
%                                TANK ELEMENTS
%-----%
fprintf(outFile,'*ELEMENT, TYPE=S4R, ELSET=SERBATOIO_F1 \n');
fascia=1;
numEle=1;
for i=1:divAlt
    for j=1:divCirc-1
        if j==(divCirc-1)
            n1=(i-1)*(divCirc-1)+j;
            n2=(i-1)*(divCirc-1)+1;
            n3=i*(divCirc-1)+1;
            n4=i*(divCirc-1)+j;
        else
            n1=(i-1)*(divCirc-1)+j;
            n2=(i-1)*(divCirc-1)+j+1;
            n3=i*(divCirc-1)+j+1;
            n4=i*(divCirc-1)+j;
        end
        if z(n1)>=virole(fascia,1)
            fascia=fascia+1;
            fprintf(outFile,'*ELEMENT, TYPE=S4R, ELSET=% s
\n', ['SERBATOIO_F', num2str(fascia)]);
            end
            fprintf(outFile,'% d, \t% d, \t% d, \t% d, \t% d \n', numEle, n1, n2, n3, n4);
            numEle=numEle+1;
            plot3(x([n1, n2, n3, n4, n1]), y([n1, n2, n3, n4, n1]), z([n1, n2, n3, n4, n1]));
        end
    end
end
%-----%
%
%                                MULTIPOINT CONSTRAINTS - LINKS
%-----%
if aggiungiMasse==1

    for i=1:length(quoteMasse)
        for j=1:divCirc-1
            n1=(i-1)*(divCirc-1)+j;

```

```

        n2=n1+length(x);
        if n1>=divCirc
            fprintf(outFile,'*MPC\nLINK, %d, %d\n', n1,n2);
        end

plot3([x(n1),xTruss(n1)], [y(n1),yTruss(n1)], [z(n1),zTruss(n1)], 'r');
    end
end

%-----%
%                ADDED MASSES - Added masses positioning                %
%-----%

    cntMassa=1;
    for i=1:length(quoteMasse)
        for j=1:divCirc-1
            n1=(i-1)*(divCirc-1)+j;
            n2=n1+length(x);
            if n1>=divCirc
                fprintf(outFile,'*ELEMENT, TYPE=MASS, ELSET=% s
\n', ['MASSA', num2str(cntMassa)]);
                fprintf(outFile,'% d,\t% d \n', numEle, n2);
            end
            numEle=numEle+1;
            cntMassa=cntMassa+1;
        end
    end

%-----%
%                ADDED MASSES - Added masses values and damping                %
%-----%

    cc1=2/(1.841^2-1)*cosh
(1.841*altezzaLiquido/raggio*quoteMasse/altezzaLiquido)/cosh(1.841*altezzaLiquido/raggio);
    cc2=2/(5.311^2-1)*cosh
(5.311*altezzaLiquido/raggio*quoteMasse/altezzaLiquido)/cosh(5.311*altezzaLiquido/raggio);
    cc3=2/(8.536^2-1)*cosh
(8.536*altezzaLiquido/raggio*quoteMasse/altezzaLiquido)/cosh(8.536*altezzaLiquido/raggio);
    ci=1-(cc1+cc2+cc3);

    primaQuota=1;
    mi=zeros(size(quoteMasse));
    for i=1:size(virole,1)-1
        ultimaQuota=find(quoteMasse==virole(i,1),1);

miTmp=densLiquido*raggio*ci(primaQuota:ultimaQuota)*EsizeAlt(i)*Esize;    %[t]
        miTmp(1)=miTmp (1)/2;
        miTmp(end)=miTmp (end)/2;
        mi(primaQuota:ultimaQuota)=mi(primaQuota:ultimaQuota)+miTmp;
        primaQuota=ultimaQuota;
    end

    cntMassa=1;
    for i=1:length(quoteMasse);
        valoreMassa=mi(i);
        for j=1:divCirc-1
            n1=(i-1)*(divCirc-1)+j;
            n2=n1+length(x);
            if n1>=divCirc
                fprintf(outFile,'*MASS,
ELSET=%s, alpha=%f\n', ['MASSA', num2str(cntMassa)], alpha);
                fprintf(outFile,'% f,\n', valoreMassa);
            end
        end
    end

```

```

        numEle=numEle+1;
        cntMassa=cntMassa+1;
    end
end
%-----%
%                               %
%                               %
%-----%
    cntMassa=1;                % Added masses constraints
    for i=2:length(quoteMasse)
        for j=1:divCirc-1
            idNodo=(i-1)*(divCirc-1)+j;
            fprintf(outFile,'*TRANSFORM, NSET=% s, TYPE=C
\n', ['NODOMASSA', num2str(idNodo)]);
            fprintf(outFile,'% f,\t% f,\t% f,\t% f,\t% f,\t% f
\n',0.0,0.0,0.0,0.0,0.0,1.0);
            fprintf(outFile,'*BOUNDARY \n');
            fprintf(outFile,'% d,\t2,\t3\n',idNodo+length(x));
            cntMassa=cntMassa+1;
        end
    end
end
fprintf(outFile,'** Name: incastro alla base Type: Displacement/Rotation\n');
% Encastre at the tank base
fprintf(outFile,'*Boundary\n');
fprintf(outFile,'NODIANELLO1, 1, 6\n');
%-----%
%                               %
%                               %
%-----%
fprintf(outFile,'*MATERIAL, NAME=STEEL \n');
fprintf(outFile,'*DENSITY \n');
fprintf(outFile,'7.85e-09,\n');
fprintf(outFile,'*ELASTIC, TYPE=ISO \n');
fprintf(outFile,'2.1E+5,\t0.3\n');
fprintf(outFile,'*PLASTIC, HARDENING=ISOTROPIC \n');
fprintf(outFile,'275,\t0\n');
fprintf(outFile,'430,\t0.039875\n');
fprintf(outFile,'*Damping,alpha=%f, beta=%f\n**\n',alpha,beta);

for i=1:size(virole,1)
    fprintf(outFile,'*SHELL SECTION, ELSET=% s,OFFSET=% f, MATERIAL=STEEL
\n', ['SERBATOIO_F', num2str(i)],0.5);
    fprintf(outFile,'% f,\n',virole(i,2));
end
%-----%
%                               %
%                               %
%-----%
fprintf(outFile,'*Elset, elset=_SuperficieInternaCilindro_SNEG, generate \n
1, % d, 1\n',n1);
fprintf(outFile,'*Surface, type=ELEMENT, name=SuperficieInternaCilindro \n
_SuperficieInternaCilindro_SNEG, SNEG \n');

if StepStatico==1
fprintf(outFile,'** STEP: static\n** \n*Step, name=statico, nlgeom=yes \n
introduzione della pressione idrostatica \n*Static \n 1., 1., 1e-05,
1.\n**\n');
fprintf(outFile,'** LOADS\n**\n** Name: self weight Type: Gravity \n*Dload
\n, GRAV, % f, 0., 0., -1.\n** \n',g);
fprintf(outFile,'** Name: pressione idrostatica Type: Pressure \n*Dload \n
SuperficieInternaCilindro, HP, % f, % f,
0.\n**\n',densLiquido*altezzaLiquido*10^4,altezzaLiquido);

```

```

fprintf(outFile, '** OUTPUT REQUESTS\n**\n*Restart, write,
frequency=0\n**\n');
fprintf(outFile, '** FIELD OUTPUT: F-Output-1\n**\n*Output, field\n');
fprintf(outFile, '*Node Output\n');
fprintf(outFile, 'CF, RF, U\n**\n');
fprintf(outFile, '** FIELD OUTPUT: F-Output-2\n**\n');
fprintf(outFile, '*Element Output, directions=YES\n');
fprintf(outFile, 'MISES, PE, PEEQ, PEMAG, S\n');
fprintf(outFile, '*Output, history, frequency=0\n');
fprintf(outFile, '*End step \n');
end

if ImplicitDynamicStep==1

acceleration=acceleration*10^3* SF(cntAccel,cntPGA); % scaled base
acceleration [mm/s^2]

fprintf(outFile, '*Amplitude, name=accelerogramma\n');
for i=1:length(time)
    fprintf(outFile, '% f,% f\n',time(i),acceleration(i));
end

fprintf(outFile, '** STEP: dynamic implicit\n**\n');
fprintf(outFile, '*Step, name=dynamic implicit, nlgeom=YES, amplitude=RAMP,
inc=%d\n', 2*length(time));

fprintf(outFile, '*Dynamic,application=TRANSIENT FIDELITY\n %f,%f,1E-
15,%f\n',time(2),time(end),time(2));

fprintf(outFile, '*Solution Technique, type=QUASI-NEWTON\n**\n');
fprintf(outFile, '** Name: baseAcc Type: Acceleration/Angular
acceleration\n');
fprintf(outFile, '*Boundary, type=ACCELERATION, AMPLITUDE=accelerogramma\n');
fprintf(outFile, 'NODIANELLO1, 1, 1, 1.\n');

fprintf(outFile, '** OUTPUT REQUESTS\n**\n*Restart, write,
frequency=0\n**\n');
fprintf(outFile, '** FIELD OUTPUT: F-Output-1\n**\n*Output, field, time
interval=%f\n',time(2));
fprintf(outFile, '*Node Output\n');
fprintf(outFile, 'CF, RF, U\n**\n');
fprintf(outFile, '** FIELD OUTPUT: F-Output-2\n**\n*Output, field, time
interval=%f\n',time(2));
fprintf(outFile, '*Element Output, directions=YES\n');
fprintf(outFile, 'MISES, PE, PEEQ, PEMAG, S\n');
fprintf(outFile, '*Output, history, frequency=0\n');

fprintf(outFile, '*End step \n');
end

fclose(outFile)

system(['abaqus job=Acc',num2str(cntAccel),'_PGA=',num2str(PGA(cntPGA)),'g
interactive cpus=4'])
end

```

Appendix E

Here the MATLAB code used for searching the control node of the structure for a given accelerogram (specified in the variable *acc*) is presented. The code develops the pseudo-equilibrium path for each node and returns as output the node that first buckles, i.e. the node that shows the lowest PGA_{cr} . The pseudo-equilibrium path is built by means of a bilinear regression model, also contained in this code. The variables *tol* and *slope* represent the main constraint in the preparation of the bilinear model. The code requires the presence in the same folder of a *.txt* file read by the command *dlmread* and containing the displacements *u1,u2* for each control node at each time. The calculation of the radial displacements is performed by means of the external function $[ur,ut]=ruotaSpostamenti(u1,u2,x,y)$ that employs the rotation matrix to calculate the tangential and radial displacements starting from those in the x and y direction and the coordinate x and y of each node. The most important outputs of the code are the time-histories of the control node (stored in the variable *controlNode_timehistory*) and its maximum responses (stored in the variable *punti*), used to built its pseudo-equilibrium path.

```
%-----%
%                               EARTHQUAKE ENGINEERING                               %
%           Added mass model of an anchored steel tanks                             %
%                               Finding the control node                             %
%-----%

acc=7;    % select the accelerogram you want to consider

PGA=[0.10,0.20,0.30,0.40,0.45,0.50,0.55,0.60,0.65,0.70,0.75]; % PGA (g)
PGAY=[0.3 0.3 0.3 0.3 0.2 0.3 0.4]; % PGAs that produce the first yielding

plot2=0;  % Maximum responses (1=yes,0=no)
plot3=0;  % Pseudo-equilibrium paths for each node (1=yes,0=no)
plot4=0;  % Pseudo-equilibrium paths for the control node (1=yes,0=no)
plot5=0;  % PGAYielding (1=yes,0=no)

tol=1;    % r^2 coefficient
slope=.55; % slope ratio -> nonlinear slope/linear slope

%----- Control nodes -----%
nodiAvanti1=566:382:5150;
x=1.47153e+004;
y=-3.96458e+003;
x1A=[x x x x x x x x x x x x x];
y1A=[y y y y y y y y y y y y y];

nodiAvanti2=377:382:4961;
x=1.49441e+004;
```

```
y=-2.98854e+003;  
x2A=[x x x x x x x x x x x x x];  
y2A=[y y y y y y y y y y y y y];
```

```
nodiaVanti3=570:382:5154;  
x=1.51083e+004;  
y=-1.99957e+003;  
x3A=[x x x x x x x x x x x x x];  
y3A=[y y y y y y y y y y y y y];
```

```
nodiaVanti4=381:382:4965;  
x=1.52070e+004;  
y=-1.00195e+003;  
x4A=[x x x x x x x x x x x x x];  
y4A=[y y y y y y y y y y y y y];
```

```
nodiaVanti5=383:382:4967;  
x=1.52400e+004;  
y=0.00000e+000;  
x5A=[x x x x x x x x x x x x x];  
y5A=[y y y y y y y y y y y y y];
```

```
nodiaVanti6=194:382:4778;  
x=1.52070e+004;  
y=1.00195e+003;  
x6A=[x x x x x x x x x x x x x];  
y6A=[y y y y y y y y y y y y y];
```

```
nodiaVanti7=387:382:4971;  
x=1.51083e+004;  
y=1.99957e+003;  
x7A=[x x x x x x x x x x x x x];  
y7A=[y y y y y y y y y y y y y];
```

```
nodiaVanti8=198:382:4782;  
x=1.49441e+004;  
y=2.98854e+003;  
x8A=[x x x x x x x x x x x x x];  
y8A=[y y y y y y y y y y y y y];
```

```
nodiaVanti9=391:382:4975;  
x=1.47153e+004;  
y=3.96458e+003;  
x9A=[x x x x x x x x x x x x x];  
y9A=[y y y y y y y y y y y y y];
```

```
nodiaDietro1=470:382:5054;  
x=-1.46481e+004;  
y=4.20607e+003;  
x1D=[x x x x x x x x x x x x x];  
y1D=[y y y y y y y y y y y y y];
```

```
nodiaDietro2=281:382:4865;  
x=-1.48929e+004;  
y=3.23393e+003;  
x2D=[x x x x x x x x x x x x x];  
y2D=[y y y y y y y y y y y y y];
```

```
nodiaDietro3=474:382:5058;  
x=-1.50733e+004;  
y=2.24779e+003;
```

```

x3D=[x x x x x x x x x x x x x];
y3D=[y y y y y y y y y y y y y];

nodiDietro4=285:382:4869;
x=-1.51885e+004;
y=1.25194e+003;
x4D=[x x x x x x x x x x x x x];
y4D=[y y y y y y y y y y y y y];

nodiDietro5=478:382:5062;
x=-1.52379e+004;
y=2.50658e+002;
x5D=[x x x x x x x x x x x x x];
y5D=[y y y y y y y y y y y y y];

nodiDietro6=289:382:4873;
x=-1.52215e+004;
y=-7.51703e+002;
x6D=[x x x x x x x x x x x x x];
y6D=[y y y y y y y y y y y y y];

nodiDietro7=482:382:5066;
x=-1.51391e+004;
y=-1.75081e+003;
x7D=[x x x x x x x x x x x x x];
y7D=[y y y y y y y y y y y y y];

nodiDietro8=293:382:4877;
x=-1.49912e+004;
y=-2.74234e+003;
x8D=[x x x x x x x x x x x x x];
y8D=[y y y y y y y y y y y y y];

nodiDietro9=486:382:5070;
x=-1.47785e+004;
y=-3.72201e+003;
x9D=[x x x x x x x x x x x x x];
y9D=[y y y y y y y y y y y y y];

controlNodes=[nodiAvanti1 nodiAvanti2 nodiAvanti3 nodiAvanti4 nodiAvanti5
nodiAvanti6 nodiAvanti7 nodiAvanti8 nodiAvanti9 nodiDietro1 nodiDietro2
nodiDietro3 nodiDietro4 nodiDietro5 nodiDietro6 nodiDietro7 nodiDietro8
nodiDietro9];
coord_x=[x1A x2A x3A x4A x5A x6A x7A x8A x9A x1D x2D x3D x4D x5D x6D x7D x8D
x9D];
coord_y=[y1A y2A y3A y4A y5A y6A y7A y8A y9A y1D y2D y3D y4D y5D y6D y7D y8D
y9D];

[controlNodes,ordine]=sort(controlNodes);
coord_x=coord_x(ordine); % vettore contenente le coord x dei nodi di
controllo ordinati
coord_y=coord_y(ordine); % vettore contenente le coord x dei nodi di
controllo ordinati

%----- Displacement time histories -----%

for cntPGA=1:length(PGA);

u=dlmread(['Acc',num2str(acc),'_PGA=',num2str(PGA(cntPGA)),'g.nodeDisp.txt'])
; % matrice contenente tempi,u1,u2

```

```

u=u(:,1:end-1); % elimino l'ultima colonna (colonna di zeri generata da
abagus)

time=u(:,1); % estraggo la prima colonna (tempo)

u=u(:,2:end); % matrice contenente tempi,u1,u2

U1=u(:,1:2:end); % matrice contenente u1 (spostamenti in x)
U2=u(:,2:2:end); % matrice contenente u2 (spostamenti in y)

for i=1:length(controlNodes)
    x=coord_x(i);
    y=coord_y(i);
    u1=U1(:,i);
    u2=U2(:,i);
    [ur,ut]=ruotaSpostamenti(u1,u2,x,y);
    Ur(:,i)=ur; % matrice contenente ur (spostamenti radiali)
end

for i=1:length(controlNodes);
ur_controlNodes.p{i}(:,cntPGA)=Ur(:,i); % inserisco i dati in una
struttura, contenente gli spostamenti radiali di ogni nodo per ogni PGA
end

end

% cerco lo spostamento radiale max
for i=1:length(controlNodes);
    for j=1:length(PGA);

cmpMax=find(abs(ur_controlNodes.p{i}(:,j))==max(abs(ur_controlNodes.p{i}(:,j)
))) );
        max_ur(i,j)=abs(ur_controlNodes.p{i}(cmpMax(1),j)); % matrice
contenente lo spost. max per ogni nodo (riga) corrispondente ai diversi
valori di PGA (colonne)
        end
    end
end

%----- Pseudo-equilibrium paths in terms of PGA -----%

for cntNodo=1:length(controlNodes);

    if plot2==1;
        h1=figure(length(controlNodes)+cntNodo)
        set(h1, 'Units', 'normalized','Position', [0 0 1 1]);
set(gcf,'color',[1 1 1]);
        grid off
        box on
        plot(max_ur(cntNodo,:),PGA,'o','Markersize',10)
        h2=title(['Maximum responses -
Node',num2str(controlNodes(cntNodo))]);
        set(h2,'color','black','fontsize',20,'fontname','cambria');
        h4=xlabel('|max u_r| [mm]');
        set(h4,'color','black','fontsize',15,'fontname','cambria');
h5=ylabel('PGA [g]');
        set(h5,'color','black','fontsize',15,'fontname','cambria');
set(gca,'fontsize',15,'fontname','cambria','LineWidth',1);

```



```

        hold on
    end

    x=max_ur(cntNodo,:);
    y=PGA;

% ----- regressione sul tratto lineare

    for i=2:length(x);

        [b,bint,r,rint,stats] = regress(y(1:i)',[ones(i,1),x(1:i)']);
        r2(i)=stats(1);

        if stats(1)<tol;
            break
        end

    end

    i=i-1;
    [b,bint,r,rint,stats] = regress(y(1:i)',[ones(i,1),x(1:i)']);
    r2(i)=stats(1);

    C1=[b(2) b(1)]; % m-q tratto lineare

% ----- regressione sul tratto nonlineare

    if i~=length(x);

        [b,bint,r,rint,stats] = regress(y(i+1:end)',[ones(length(x)-
i,1),x(i+1:end)')]);

        C2=[b(2) b(1)]; % m-q tratto nonlineare

        if C2(1)<slope*C1(1)
% ----- punto di ginocchio

            x_cr(cntNodo)=(C2(2)-C1(2))/(C1(1)-C2(1));
            y_cr(cntNodo)=C2(1)*x_cr(cntNodo)+C2(2);

            disp(['Nodo ',num2str(controlNodes(cntNodo)),' - Knee point
coordinates: u_r=',num2str(x_cr(cntNodo)),' [mm],
PGA=',num2str(y_cr(cntNodo)),' g'])

            xp1=x(1):.001:x_cr(cntNodo);
            xp2=x_cr(cntNodo):.001:max(x);

            if plot3==1;
                h1=figure(2*length(controlNodes)+cntNodo);
                box on
                grid off
                hold on
                %set(h1, 'Units', 'normalized','Position', [0 0 1 1]);
            set(gcf,'color',[1 1 1]);
                plot(x,y,'o','Markersize',10);
                plot(x_cr(cntNodo),y_cr(cntNodo),'r-
x','Markersize',15,'LineWidth',3)
                plot(xp1,xp1*C1(1)+C1(2))
                plot(xp2,xp2*C2(1)+C2(2))

```

```

                h2=title(['Pseudo-equilibrium path, ', 'Node
', num2str(controlNodes(cntNodo))]);
                set(h2, 'color', 'black', 'fontsize', 20, 'fontname', 'cambria');
h4=xlabel('max|u_r| [mm]');
                set(h4, 'color', 'black', 'fontsize', 15, 'fontname', 'cambria');
h5=ylabel('PGA [g]');
                set(h5, 'color', 'black', 'fontsize', 15, 'fontname', 'cambria');
set(gca, 'fontsize', 15, 'fontname', 'cambria', 'LineWidth', 1);
                end
            else
                disp(['Nodo ', num2str(controlNodes(cntNodo)), ' - Insufficient
nonlinear slope - Here the response is assumed to be still linear'])
            end
        else
                disp(['Nodo ', num2str(controlNodes(cntNodo)), ' - Here the response is
still linear'])
        end
    end
end

% ----- punto di controllo
for i=1:length(y_cr);
    if y_cr(i)==0;
        y_cr(i)=100; % porto la PGA critica dei pti che rimangono in campo
lineare a 100, per evitare che questi punti vengano presi come pti di
controllo
    else
        y_cr(i)=y_cr(i);
    end
end

cmpMin=find(y_cr==min(y_cr)); % ricerca della PGA critica più bassa - cmpMin
indica la posizione del nodo di controllo all' interno del vettore
controlNodes
disp('-----');
disp(['CONTROL NODE: ', num2str(controlNodes(cmpMin)), ', PGA_cr=
', num2str(min(y_cr)), 'g']);

controlNode_timehistory(:,1)=time; % memorizzo le time histories dello
spostam. radiale del nodo di controllo
controlNode_timehistory(:,2:length(PGA)+1)=ur_controlNodes.p{cmpMin}; %
memorizzo le time histories dello spostam. radiale del nodo di controllo
punti=max_ur(cmpMin(1),:); % memorizzo gli spostamenti radiali max del nodo
di controllo

if plot4==1;
    cmpMin=cmpMin(1);
    x=max_ur(cmpMin,:);
    y=PGA;
    for i=2:length(x);
        [b,bint,r,rint,stats] = regress(y(1:i)', [ones(i,1), x(1:i)']);
        r2(i)=stats(1);
        if stats(1)<tol;
            break
        end
    end
    end
    i=i-1;
end

```

```

    [b,bint,r,rint,stats] = regress(y(1:i)',[ones(i,1),x(1:i)']);
    r2(i)=stats(1);
    C1=[b(2) b(1)]; % m-q tratto lineare
    [b,bint,r,rint,stats] = regress(y(i+1:end)',[ones(length(x)-
i,1),x(i+1:end)']));
    C2=[b(2) b(1)]; % m-q tratto nonlineare
    xp1=x(1):.001:x_cr(cmpMin);
    xp2=x_cr(cmpMin):.001:max(x);
h1=figure(1000);
box on
grid off
hold on
%set(h1, 'Units', 'normalized','Position', [0 0 1 1]);
set(gcf,'color',[1 1 1]); ylim([0 0.8])
plot(xp1,xp1*C1(1)+C1(2),'k')
plot(xp2,xp2*C2(1)+C2(2),'k')
plot(x,y,'o','Markersize',10,'color','k','MarkerFaceColor','k','MarkerEdgeCol
or','k');
plot(x_cr(cmpMin),y_cr(cmpMin),'r-x','Markersize',25,'LineWidth',3)
h2=title(['Pseudo-equilibrium path, Accelerogram ',num2str(acc),' Node
',num2str(controlNodes(cmpMin)),' (control node)']);
set(h2,'color','black','fontsize',20,'fontname','cambria');
h4=xlabel('max|u_r| [mm]');
set(h4,'color','black','fontsize',15,'fontname','cambria'); h5=ylabel('PGA
[g]');
set(h5,'color','black','fontsize',15,'fontname','cambria');
set(gca,'fontsize',15,'fontname','cambria','LineWidth',1);
h1=gtext(['Critical PGA=',num2str(chop(y_cr(cmpMin),3)),'g']);
set(h1,'color','r','fontsize',18,'fontname','cambria');
end

if plot5==1;
figure(1000);
box on
grid off
hold on
plot([0 max(x)],[PGAy(acc) PGAY(acc)],'b:','Linewidth',3)
h1=gtext('First yielding');
set(h1,'color','b','fontsize',18,'fontname','cambria');
end

```


Notation

a	Dimensionless frequency function
b	Dimensionless parameter indicating the construction quality
A_c	Convective pseudo-acceleration
A_{cn}	Pseudo-acceleration of the n^{th} convective mode
A_f	Pseudo-acceleration of a simple oscillator with circular frequency ω_f
A_g	Horizontal ground-acceleration, time history
a_g	Horizontal peak ground acceleration
a_{vg}	Vertical peak ground acceleration
A_i	Impulsive pseudo-acceleration
A_v	Vertical ground acceleration, time history
A_{vf}	Pseudo-acceleration corresponding to T_v
C_{ij}	Impulsive coefficient of the j^{th} impulsive mode
C_{cn}	Convective coefficient of the n^{th} convective mode
C_n^p	Dimensionless coefficient for the hydrodynamic pressure along the tank wall
C_n^M	Dimensionless coefficient for the overturning moment on the tank wall
$C_n^{M'}$	Dimensionless coefficient for the overturning moment on the tank base
C_n^Q	Dimensionless coefficient for the base shear on the wall
C_ϑ	Buckling factor
D	Inside diameter of the tank
E	Joint efficiency
E_w	Modulus of elasticity of the tank material
f_{cn}	Natural cyclic frequency of the n^{th} convective mode
f_{ij}	Natural cyclic frequency of the j^{th} impulsive mode
f_{mb}	Critical buckling stress with regard to the “elastic buckling” limit state
f_{pb}	Critical buckling stress with regard to the “elastic-plastic buckling” limit state
f_y	Yield strength of steel
G_s	Shear modulus of the soil

g	Gravity acceleration constant $9,81 \text{ m/s}^2$
H	Height of the stored liquid
H_w	Height of the tank walls
h_c	Convective height for the calculation of the overturning moment above the base
h'_c	Convective height for the calculation of the overturning moment below the base
h_i	Impulsive height for the calculation of the overturning moment above the base
h'_i	Impulsive height for the calculation of the overturning moment below the base
I_0	Modified Bessel function of order 0
I_1	Modified Bessel function of order 1
I'_1	First derivative of the modified Bessel function of order 1
J	Anchorage ratio
J_1	Bessel function of the first order
k_f	Stiffness of the deformable tank
k_w	Pressure transformation coefficient
k_x	Horizontal stiffness of the foundation
k_θ	Rocking stiffness of the foundation
L	Uplifted length in unanchored tanks
M	Total overturning moment above the base plate
m	Total mass of the stored liquid $= \rho\pi RH^2$
M'	Total overturning moment below the base plate
M_c	Convective contribution to the overturning moment above the base plate
M'_c	Convective contribution to the overturning moment below the base plate
m_c	Convective mass of the stored liquid
m_f	Flexible mass component
M_i	Impulsive contribution to the overturning moment above the base plate
m_i	Impulsive mass of the stored liquid
M'_i	Impulsive contribution to the overturning moment below the base plate
m_r	Mass of the tank roof
m_{tot}	Total mass of the filled tank (including the foundation)
m_w	Mass of the tank wall
m_0	Mass of the foundation
N_c	Convective hoop membrane force in tank shell
N_h	Hydrostatic membrane force

N_i	Impulsive hoop membrane force in tank shell
P	Total pressure, including hydrostatic and hydrodynamic contribution p_{stat} , p
p	Total hydrodynamic pressure, including the three contributions p_i , p_c , p_v
p_c	Convective pressure component resulting from the horizontal earthquake component
p_i	Impulsive pressure component resulting from the horizontal earthquake component
p_{stat}	Hydrostatic pressure
p_v	Pressure component resulting from the vertical earthquake excitation
Q	Total base shear
q	Behavior factor
Q_c	Convective contribution to the base shear
Q_i	Impulsive contribution to the base shear
R	Inside radius of the tank
R_w	Response modification factor
R_0	Radius of the circular foundation
r	Cylindrical coordinate in radial direction
SF	Safety factor
S_e	Elastic pseudo-acceleration
S_d	Design pseudo-acceleration
t	Temporal coordinate
t_a	Thickness of the bottom plate
T_c	Natural period of the first convective mode
T_{cn}	Natural period of the n^{th} convective mode
T_f^*	Modified natural period for the flexible component
T_i	Natural period of the fundamental impulsive mode (including tank inertia)
T_i^*	Modified natural period for the impulsive component
T_{ij}	Natural period of the j^{th} impulsive mode
T_v	Time period of vertical mode
t_w	Thickness of the tank wall
u	Displacement of the tank wall at the surface of the liquid at any time t
\dot{u}	Velocity of the tank wall at the surface of the liquid at any time t
\ddot{u}	Acceleration of the tank wall at the surface of the liquid at any time t
v_r	Velocity component in the radial direction
v_s	Velocity of shear wave propagation in the soil

v_z	Velocity component in the vertical direction
v_θ	Velocity component in the tangential direction
W	Total weight of the stored liquid
w	Vertical uplift in unanchored tanks
w_L	Weight of the fluid content that resists the overturning moment in unanchored tanks
W_r	Weight of the tank roof
w_r	Weight of the tank roof, distributed on the perimeter
W_w	Weight of the tank wall
w_w	Weight of the tank wall, distributed on the perimeter
x	Ground displacement in the x-direction at any time t
\dot{x}	Ground velocity in the x-direction at any time t
\ddot{x}	Ground acceleration in the x-direction at any time t
y	Distance from liquid surface to analysis point
z	Vertical Cartesian coordinate
$\hat{\alpha}$	Knockdown factor adopted by API 650
α_x	Frequency-dependent factors converting horizontal static stiffness into dynamic one
α_θ	Frequency-dependent factors converting rocking static stiffness into dynamic one
β	Frequency ratio
β_x	Frequency-dependent factors providing a radiation damping value for horizontal motion
β_θ	Frequency-dependent factors providing a radiation damping value for rocking motion
γ	Slenderness parameter = H/R , but also safety factor in ECCS recommendation
γ_I	Importance factor
δ	Sloshing wave height, but also maximum imperfection amplitude in buckling's formulas
ς	Dimensionless height of the stored liquid = z/H
θ	Rotation of the plastic hinge in the tank base
ϑ	Cylindrical coordinate angle
λ_n	n^{th} root of the first derivative of the Bessel function of the first kind and first order
ν_s	Poisson's ratio of the soil
ν_w	Poisson's ratio of the tank material, approximately 0.30 for steel and 0.20 for concrete
ξ	Dimensionless distance from the tank vertical axis = r/H
ξ_m	Material damping in the tank
$\bar{\xi}_i$	Modified damping ratio
ξ_s	Damping ratio of the soil

ρ	Mass density of the stored liquid
ρ_s	Mass density of the soil
ρ_w	Mass density of the tank walls
$\bar{\sigma}$	Knockdown factor adopted by Eurocode 8
σ_c	Maximum longitudinal (vertical) shell compression stress
σ_{c1}	Critical Euler's axial buckling stress (theoretical or ideal buckling stress)
$\sigma_{\theta,c1}$	Critical Euler's circumferential buckling stress
σ_p	Hoop stress in the shell, induced by internal pressure
σ_T	Total tensile hoop stress in the shell
σ_0	Buckling stress parameter
ϕ	Velocity potential function
ϕ_c	Convective contribution to ϕ
ϕ_i	Impulsive contribution to ϕ
ψ	Vibration mode dimensionless function
ω	Dimensionless length parameter, but also forcing frequency
ω_{cn}	Natural circular frequency of the n^{th} convective mode

References

- [1] ACI 350.3-06: *Seismic Design of Liquid-Containing Concrete Structures*. An American Concrete Institute Standard, 2001.
- [2] API 650: *Welded Tanks for Oil-Storage*. American Petroleum Institute Standard, Washington D.C., 1998.
- [3] Baker, J. W.: *Vector-valued ground motion intensity measures for probabilistic seismic demand analysis*. Ph. D. Dissertation, Department of Civil and Environmental Engineering. Sanford, CA, U.S., University of Stanford, 2005.
- [4] Bayraktar A., Sevim B., Altunisik A.C., Turker T.: *Effect of the model updating on the earthquake behavior of steel storage tanks*. Journal of Constructional Steel Research, 2009.
- [5] Barton D. C., Parker J. V.: *Finite element analysis of the seismic response of anchored and unanchored liquid storage tanks*. Earthquake Engineering and Structural Dynamics, 1987.
- [6] Brown K. J., Rugar P. J., Davis C. A., Rulla T. A.: *Seismic performance of Los Angeles water tanks*. Proc. Fourth U.S. Conf. On Lifeline Earthquake Engrg., M. J. O'Rourke, Editor, ASCE, New York, NY, 668-675, 1995.
- [7] Chen J.F., Rotter J.M. and Teng J.G.: *Strengthening silos and tanks against elephant's foot buckling*. Advance in Steel Structures, Vol. I, published by Elsevier Ltd, 2005.
- [8] Chopra A.K., *Dynamics of Structures – Theory and Applications to Earthquake Engineering*, Pearson Prentice Hall New Jersey, 2007.
- [9] Cornell C.A., Jalayer F. et al.: *Probabilistic Basis for 2000 SAC Federal Emergency Management Agency Steel Moment Frame Guidelines*. Journal of Structural Engineering 128(4): 526 - 533, 2002.
- [10] Di Carluccio A., Fabbrocino G., Manfredi G.: *Risposta Sismica di serbatoi Atmosferici per Olio Combustibile*. Anidis, Bologna, 2009.

- [11] Eurocode 3: *Design of steel structures, Part 1-6: Strength and Stability of Shell Structures*. European Committee for Standardization, Bruxelles, 2007.
- [12] Eurocode 8: *Design of structures for earthquake resistance, Part 1: General rules, seismic actions and rules for buildings*. European Committee for Standardization, Bruxelles, 2004.
- [13] Eurocode 8: *Design of structures for earthquake resistance, Part 4: Silos, tanks and pipelines*. European Committee for Standardization, Bruxelles, 2006.
- [14] European Convention for Constructional Steelwork (ECCS): *Buckling of Steel Shells-European Recommendations*. Bruxelles, 1988.
- [15] Fischer F.D., Rammerstorfer F.G., Scharf K.: *Earthquake Resistant Design of Anchored and Unanchored Liquid Storage Tanks under Three-Dimensional Earthquake Excitation*. G.I. Schuëller (Ed.), Springer Verlag, Berlin, 1991.
- [16] Fischer F.D., Rammerstorfer F.G., Scharf K.: *Storage tanks under earthquake loading*. G.I. Schuëller (Ed.), ASME Applied Mechanics Review, 1990.
- [17] Habenberger J., Schwarz J.: *Seismic Response of Flexibly Supported Anchored Liquid Storage Tanks*, Proc. 13th European Conference on Earthquake Engineering, London, 2002.
- [18] Hamdan F.H.: *Seismic behaviour of cylindrical steel liquid storage tanks*. Journal of Constructional Steel Research, 1999.
- [19] Haroun M.A.: *Behavior of Unanchored Oil Storage Tanks: Imperial Valley Earthquake*. Journal of Technical topics in Civil Engineering, Vol 109, ASCE, 1983.
- [20] Haroun M.A.: *Mitigation of elephant-foot bulge formation in seismically-excited steel storage tanks*. 18th International Conference on Structural Mechanics in Reactor technology, Beijing, China, August 2005.
- [21] Haroun M.A.: *Implications of recent nonlinear analysis on seismic standards of liquid storage tanks*. Nuclear Engineering and Design, 2002.
- [22] Haroun M.A., Housner G.W.: *Earthquake Response of Deformable Liquid Storage Tanks*. Journal of Applied Mechanics, Vol.48, pp.411-417, 1981.
- [23] Hibbit H.D., Karlsson B.I., Sorensen P.: *ABAQUS Explicit User's Manual*, 2002.
- [24] Hibbit H.D., Karlsson B.I., Sorensen P.: *ABAQUS Standard User's Manual*, 2002.

- [25] Hibbit H.D., Karlsson B.I., Sorensen P.: *ABAQUS Theory Manual*, 2002.
- [26] Housner G.W.: *The dynamic behavior of water tanks*. Bulletin of the Seismological Society of America, Vol.53, No.2, pp.381-387, 1963.
- [27] Iervolino I., Fabbrocino G., Manfredi G.: *Fragility of standard industrial structures by a response surface based method*. Journal of Earthquake Engineering, 2004.
- [28] Jaiswal O.R. et al.: *Review of Code Provisions on Seismic Analysis of Liquid Storage Tanks*. IITK-GSDMA Project on Building Codes, 2003.
- [29] Koller M.G., Malhotra P.K.: *Seismic evaluation of unanchored cylindrical tanks*. 13th World Conference on Earthquake Engineering, Vancouver, 2004.
- [30] Malhotra P.K., Wenk T. and Wieland M.: *Simple procedure for Seismic Analysis of Liquid-Storage Tanks*. Structural Engineering International, 2000.
- [31] Nachtigall I., Gebbeken N., Urrutia-Galicia J.L.: *On the analysis of vertical circular cylindrical tanks under earthquake excitation as its base*. Engineering Structures, 2002.
- [32] Natsiavas S.: *An Analytical Model for Unanchored Fluid-Filled Tanks Under Base Excitation*. Journal of Applied Mechanics, Vol 55, 1988.
- [33] Natsiavas S., Babcock C.D.: *Behavior of Unanchored Fluid-Filled Tanks Subjected to Ground Excitation*. Journal of Applied Mechanics, Vol 55, 1988.
- [34] NTC08: *Norme Tecniche per le Costruzioni, Capitolo 3*. Decreto Ministeriale 14.01.2008.
- [35] O'Rourke M.J., Eeri M., So P.: *Seismic Fragility Curves for On-Grade Steel Tanks*. Earthquake spectra, 2000.
- [36] Peek R.: *Analysis of unanchored liquid storage tanks under lateral loads*. Earthquake Engineering and Structural Dynamics, 1988.
- [37] Peek R., Jennings P.C.: *Simplified analysis of unanchored tanks*. Earthquake Engineering and Structural Dynamics, 1988.
- [38] Priestley N.: *Seismic Design of Storage Tanks*. Recommendations of a Study Group of the New Zealand National Society for Earthquake Engineering, December 1986.

- [39] Rossi F., Tavano M.: *Elasto-Plastic Analyses of Cylindrical Liquid-Storage Tanks under Earthquake Excitation*. Computational Mechanics Project Work, University of Bologna, A.A. 2010-2011.
- [40] Salzano E., Iervolino I., Fabbrocino G.: *Seismic risk of atmospheric storage tanks in the framework of quantitative risk analysis*. Journal of Loss Prevention in the Process Industry, 2003.
- [41] Scharf K.: *Contribution to the Behaviour of Earthquake Excited Above-Ground Liquid Storage Tanks*. Doctoral Thesis, Institute of Light Weight Structures, University of Vienna, 1989.
- [42] Seiler C., Wunderlich W.: *Nonlinear treatment of liquid-filled storage tanks under earthquake excitation by quasistatic approach*. Computers & Structures, 2000.
- [43] Simitises G.J., Hodges D.H.: *Fundamentals of structural stability*. Butterworth-Heinemann Ed., 2005.
- [44] Talaslidis D.G., Monolis G.D., Paraskevopoulos E., Panagiotopoulos C., Pelekasis N., Tsamopoulos J.A.: *Risk analysis of industrial structures under extreme transient loads*. Soil Dynamics and Earthquake Engineering, 2004.
- [45] Tanov R., Tabiei A.: *Static and dynamic buckling of laminated composite shells*, Mechanics of Composite Materials and Structures, 1999, 6:195-206.
- [46] Tothong P., Luco N.: *Probabilistic seismic demand analysis using advanced ground motion intensity measure*. Earthquake Engineering and Structural Dynamics **36**:1837–1860, 2007.
- [47] Veletsos A.S.: *Seismic response and design of liquid storage tanks*. Guidelines for the seismic design of oil and gas pipeline systems, Technical Council on Lifeline Earthquake Engineering, ASCE, N.Y., pp. 255-370, 443-461, 1984.
- [48] Veletsos A.S., Shivakumar P.: *Dynamic response of tanks containing liquids or solids*. Department of Civil Engineering, Rice University, Houston, Texas, 1997.
- [49] Veletsos A.S., Tang Y.: *Dynamic Response of Flexibly Supported Liquid-Storage Tanks*. Journal of Structural Engineering, 1992.
- [50] Veletsos A.S., Tang Y.: *Rocking Response of Liquid Storage Tanks*. Journal of Engineering Mechanics, ASCE, Vol 113, 1987.

- [51] Veletsos A.S., Tang Y.: *Soil-Structure Interaction Effects for Laterally Excited Liquid-Storage Tanks*. Journal of Earthquake Engineering and Structural Dynamics, 1990.
- [52] Virella J.C., Godoy L.A., Suarez L.E.: *Dynamic buckling of anchored steel tanks subjected to horizontal earthquake excitation*. Journal of Constructional Steel Research, 2005.
- [53] Virella J.C., Godoy L.A., Suarez L.E.: *Effect of Pre-Stress States on the Impulsive Modes of Vibration of Cylindrical Tank-liquid Systems under Horizontal Motions*. Journal of Vibration and Control, 2005.
- [54] Virella J.C., Godoy L.A., Suarez L.E.: *Fundamental modes of tank liquid systems under horizontal motions*. Engineering Structures, 2005.
- [55] Wunderlich W., Seiler C., Schwarz J., Habenberger J.: *Seismic response and failure mechanism of flexibly supported liquid storage tanks*. 12th World Conference on Earthquake Engineering, Auckland, New Zealand, 2000.
- [56] Yang J.Y.: *Dynamic behavior of fluid-tank systems*. Ph.D. Dissertation, Rice University, Houston, Texas, 1976.

